Development of a multi-distance, multi-channel broadband near-infrared spectroscopy system to investigate the spatial variation in cellular oxygen metabolism in the healthy and injured adult human brains

Phong Thanh Phan

A thesis submitted to University College London

for the Degree of Doctor of Philosophy (Ph.D)

University College London (UCL)

Department of Medical Physics and Biomedical Engineering

August, 2017

Declaration

I, Phong Thanh Phan, confirm that the work presented in this thesis is my own. Where information has been derived from other sources, I confirm that this has been indicated in the thesis.

Abstract

This PhD thesis describes the progressive development of a multi-channel, multi-distance broadband NIRS system designed to measure the concentration changes in oxygenated haemoglobin (HbO_2), deoxygenated haemoglobin (HHb), and especially the oxidation state of cytochrome-c-oxidase (oxCCO) across multiple regions of the adult human brain. The system was developed using an iterative approach, through two major iterations. At each iteration, in vivo tests in healthy adult volunteers were performed to test the system capability. The first iteration was the pseudo broadband diffuse optical tomography system, achieved by physically moving one source fibre and eight detector fibres across multiple positions in a fixed 3D printed probe holder. A functional activation task involving the visual cortex was used as an in vivo test of this approach. The second iteration was the full multi-channel, multi-distance broadband NIRS system, achieved by increasing the number of source and detector fibres and integrating a time-multiplexing mechanism for the sources. The capability of this system was tested using functional activation tasks involving both the visual and frontal cortices. The final version of the system was then used in the neurointensive care unit to monitor the frontal regions of patients with acute brain injury, demonstrating the capability for monitoring the temporal and spatial variations in cerebral haemodynamics and oxygen metabolism.

The multi-channel, multi-distance broadband NIRS measurements acquired from various functional activation studies and the clinical study have provided evidence for the existence of a spatially dependent Δ[oxCCO] signal. More importantly, they show that the spatial variation in Δ[oxCCO] can be monitored using a multi-channel broadband NIRS approach. The measurements collected during various stages of system development have allowed the implementation of the oxCCO image reconstruction algorithm, reconstructing 3D tomographic images of oxCCO for the first time. The combined developments in hardware engineering, data acquisition, clinical studies and image reconstruction open up a whole new avenue for the investigation of cerebral oxygen metabolism in the healthy and injured adult human brain.

Impact Statement

The work presented in this thesis has provided the fundamental experimental data and tools for future research and development of a whole new range of medical devices that can be used in both research and clinical medicine.

The multi-channel broadband near-infrared spectroscopy system developed as a result of this PhD can be used for future neuroscience research to investigate the spatial variation of cerebral oxygen metabolism during cognitive processes or for future clinical research to investigate pathological mechanisms in patients with brain injury. In terms of future research, this work has provided evidence to support a new avenue of NIRS research using the spatially resolved oxCCO signal together with traditional NIRS parameters to understand more about the coupling between haemodynamic changes and metabolism in various scenarios. Given the inherent benefits of NIRS as a non-invasive and portable technique, this can bring the ability to measure changes in cerebral oxygen metabolism to the bedside or even in non-laboratory-based experimental protocols to investigate metabolic processes in the healthy and injured brain.

In term of clinical practice, this work has demonstrated the potential benefits of having multi-regional measurements of cerebral oxygen metabolism in that it can provide a regional measurement of cerebral autoregulation in the injured brain. Moreover, the images reconstructed from the multi-channel broadband data reveal some interesting temporal and spatial variations in the haemodynamics and metabolism of the injured brain. In the future, this work can be extended to provide real-time 3D tomographic images of cerebral haemodynamics and metabolism at the bedside of patients with acute brain injury. This can provide clinicians with the additional information at the right time to identify regions with deranged cerebral autoregulation and individualise treatments to improve clinical outcomes. This is the first step of realising a suite of technology that can provide clinicians with real-time information about the state of the brain through the use of non-invasive technology.

Acknowledgements

I would like to thank my supervisors: Professor Clare Elwell, who has provided me with a wonderful subject matter for my PhD and has been inspirational, encouraging and always supportive during the course of my PhD ; and Dr Ilias Tachtsidis, who has not only been the source of wisdom but also a source of motivation for the work that I have done. I also want to thank Dr Sabrina Brigadoi for her incredible support with the image reconstruction part of this work.

I am indebted to Dr David Highton who has not only been a great mentor but also a good friend who has been patient, kind and knowledgeable guiding me through this work. This project would not have been successful without his hard work. I also want to thank Professor Martin Smith who has been incredibly supportive in guiding me through the clinical work and in the writing of the clinical chapter of this thesis.

I have been very fortunate to undertake this PhD in the Department of Medical Physics and Biomedical Engineering where everyone is really friendly and supportive, making my every day in the office a pleasure. I have made some wonderful friends who share my every day with during the past three years: Gemma, Izzy, Fred. Thank you all for making it a pleasant journey. I also would like to thank other members of the Multimodal Spectroscopy group who have always been there to help me along the way: Paola, Josh, Matthew, Luca, Suzi. I also want to thank the "engineers" Danial, Dimitrios and Prash for always being there to answer all my engineering questions.

I must also thank my Vietnamese friends from VietPro, VietStartups, SVUK, VietSocs that make London feel more like home and with whom I shared a lot of good student memories with during the last three years. Thank you all for letting me be who I am and appreciate my presence.

I am greatly in debt to my parents and my family for their unconditional love, support and encouragement, without which I could not have achieved what I have today. I must also thank the youngest member of my family, my nephew Bean, who has brought a new grain of happiness to my whole family.

Publications and Presentations Resulting from this Work

Conference Presentations

- ISOTT 2017 - Presentation **Phong Phan**, David Highton, Sabrina Brigadoi, Martin Smith, Ilias Tachtsidis and Clare Elwell. Monitoring the spatial variation in haemodynamics and cellular oxygen metabolism in patients with acute brain injury using multi-channel broadband NIRS. In 45th Annual Meeting of the International Society of oxygen transport in tissue (ISOTT 2017) Halle, Germany.

- UCL Neuroscience Symposium 2017 - Poster **Phong Phan**, David Highton, Sabrina Brigadoi, Ilias Tachtsidis and Clare Elwell. Non-invasive optical monitoring of brain metabolism in the adult brain using broadband near-infrared spectroscopy imaging. In UCL Neuroscience Symposium 2017, London, UK.

- BMLA 2017 - Presentation **Phong Phan**, David Highton, Sabrina Brigadoi, Martin Smith, Ilias Tachtsidis and Clare Elwell. Multi-channel multi-distance broadband near-infrared spectroscopy system to measure the spatial response of cellular oxygen metabolism. In 2017, 35th Annual conference of British Medical Laser Association (BMLA 2017), Manchester, UK.

- OSA 2016 - Presentation **Phong Phan**, David Highton, Martin Smith, Ilias Tachtsidis and Clare Elwell (2016). A new multi-channel broadband near-infrared spectroscopy system to measure spatial distribution of cytochrome-c-oxidase and tissue oxygenation. In Biomedical optics conference 2016, Miami, Florida, USA. OSA Technical Digest (online) (Optical Society of America, 2016), paper OM4C.3 `https://doi.org/10.1364/OTS.2016.OM4C.3`

- ISOTT 2016 - Presentation **Phong Phan**, David Highton, Martin Smith, Ilias Tacht-

sidis and Clare Elwell (2016). Spatial distribution of cellular oxygen metabolism in the presence of normal haemodynamic responses during frontal love activation using broadband near-infrared spectroscopy. In 44th Annual Meeting of the International Society of oxygen transport in tissue (ISOTT 2016) Chicago, USA.

- fNIRS 2016 - Presentation **Phong Phan**, David Highton, Jonathan Lai, Ilias Tachtsidis, Martin Smith and Clare Elwell (2016). A new multichannel broadband near-infrared spectroscopy system to measure the spatial distribution of cellular oxygen metabolism and tissue oxygenation. In 2016 Biennial meeting of the Society for functional near infrared spectroscopy (fNIRS 2016) Paris, France.

- fNIRS 2016 - Presentation David Highton, Danial Chitnis, **Phong Phan**, Robert J Cooper, Simone Quaggia, Ilias Tachtsidis, Nicholas Everdell, Jeremy Hebden, Martin Smith and Clare Elwell. Multi-wavelength diffuse optical tomography to resolve cytochrome c oxidase. (fNRIS 2016) Paris, France.

- SNACC 2016 - Presentation David Highton, **Phong Phan**, Sabrina Brigadoi, Ilias Tachtsidis, Clare Elwell and Martin Smith. Spatial characterization of haemodynamic regulation following acute brain injury using broadband diffuse optical spectroscopy. SNACC 44th Annual Meeting (Chicago 2016), Chicago, USA.

- IARS 2016 - Presentation David Highton, **Phong Phan**, Sabrina Brigadoi, Jonathan Lai, Ilias Tachtsidis, Clare Elwell and Martin Smith. Imaging mitochondrial redox status following brain injury using diffuse optical spectroscopy. International Anesthesia Research Society 2016 Annual Meeting (San Francisco 2016), San Francisco, USA.

- ISOTT 2015 - Presentation **Phong Phan**, David Highton, Sabrina Brigadoi, Ilias Tachtsidis and Clare Elwell. Investigating the spatial distribution of cytochrome c oxidase in the visual cortex using broadband near infrared spectroscopy. (ISOTT 2015), Wuhan, China.

- UCL Neuroscience Symposium 2015 – Poster **Phong Phan**, David Highton, Sabrina Brigadoi, Ilias Tachtsidis and Clare Elwell. Spatial distribution of changes in oxidised cytochrome c oxidase during visual stimulation using broadband near infrared spectroscopy imaging. (UCL 2015), London, UK.

First-authored Published Articles

- **Phong Phan**, David Highton, Sabrina Brigadoi, Ilias Tachtsidis, Martin Smith, Clare Elwell (2016). Spatial distribution of changes in oxidised cytochrome c oxidase during visual stimulation using broadband near infrared spectroscopy imaging. Adv Exp Med Biol. 923:195-201. doi:10.1007/978-3-319-38810-6_26

- **Phong Phan**, David Highton, Jonathan Lai, Martin Smith, Clare Elwell and Ilias Tachtsidis (2016). Multi-channel multi-distance broadband near-infrared spectroscopy system to measure the spatial response of cellular oxygen metabolism and tissue oxygenation. Biomedical Optics Express 7(11), 4424-4440. doi:https://doi.org/10.1364/BOE.7.004424

Other Published Articles

- Danial Chitnis, Dimitrios Airantzis, David Highton, Rhys Williams, **Phong Phan**, Valsiliki Giagka, Samuel Powell, Robert J Cooper, Ilias Tachtsidis, Martin Smith, Clare Elwell, Jeremy C Hebden, Nicholas Everdell. Toward a wearable near infrared spectroscopic probe for monitoring concentrations of multiple chromophores in biological tissue in vivo. Review of Scientific Instruments 87(6):065112 (June 2016). doi:http://dx.doi.org/10.1063/1.4954722

- Sabrina Brigadoi, **Phong Phan**, David Highton. Samuel Powell, Robert J. Cooper, Jeremy Hebden, Martin Smith, Ilias Tachtsidis, Clare Elwell and Adam P. Gibson. Image reconstruction of oxidized cerebral cytochrome C oxidase changes from broadband nearinfrared spectroscopy data. Neurophotonics 2017 Apr; 4(2): 021105. doi:10.1117/1.NPh.4.2.021105

- David Highton, **Phong Phan**, Sabrina Brigadoi, Ilias Tachtsidis, Clare Elwell and Martin Smith (2016). Spatial characterization of haemodynamic regulation following acute brain injury using broadband diffuse optical spectroscopy. SNACC 2016. doi:10.1097/ANA.0000000000000358

Contents

List of Figures

List of Tables

Abbreviations

ABI acute brain injury. 35

ABP arterial blood pressure. 45

ATP adenosine triphosphate. 48

BBB blood-brain barrier. 41, 43

BOLD blood-oxygen-level-dependent. 50

BORL Biomedical Optics Research Laboratory. 34

CA cerebral pressure autoregulation. 44

Ca^{2+} calcium. 46

CBF cerebral blood flow. 40

CCD charge-coupled device. 81

CCO cytochrome c oxidase. 34

CO_2 carbon dioxide. 49

CoG centre of gravity. 104

CPP cerebral perfusion pressure. 45

CW continuous-wave. 59

DLPFC dorsolateral prefrontal cortex. 167

DOT diffuse optical tomography. 93

ECM extracellular matrix. 51

EDCF endothelium-derived contracting factor. 46

EDRF endothelium-derived relaxing factor. 46

EEG electroencephalography. 55

ERP event-related potential. 55

ETC electron transport chain. 53, 66

$FADH_2$ flavin adenine dinucleotide. 53

FD frequency domain. 77

FDG fluorodeoxyglucose. 56

fMRI functional magnetic resonance imaging. 47, 57

fNIRS functional near-infrared spectroscopy. 47, 57

FV flow velocity. 174

H^+ protons. 53

HbO_2 oxygenated haemoglobin. 34

HHb deoxygenated haemoglobin. 34

ICP intracranial pressure. 45

K^+ postassium ion. 49

MBLL modified Beer-Lambert law. 70

MDBBS multi-distance broadband instrument. 85

MEG magnetoencephalography. 56

Mx mean velocity index. 175

Na^+ sodium ions. 51

NADH nicotinamide adenine dinucleotide. 53

NIR near-infrared. 34, 57, 59

NIRS near-infrared spectroscopy. 34

NO nitric oxide. 49

NVU neurovascular unit. 41

oxCCO oxidised cytochrome c oxidase. 59

pCO_2 partial pressure of CO_2. 49

PET positron emission tomography. 47

PG prostaglandin. 50

PRx pressure reactivity index. 175

SMC smooth muscle cell. 42, 43, 46

SPECT single photon emission tomography. 56

SRS spatially resolved spectroscopy. 75

TCD transcranial Doppler. 174

TOI tissue oxygenation index. 75

TR time-resolved. 77

Nomenclature

A attenuation. 62

I light intensity. 60

T specific transmittance. 62

Δ change. 73

α specific absorption coefficient. 62

ϵ specific extinction coefficient. 62

λ wavelength. 63

μ_a absorption coefficient. 60

μ_s scattering coefficient. 69

c velocity of light. 76

c concentration. 61

D diffusion coefficient. 76

DPF differential pathlength factor. 71, 78

G light loss due to scattering. 71

k extinction coefficient. 61

R intensity of the reflected light. 76

Chapter 1

Introduction

This chapter introduces the technique of near-infrared spectroscopy, its clinical relevance and the motivation and objectives behind the work presented in this thesis. The main motivation of this work emerges from the benefits of having a non-invasive instrument that can monitor changes in cerebral oxygen metabolism across multiple regions in the adult human brain. This instrument can potentially be used to monitor the spatial variation in cerebral metabolism in the injured brain to provide relevant clinical information to guide targeted therapy that can improve clinical outcomes.

1.1 Near-infrared spectroscopy introduction

Near-infrared spectroscopy (NIRS) is a non-invasive, non-ionising optical technique that uses light in the near-infrared (NIR) region of the spectrum to interrogate biological tissue. Within this region of the spectrum, three compounds absorb light strongly: oxygenated haemoglobin (HbO_2), deoxygenated haemoglobin (HHb) and cytochrome c oxidase (CCO). The measurements derived from the changes of HbO_2 and HHb can provide information about the changes in cerebral haemodynamics and oxygenation while the measurement derived from the changes of CCO can provide insights into the changes in cerebral cellular oxygen metabolism. NIRS has for many years been used to investigate changes in haemodynamics and metabolism of various types of biological tissues [1], [2].

To date, most commercial NIRS devices rely on a dual wavelength approach, limiting their capabilities to the measurements of HbO_2 and HHb [3]. These measurements are not directly related to changes in metabolic activity during neuronal activation. Over recent decades the Biomedical Optics Research Laboratory (BORL) at UCL has been developing novel optical systems and methods with a particular focus on the measurement

of CCO to inform on cellular oxygen metabolism. Simultaneous measurements of CCO and haemoglobin signals may provide complementary information on the haemodynamics, oxygenation and metabolism of biological tissue.

In order to accurately monitor changes in CCO, a compound that exists in a much lower concentration in tissue compared to haemoglobin, a broadband NIRS system measuring the intensity changes over more than 100 wavelengths is needed. Our group has expertise in building these systems and we have developed and used several broadband NIRS devices to investigate the measurement of CCO in the animal brain, the adult brain and the neonate brain. [4]–[16]. However, these systems only have the capability of monitoring the CCO signal over one or two areas. Given that NIRS measurements are only sensitive to the brain area directly below the locations of the source-detector pairs, this limits the brain areas that can be monitored and more importantly, the result is critically dependent on the placement of these single source-detector probes. Moreover, if only a limited number of measurement channels is used, inadequate data are acquired to allow image reconstruction of spatial changes in any of the chromophores. In this thesis, a new multi-channel, multi-distance broadband NIRS system will be presented to overcome these issues and provide, for the first time, the capability to provide images of localised measures of CCO.

1.2 Clinical introduction

There is significant interest in using NIRS in the clinical setting following studies showing that treatment guided by NIRS can improve clinical outcomes in specific clinical scenarios where there is an increased risk of cerebral ischemic injury [17]. In the case of acute brain injury (ABI) where there is significant morbidity and mortality, multi-modal continuous monitoring is necessary to understand the multi-factorial and complex nature of the pathophysiology. Two components in particular have been identified as having key importance in brain injury: reduction in substrate delivery below critical thresholds and failing cellular metabolism characterised by the inability of the mitochondria to utilize the delivered oxygen and glucose, resulting in profound energy crisis within the injured brain [18]. This failure of oxygen metabolism may occur without cerebral ischemia and be spatially varying [19]. As a result, there is a clinical need to simultaneously monitor the oxygenation, haemodynamics and metabolism in the injured brain across multiple regions to identify the time critical windows for an individual patient to deliver targeted treatments to prevent secondary injury and improve outcomes.

However, as mentioned earlier, most commercial NIRS devices do not have the capability to measure CCO and in-house systems optimised for the measurement of CCO provide only a limited number of channels, limiting the measurement of metabolism to one or two areas of the brain. This project is aimed at filling that unmet clinical need of monitoring the brain of patients with acute brain injury with a system that can monitor oxygenation, haemodynamics and metabolism across multiple areas simultaneously. Spatially resolved CCO may provide useful insights into the heterogeneity of the cellular metabolic processes in the injured brain and help identify regions with metabolic crisis. Those insights can be used to optimise treatments for every individual patient and as a result, improve clinical outcomes.

1.3 The iterative development process

We have taken an iterative approach in the development process of the multi-channel, multi-distance broadband NIRS system. The final iteration of the system is the result of developments in hardware, data acquisition, data analysis and image reconstruction. At each iterative step, functional activation tasks were used as a testing platform to evaluate the capability of the system to monitor changes in oxygenation, haemodynamics and metabolism in the adult brain.

1.4 Motivations and objectives

This work was motivated by both the clinical and research need for a NIRS system that has the capability of measuring the changes in CCO over multiple regions as described earlier. It is important to state that the work presented in this thesis brings together and expands the previous work on developing NIRS instrumentation and monitoring the adult human brain during functional activation and brain injury studies. This work requires overcoming both the technical and clinical challenges with innovative analysis to investigate the feasibility of monitoring the spatial variation of CCO signal across the adult human brain. Therefore, the focus of this PhD is to develop a novel multi-channel, multi-distance broadband NIRS system to monitor the variation in the CCO signal across multiple regions of the healthy and injured adult human brains. With that in mind, the specific objectives of this PhD are:

- To develop a pseudo broadband diffuse optical tomography system to validate the feasibility of monitoring the spatial variation of CCO response.

- To design and develop a multi-channel, multi-distance broadband NIRS system that can simultaneously monitor changes in the CCO signal across multiple areas of the adult human brain together with changes in oxygenation and haemodynamics.
- To demonstrate the use of the multi-channel system to monitor the variation in CCO response in healthy volunteers during functional activation tasks and in patients with acute brain injury.
- To develop signal processing methods to extract insights from the multi-channel data sets collected from patients with brain injury.
- To facilitate the development of an image reconstruction algorithm for CCO using the multi-channel, multi-distance broadband NIRS data collected by the system.

1.5 Thesis overview

This thesis describes the progressive evolution of a broadband NIRS system into a multi-channel, multi-distance system with the capability of monitoring concentration changes of oxidised CCO together with the changes in haemoglobin concentrations. At each step of development, specific experiments with a small number of subjects were done to test the working of the system. This is similar to what has previously been done in the field of NIRS, with proof of principle studies requiring a small number of subjects.

For the background information, Chapter 2 provides the details about the functional anatomy of the human brain with focus on the neurovascular unit, the regulation of cerebral blood flow and the metabolic processes in the brain. Neuromonitoring techniques will also be discussed to provide the background on brain monitoring techniques. Chapter 3 provides the fundamentals of NIRS, a brief review on NIRS instrumentation that can measure CCO signal, a summary of NIRS studies investigating the measurement of CCO in the adult brain and the technical details of a broadband NIRS system that was used to develop the multi-channel, multi-distance system of this thesis.

Chapter 4 covers the first iterative step of the development process, resulting in the pseudo broadband diffuse optical tomography system. That system was then used to validate the feasibility of monitoring the spatial variation in the response of CCO to a visual functional activation task. Chapter 5 covers the whole development of the multi-channel, multi-distance broadband NIRS system from the upgrade of the hardware and software to the development of the analysis algorithm. It also describes the testing of the system with phantom studies, the in vivo experiments with cuff occlusion studies,

visual functional activation study and prefrontal cortex functional activation study.

Chapter 6 provides the results from a pilot clinical study investigating the use of the multi-channel, multi-distance broadband system to monitor changes in oxygenation, haemodynamics and metabolism in patients with acute brain injury. The thesis closes with a brief summary of the current experiments and planned future experiments utilising the capability of the system and a discussion of the future continuation of this work.

1.6 Personal Statement

The work presented in this thesis can be separated in four parts: the development of the instrumentation, the design of functional activation tasks and its data collection, the clinical data collection and the analysis of the data. This requires the collaborative effort of a number of individuals and it is important to acknowledge the effort of those individuals and to highlight the work that I carried out.

The development of the instrumentation was carried out by myself with the guidance of my colleagues and supervisors. This involved modifying the working of the system with additional optical components, designing optical fibres and probe holders and integrating the new functionality into existing software to bring together the modified hardware and software. Preliminary testing and characterisation of the system were also done by myself.

The design of the functional activation tasks and its data collection were done by myself while the clinical data collection required the help of my clinical colleague Dr David Highton, an anaesthetics registrar. Dr Highton and I, with the guidance of our supervisors (Dr Ilias Tachtsidis, Professor Clare Elwell and Professor Martin Smith) integrated the multi-channel, multi-distance broadband NIRS system into the neurocritical care unit to collect multi-modal data sets from brain injured patients . As well as data collection, I was responsible for the quality of the optical data, the synchronising of the data and the development of analysis algorithm.

All the data analysis presented in this thesis were done by myself with the exception of the image reconstruction which required the expertise of Dr Sabrina Brigadoi. I collected and pre-processed the multi-distance, multi-channel broadband data before passing it to Dr Brigadoi to run it through an image reconstruction algorithm to produce tomographic images of concentration changes. The development of this reconstruction algorithm was facilitated by the work presented in this thesis.

Some results from the work presented in this thesis have been published in peer-reviewed journals. I have written two first-authored papers and assisted in another three papers published by my colleagues, the details of which are presented in the previous section.

Chapter 2

Functional anatomy and physiology of the adult human brain

This chapter describes the fundamental functional anatomy and physiology of the healthy adult human brain. These background information is essential to assist the understanding and interpretation of NIRS parameters. This chapter begins with a brief overview of the functional anatomy of the human brain and its functional unit, before exploring different mechanisms regulating cerebral blood flow (CBF) and metabolism. Finally, different neuroimaging techniques that can be used to investigate the functioning brain are discussed to put NIRS technology into perspectives.

2.1 Functional anatomy of the brain and the regulation of cerebral blood flow

The brain is the most complex and active organ of the human body. It has a constantly high metabolic demand for nutrients and oxygen for normal functionality. In a normal healthy adult, the brain receives more than 15% of blood flow from cardiac output despite taking up only 2% of body weight [20]. However, the brain has a limited capacity to store energy and it relies on the change in CBF for the delivery of nutrients and oxygen to match its varying demand and for the removal of carbon dioxide and other waste products. Although there is some degree of homeostasis in most body systems, homeostasis in the brain is extraordinary with many overlapping mechanisms to ensure

the matching of CBF and metabolic demand as the brain is extra-sensitive to under or overperfusion. Any mismatch in supply and demand can result in severe metabolic consequences [21] and pathologies [22], [23]. The control of CBF is complex and not fully understood. However, previous studies have identified three key mechanisms that ensure that the transport of nutrients and oxygen is continuous and in an organised manner to fulfil the demand of neural tissue. These are cerebral pressure autoregulation, maintaining a relatively constant CBF in the face of changing perfusion pressure, functional hyperaemia (or flow-metabolism coupling), increasing CBF to active regions of the brain, and neurogenic regulation, modulating CBF directly in the face of changing activity [24]. These overlapping mechanisms work closely with each other using some key structural components to create a coordinated regulation of CBF. In this section of the thesis, those key structural components, that together constitute the neurovascular unit, will be discussed in detail before investigating individual mechanisms of CBF regulation.

2.1.1 Neurovascular Unit

Neurovascular unit (NVU) is a group of cells that are in intimate anatomical and chemical relationship with each other to establish a functional whole that can detect changes in neural tissue and trigger necessary responses to regulate CBF to meet metabolic demands [25]. The key components of the NVU are neurons, astrocytes and endothelial cells that interact with each others through positive and negative feedback mechanisms [26]. Each component seems to have a specific but not fully established role but they maintain dynamic linkages among themselves under normal physiological conditions. Neurons and astrocytes work closely with each other during signal transduction to mediate the release of neurotransmitters and their re-uptake at synapses whereas astrocytes and endothelial cells work closely with each other at the blood-brain barrier (BBB) to maintain its integrity (Figure 2.1). Neurons, astrocytes and endothelial cells work closely with each other to regulate CBF to meet metabolic demand.

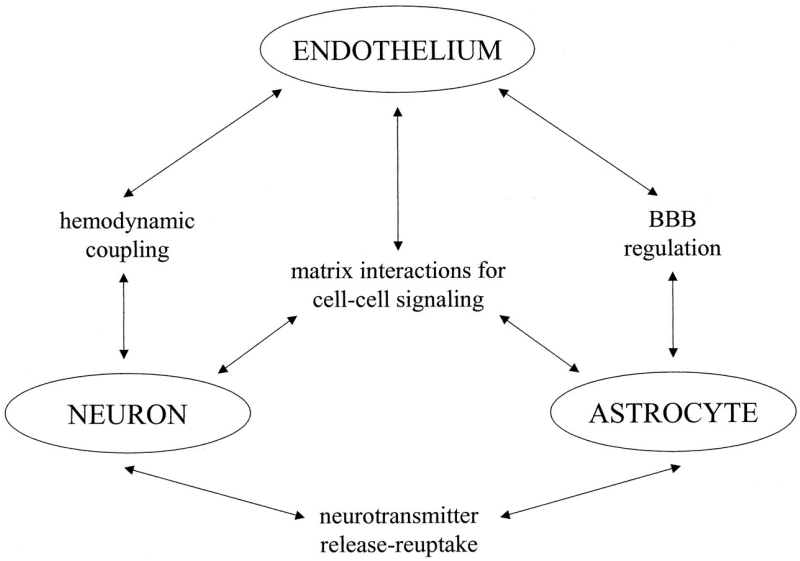

Figure 2.1: Schematic showing the interactions between fundamental components of the NVU ([27]).

2.1.1.1 Neurons

Neurons are the basic working unit of the brain. All neurons are electrically excitable and they can transmit and receive signals through electrochemical processes. These cells can transmit information to other neurons, glial cells, muscle cells and gland cells. A typical neuron has a cell body, dendrites and an axon. Dendrites are thin structures that arise from the cell body to receive signals from axons of other neurons via synapses. An axon is an elongated cellular extension from the cell body to transmit an electrical signal. Neurons are considered the central component of the NVU as they can detect small variations in the availability of nutrients, oxygen and other metabolic wastes in their surrounding microenvironment and transform these signals into electrical and chemical signals to other neurons or other components of the NVU to turn on corresponding adjustment mechanisms [28]. There is evidence showing that neurons can directly control the vascular tone of blood vessels via the innervation of smooth muscle cells (SMCs) or indirectly through the interaction with astrocytes, endothelial cells and other interneurons to control blood flow to their surrounding environment (Figure 2.2) [29], [30].

2.1.1.2 Astrocytes

Astrocytes are an important type of glial cells that play the central supporting role in the NVU. Astrocytes have a characteristic star-shaped morphology due to the presence of multiple processes, some of which envelop synapses made by neurons while others are in close contact with the vascular tree. Astrocytes also have end-feet that are closely

applied to the wall of cerebral microvessels (Figure 2.2). Therefore, astrocytes provide the link between the cells in the vasculature and the neurons, facilitating the coupling between neural activity and change in CBF. Astrocytes perform several roles, many of which are still not fully elucidated. Within the NVU, astrocytes do not only support endothelial cells to form the BBB, a selective barrier formed by endothelial cells that line cerebral microvessels, but also assist neurons to perform their functions [31].

2.1.1.3 Endothelial cells

Endothelial cells are squamous cells that form the vascular endothelium, the inner lining of blood vessels, and provide a single cell barrier between the blood and the wall of the vessels. Adjacent endothelial cells are linked with each other by complex tight junctions, forming the BBB that forces molecules from the bloodstream to take the transcellular route to get through the BBB rather than the paracellular route through the junctions (Figure 2.2) [26]. This mechanism allows strict regulation of substance movement to the brain tissue. Apart from being the physical barrier between the bloodstream and the brain tissue, endothelial cells are in constant communication with neurons and astrocytes to regulate CBF via the release of vasoactive substances. These vasoactive substances can have direct effects on vascular SMCs to initiate vasoconstriction or vasodilation to control CBF.

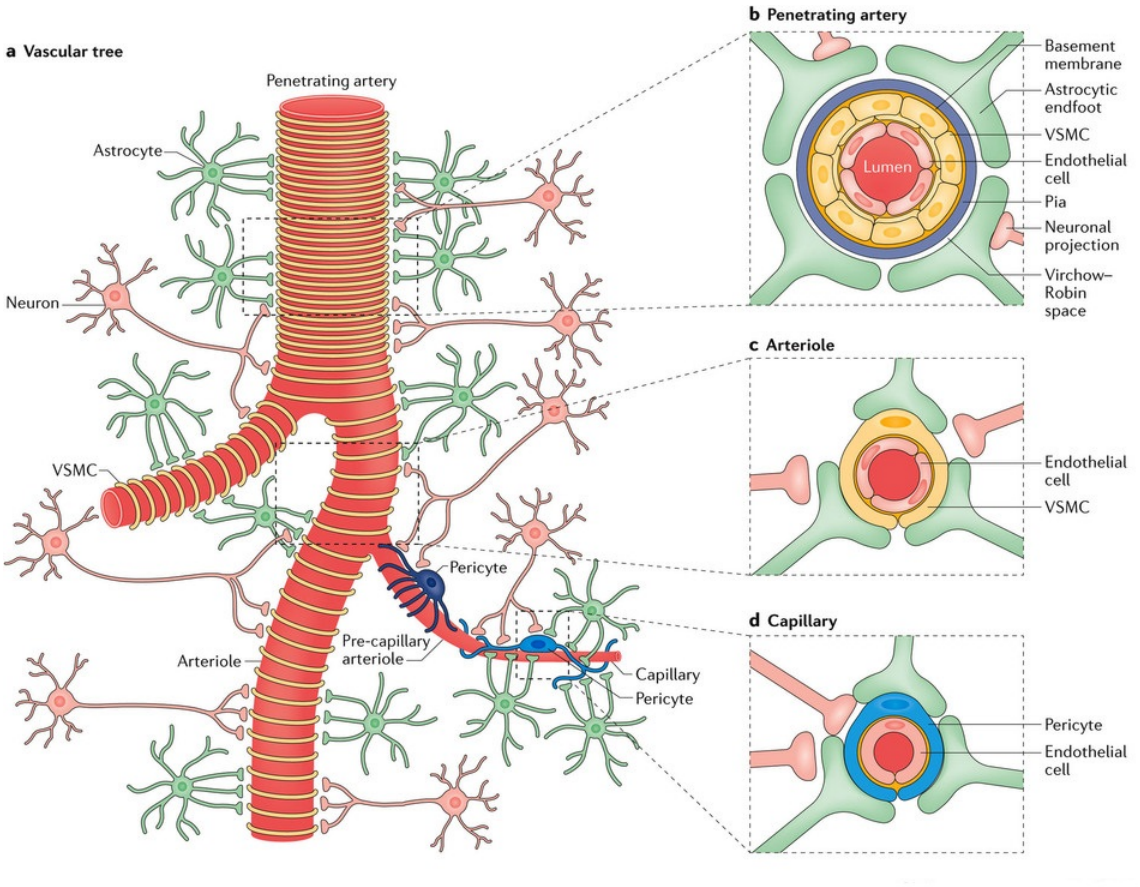

Figure 2.2: Key components of the NVU that regulate CBF along the vascular tree. There are three cell types that play the key roles in the regulation of CBF. They are neurons, astrocytes and endothelial cells. Neurons (red) are the central component of the NVU with the ability to sense small variations in the availability of nutrients, oxygen and other metabolic waste products. They are in constant communication with other neurons, astrocytes (green) and endothelial cells (light red in b-d) to regulate CBF. Astrocytes have end-feet that are in close contact with the wall of cerebral microvessels as demonstrated in b,c and d. Endothelial cells are connected with each other via tight junctions to form the BBB. ([32]).

2.1.2 Regulation of cerebral blood flow

As mentioned above, CBF is tightly regulated by several overlapping mechanisms that are interplayed with each other to produce a characteristic haemodynamic response to the increase in neuronal activity. Components of the NVU play the central role in these homeostatic mechanisms. In this section, we will describe two fundamental mechanisms of the regulation of CBF.

2.1.2.1 Cerebral pressure autoregulation

Cerebral pressure autoregulation (CA) is the process by which cerebral arteries maintain a constant blood flow in the cerebral circulation in the face of changing perfusion pressure, ensuring that in normal physiological conditions, neural tissue can receive

sufficient nutrients and oxygen for normal activity [33]. Alternatively, it can be defined by the ability of the cerebral vasculature to change its calibre in response to changes in arterial blood pressure. A fall in perfusion pressure causes rapid vasodilation of cerebral blood vessels while a rise in perfusion pressure leads to vasoconstriction [34]. This is critical to the normal functionality of the brain in different physiological conditions as neural tissue is intolerant to ischemia. CA operates within a wide but limited range of cerebral perfusion pressure (CPP), where CPP is equivalent to the difference between arterial blood pressure (ABP) and intracranial pressure (ICP). Early studies have convincingly documented that when CPP is within the range of 50 to 160 mmHg, CBF is maintained at a relatively constant level [24]. When CPP gets below or above these limits, CA may be impaired and CBF becomes pressure-dependent [35], [36]. This phenomenon is summarised by a classic sigmoidal curve in Figure 2.3. Although CA occurs over a short time scale, it is not instantaneous. Previous studies have suggested that when there are step changes in ABP, the restoration of blood flow to the pretest level can take more than four seconds ([33]). This means that even when CA is intact, an abrupt drop in ABP can result in a transient drop in CBF before autoregulation brings it back to normal level.

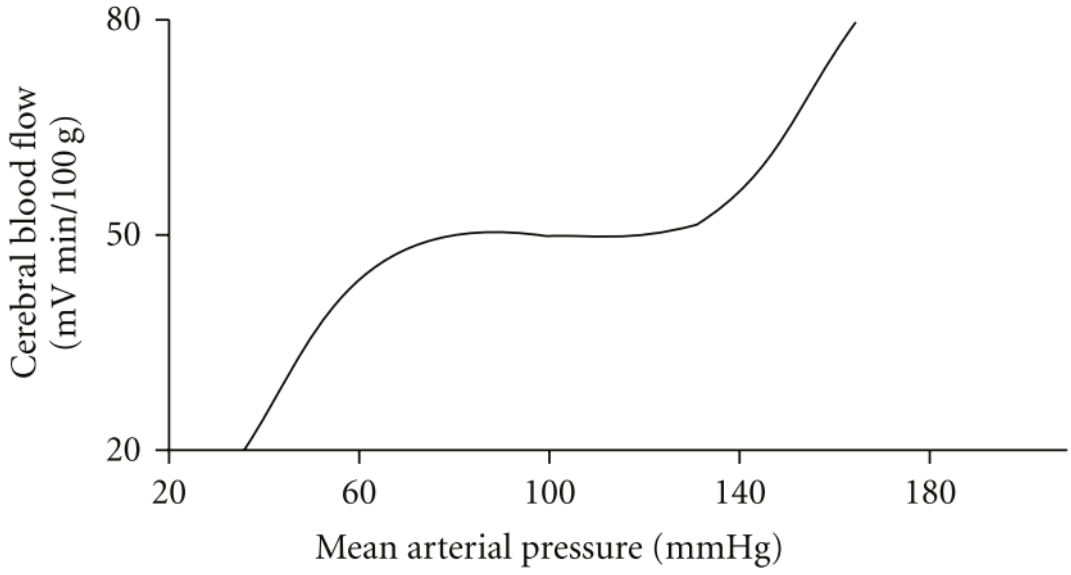

Figure 2.3: An idealised curve demonstrating the basis of CA. In an ideal situation, there is little variation in CBF when CPP is within 50 to 150 mmHg. Above or below these values, a small change in CPP results in a large change in CBF. (Taken from [24]).

Several mechanisms have been proposed to explain CA. As we view CA as a metabolic independent control of CBF (metabolic dependent control i.e functional hyperaemia will be discussed later), only mechanisms that cause changes in cerebral vascular tone as a result of changes in CPP are considered here. These include myogenic response and

endothelial contribution. These mechanisms act together to modulate and fine-tune the response of the cerebral vasculature to changing blood pressure.

Myogenic response, first described by Bayliss in 1902 [37], is considered an intrinsic property of SMCs characterised by the constriction of the vessel in response to an increase in transmural pressure and its dilatation in response to decrease in pressure [38], [39]. Using isolated vessel techniques, the response has been established to depend mainly on the reaction of SMCs in the wall of small arteries and arterioles and not on either nerves or endothelium [40], [41]. The myogenic response exists in several networks of small arteries and arterioles; its response varies with vessel diameter and it is different in different vascular beds [42]. The mechanism behind the myogenic response is not fully elucidated but there is evidence suggesting that the increase in transmural pressure may activate non-selective stretch-activated ion channels present on the SMCs, resulting in the depolarisation of SMC membrane which leads to the opening of voltage-gated calcium (Ca^{2+}) channels on SMCs. The influx of extracellular Ca^{2+} results in an increase in the concentration of intracellular Ca^{2+} and the contraction of SMCs, a response that disappears in the presence of voltage-gated Ca^{2+} channel inhibitors. A more detailed discussion of cellular mechanisms of individual events of the myogenic response can be found in [42].

The cerebrovascular endothelium plays a central role in the regulation of CBF through the production and the release of vasoactive molecules that can lead to vasoconstriction or vasodilatation, constantly modulating the vascular tone [43]. Furthermore, it can respond to or modify circulating vasoactive substances in the bloodstream to have vascular effect. Two main factors that have been proposed to activate the activity of cerebrovascular endothelium. These are the change in shear stress and the change in transmural pressure. The increase in shear stress (or flow velocity) was shown to result in vasodilation [44] while the increase in transmural pressure was demonstrated to result in vasoconstriction [45]. The mechanisms of these responses are not fully understood but accumulating evidence suggests that there is a mechanoreception mechanism present in the endothelial cells that detects the changes in shear stress and transmural pressure. These lead to the release of endothelium-derived relaxing factor (EDRF) or endothelium-derived contracting factor (EDCF) that can diffuse to the vascular SMCs to result in their relaxation or contraction [46].

2.1.2.2 Functional hyperaemia

Functional hyperaemia is the process characterised by the microscopic local increase in CBF to specific regions of active neural tissue. This increase in CBF delivers nutrients and oxygen to the neural tissue and washes out metabolic waste products and carbon dioxide via a complex and highly developed vascular system. However, the increase in CBF far exceeds the local requirement, especially for oxygen, resulting in regions of hyperoxygenation [47], [48]. This oversupply of oxygen is the basis for haemodynamic-based functional neuroimaging techniques such as functional magnetic resonance imaging (fMRI), detecting the decrease in the concentration of deoxygenated haemoglobin, functional near-infrared spectroscopy (fNIRS) which detects the increase in concentration of HbO_2 and the decrease in concentration of HHb or positron emission tomography (PET) which detects the increase in blood flow of a biologically active labelled tracer in the body (See Figure 2.4). These functional imaging modalities will be discussed in detail in section 2.2. The rationale behind the over supplying of oxygen to regions of activation is not fully understood and is an active area of research.

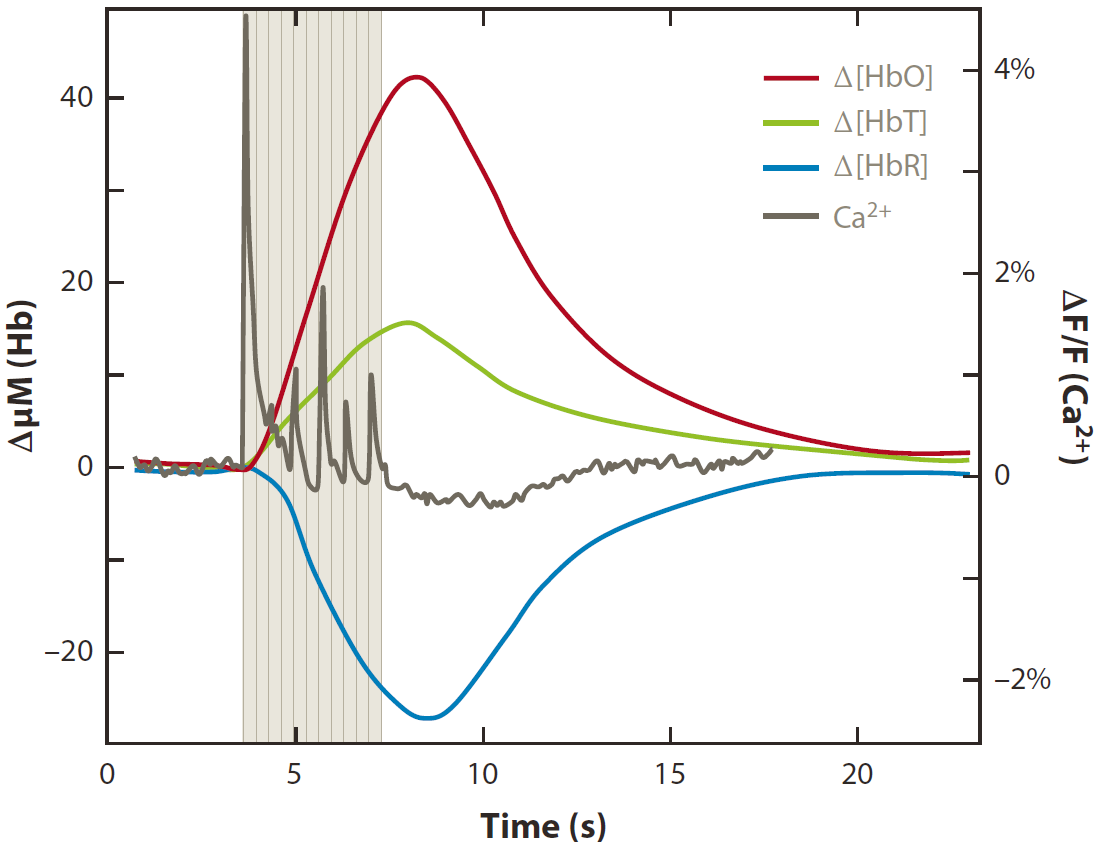

Figure 2.4: A typical haemodynamic response in the rat somatosensory cortex after four seconds of forepaw stimulation [49]. Dark grey trace shows the calcium response. Green trace shows an increase in the total haemoglobin corresponding to the dilation of blood vessels. A typical response of functional activation was recorded with an increase in concentration of oxygenated haemoglobin (red trace) and a decrease in concentration of deoxygenated haemoglobin (blue trace), indicating a net overoxygenation of the tissue.

There are some specific vascular features evidenced during functional hyperaemia. Capillaries are suggested to expand physically during functional hyperaemia [50] which may explain the increase in total capillary concentration of haemoglobin observed in various studies [49], [51]. Specific arteriolar branches of pial arteries dilate rapidly, extending up to more than one mm away from the centre of the activated region [52], [53]. There is evidence of propagation of vasodilation from small specific vessels to a larger number of nearby larger vessels [52], [53]. Veins do not change diameter during functional activation but the velocity of blood flow in veins is increased during this event.

The primary process underlying functional hyperaemia is termed neurovascular coupling, which describes the close temporal and regional linkage of neuronal activity and CBF responses [54]. This process is still under active investigation but the fundamental sequence of events can be summarised as followed [55]. An increase in neuronal activity leads to an increase in adenosine triphosphate (ATP) consumption and the release of metabolic waste products. Neurons replenish this energy by the process of oxidative

metabolism which requires nutrients and oxygen. These are supplied by a coordinated increase in CBF. Although the investigation of the mechanism underlying neurovascular coupling is a complex matter, several candidates are thought to be involved in the sequence of coordinated events. These are the components of the neurovascular unit discussed earlier: endothelial cells, neurons, astrocytes [56].

There are several proposed mechanisms suggesting the concerted sequences of events carried out by these components of the NVU to bring about the localised increase in CBF following neuronal activation. Some popular mechanisms of neurovascular coupling are discussed individually before they are brought together using an integrated model trying to describe the sequence of events underlying neurovascular coupling.

Metabolic hypothesis: CBF is directly controlled by energy demand. Blood flow is controlled by feedback mechanisms that are sensitive to variation in the concentration of ionic and molecular metabolic by-products of cellular metabolism. These metabolic by-products of neuronal activity (including but not limited to postassium ion (K^+), nitric oxide (NO), adenosine, carbon dioxide (CO_2) and arachidonic acids) may directly or indirectly trigger vasodilation or vasoconstriction via depolarisation or hyperpolarisation of the vascular SMCs. One specific molecule to consider is CO_2 as CBF is highly sensitive to changes in arterial partial pressure of CO_2 (pCO_2) [57]. When pCO_2 is higher than normal, CBF increases to attenuate the rise and when pCO_2 is lower than normal, CBF decreases to attenuate the fall. This may be explained by the effect of CO_2 on pH. Increase in pCO_2 leads to a decrease in pH which in turn opens K^+ channels on vascular endothelial cells [57]. This leads to hyperpolarisation of the endothelial cells due to the efflux of the cation. The hyperpolarisation can be transmitted from endothelial cells to SMCs and neighboring endothelial cells via myoendothelia and gap junctions respectively resulting in the closure of voltage-gated Ca^{2+} channels in SMCs and vasodilation. Furthermore, the change in pH due to change in pCO_2 can also initiate the release of vasoactive molecules from endothelial cells to cause vasoconstriction/vasodilation.

Neurogenic hypothesis: this is a feed-forward mechanism where neurovascular coupling is mediated by neuronal mechanisms using the glial pathway or using the direct influence of neurons on SMCs rather than by mechanisms that sense energy consumption. In the glial pathway, astrocytes have been widely believed to have significant involvement in neurovascular coupling after a study showed that the uncaging of Ca^{2+} in astrocytic end-feet resulted in the dilatation of adjacent arterioles [58]. It was suggested that the buildup of glutamate from local neural activity may act on metabotropic glutamate receptors (mGluR5s) on astrocytes to result in the increased intracellular Ca^{2+}

concentration. This can result in the generation of arachidonic acid derivatives, such as prostaglandins (PGs) capable of causing vasodilation by their direct action on SMCs. However, recent studies have shown evidence that questions the role of astrocytes in neurovascular coupling. Firstly, the measureable increases in astrocytic Ca^{2+} occurs after the onset of arteriolar dilation [59]. Secondly, mice lacking receptors for intracellular Ca^{2+} signalling still exhibit functional hyperaemia [59]. Thirdly, astrocytes do not express mGluR5s receptors in the adult brain which play the key role in the pathway for glutamate-mediated astrocyte activation [60]. And lastly, astrocytes are not directly in contact with pial arteries above the cortical surface [61]. In the direct pathways, neurons act directly on SMCs (direct neuronal innervation of SMCs) or products of neural activity diffuse directly to have effect on SMCs. There is evidence suggesting that acetylcholine released by the basal forebrain can modulate regional blood flow [62], [63] and cortical interneurons are able to release vasoactive substances such as VIP, NO (dilation) and NPY, SOM (constriction) that can cause changes in blood flow [64]. These mechanisms provide alternative routes to local coupling within the cortex.

Propagated vasodilation: Endothelial cells are hyperpolarised after being activated and this hyperpolarisation can propagate electrically within the endothelium to cause dilation of a selected group of vessels to create a defined area of functional hyperaemia. Another view is that after being activated, there is a calcium wave that can propagate slowly causing dilation of SMCs via endothelial release of NO and prostagnoids.

As a result of multiple hypotheses, an integrated model can be used to explain neurovascular coupling [65]. Initiation of functional hyperaemia can be at the level of capillary endothelial cells via the actions of astrocytes, pericytes, neurons or the direct diffusion of products of neural activity to the blood vessels. After the initial spark via different mechanisms, the wave of vascular dilation travels retrograde from the focal point of activation along the selective vascular route, recruiting specific arterial branches to create an optimally localised area of functional hyperaemia.

This localised area of functional hyperaemia can be measured by fMRI as an increase in the blood-oxygen-level-dependent (BOLD) signal as the concentration of HHb decreases, and by fNIRS as an increase in concentration of HbO_2 and a decrease in concentration of HHb. However, these signals only measure the changes in CBF secondary to neuronal activation. It should be emphasised that there is a clear difference between the concept of neuronal activation and the focal increase in CBF. In the next section, the metabolic process of neuronal activation, the actual process of neuronal activity will be discussed.

2.1.3 Cellular mechanisms in neuronal activity

At the cellular level, it is the group of neurons that is activated during functional activation. To understand the basis of the process, resting potential of neuron needs to be discussed.

2.1.3.1 Resting membrane potential of neurons

Neurons at rest have a resting membrane potential around -65mV. This is the result of a combination of many equilibrium potentials but most important is the action of K^+ ions. Sodium/Potassium pumps (Na^+/K^+ pumps) utilise an ATP to pump 3 sodium ions (Na^+) out of the cell to the extracellular matrix (ECM) and $2K^+$ into the cell cytosol to create a chemical gradient where K^+ is more concentrated inside the membrane and Na^+ is more concentrated outside the membrane (Figure 2.5). Additionally, the membrane is selectively permeable to ions; its permeability to K^+ is extremely high compared to other ions. As a result, there is a large movement of K^+ from cytosol to ECM, going down the concentration gradient. This outward movement of K^+ also makes the inner side of the membrane more negative. The negatively charged inner membrane creates an electrical gradient across the membrane, preventing the escape of positively charged ions from the cytosol. The movement of K^+ occurs until the chemical gradient is balanced by electrical gradient created by the build-up of negative charge on the inner surface of the membrane. This is the reason why the resting potential of neurons is close to the equilibrium potential of K^+ (-80mV). Similar process can be applied to Na^+ ion, another principle ion playing an important role in establishing the resting membrane potential (Figure 2.5).

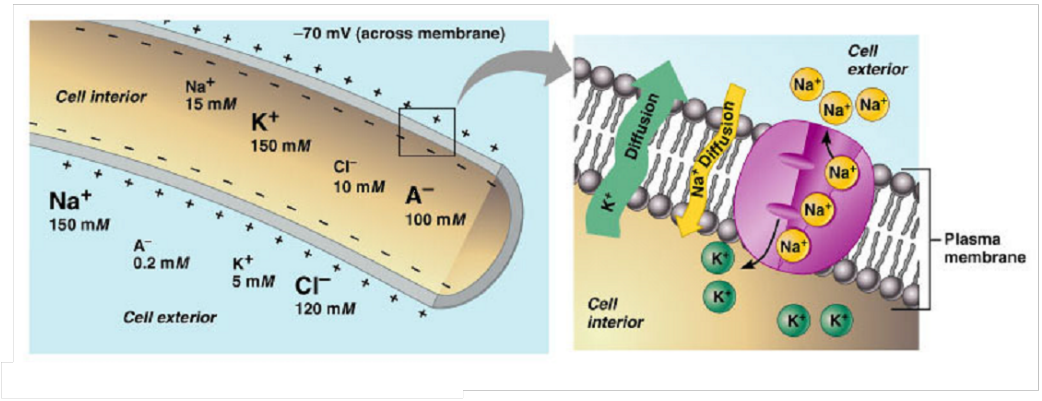

Figure 2.5: Ionic exchange processes that establish the resting membrane potential in neurons. Sodium/Potassium pump (purple) pumps $3Na^+$ out of the cell in exchange to $2K^+$ into the cell. Due to the selective permeability of the cell membrane to different ions and the balancing between the electrical gradient and the chemical gradient, the inner side of the membrane becomes negative. [66]

2.1.3.2 Action potential

When a neuron is activated, the resting potential is disrupted and an action potential is generated. Action potentials propagate along the axon of the neuron to its terminal end where it is in contact with other neurons via synapses or with motor cells via neuromuscular junctions. An action potential is a short-lasting event in which the membrane potential rises and falls to communicate with other neurons. During an action potential, Na^+ channels are opened, allowing an influx of Na^+ ions into the cell cytosol, causing the membrane potential to depolarise. Depolarisation of the membrane causes more Na^+ channels to open and further influx of Na^+ ions causing the membrane potential to be positive. At a threshold potential, Na^+ channels close and K^+ channels open, allowing the efflux of K^+ to repolarise the membrane. Repolarisation also requires the action of Na^+/K^+ pumps, pumping $3Na^+$ out of the cell and $2K^+$ into the cell. The membrane potential overshoots the resting potential by a small amount (hypepolarisation) before getting back to the resting potential.

2.1.3.3 Cellular metabolic processes

The action of Na^+/K^+ pumps plays the vital role in re-establishing the resting potential for neurons after an action potential, making them ready for the next wave of action potentials. This explains why a large amount of ATP utilised by the brain is expended in this process. The ATP needed for this process is generated by the oxidative phosphorylation of glucose in cells. In brief, the process can be summarised in the equation:

$$C_6H_{12}O_6 + 6O_2 + 38ADP + 38P_i \rightarrow 6CO_2 + 6H_2O + 38ATP \quad (2.1)$$

One glucose molecule is converted into two pyruvate molecules through glycolysis, generating two ATP and two nicotinamide adenine dinucleotide (NADH). When there is adequate oxygen in the cells, the majority of pyruvates will enter the citric acid cycle – a highly efficient aerobic process to generate energy. The rates of glycolysis and citric acid cycle are tightly coupled with the ATP requirement of the cell; in the case of a neuron, it is mainly to re-establish the resting potential after the wave of action potentials. The outputs of the citric acid cycle are mostly potent electron donors – NADH and flavin adenine dinucleotide ($FADH_2$) that have the ability to generate ATP through the electron transport chain (ETC).

The ETC takes place in the inner membrane of the mitochrondia and it comprises of a series of compounds embedded in the membrane to carry out redox reactions to transfer electrons from electron donors (mainly NADH and $FADH_2$) to electron acceptors (oxygen) (Figure 2.6). This transfer of electrons is coupled with the transfer of protons (H^+) across the membrane to create a proton gradient that can be used to synthesise ATP from ADP and Pi through the activity of ATP synthase [67]. This process accounts for most of the ATP production in cells.

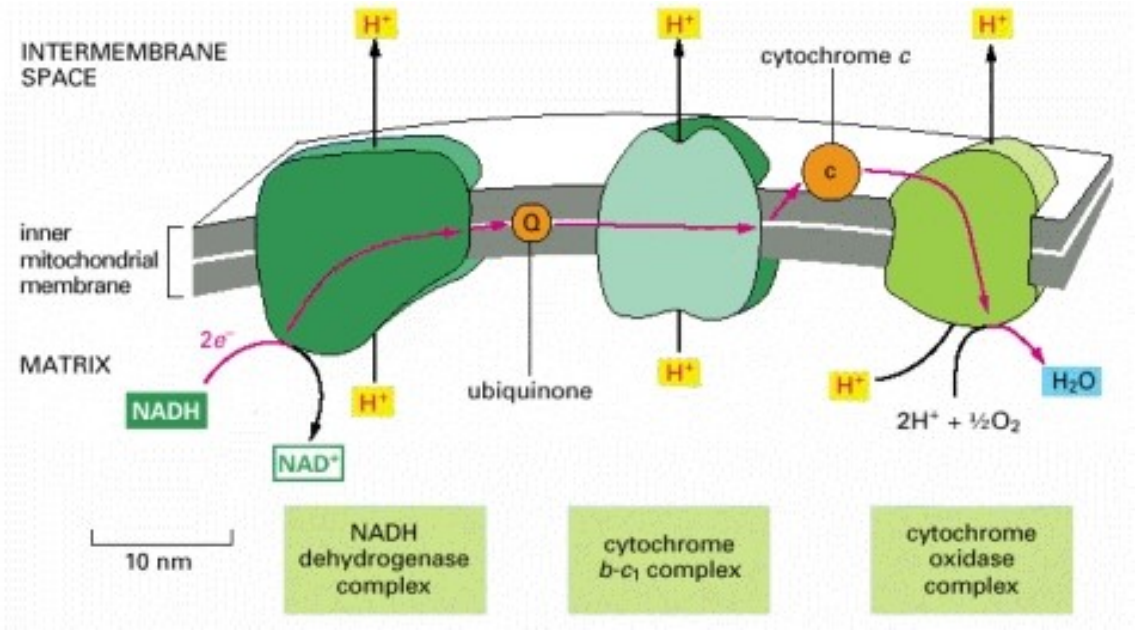

Figure 2.6: Series of redox reactions in the mitochondrial electron transport chain that transfer electrons from electron donors (NADH/$FADH_2$) to oxygen to generate a proton gradient across the inner membrane of the mitochondria. This proton gradient can be used by the ATP synthase to produce ATP for cellular activity. [67]

In the ETC, electrons pass successively from NADH to NADH dehydrogenase, ubiquinone,

cytochrome b-c_1, cytochrome c, CCO and then oxygen [67]. The transfer of electrons through NADH dehydrogenase, cytochrome b-c_1 complex and CCO is coupled with the transport of H^+ from the matrix to the intermembrane space, generating a proton gradient across the inner membrane of the mitochondria [68]. In the case of $FADH_2$, electrons are first passed to ubiquinone rather than NADH dehydrogenase and then follows a similar path.

The rate of flow of electrons through the ETC is dependent on three main factors: changes in substrate supply, changes in energy demand (ATP turnover), and changes in oxygen level, and each of these factors affects the oxidation status of components of the ETC differently [69]. In general, it is assumed that an increase in substrate supply leads to an increase in the electron flux and a decrease in the oxidation level of all members of the ETC; an increase in oxygen level causes an increase in the electron flux and an increase in oxidation level of all members of the ETC; an increase in ATP turnover results in an increase in flux and has a various effects on the oxidation status [69].

During functional activation where there is a change in energy demand, the change in oxidation status of components within the ETC is not theoretically simple [11]. Considering the oxidation status of CCO, the terminal member of the ETC and therefore responsible for more than 95% of oxygen metabolism, there is experimental evidence suggesting that the oxidation status of CCO increases during functional activation [70], [71]. However, there is also evidence suggesting that CCO can be either reduced or oxidised during functional activation [11]. More work needs to be done to investigate the changes in the oxidation status of CCO during functional activation and broadband near-infrared spectroscopy with the ability to measure the redox changes of CCO non-invasively, appears to be the only feasible method. This will be discussed in chapter 3 of this thesis. The next section will summarise currently available brain monitoring/neuroimaging techniques that can monitor brain function.

2.2 Functional neuroimaging techniques

Functional neuroimaging is used to investigate and understand various aspects of brain function. It is usually used with the aim to understand the relationship between brain areas and specific mental functions. In this thesis, the basis of some common neuroimaging techniques as well as their advantages and disadvantages will be discussed.

2.2.1 Electroencephalography

Electroencephalography (EEG) is an electrophysiological monitoring technique to record electrical activity of the brain. By placing electrodes on the scalp, the technique measures the variation in electrical potential difference produced as a result of synchronous electrical activity of thousands of neurons across a given brain volume. EEG is therefore considered a direct measure of brain activity. The fundamental principle of EEG is based on the fact that neurons are constantly exchanging ions with the extracellular matrix to maintain their resting membrane potential and to propagate action potentials. Provided that ions of the same charge repel each other, ionic exchange by thousands of neurons that are synchronised in activity produces an electrical potential difference that is large enough to be detected at the scalp. Pyramidal neurons on the cerebral cortex are believed to be the main source of EEG activity as they are aligned to each other and they work synchronously during brain activity [72]. Event-related potential (ERP) is a specific pattern of brain electrophysiological response measured by EEG as a direct result of a specific stimulus presented to the subject. This pattern is distinctive from spontaneous background potentials and can be resolved using signal averaging techniques. As the ERP is time-locked to the stimulus, the block averaging process will average out the random noise and reveal the ERP caused by the stimulus. This provides a direct measure of brain activity during functional activation with a very high temporal resolution up to one millisecond as there is no measurable conduction delay between brain activity generated inside the head and the potential difference recorded from the scalp [73]. EEG has certain advantages and disadvantages in comparison with other neuroimaging techniques. Despite having a very poor spatial resolution, EEG offers very high temporal resolution with common sampling rates varying between 250 to 2000 Hz. With significantly low hardware cost compared to other techniques, it is not restricted to specialised facilities and can be used in a clinical environment with other monitoring techniques such as fNIRS. EEG measurements do not involve the use of high intensity magnetic fields (as in fMRI) or the use of radioligands (as in PET). However, EEG has a poor signal to noise ratio that requires sophisticated data analysis techniques and a large number of subjects to derive useful information.

2.2.2 Positron Emission Tomography

Positron emission tomography is a nuclear medicine functional imaging technique that is commonly used for the imaging of glucose metabolism of tissue. It detects pairs of gamma

rays moving in opposite directions emitted by the annihilation between a positron emitted from the radioactively labelled tracer and an electron in the tissue. The most commonly used tracer in PET is fluorodeoxyglucose (FDG), an analog of glucose. This tracer is taken up and accumulated in cells that have high rate of glucose metabolism, resulting in the intense radiolabelling of tissues with high glucose uptake such as the brain, liver and tumour cells. Before the widespread use of functional magnetic resonance imaging, PET was the popular method for functional brain imaging. However due to the fact that positron emitting radioisotopes have short half-lives, PET facilities have to be placed in proximity to a cyclotron where these radioisotopes are produced. This poses the issue of practicality and in conjunction with the use of radioactive tracer, PET is now mostly limited to research facilities. The greatest benefit of PET is that different tracers can be used to investigate different parameters of the working brain. Oxygen-15 can be used in PET to enable the measurement of CBF and cerebral metabolic rate of oxygen while FDG can be used to investigate cerebral glucose metabolism.

2.2.3 Singe photon emission computed tomography

Single photon emission tomography (SPECT) is a nuclear medicine tomographic imaging technique that requires the injection of gamma-emitting tracer into the bloodstream of the patient. The gamma rays emitted from the tracer are detected by a gamma camera. The tracer commonly used in SPECT functional brain imaging is technitium-99m hexamethylpropylene amine oxime (^{99m}Tc-HMPAO) that is taken up by brain tissue in a manner that is proportional to blood flow, allowing CBF to be estimated. As change in CBF in the brain during functional activation is coupled with local neural metabolism, SPECT with ^{99m}Tc-HMPAO tracer can be used to assess brain metabolism regionally. In this sense, ^{99m}Tc-HMPAO SPECT scanning is similar to FDG PET scanning, both of which can assess regional brain metabolism. In comparison to PET, SPECT requires less expensive equipment; the radioisotopes used as tracers are less expensive and have longer half-lives, allowing them to be delivered to hospitals weekly. As a result, SPECT is more widely available.

2.2.4 Magnetoencephalography

Magnetoencephalography (MEG) is a functional neuroimaging technique that records the magnetic fields produced by the naturally occurring electrical activity in the brain by the use of magnetometers. The technique is based on the fact that synchronised neuronal activity induces a weak magnetic field. However, this magnetic field is considerably

smaller than the magnetic noise in the urban environment. As a result, to detect this signal, magnetic shielding and a very sensitive magnetometer are required which limits the use of the technique outside special research facilities. MEG has the advantage of being a non-invasive technique, using no ionising radiation and measuring brain activity directly with high temporal resolution. MEG has been used to study cognitive processes such as vision, language processing in fetuses and newborns.

2.2.5 Functional magnetic resonance imaging

fMRI is the most common functional neuroimaging technique that is used to detect brain activity by measuring the changes in the magnetic resonance signal associated with the increase in blood flow to the active regions of the brain. The technique relies on the coupling of neuronal activity and cerebral blood flow as discussed in previous section. To generate a magnetic resonance signal (MR signal), a strong, static magnetic field is applied to align the nuclei in the brain. Gradient magnetic fields are then applied to spatially locate nuclei in the field of view before a radiofrequency (RF) pulse is used to excite the nuclei to a higher magnetization state. After the RF pulse is removed, nuclei slowly go back to their original state emitting energy that can be measured by a radiofrequency coil that surrounds the subject. In the case of fMRI, hyperoxygenation at the active brain region due to functional hyperaemia leads to a decrease in the concentration of deoxygenated haemoglobin. Given that deoxygenated haemoglobin is paramagnetic, its decrease in concentration leads to an increase in MR signal at the active brain region which is the fundamental basis of fMRI blood oxygen level dependent signal (BOLD signal). fMRI has the advantage of having a very high spatial resolution that can enable visualisation of both structural and functional information simultaneously. It does not involve ionising radiation and is a non-invasive technique. However, the drawbacks of the technique are that it has a low temporal resolution, is expensive and requires the scanning subject to be transported to the MR facility.

2.2.6 Functional near-infrared spectroscopy

fNIRS is a non-invasive, optical functional neuroimaging technique that uses NIR light to investigate changes in haemodynamics associated with neuronal activity. Traditionally, fNIRS instrumentation allows the calculation of changes in the concentration of HbO_2 and HHb by measuring the attenuation of NIR light through the human brain. This method relies on the principle of neurovascular coupling, which is similar to the fMRI BOLD technique. However, in additional to the measurement of HbO_2 and HHb,

fNIRS can measure the concentration changes of oxidised CCO which can be used as a biomarker for cellular oxygen metabolism. During functional activation, the increase in CBF to the active brain regions creates regions of hyperoxygenation as discussed above. This is reflected in fNIRS by an increase in concentration of oxygenated haemoglobin and a decrease in the concentration of deoxygenated haemoglobin (Figure 2.7). fNIRS has several advantages over other functional imaging techniques. Firstly it is a non-invasive technique that does not require the subjects to be in a restricted environments as in the case of PET, SPECT and fMRI. As a result, it can be used at bedside to monitor critically ill patients. Moreover, it does not involve the use of radioisotopes or contrasts agents to produce functional images which proves to be favourable for neuroscience studies. It has a high temporal resolution, allowing measurements to be acquired at high sampling rate up to 250 Hz [3]. Last but not least, its simple set up allows miniaturization of the equipment towards wireless, portable fNIRS systems [74].

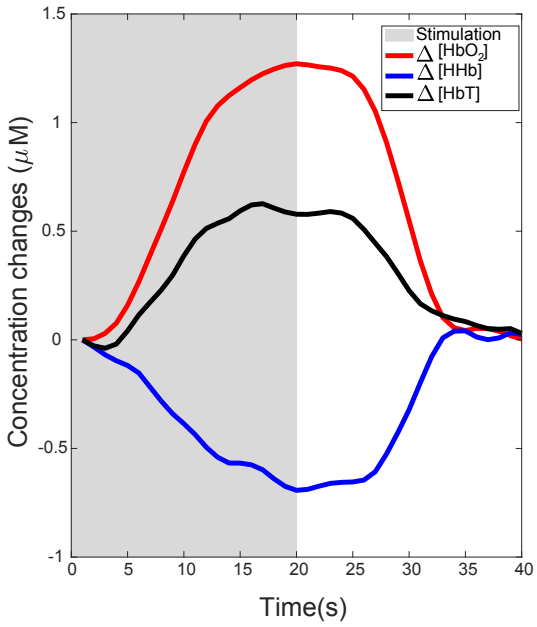

Figure 2.7: A typical haemodynamic response to functional activation measured by fNIRS showing an increase in concentration change in oxygenated haemoglobin (red trace), a decrease in concentration change in deoxygenated haemoglobin (blue trace) and an increase in concentration change of total haemoglobin.

Chapter 3

Near-infrared spectroscopy and imaging

This chapter describes the fundamentals of NIRS including light tissue interaction processes, different techniques to retrieve tissue information in NIRS, an overview of different types of NIRS instrumentation, an overview of NIRS CCO instrumentation and previously published studies investigating the CCO signal. The image reconstruction process using NIRS data will also be discussed. This information on the NIRS technique with a special focus on NIRS broadband instrumentation is the basis for the next three original chapters of this thesis describing the iterative development process and the application of the multi-channel, multi-distance broadband NIRS system to monitor the CCO signal across multiple brain regions.

3.1 Fundamentals of near-infrared spectroscopy

Near-infrared spectroscopy is a non-invasive, non-ionising technique to assess the changes in haemodynamics and metabolism of biological tissue using light in the NIR region of the electromagnetic spectrum (650-950 nm) [75]. The technique is based on the fact that the diffusely scattered NIR light through tissue contains information about tissue that can be retrieved by a variety of NIRS techniques. In this thesis, the instrumentation was developed using the continuous-wave (CW) NIRS technique. With CW technique, it is possible to monitor changes in the concentration of three physiologically interesting chromophores: HbO_2, HHb and oxidised cytochrome c oxidase (oxCCO) which will be discussed in detail in later sections. NIRS techniques exploit the facts that:

- biological tissues have relatively low absorption in the NIR region, creating a window of transparency in the electromagnetic spectrum;
- NIR light is either absorbed by chromophores, optical absorbers, or scattered by biological tissues;
- NIR light can penetrate deep enough into biological tissue as the amount of light being scattered is much larger than the amount of light being absorbed;
- most of the attenuation of NIR light is due to chromophores in small blood vessels ($<$ 1mm in diameter).

To better understand and interpret NIRS signals, the process of light transport in tissue has to be discussed in detail.

3.1.1 Light Transport in Tissue

Light transport in tissue is a complex process; however, it can be simplified using approximations and assumptions with theoretical models to have two individual processes: absorption and scattering, both of which attenuate the light as it passes through the tissue. These effects depend on both the wavelength of light and the complexity of tissue structure. In these next sections, the basics of light absorption and light scattering will be discussed individually before the combined effect that determines light attenuation in tissue is considered.

3.1.1.1 Light Absorption

The simplest case of absorption happens when light travels through a *non-scattering, homogeneous* absorbing medium. In 1729, Pierre Bouguer described his observation that successive layers of a non-scattering, homogeneous medium of equal thickness absorb the same fraction of light intensity I incident upon them. In 1760, Johann Henry Lambert mathematically described the relationship in his book on the measurement of light, *Photometria*:

$$\frac{\delta I}{I} = -\mu_a \cdot \delta d \tag{3.1}$$

$\frac{\delta I}{I}$ is the fraction of incident light being absorbed by the medium. μ_a (cm^{-1}) is the absorption coefficient of the medium and is defined as the probability that a photon gets absorbed in the medium per unit length it travels. δd is the thickness of the medium. Integration of equation 3.1 gives the Lambert-Law:

$$I = I_0 e^{-\mu_a \cdot d}. \tag{3.2}$$

I is the transmitted light intensity after it has passed through d (cm) thickness of a non-scattering, homogeneous, absorbing medium having an absorption coefficient of μ_a (cm^{-1}). I_0 is the incident light intensity (Figure 3.1).

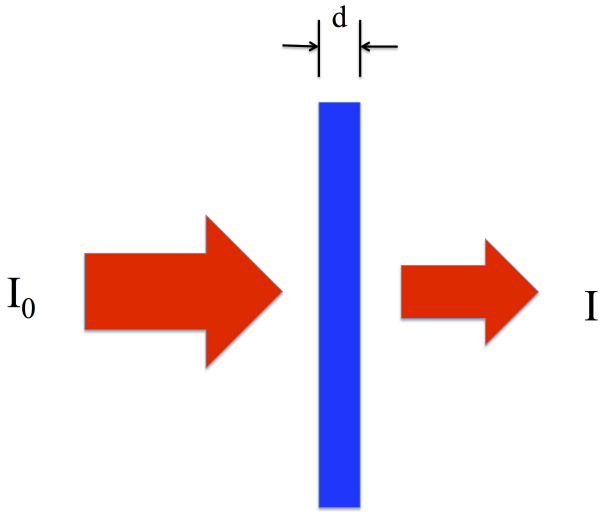

Figure 3.1: Cuvette model for an absorbing, non-scattering, homogeneous medium where the Lambert Law can be used to describe the attenuation of light.

Equation 3.2 can be expressed in terms of log to the base 10 as:

$$I = I_0 10^{-k \cdot d} \tag{3.3}$$

where k (cm^{-1}) is the extinction coefficient and is related to μ_a by equation 3.4

$$\mu_a = k \ln 10. \tag{3.4}$$

August Beer established the proportional relationship between the concentration, c (molar), of the absorbing compound in a non-absorbing solution and the absorption coefficient, μ_a.

$$\mu_a = \alpha \cdot c \tag{3.5}$$

For base 10, the relationship is

$$k = \epsilon \cdot c \tag{3.6}$$

α is the specific absorption coefficient ($molar^{-1} \cdot cm^{-1}$) and ϵ is the specific extinction coefficient ($molar^{-1} \cdot cm^{-1}$). Combining equations from Lambert's Law (equation 3.2 and 3.3) and Beer's Law (equation 3.5 and 3.6) results in the Beer-Lambert Law for both natural log and base 10 log:

$$I = I_0 e^{-\alpha \cdot c \cdot d} \tag{3.7}$$

$$I = I_0 10^{-\epsilon \cdot c \cdot d} \tag{3.8}$$

Transmittance T is defined as the ratio between the transmitted intensity I and the incident intensity I_0. Attenuation A of a non-scattering, absorbing medium is defined as the $-log_{10}$ of transmittance:

$$T = \frac{I}{I_0} \tag{3.9}$$

$$A = -\log_{10} T = \log_{10} (\frac{I_0}{I}) = \epsilon \cdot c \cdot d \tag{3.10}$$

Equation 3.10 can be expanded to n absorbing compounds in a non-absorbing solution. The absorbance of a solution containing a mixture of absorbing compounds is the sum of the absorbances of individual attributed compounds each with a specific extinction coefficient and a concentration:

$$A = \epsilon_1 \cdot c_1 \cdot d + \epsilon_2 \cdot c_2 \cdot d + ... = \sum_i \epsilon_i \cdot c_i \cdot d. \tag{3.11}$$

The Beer-Lamber Law assumes that the incident light is monochromatic, perfectly collimated and all the light incident on the material is either transmitted or absorbed. Light loss due to scattering and reflection at tissue interfaces, prominent phenomena in biological tissue, are not taken into account. These issues will be discussed in later section. In the next section, optical absorbers in biological tissue usually referred to as *chromophores* will be discussed.

3.1.1.2 NIR chromophores in biological tissue and NIR window of transparency

Chromophores are compounds that absorb light in the spectral region of interest. Each chromophore has its own individual absorption spectrum describing the level of absorption at each wavelength. Biological tissue can be approximated as a mixture of many

different chromophores, each of which has its own absorption spectrum and concentration. The overall absorption or attenuation of light due to biological tissue depends mostly on the consisting chromophores and their concentrations. In NIRS, the chromophores of interest are those whose absorption spectra vary with oxygenation status. However, it is important to notice that other principle tissue chromophores that remain at a constant concentration (at least during the period of the experiment) also contribute to the total light loss. In the following sections, absorption characteristics of principle chromophores and of chromophores that change their absorption spectra due to oxygenation will be discussed.

Water Water is a chromophore that is present at the highest concentration in biological tissue. Typically, $60 - 90\%$ of the total body mass is comprised of water [76]. As a result, it is considered the dominant tissue chromophore in NIRS and its absorption spectrum determines the spectral region that can be used for spectroscopic measurement. From Figure 3.2, it can be seen that beyond 900 nm, absorption by water rises sharply as wavelength λ increases. The high absorption of water in this region of the spectrum causes the photons at these wavelengths to travel only a short distance in tissue, limiting the tissue thickness through which light can penetrate. From 650 to 900 nm, the absorption of light by water is relatively low, creating a window of transparency in the tissue across which light can penetrate to a certain depth to produce meaningful spectroscopic measurements.

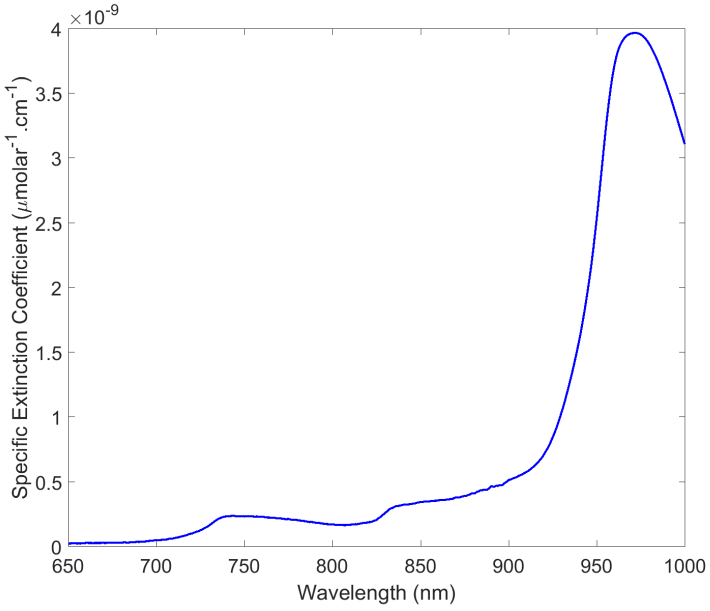

Figure 3.2: Specific extinction coefficient of water from 650 nm to 1000 nm. Spectral data were taken from UCL BORL website [77].

Lipids Distribution of lipids varies greatly among tissue types. Lipids can be considered as constant absorbers, contributing to total attenuation as their concentration in tissue tend to remain constant during the course of a clinical measurement. The absorption spectrum of lipids is approximately similar to water with low absorption in the NIR region.

Superficial tissues Superficial tissues such as skin, bone and muscles are also important in spectroscopic measurements. Although the absorption spectra of these tissues are not dependent on oxidation status, they contribute to total light attenuation.

Skin The human skin typically has three layers: epidermis, dermis and hypodermis. The epidermis is the outermost layer of the skin, containing no blood vessels, and melanocytes. The chromophore that needs to be considered in the epidermis is melanin. Melanin, produced by melanocytes, is a natural pigment and an effective absorber of light. Although the absorption of light due to melanin is constant, its concentration in the epidermis determines the amount of light that can be transmitted through the skin to the underlying layers of tissue. The dermis is the layer underneath the epidermis consisting of mostly connective tissue. In the dermis, there are hair follicles, sweat glands, sebaceous glands, apocrine glands, lymphatic vessels and subcutaneous blood vessels. Tissues in this layer contain the three main NIRS absorbers i.e. haemoglobins in the blood vessels and CCO. Changes in the oxygenation of these NIRS absorbers in this layer may contaminate NIRS measurements of changes of chromophores in the brain. Hair follicles in the dermis play a similar role as melanin in the epidermis as an attenuator of light. This issue is important to consider when making spectroscopic measurements in regions of the head that are usually covered by hair. The hypodermis is the layer beneath the dermis and its main role is to act as a fat storage, containing lobules of fat and blood vessels that give branches to the vessels in the dermis. Haemoglobins in the blood vessels in the hypodermis also contribute to the attenuation of NIR light through the head.

Bone and Muscles The absorption of NIR light by bone is very little in comparison to other tissues and most of that absorption is due to the haemoglobin present in the tiny blood vessels supplying the bone tissue. Muscles, especially facial muscles such as frontalis and temporalis, contain myoglobin and supplying blood vessels that may also contribute to the attenuation of NIR light when measurements of cerebral haemodynamics are recorded from the frontal lobe or the temporal lobe.

Although constant attenuation of light due to these superficial tissue layers is not

of particular interest in NIRS, it is worth remembering that changes in blood flow and oxygenation in the superficial tissue layers may contaminate NIRS measurements of the underlying changes in cerebral haemodynamics and metabolism.

Haemoglobin Haemoglobin is one of the most important absorbers of NIR light in NIRS. Haemoglobin is the oxygen-transport protein in the red blood cells. It carries oxygen from the lungs, in the form of oxygenated haemoglobin, to all other tissues in the body through a dense network of blood vessels and carries the deoxygenated form of haemoglobin back to the lungs. As discussed in chapter 2, an increase in neuronal activity in an area of the brain results in an increase in blood flow to that area via the process of neurovascular coupling. This brings a surplus supply of oxygenated haemoglobin to the tissue, creating changes in the concentration of different species of haemoglobin. Therefore, the ability to measure changes in the concentration of these different species will give us an insight into how different areas of the brain behave in response to certain conditions. The two main species of haemoglobin are oxygenated (HbO_2) and deoxygenated (HHb) haemoglobin. This is because oxygen binds to haemoglobin in a reversible manner:

$$HbO_2 + H^+ \rightleftharpoons HHb + O_2 \tag{3.12}$$

The binding of oxygen to haemoglobin induces a conformational change in the molecular structure of the protein and a resulting change in its absorption spectrum. The absorption spectra of HbO_2 and HHb are shown in Figure 3.3. In the NIR region of the spectrum from 650 to 900 nm, there are significant differences in the absorption spectra of the two chromophores. It is these differences that are fundamental to NIR biomedical techniques, allowing the contribution of each chromophore to the overall attenuation to be separated and quantified.

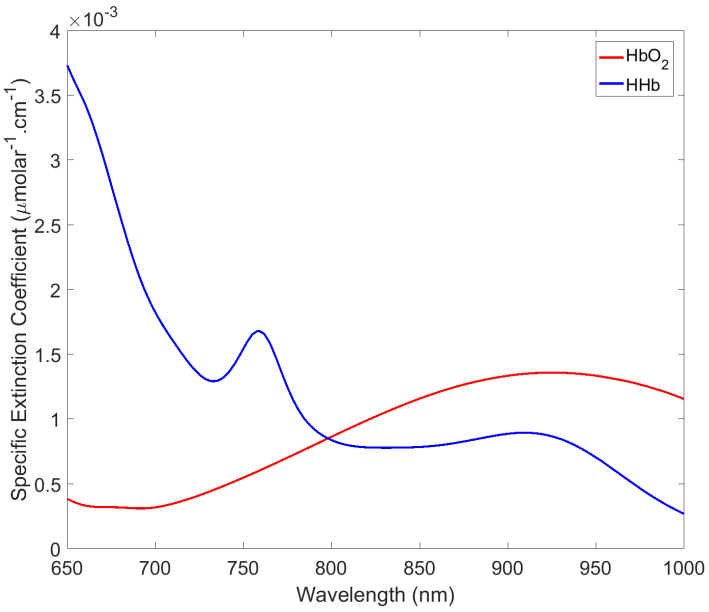

Figure 3.3: Specific extinction coefficient of oxygenated (red) and deoxygenated (blue) haemoglobins from 650 nm to 1000 nm. Spectral data were taken from UCL BORL website [77].

Cytochrome c oxidase Cytochrome c oxidase (CCO) is the terminal enzyme of the ETC, catalysing the electron transfer from cytochrome c to oxygen in the inner membrane of cellular mitochondria. It is responsible for more than 95% of cellular oxygen metabolism in tissue [78]. The role of CCO in the ETC has been briefly discussed in chapter 2. Therefore, the biochemistry of CCO is the focus here. CCO has four redox active centres: two haem groups (a and a_3) and two copper centres (Cu_a and Cu_b). Haem a_3 group and Cu_b centre form a binuclear unit that is the oxygen binding site of CCO. It is the donation of electrons from this unit to oxygen that accounts for most of the oxygen consumption in biological tissue. The two remaining redox centres, Cu_a and haem a group, donate electrons to haem a_3 group and Cu_b centre. When electrons pass between these redox active centres through a series of redox reactions, changes in optical property occur. However, the absorption of NIR light from CCO is primarily due to the Cu_a centre, with a strong peak centred around 830 to 840 nm in the oxidised form [75]. The difference absorption spectrum between the oxidised and reduced versions of CCO is shown in Figure 3.4. As the total concentration of CCO remains constant during the period of clinical measurement, the difference in the absorption spectrum between the oxidised and the reduced states of the enzyme can be utilised to obtain the concentration changes of oxidised CCO, or the oxCCO signal which is a measure of the redox state of the enzyme, reflecting the balance between cerebral energy supply and demand [18]. As can be seen from Figure 3.4, the difference absorption spectrum of CCO has the same magnitude of those

for haemoglobin species. However, the concentration of CCO in tissue is approximately 10% of that of haemoglobin [79], making it more challenging to resolve concentration changes of this chromophore with high accuracy.

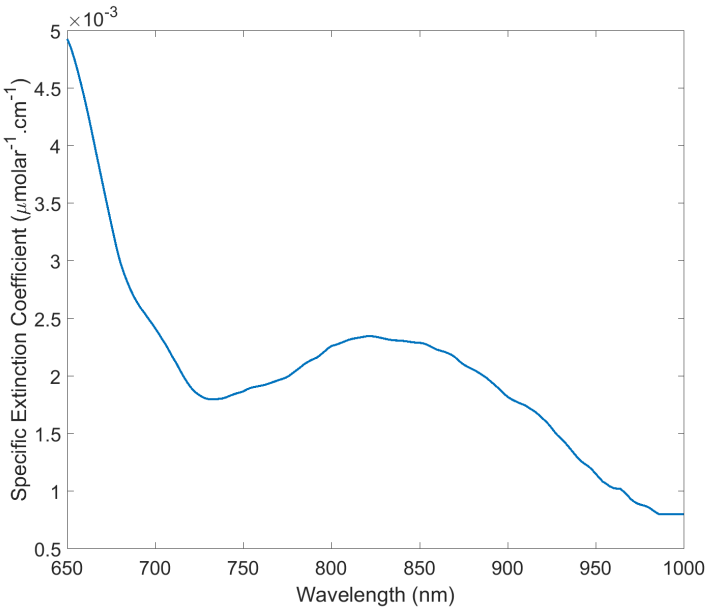

Figure 3.4: Specific extinction coefficient of the difference spectrum between the oxidised and reduced CCO. Spectral data was taken from UCL BORL website [77].

NIR Window of transparency As water and haemoglobin are present in very high concentrations in tissue, their absorption spectra determine the wavelengths of light that can penetrate through the tissue. As can be seen from Figure 3.5, water absorbs strongly at wavelengths greater than 900 nm and lower than 200 nm. Similarly, haemoglobin is a strong absorber at wavelengths below 600 nm. The spectroscopic window between 600 nm to 900 nm with the characteristics of low absorption of both water and haemoglobin allows light to penetrate through superficial tissues to reach tissues at sufficient depth (e.g. brain tissue and capillaries on the surface of grey matter) to have meaningful spectroscopic measurements. Within this NIR window of transparency, light scattering is the most dominant light-tissue interaction in biological tissue and as a result, the incident light diffuses rapidly through biological tissue. This process will be discussed in the next section.

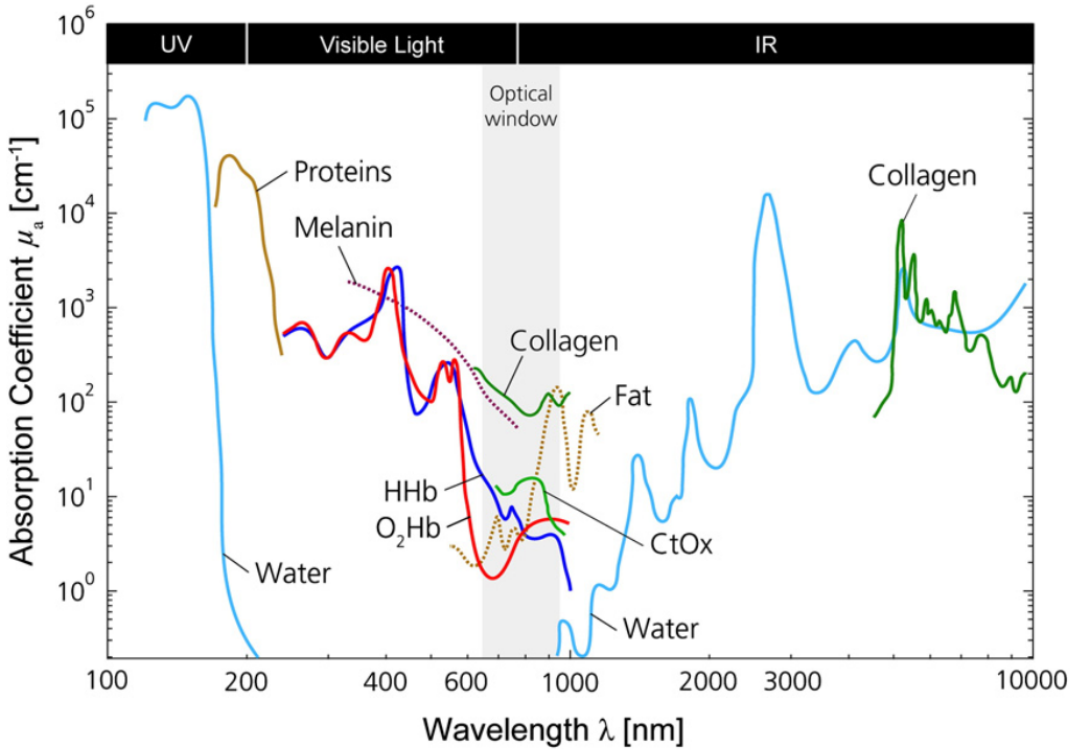

Figure 3.5: Absorption spectra (natural logarithm base) for different chromophores in human tissues from 100 nm to 10,000 nm. Spectra are given with the specific concentration in mM. Chromophores included are HbO_2, HHb, CCO, proteins, water, collagen and fat. Taken from [3]

3.1.1.3 Light scattering

Light scattering is the process during which the direction of travel or the energy of the incident photon is altered due to the interaction with matter. In biological tissue, scattering is the dominant type of light-tissue interaction, accounting for most of the attenuation of incident light. Scattering events can be divided into two types: elastic scattering and inelastic scattering. Elastic scattering is the process in which energy of the incident photon is reserved and the scattered photon has the same frequency as the incident photon but with a different direction. Inelastic scattering, on the other hand, is characterised by the increase or decrease in energy level of the incident photon due to the interaction with matter and as a result the scattered photon has a different frequency than the incident photon. In biological tissue, virtually all scattering events are elastic with no change in energy and the photon only changes direction. Inelastic scattering is generally neglected in biomedical optics. The type of elastic scattering events that occur in biological tissue is determined by the size of the scattering particle, the wavelength of the incident light and the refractive indices of the scattering medium.

Rayleigh scattering When the diameter of the scattering particle is much smaller than the wavelength of the incident light $\lambda >> \pi d$, Rayleigh scattering occurs during which the arrival of the incident photon momentarily raises the energy of the particle. The particle, at the higher energy state, radiates a photon with the same energy but in a different direction. For NIR light of wavelengths of about 1000 nm, a scattering particle must be smaller than 100 nm to be considered as a Rayleigh scattering particle. This is the size of cell organelles such as mitochondria. Rayleigh scattering intensity is inversely proportional to the fourth power of the wavelength; has a strong dependency on the size of the particles and the intensity of the scattered radiation is identical in the forward and reverse directions.

Rayleigh-Gans-Debye Approximation Rayleigh theory can be extended to a scattering particle of larger diameter as long as the refractive index of the particle is close to that of the background. In this case, larger scattering particles ($\lambda > \pi d|n-1|$, $|n-1| < 1$, n is the refractive index) can be treated as a collection of Rayleigh scattering particles and the overall scattering is the sum of all individual scattering events of each Rayleigh scattering particle.

Mie Theory of Scattering Rayleigh theory breaks down when the size of the particle gets larger than 10% of the wavelength of the incident radiation. In those cases, Mie theory can be used to model light scattering. Mie scattering is independent of wavelength and larger in the forward direction. The greater the particle size, the more light is scattered in the forward direction.

Estimation of light scattering The attenuation of the incident light by scattering alone (Figure 3.6) can be described similarly to the case of absorption in equation 3.2:

$$I = I_0 e^{-\mu_s \cdot d}. \tag{3.13}$$

Where μ_s (mm^{-1}) is the scattering coefficient, representing the probability that a photon will be scattered per unit length travelled in the scattering medium. Similar to μ_a in equation 3.5, μ_s is the product of total scattering cross section of a particle and the number density of those particles in the scattering medium.

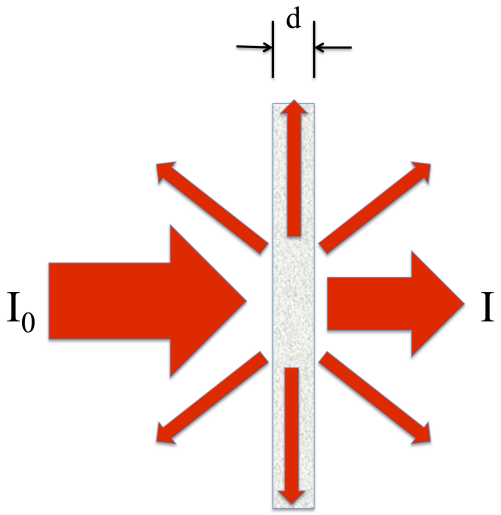

Figure 3.6: Cuvette model for scattering medium

However, equation 3.13 is only valid for the case of single scattering event, and it cannot be used for the multiple scattering event scenarios. However, due to the complexity of biological tissue with a mixture of different types of particles, each with different shapes and sizes and either homogeneous or heterogeneous, multiple scattering is the dominant event. In that case, it is difficult to estimate the total light attenuation due to scattering which is dependent on various factors. Therefore, the calculation of the absolute concentration of chromophores in tissue is a complex matter and is out of the scope of this thesis. However, light loss due to both absorption and scattering (total light attenuation) has to be taken into account in spectroscopic measurements in order to resolve changes in optical properties accurately.

3.1.1.4 Light attenuation

When light travels through biological tissue, it is attenuated by both absorption and scattering and the effect of both processes has to be taken into account when considering spectroscopic measurement. For an absorption-only medium, equation 3.10 and equation 3.11 can be used to describe light attenuation by one or more chromophores respectively in tissue. However, given that biological tissue is a highly scattering medium, these equations cannot be applied directly as they do not account for light loss due to scattering. The modified Beer-Lambert law (MBLL) developed by Delpy [80] takes into account light loss due to scattering and increased optical pathlength of scattered photons. As a result, the attenuation of light can be approximated using the following equation:

$$A = \sum_i \epsilon_i \cdot c_i \cdot d \cdot DPF + G. \tag{3.14}$$

A: total attenuation of light through an inhomogeneous tissue (OD)

DPF: differential pathlength factor to account for the increase in the distance travelled by photons due to multiple scattering (dimensionless)

d · DPF is the differential pathlength or the effective optical pathlength (cm)

G is the total light loss due to scattering and other boundary losses.

ϵ_i is the specific extinction coefficient of chromophore i ($molar^{-1}.cm^{-1}$)

c_i is the concentration of chromophore i (molar)

G is a geometry-dependent factor and is difficult to estimate. As a result, using conventional spectroscopy methods it is not possible to measure absolute attenuation in a scattering medium and so absolute concentrations of chromophores cannot be resolved. However, the attenuation due to scattering can be assumed to be constant at any given wavelength (but it is wavelength–dependent i.e. different at different wavelengths). This allows the use of MBLL to estimate the changes in concentrations of chromophores in biological tissues based on the change in attenuation measured. This is the basis for differential spectroscopy which will be discussed in the next section. DPF values depend highly on the degree of light scattering and weakly on the μ_a of the tissue. The relationship between DPF and μ_a can be demonstrated using theoretical attenuation data generated using a diffusion equation model as a function of μ_a in a scattering and non-scattering medium. The attenuation of light as a function of μ_a with four different scattering media is shown in Figure 3.7. The DPF can be determined as the slope of the curve.

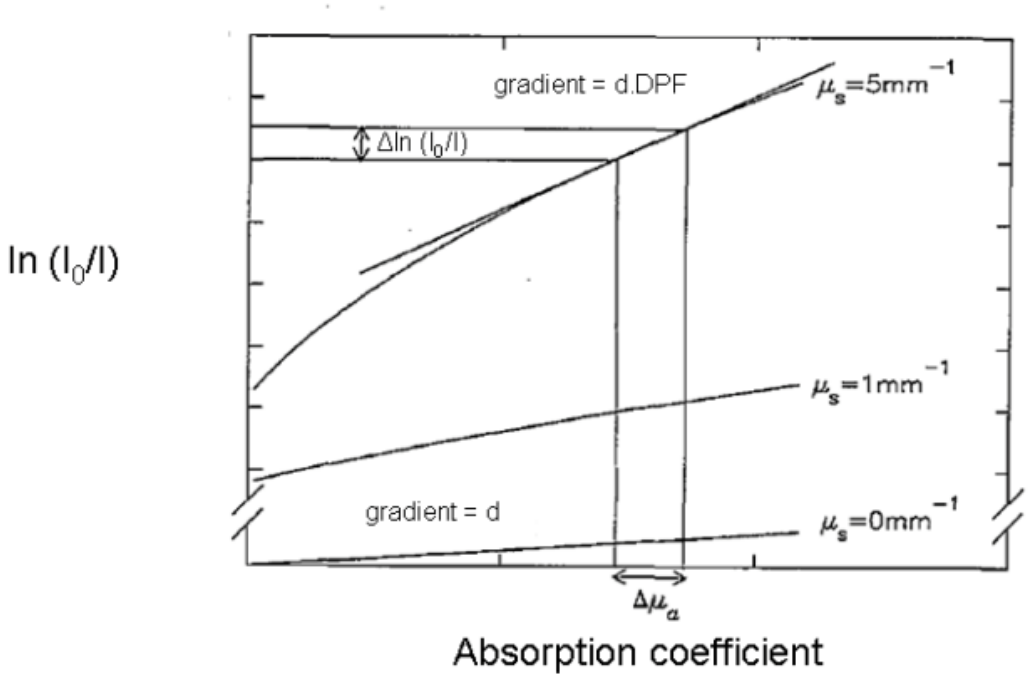

Figure 3.7: Theoretical relationship between attenuation and the absorption coefficient. The local gradient of the curve is equal to the optical pathlength $d \cdot DPF$ in the scattering medium $\mu_s > 0$. The gradient of the line in the non-scattering medium (μ_s =0) is equal to the geometric pathlength. Taken from [81]

Based on this theoretical data, DPF appears to increase with increasing μ_s and decrease with increasing μ_a. As μ_a and μ_s are wavelength-dependent, DPF is also wavelength-dependent. As in Figure 3.7, if the change in attenuation measured is small enough compared to the total attenuation, the DPF can be assumed to be constant for a given tissue.

It is important to stress the three strong assumptions that are made to derive the MBLL [1] to understand the limitations as well as to be aware when interpreting NIRS parameters:

- scattering stays constant or changes negligibly during the period of measurement. This assumption allows the subtraction of light loss due to scattering when considering the *change* in attenuation. Moreover, it also allows the assumption that the DPF at a certain wavelength is constant. This assumption, in the case of cerebral haemodynamics, is plausible as the change in blood flow due to neural activity will change the absorption coefficient (due to changes in proportion of different species of haemoglobin and CCO) of the tissue more strongly than it does to the scattering coefficient (due to changes in the scattering particles or the structure of the sampling volume- the neuronal tissue). However, there are cases where this assumption

is unrealistic such as in brain injury where there are changes in scattering of the tissue [82].

- the change in absorption in the sampling volume is homogeneous. This assumption is often invalid given that absorbers are non uniformly distributed in tissue. Two kinds of errors can arise where the limitation of this assumption is not taken into account: 1) partial volume effect where the estimated concentration change by the MBLL is an underestimate of the real concentration change [83] and 2) cross-talk between chromophores where the estimated change in one chromophore is influenced by the change of another chromophore [71].

- the medium in which the changes in absorption are monitored is homogeneous. This is certainly wrong in biological tissues where the tissue is a complex mixture of different substances and NIR light passes through several tissue layers both before and after passing through the brain tissue.

Even though there are limitations in the MBLL, its development has made a significant advance in NIRS and as a result, most commercial NIRS instrumentation rely on this method [3].

3.2 Differential spectroscopy

As mentioned above, due to the fact that the value of G is unknown and is dependent on the measurement geometry and the scattering characteristics of the tissue interrogated, absolute concentrations cannot be derived from the MBLL (equation 3.14). However, if G does not change during the period of measurement, *changes* in the concentration of chromophores can be calculated from the measured *changes* in attenuation. For simplicity's sake, consider the medium with only one chromophore, at time t_1, its concentration in the medium is c_1 and at time t_2, its concentration is c_2. The measured attenuation at two time points is A_1 and A_2 respectively. Using the MBLL, we have:

$$A_1 = \epsilon \cdot c_1 \cdot d \cdot DPF + G \tag{3.15}$$

$$A_2 = \epsilon \cdot c_2 \cdot d \cdot DPF + G \tag{3.16}$$

The Δ in concentration of the chromophore ($\Delta c = c_2 - c_1$) can be calculated from the change in measured attenuation ($\Delta A = A_2 - A_1$) where G cancels out.

$$\Delta A = \epsilon \cdot \Delta c \cdot d \cdot DPF \tag{3.17}$$

Expanding the equation 3.17 to i number of chromophores

$$\Delta A = \sum_i \epsilon_i \cdot \Delta c_i \cdot d \cdot DPF \tag{3.18}$$

Expanding the equation 3.18 to j number of wavelengths

$$\Delta A_{\lambda j} = \sum_{i,\lambda j} \epsilon_{i,\lambda j} \cdot \Delta c_i \cdot d \cdot DPF \tag{3.19}$$

Equation 3.19 is the basis of differential spectroscopy, the technique that can be used to calculate concentration changes of tissue chromophores such as HbO_2, HHb and oxCCO. To solve for concentration changes of two chromophore, HbO_2 and HHb, measurements of changes in attenuation at two wavelengths are needed:

$$\begin{bmatrix} \Delta A_{\lambda_1} \\ \Delta A_{\lambda_2} \end{bmatrix} = \begin{bmatrix} \epsilon_{HbO_2,\lambda_1} & \epsilon_{HHb,\lambda_1} \\ \epsilon_{HbO_2,\lambda_2} & \epsilon_{HHb,\lambda_2} \end{bmatrix} \begin{bmatrix} \Delta c_{HbO2} \\ \Delta c_{HHb} \end{bmatrix} \cdot d \cdot DPF \tag{3.20}$$

Solving equation 3.20 for concentration changes of HbO_2 and HHb:

$$\begin{bmatrix} \Delta c_{HbO_2} \\ \Delta c_{HHb} \end{bmatrix} = \frac{1}{d \cdot DPF} \begin{bmatrix} \epsilon_{HbO_2,\lambda_1} & \epsilon_{HHb,\lambda_1} \\ \epsilon_{HbO_2,\lambda_2} & \epsilon_{HHb,\lambda_2} \end{bmatrix}^{-1} \begin{bmatrix} \Delta A_{\lambda_1} \\ \Delta A_{\lambda_2} \end{bmatrix}. \tag{3.21}$$

3.3 Broadband near-infrared spectroscopy

In theory, it should be possible to resolve concentration changes of three chromophores, HbO_2, HHb and oxCCO using three wavelengths. However, there are some specific issues that need to be considered regarding resolving the oxCCO signal. Although the difference absorption spectrum of CCO is similar in magnitude to those of HbO_2 and HHb, the concentration of CCO in the brain is approximately one order of magnitude less than that of the other two chromophores [84]. This makes the measurement of CCO more challenging and raises the question whether the CCO signal is a crosstalk artefact resulting from the insufficient separation of chromophores from algorithm errors [71], [85]–[87]. Several studies have demonstrated the independence of the oxCCO signal from the haemoglobin signals, and that fitting the CCO spectrum results in a better fit of the measured attenuation data [6], [12], [71]. Moreover, the CCO signal demonstrates a brain specificity characteristic that is not seen in the haemoglobin signals [12]. Mod-

elling work has suggested that measuring light attenuation at multiple wavelengths can minimise the errors from the algorithm and result in more accurate measurements [88]. As a result, measurement of Δ[oxCCO] is usually acquired by broadband spectroscopy system, measuring light attenuation across a continuous portion of the spectrum. In this thesis, the UCLn algorithm [88] is used to analyse that measured broadband spectrum to resolve concentration changes of chromophores. The UCLn equation is given below:

$$\begin{bmatrix} \Delta c_{HbO_2} \\ \Delta c_{HHb} \\ \Delta c_{oxCCO} \end{bmatrix} = \frac{1}{d.DPF} \begin{bmatrix} \epsilon_{HbO_2,\lambda_1} & \epsilon_{HHb,\lambda_1} & \epsilon_{oxCCO,\lambda_1} \\ \epsilon_{HbO_2,\lambda_2} & \epsilon_{HHb,\lambda_2} & \epsilon_{oxCCO,\lambda_2} \\ \vdots & \vdots & \vdots \\ \epsilon_{HbO_2,\lambda_n} & \epsilon_{HHb,\lambda_n} & \epsilon_{oxCCO,\lambda_n} \end{bmatrix}^{-1} \begin{bmatrix} \Delta A_{\lambda_1} \\ \Delta A_{\lambda_2} \\ \vdots \\ \Delta A_{\lambda_n} \end{bmatrix} \tag{3.22}$$

The MBLL only allows calculation of concentration changes of chromophores from an arbitrary baseline, not the absolute concentration. Its measurement is sensitive to changes in the coupling between optodes and tissue and changes in the tissue surface – such as subcutaneous skin circulation. In addition to the MBLL, there is another NIRS technique to resolve an absolute index of tissue oxygenation which will be discussed in the next section.

3.4 Spatially resolved spectroscopy

Spatially resolved spectroscopy (SRS) is a technique based on light attenuation being measured at several different source-detector distances to derive the ratio between HbO_2 and (HbO_2 + HHb), also known as the tissue oxygenation index (TOI) (3.23) [89]. The technique uses the solution to the diffusion equation which is a special case of the radiative transfer equation to derive the scaled absolute concentration of HbO_2 and HHb which will be discussed in detail later.

$$TOI = \frac{kHbO_2}{k(HbO_2 + HHb)} \times 100\%. \tag{3.23}$$

SRS assumes that the coupling between the optodes and the tissue is the same for different source-detector distances and the superficial layers of tissue affect all the measurements of attenuation in the same way so that their effects cancel out. This means that SRS measurements are more sensitive to cerebral changes. Using the technique during carotid endarterectomy, Al-Rawi concluded that the TOI value measured by the NIRO 300 reflects changes in cerebral tissue oxygenation and it was predominantly associated

with internal carotid clamping [90]. To understand the nature of the SRS technique, a closer look at the diffusion equation is necessary.

Propagation of photons in tissue can be described using the diffusion equation [91]. For a semi-infinite half-space geometry, the intensity of the reflected light R from an impulse input can be expressed using the following equation:

$$R(\rho,t) = (4\pi Dct)^{-3/2}\frac{1}{\mu_s'}t^{(-5/2)}exp(-\frac{\rho^2+\mu_s'^{-2}}{4Dct}-\mu_a ct). \tag{3.24}$$

R is the reflected intensity;

ρ , t are the distance and time from the impulse input;

μ_a is the absorption coefficients;

μ_s' is the reduced scattering coefficients which is a product of μ_s and a factor pertaining to the anisotropy of tissue scattering.

$D = 1/3(\mu_a + \mu_s')$ is the diffusion coefficient and c is the velocity of light.

For continuous wave systems, the intensity $I(\rho)$ is the integral of R over time and the attenuation is the negative log of $I(\rho)$

$$A(\rho) = -log_{10}\int_0^\infty R(\rho,t)\delta t \tag{3.25}$$

Substituting the expression derived for $R(\rho)$ in equation 3.24 into equation 3.25, differentiating with respect to ρ and letting $\mu_s' \approx \mu_s' + \mu_a$ (from $\mu_s' \gg \mu_a$) gives:

$$\frac{\delta A}{\delta \rho} = \frac{1}{\ln(10)}(\sqrt{3\mu_a\mu_s'}+\frac{2}{\rho}). \tag{3.26}$$

μ_s' can be assumed to be constant. However, to increase accuracy, the decrease of $\mu_s'(\lambda)$ over wavelength is taken into account by the equation:

$$\mu_s' = k(1-h\lambda) \tag{3.27}$$

where k is an unknown constant and h is the slope of the wavelength dependency of μ_s' and is set to 8.5 x 10^{-4} nm^{-1} [82].

Combining equations 3.27 and 3.26 to solve for $k \cdot \mu_a$:

$$k\mu_a(\lambda) = \frac{1}{3(1-h\lambda)}(\ln(10)\frac{\delta A(\lambda)}{\delta\rho}-\frac{2}{\rho})^2. \tag{3.28}$$

Given that $\mu_a = \ln(10) \cdot \epsilon \cdot c$, equation 3.28 can be used to solve for scaled concentrations of HHb and HbO_2 using two wavelengths:

$$\begin{bmatrix} k\mu_{a,\lambda_1} \\ k\mu_{a,\lambda_2} \end{bmatrix} = \ln(10) \begin{bmatrix} \epsilon_{HbO_2,\lambda_1} & \epsilon_{HHb,\lambda_1} \\ \epsilon_{HbO_2,\lambda_2} & \epsilon_{HHb,\lambda_2} \end{bmatrix} \begin{bmatrix} kc_{HbO_2} \\ kc_{HHb} \end{bmatrix}. \tag{3.29}$$

Solving for scaled concentrations of HbO_2 and HHb

$$\begin{bmatrix} kc_{HbO_2} \\ kc_{HHb} \end{bmatrix} = \frac{1}{\ln(10)} \begin{bmatrix} \epsilon_{HbO_2,\lambda_1} & \epsilon_{HHb,\lambda_1} \\ \epsilon_{HbO_2,\lambda_2} & \epsilon_{HHb,\lambda_2} \end{bmatrix}^{-1} \begin{bmatrix} k\mu_{a,\lambda_1} \\ k\mu_{a,\lambda_2} \end{bmatrix}. \tag{3.30}$$

When calculating TOI, the scaling factor k is cancelled out as shown in equation 3.31.

$$TOI = \frac{HbO_2}{(HbO_2 + HHb)} \times 100\%. \tag{3.31}$$

3.5 NIRS instrumentation

There are three different types of NIRS instrumentation, each of which utilises a different approach to resolve the specific tissue information [92] (Figure 3.8). Continuous-wave (CW) NIRS system is the focus here; however, frequency domain (FD) NIRS system and time-resolved (TR) NIRS system are summarised briefly for completeness. CW systems measure the variation in the light intensity passing through the tissue. FD systems measure the change in the intensity and the phase shift of the modulated intensity injected into the tissue. TR systems measure the variation in both the intensity of light and the time of flight of photons through the tissue. In this thesis, all of the data presented was acquired using CW systems. As a result, detailed discussion about CW systems will be provided and only brief introductions will be given for the other two techniques.

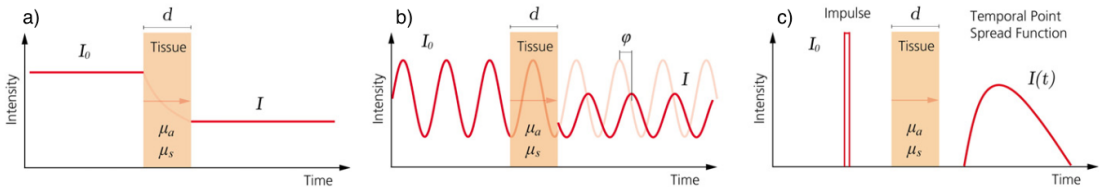

Figure 3.8: Three different types of NIRS systems. a) Continuous wave NIRS system emits light at constant intensity to the tissue and measure the intensity of diffusely reflected light reemerging from the tissue. b) Frequency domain NIRS emits light at modulated intensity and frequency and measures the intensity and the phase shift of the reflected light. The latter corresponds to the time of flight. c) Time domain NIRS system emits an extremely short pulse of light to the tissue and measures the intensity and the time of flight of photons which constitute a temporal point spread function. Taken from [3]

3.5.1 Frequency Domain Systems

Frequency domain systems modulate the light intensity delivered to tissue at high frequency (5 MHz to 1GHz) and measure both the intensity of the diffusely reflected light and the phase shift (corresponding to the time of flight of photons through tissue). By detecting the changes in amplitude and the phase shift of the reflected intensity, absorption coefficients (μ_a), scattering coefficients (μ_s) and DPF can be calculated continuously.

3.5.2 Time Resolved Systems

Time-resolved systems deliver short impulses of light (a few picoseconds) through the tissue and measure the time of flight of individual photons through the tissue. This results in the temporal point spread distribution of photons (TPSF). TPSF has a characteristic shape spanning to several nanoseconds because of the effect of light scattering on the optical pathlength of photons – a histogram of the number of photons on the y axis and their arrival times on the x axis. This histogram can be used to calculate the absorption (μ_a) and the reduced scattering coefficients (μ_s'). The absorption coefficient can be used later to calculate the absolute concentration of chromophores in tissues.

3.5.3 Continuous Wave System

CW systems deliver light at a constant intensity to the tissue of interest and measure the intensity of the light re-emerging from it. This allows changes in attenuation, ΔA, due to changes in optical properties of tissue to be recorded continuously. Usually, at least two different wavelengths are used to obtain spectral information. Using appropriate algorithms [88], the changes in concentration of different chromophores present in the tissue can be calculated. CW systems are the simplest, the least expensive of all NIR systems and they are stable and allow a remarkable amount of useful information to be obtained. As a result, most commercial NIRS systems use this approach [3] and there are many clinical successes as detailed in [1].

The most basic CW NIRS system has one source-detector pair that can probe one region of tissue of interest. This setup has been employed successfully in numerous clinical studies [1]. However, planar arrays of sources and detectors can be used to monitor multiple regions of interest simultaneously to enable both high spatial resolution and large coverage. In this case, due to the density of measurement channels and the fact that each NIR source and detector may support multiple measurements, illumination by sources has to be encoded and decoded while detectors acquire data continuously.

Three popular encoding techniques that are employed by CW NIRS systems are spatial, temporal and frequency encoding. With spatial encoding, sources are located at sufficient distance apart such that there is a minimal level of double illumination to any single detector when both sources are illuminated. In temporal encoding, sources are illuminated sequentially in certain time steps that can provide the balance of delivering sufficient amount of light to tissue and sufficient sampling rate. In frequency encoding, sources can be illuminated in parallel but they are intensity-modulated at different frequencies. The detected intensity from each source can be separated by frequency using Fourier Transform or lock-in amplifiers. Multiple encoding methods have been utilised to increase the density of measurement channels to acquire high density diffuse optical tomography images of oxygenated and deoxygenated haemoglobin using two wavelengths as demonstrated by Eggebrecht and colleagues [93].

Despite having the advantages of easy setup, low cost and yielding a tremendous amount of useful information, CW systems have two fundamental drawbacks that need to be considered. First of all, CW systems are highly sensitive to any changes in source detector coupling to the subject. The variation in pressure applied to both source and detector fibres during a clinical experiment can introduce a significant change in the intensity measurement. Sweating, frowning or any actions that introduce movements to the sources and detectors independently can also create a large change in intensity. The variation in the distribution of hair when the measurements are acquired in regions apart from the frontal cortex also poses challenges for the optode coupling. However, these variations can be minimised by having a good headgear and probe holder design. The other limitation of CW technique is that it is only sensitive to the tissue immediately below the source-detector pair as described by the photon measurement density function (PMDF) [94]. In general. increasing the distance between the source and the detector will increase the number of photons passing through deeper tissues, therefore increase the sensitivity of the channel to brain tissue. However, increasing the source detector distance is at the expense of signal-to-noise (SNR) ratio, simply because fewer photons can reach the detector. In the adult population, source detector separation of 30 mm is a good compromise between having a reasonable sensitivity to the cortex and having enough light to have a reasonable SNR.

Although there are certain limitations, CW systems have found widespread use due to their simplicity and the amount of useful physiological information that can be obtained. As a result, there is a wide range of commercially available CW NIRS systems on the market [3]. System complexity ranges from devices with a single source-detector pair

to devices that have the capability of full head imaging. Some manufacturers have developed integrated boards housing both sources and detectors that can be coupled directly to the scalp [95] while others depend on the use of optical fibres to transmit light and receive light. Most systems have a compact design and are transportable on carts; however, there are some systems that are designed to be fully portable, wirelessly transport the data to a PC or store them in an SD card. Most commercial NIRS systems that use two or three wavelengths generated by lasers or LEDs only have the capability to resolve the haemoglobin concentration changes ($\Delta[HbO_2]$ and Δ[HHb]). Most systems that have the capability to measure changes in oxCCO were built in-house and those systems only have one or two channels. More information regarding CW NIRS instrumentation can be found in a review by Scholkmann [3].

This thesis focuses on the CW technique to resolve changes in the concentration of oxCCO in the adult human brain. This requires a special type of CW system called broadband NIRS spectroscopy system. Before discussing the explicit details of a broadband NIRS system, it is essential to understand the basic components of a CW system.

3.5.4 Components of a CW NIRS instrumentation

CW NIRS instrumentation is, in principle, the simplest among the three types of NIRS instrumentation. A basic setup for a CW system consists of (1) a NIR light source, (2) light transporting medium from the light source to the tissue and from tissue to photodetector and (3) photodetector to detect the reflected light from the tissue. Each of these components will be discussed in detail in the following session to give a basic understanding of the specifications of a standard CW NIRS system. Some specific focus will be given to the optimisation of the system for the measurement of oxCCO.

3.5.4.1 Light source

Most commercial CW systems utilise LEDs or lasers at specific discrete wavelengths as sources. These sources typically have two wavelengths to resolve $\Delta[HbO_2]$ and Δ[HHb] [3]. However, to resolve Δ[oxCCO] accurately, broadband light sources emitting light from a continuous portion of the spectrum from 650 nm to 900 nm is the gold standard. This can typically be achieved using a thermally-stable white light source with optical filters attenuating light with wavelengths below 650 nm and above 900 nm. A typical broadband spectrum with high intensity in the NIR region is shown in Figure 3.9.

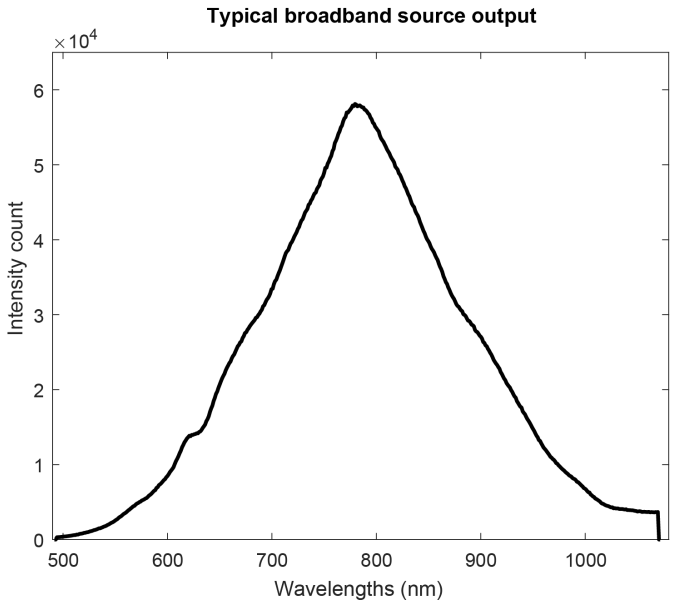

Figure 3.9: Typical broadband source output with high intensity in the NIR region of the spectrum

Two of the most important characteristics of a CW NIRS broadband light source are optical power and optical stability. Ideally, optical power is chosen to maximise the intensity at the detector, resulting in high signal to noise ratio and the ability to probe deep tissues. However, high irradiation may lead to tissue heating causing changes in the tissue architecture which may lead to discomfort and damage. For safety reasons, the amount of light output from sources of most NIR systems operating in continuous mode is kept below $2mW/mm^2$. Source stability is an important feature for the NIRS light source. This is because any variation in the intensity due to the light source itself will introduce more noise to the signals measured at the detector. Instability can be accidentally introduced by noisy power supply or due to temperature effects on the light source. These factors can be mitigated by careful design of the light source.

3.5.4.2 Photodetector

Most commonly used photodetectors in commercial CW NIRS systems are photodiodes (Figure 3.10a) and avalanche photodiodes. Both of these use the principle of the photoelectric effect to convert light to electrical signals. However, for broadband CW NIRS systems, charge-coupled devices (CCDs) (Figure 3.10b) are commonly used in combination with a spectrograph and series of lenses. This is because these systems need to record the intensity of the diffusely reflected light across a continuous portion of the spectrum. The incoming light to the spectrometer is directed through a series of lenses before being separated into its wavelength components by a diffraction grating. The spec-

trum is collected by the CCD camera. Because light loss occurs during these processes, the spectrometer must be designed to ensure a high throughput of light and a low noise characteristic. CCD cameras are usually cooled to reduce the thermal dark count.

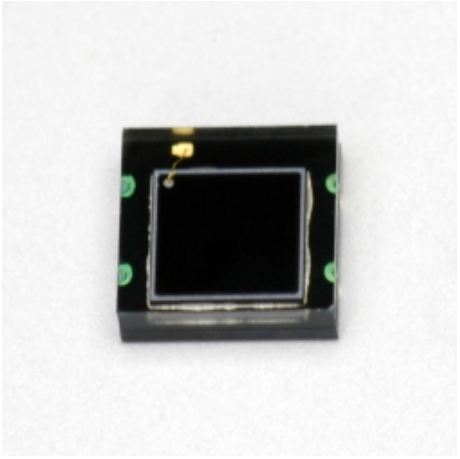

(a) Hamamatsu S12158-01CT photodiode

(b) Pixis:1024f CCD camera

Figure 3.10: Commonly used photodetectors for CW NIRS systems.

3.5.4.3 Light transport medium

Optical fibres are commonly used as the light transport medium for broadband NIRS systems. They carry light from the source to the subject (source fibres) and collect the reflected light from the subject to the spectrometer (detector fibres). Detector fibres are usually designed to have high numerical aperture to increase the amount of light collected. When using optical fibres, it is important to ensure that light coupling at both the sources and the detectors to the scalp is optimal. This is important because, as mentioned in the previous section, CW technique is highly sensitive to changes in optical coupling and any changes may introduce artefacts to spectroscopic measurements. Achieving good optical coupling is challenging when carrying out experiments on the hairy region of the head as hair has to be moved away from all the detectors and the sources to ensure high intensity. Moreover, light intensity, in this case, is highly dependent on hair colour, hair density and skin pigmentation. Regarding the design of optical fibres, the subject ends of all fibres have to be carefully designed so as to make sure that they can be easily coupled to the skin through the use of probe holders which will be discussed in the next section.

The advantages of using optical fibres as the transport medium are that they allow flexibility in source detector arrangements; they are inherently safe as there are no electronics coming into contact with the subject. They also allow the system to be further away from the subject. However, optical fibres may become bulky and heavy as the

number of sources and detectors increases. Some form of weight bearing system must be used to mitigate this shortcoming to ensure good optical coupling and comfort for the subject. Because of those features of optical fibres, some commercial NIRS systems have a design where sources and detectors are integrated on a single chip. As a result, these can be coupled directly to the skin without the need of using optical fibres.

3.5.4.4 Probe holders - head gear

For broadband NIRS systems with optical fibres, probe holders must be used to fix these fibres in place during clinical experiments to ensure good optical coupling (an example is shown in Figure 3.11). Holder design has to be optimised for each specific clinical experiment and each subject type. For example, in infant studies, movements are unavoidable and therefore any probe holder design has to ensure that both sources and detectors are tightly coupled to the scalp to minimise artefacts generated by movements (Figure 3.12). In some other experiments, probe holder design has to allow clearance of hair from beneath the sources and detectors. Another important function of probe holders is to fix the distance between source-detector pairs. This can be achieved by making the probe holder with a material with suitable flexibility or introducing fixed-distance connections between the source-detector pairs.

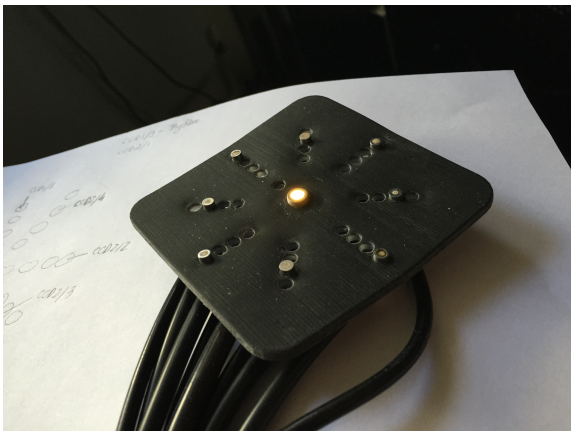

Figure 3.11: A 3D printed probe holder designed to hold one central source and eight surrounding detectors.

Figure 3.12: Head gear design for clinical experiment with babies (image from Centre for Brain and Cognitive Development, Birkbeck)

to hold sources and detectors tightly to the scalp to prevent movement artefacts.

3.5.5 CW-NIRS instrumentation with the capability of measuring changes in oxCCO concentration

Current commercial systems do not have the capability to measure Δ[oxCCO] accurately [3] (as of August 2017). Most CW-NIRS systems with the capability of measuring changes in oxCCO were developed in-house with only a limited number of channels. Table 3.1 provides a brief summary of NIRS instrumentation that has the capability of investigating the Δ[oxCCO] signals. Most of the systems to date only have a limited number of channels populated within one or two regions to monitor the haemodynamic and metabolic changes. However, investigation of localisation of functional brain activity or localised brain injury requires monitoring over multiple regions of the brain. There is an unmet need for a non-invasive multi-channel broadband NIRS system that can monitor the haemodynamic changes and cellular oxygen metabolism over multiple areas of the adult human brain.

Table 3.1: Brief summary of NIRS oxCCO instrumentation as of August 2017

NIRS Systems	Number of λ	Number of source(s)	Number of detector(s)	Number of channels used	Multi-distance/TOI
Duke 1 [96]	3	1	1	1	No/No
Duke 2 [97]	4	1	1	1	No/No
UCL 1 [98]	4	1	1	1	No/No
Keele 1 [99]	3	1	1	1	No/No
Keele 2 [100]	4	1	1	1	No/No
NIRO 1000 [101]	6	1	1	1	No/No
NIRO 500 [102]	4	1	1	1	No/No
NIRO 300 [90]	4	1	3	1	Yes/Yes
UCLn [6], [7], [103]	Broad-band	1	1	1	No/No
UCLn - CYRIL [13]	Broad-band	2	8	2	Yes/Yes
UCL Hydrid [12]	Broad-band	2	8	2	Yes/Yes
Humboldt 1 [70]	Broad-band	1	1	1	No/No
Humboldt 2 [71]	Broad-band	1	4	4	No/No
Ryerson 1 [104]	Broad-band	2	2	2	No/No

3.5.6 The multi-distance broadband NIRS system in BORL

This section gives the specifications of the dual-channel multi-distance broadband instrument (MDBBS) built previously in BORL [11], [105]. The system has two channels, each of which has the three typical components of a broadband CW NIRS system: a white light source, a CCD camera that is incorporated into the spectrograph and optical fibres (Figure 3.13).

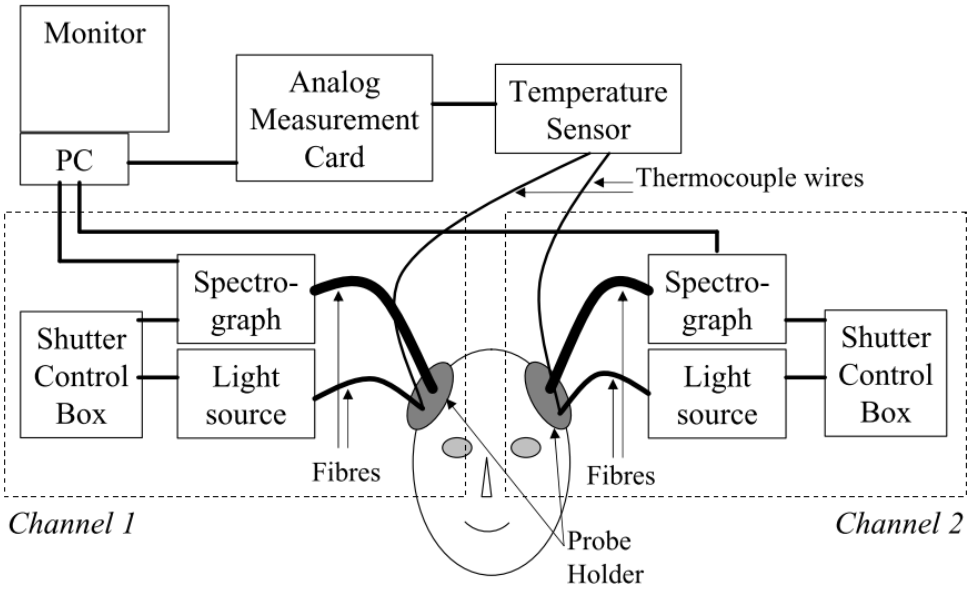

Figure 3.13: Schematic diagram showing the components of the MDBBS system built in BORL.Taken from [106].

Each channel of the MDBBS system utilises a 50W halogen bulb as a white light source emitting broadband light which is band-pass filtered to remove wavelengths below 504 nm and above 1068 nm to reduce the temperature effect. All the main components of the light source are given in Figure 3.14. The light from each light source is directed to the subject via a single light source fibre with a fibre diameter of 4 mm. The diffusely reflected light from the subject is collected using four detector fibres placed at four different distances away from the light source. Detector fibres at 20 mm and 25 mm have a fibre diameter of 1mm, whereas detector fibres at 30 mm and 35 mm have a diameter of 2 mm and 3 mm respectively as shown in Figure 3.15. The light from the detector fibres is passed to a lens-based spectrograph (Figure 3.16). The spectrograph contains Minolta MC Rokkor lenses with a focal length of f= 58 mm and a f-number of f/# = 1:12 to provide a higher throughput of light. A diffraction grating (Thorlabs GR50-0310) with 300 grooves per mm that is blazed at 1000 nm is used optimise the reflection in NIR region of the spectrum. The light spectrum is detected by a CCD camera (PIXIS:512f, Princeton Instruments) with chip dimension of 12.3 mm x 12.3 mm corresponding to 512 x 512 pixels. The CCD camera is cooled to -70°C to reduce thermal noise and increase sensitivity.

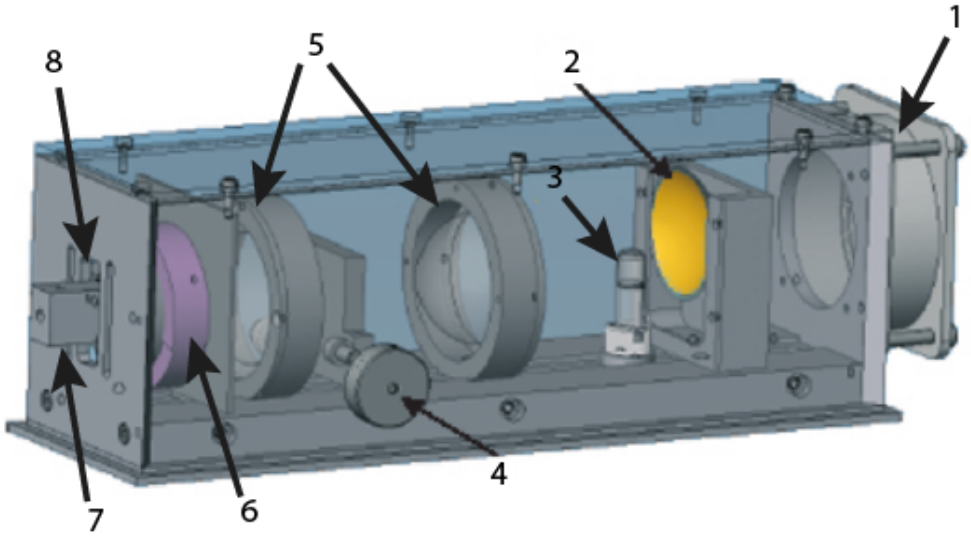

Figure 3.14: In-house built light source.1) Ventilator. 2) Gold plated concave mirror. 3) Halogen bulb. 4) Metal plate. 5) Optical lenses. 6) Magnetic shutter. 7) Entrance for source fibre. 8) Band-pass filter. Taken from [106].

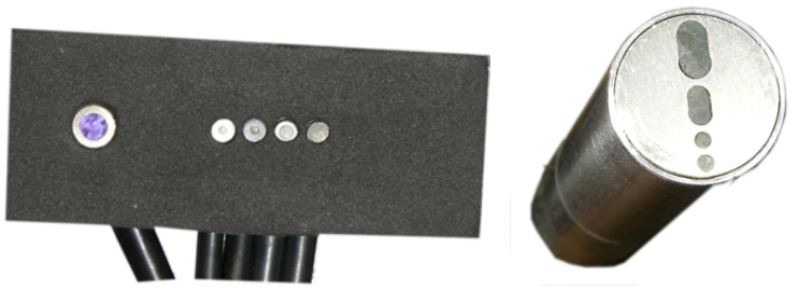

Figure 3.15: One channel of the MDBBS system. a) A source fibre and four detector fibres, each with different diameters placing at 20, 25, 30 and 35 mm away from the source. b) Ferule (spectrometer end) of the detector fibres showing the oval crossed section with different diameters. Taken from [106].

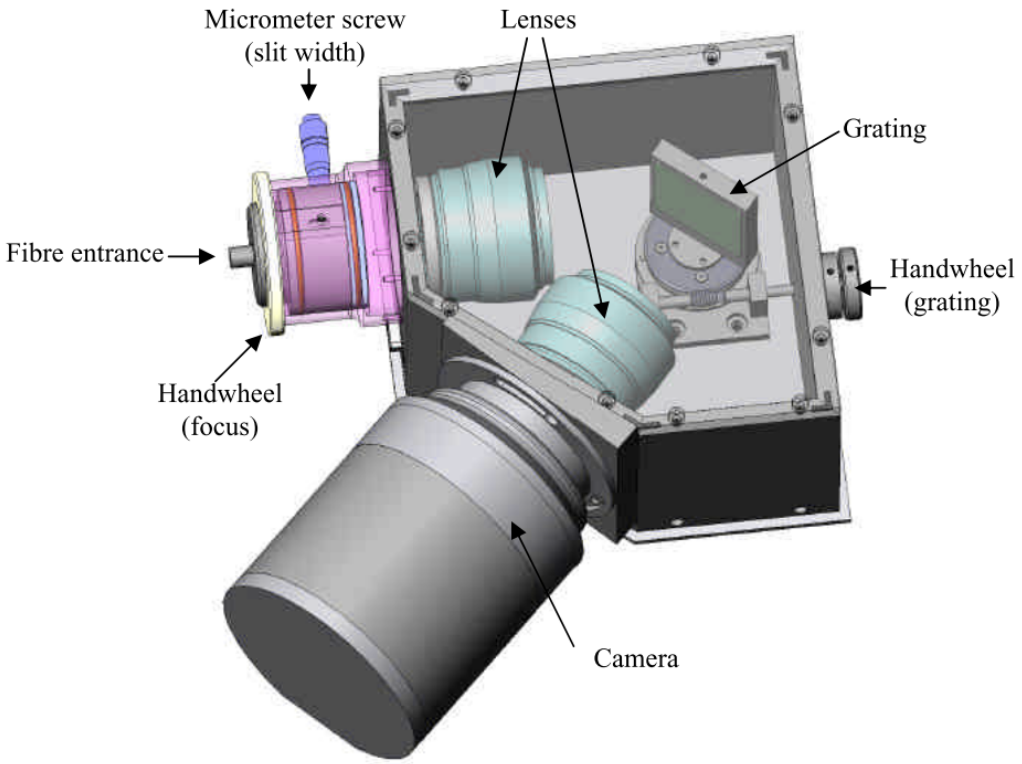

Figure 3.16: The spectrograph and camera of a channel of the MDBBS system. Taken from [106].

Overall, the MDBBS has two channels, each of which has its own light source fibre, detector fibres, a spectrograph and a CCD camera. With this arrangement of optical fibres, the system can be used to monitor two brain regions simultaneously. Each region is monitored by one source and four detector fibres. As mentioned earlier, the main objective of this thesis is to develop a system that can monitor cellular oxygen metabolism across multiple regions of the adult human brain. As a result, iterative development was introduced to this MDBBS system to develop it into a multi-channel system with the capability of measuring oxCCO across multiple regions. However, before discussing the process of system development, it is important to have an overview of in vivo human studies investigating the oxCCO signal and their results. This will give the foundations for the understanding and interpretation of the spatial changes in oxCCO in the next few chapters.

3.6 CCO studies in the healthy adult brain

This section provides an overview of NIRS studies using broadband instrumentation to investigate the change in CCO redox state reflected by the Δ[oxCCO] signal in the adult

human brain. Given the position of CCO in the electron transport chain, the redox state of CCO reflects the balance between electron supply from cytochrome c and electron demand from oxygen molecules. Although there are many factors that can influence this supply and demand, the most significant is the availability of molecular oxygen [85]. This is the reason that the BORL group at UCL has performed several volunteer studies during which changes in cerebral oxygen delivery was manipulated through systemic physiological challenges and functional activation tasks. The details of those will be discussed here.

3.6.1 Volunteer studies with systemic challenges

In this section, published studies that investigated the response of oxCCO signal to challenges that cause an increase in cerebral oxygen delivery (hyperoxia and hypercapnia) and those that cause a decrease in cerebral oxygen delivery (hypoxia and hypocapnia) in the healthy adult volunteers will be discussed. The hypothesis for these studies was that challenges which increase cerebral oxygen delivery would result in an increase in the Δ[oxCCO] signal measured by broadband NIRS and challenges that decrease cerebral oxygen delivery would result in a decrease in the Δ[oxCCO] signal.

Early studies of this kind were done in the 1990s by Jobsis's group at Duke University, North Carolina, USA. Sustained isocapnic hypoxia challenge during which arterial oxygen saturation (Sa_{O2}) was maintained at 80% was used to assess the change in the oxidation state of CCO. Four wavelength NIR instrumentation using a single channel with source detector separation of 35 mm was used to collect the optical data. A significant decrease in oxCCO signal was evidenced during the challenge [107]. Much later in 2007, Tisdall et al. [5] used a broadband spectroscopy system having one channel with the same source detector separation and the UCLn algorithm to evaluate the concentration changes of HbO_2, HHb and oxCCO during hypoxemia [5]. A significant decrease in the Δ[oxCCO] signal was again observed. Moreover, distinct differences between the oxCCO signal and the haemoglobin signals were demonstrated in individual and group data. A significant correlation was found between a measure of cerebral oxygen delivery and Δ[oxCCO] but not with either Δ[HbT] or Δ[HbDiff]. As a result, the author suggested that Δ[oxCCO] signal has clinical relevance and is a more reliable marker of reduced cerebral oxygen delivery during hypoxemia than the other two NIRS signals. A later study by Kolyva et al. confirmed this decrease in Δ[oxCCO] signal by using a hybrid optical spectrometer (pHOS), combining multi-distance frequency and broadband spectrometers [11]. The pHOS was designed to address the technical issues hindering the

accuracy of oxCCO measurements [10], notably the changes in optical scattering [85], [86] and insufficient separation of chromophores by the resolving algorithm [6], [71], [85]–[87].

During hyperoxia, the expected increase in cerebral oxygen delivery is hypothesised to result in an increase in the Δ[oxCCO] signal. This was demonstrated in a study by Tachtsidis and colleagues where hyperoxia was achieved by increasing the inspired fraction of oxygen (FiO_2) to greater than 90% [108]. They measured Δ[oxCCO], Δ[HbO_2], Δ[HHb] and TOI using a broadband NIRS system having one channel with source detector separation of 35 mm. Mean blood flow velocity in the middle cerebral artery (Vmca) was measured using transcranial Doppler. There was significant positive correlation between Δ[oxCCO] and TOI and between Δ[oxCCO] and Δ[HbDiff] while negative correlation was found between Δ[oxCCO] and Vmca/Δ[HbT]. The author concluded that Δ[oxCCO] increased during the challenge and it was highly associated with brain tissue oxygenation. Later, Kolyva et al. repeated the study using the pHOS and the same result was found [12]. Moreover, the author also showed that the magnitude of Δ[oxCCO] decrease was dependent on the source detector separation, the first evidence of its kind showing the brain specificity of the Δ[oxCCO] signal.

The response of the Δ[oxCCO] signal to changes in partial pressure of carbon dioxide (P_aCO_2) was investigated in 2009 by Tachtsidis and colleagues through a hypercapnia study [108]. In this study, the percentage of inspired CO_2 was increased by mixing 6% of CO_2 to the inspired gas and the subjects were monitored using a broadband system having one channel with SDS of 35 mm. The authors demonstrated increases in Δ[oxCCO], TOI, Δ[HbDiff], Δ[HbT] and Vmca during hypercapnia challenge and they concluded that the increase in Δ[oxCCO] is highly correlated with the increase in brain tissue oxygenation. Later, Kolyva et al. confirmed the increase of Δ[oxCCO] during hypercapnia using the pHOS system [12]. Moreover, the author also found a decrease in Δ[oxCCO] during hypocapnia induced by hyperventilation.

Thanks to technological advances in the pHOS system, Kolyva et al. were able to measure Δ[HbO_2], Δ[HHb] and Δ[oxCCO] at multiple source detector separations (20, 25 ,30 and 35 mm) simultaneously during challenges that increase cerebral oxygen delivery (hyperoxia and hypercapnia) and challenges that decrease cerebral oxygen delivery (hypoxia and hypocapnia) [12]. The authors concluded that Δ[oxCCO] increased during challenges that increased cerebral oxygen delivery and decreased during challenges that decreased cerebral oxygen delivery. Moreover, the Δ[oxCCO] signal demonstrated a depth dependent response, with an increase in signal amplitude with increasing source detector

separation. This depth dependent response of the Δ[oxCCO] signal is distinctly different from that of the Δ[HbT] and Δ[HbDiff] signals which seldom show a gradient change in magnitude depending on penetration depth. This is one of the first studies to support the hypothesis that Δ[oxCCO] signal is a brain specific signal of cerebral metabolism, superior to haemoglobin signals in this aspect.

Collectively, these studies demonstrated that the oxCCO signal may be a more reliable measurement of cerebral changes in comparison to the traditional haemoglobin signals, showing a superior specificity to the brain.

3.6.2 Functional activation studies

During functional activation, the increase in neuronal activity results in an increase in oxidative metabolism that is linked to the dilation of blood vessels through the process of neurovascular coupling. This dilation of blood vessels leads to an increase in cerebral blood flow to the regions of neuronal activity, providing an excess supply of oxygen. This results in regions of hyperoxygenation usually referred to as functional hyperemia.

NIRS, with the advantage of being non-invasive, has long been used as a tool to study haemodynamic changes in response to functional activation in healthy adult volunteers. A typical functional haemodynamic response measured by NIRS is characterised by an increase in $\Delta[HbO_2]$ and a decrease in Δ[HHb]. This has been demonstrated in several cognitive, motor, sensory and visual studies. Obrig and Villringer provide an excellent review on this topic [1]. Most studies to date have investigated functional activation via the change in cerebral haemodynamics secondary to neuronal activity. There are certain concerns in characterising functional activation using only vascular related changes. One of those is the issue of false positives (the possibility of getting haemodynamic changes similar to functional activation that are not due to neuronal activity but due to changes in intracerebral haemodynamics caused by task-related systemic changes and/or changes in extracerebral haemodynamics) and false negatives (the possibility of having a neuronal-induced functional haemodynamic response being masked or attenuated by systemic-induced intracerebral changes or extracerebral contamination) [109]. The Δ[oxCCO], a measure of oxygen metabolism, may provide a more direct measure of neuronal activity during functional activation. The Δ[oxCCO] signal, together with $\Delta[HbO_2]$ and Δ[HHb], may offer valuable insight into understanding the mechanism of neurovascular coupling. This is a unique feature of NIRS as a monitoring modality as it has the ability to measure both intravascular and intracellular events simultaneously. Despite being an appealing non-invasive marker of cellular oxygen metabolism, measur-

ing Δ[oxCCO] signal is challenging. As a result, there are only a few studies investigating the response of the signal during functional activation and these will be discussed here.

Using functional visual stimulation with reversing checkerboard, Heekeren et al. showed that CCO in the occipital cortex in the adult human subjects was transiently oxidised during functional activation and this could be measured by the Δ[oxCCO] signal using broadband NIRS [70]. The maximum group averaged change in the concentration of oxCCO was 0.05 ± 0.01 μM, together with the maximum concentration changes of 0.12 ± 0.03 μM and -0.10± 0.01 μM for HbO_2 and HHb respectively. The authors demonstrated that the difference attenuation spectrum between stimulation and rest could not be fully explained by $\Delta[HbO]_2$ and Δ[HHb] alone. When Δ[oxCCO] was included in the analysis, the difference spectrum could be fully explained and the residual of the fitting model was randomly distributed. This is the first study of its kind showing the evidence of an increase in the oxidation state of CCO in the adult human cortex during functional activation. The authors suggested that this increase in Δ[oxCCO] signal was not due to the increase in the oxygen tension but due to the decrease in the proton electrochemical gradient that led to an increase in the rate of electron exit from CCO. Such interpretation demonstrated evidence that the Δ[oxCCO] signal could provide an intriguing insight into the cellular processes following functional activation.

Using two types of visual stimulation to differentially activate areas of either rich (blob areas) or poor (interblob areas) CCO content and a layered head model to calculate potential cross talk, Uludag et al. concluded that the changes in Δ[oxCCO] signal cannot be modelled as a pure cross talk artefacts [71] as suggested previously using Monte Carlo simulations on layered head model [87] and this could be taken as an argument in favour of the existence of changes in Δ[oxCCO] in response to functional activation. The observed change in the first part of this study for both stimuli was similar to that in the study published previously by Heekeren et al. [70].

Kolyva et al. used a dual channel FD system and two single-channel multi-distance CW broadband system to interrogate the same tissue segment simultaneously, and hence determine μ_a and $\mu_{s'}$ during a frontal lobe activation task. The authors reported a heterogeneous response of Δ[oxCCO] signal to functional activation between subjects, in the presence of the typical haemodynamic responses. Although there was not a significant change in the Δ[oxCCO] signal in the group average during the anagram solving task, a majority of the subjects showed a significant increase in Δ[oxCCO] but some showed a significant decrease. The maximum magnitude changes in Δ[oxCCO] are + 0.6 μM and -0.4 μM for the positive and the negative changes respectively. The authors suggested that

the heterogeneity observed in the Δ[oxCCO] signal may be due to the fact that there are spatial and temporal variations in the response of mitochondrial redox system and that NIR light interrogates different regions of the cortex in different subjects. This means that observed heterogeneous responses in Δ[oxCCO] were due to the spatial sensitivity of the measuring system rather than due to a fundamental difference in the underlying physiology.

The result reported by Kolyva et al. raised a question of whether there is a spatial variation in the response of Δ[oxCCO] across the cerebral cortex and whether it can be measured using broadband spectroscopy. From our knowledge to date, a system that can monitor Δ[oxCCO] signal across multiple regions of the cortex has not been developed (Table 3.1). A system that has the capability of measuring Δ[oxCCO] across multiple regions of the cortex in addition to the traditional NIRS parameters will prove useful in providing insights into understanding mechanisms of neurovascular coupling and oxidative metabolism in the healthy and injured brains. The existing broadband system built by our group, the MDBBS system, will be used as a basis for the development of a multi-channel, multi-distance broadband system. Progressive development of the system will be discussed in chapter 4 and 5 of this thesis. Results from functional activation experiments investigating the Δ[oxCCO] signal with the modified system will also be discussed.

3.7 Image reconstruction methods in NIRS

Traditional NIRS devices use a small number of light sources and detectors to probe a focal brain region of interest and provide channel-wise, time-series measurements of changes of concentration of chromophores with good temporal resolution but with limited spatial resolution. With an increasing number of measurement channels, it is challenging to analyse data using channel-wise analysis within a subject or among a group of subjects to extract useful physiological information. Diffuse optical tomography (DOT) aims to combine information from multi-distance, multi-channel measurements acquired in NIRS to produce spatially resolved images [92]. These images can provide information about specific absorption and scattering properties of biological tissues or physiological parameters of interest and provide a different direction to analyse NIRS parameters.

Generally, DOT images can fall into two categories: topography and tomography. Although the distinction between the two is blurred, topography is generally used to describe methods that produce two dimensional (2D) images with limited depth information

while tomography is used to refer to methods that produce three dimensional (3D) images. In this thesis, images of changes in NIRS parameters will be reconstructed using a tomographic approach, producing 3D images with depth information from measurements acquired from the healthy and injured adult brains.

Recently it has been shown that distributed brain functions and networks can be mapped with high spatial resolution using a high-density DOT system and these maps have a strong correspondence to maps that were obtained by fMRI in the same subject [93]. However, unlike fMRI, DOT is limited to imaging the superficial cortex and cannot access deep subcortical brain structures. Despite this limitation, there is a strong rationale for the use of DOT technique for its non-invasiveness and portability. It can be used in subjects that cannot be transported into MRI machines such as neonates, patients with implanted devices or critically ill patients in neurointensive care unit that require bedside monitoring. Moreover, with the measurement of Δ[oxCCO], DOT has the potential to reconstruct 3D images of cellular oxygen metabolism of the adult human brain with high spatial resolution; this advantage has never been demonstrated before with modalities that utilise the measurement of blood flow for imaging such as fMRI and traditional fNIRS. This can provide an unprecedented opportunity to monitor and understand brain pathologies in which neurovascular coupling, the process that couples changes in blood flow to changes in metabolism as discussed in chapter 2, may be disturbed, resulting in an abnormal response. Such pathologies can alter the relationship between haemodynamics and metabolism and an additional co-localised measure of cellular oxygen metabolism can provide a complete picture into the pathway of pathologies and rationale for future management strategies.

3.7.1 The process of image reconstruction

The process of reconstructing images in DOT consists of three steps: (1) acquiring a subject specific, multilayer and anatomically accurate head model; (2) modelling the process of light transport through this head model given an array of sources and detectors (the forward problem), (3) reconstructing images of concentration changes by solving the inverse problem. Each of the steps of the reconstruction process will be briefly discussed here to provide an understanding of the reconstruction process that was utilised in this thesis. Details of the image reconstruction method used in this thesis can be found in [110].

To acquire a subject specific, multi-layer and anatomically accurate head model, it is best to register a head model to subject specific anatomical MRI images. Knowledge of

specific brain anatomy from MRI images can allow accurate registration of DOT image to the cerebral cortex and significant improvement of the image by providing some restraints to the ill-posed DOT image reconstruction problem. However, requiring subjects MRI scans to perform DOT undermines the fundamental advantage of being portable and applicable to vulnerable subjects. An alternative is to use a multilayer 3D atlas head model that can be transformed to the specific subject space using positions of sources, detectors and cranial landmarks of the subject's head in 3D space, usually recorded by electromagnetic tracking system [111], [112]. The atlas used to reconstruct images in this thesis was built by Dr Brigadoi and Dr Cooper [113] based on the nonlinear MNI-ICMB152 atlas [114].

To solve the forward problem, a model of how light propagates through this head model is generated by finite-element method (FEM) approach using Toast++ [115], defining the relationship between the changes in optical properties to changes in the measured signals. The result of this step is a grey matter sensitivity matrix or a Jacobian for any given source detector array configuration.

To solve the inverse problem and reconstruct optical properties of tissue at each FEM node, the solution of the forward model or the Jacobian has to be inverted and the result is projected to a volumetric mesh and the cortical grey matter surface mesh. This step is the most computationally expensive and under-determined.

3.7.2 Type of data needed for DOT tomography

Image reconstruction using the DOT tomography approach requires specific data sets that have multi-distance measurement channels to probe the tissue of interest at multiple depths. Moreover, multiple overlapping channels are required to acquire sufficient spatial resolution to distinguish localised functional brain activity. Present commercial NIRS systems that have the capability of measuring Δ[oxCCO] do not have the capability of acquiring multi-distance, multi-channel measurements while in-house systems developed explicitly to measure Δ[oxCCO] signal do not allow overlapping, multi-channel measurements. In the next two chapters of this thesis, progressive development of the MDBBS system in BORL to a multi-distance, multi-channel broadband NIRS system with the capability of investigating Δ[oxCCO], $\Delta[HbO_2]$ and Δ[HHb] over multiple regions of the adult human brain will be discussed. Data sets collected from different stages of system development were used to facilitate the implementation of an image reconstruction algorithm to reconstruct concentration changes of oxCCO into tomographic images.

Chapter 4

Development of a pseudo broadband diffuse optical tomography system and its application

This chapter describes the first development of the dual-channel MDBBS system described previously in chapter 3 into a pseudo broadband diffuse optical tomography (DOT) system to acquire multi-channel, multi-distance broadband NIRS data sets. A visual functional activation paradigm was used as a testing platform to test the capability of the upgraded system to monitor Δ[oxCCO], Δ[HbO_2] and Δ[HHb] across multiple regions of the adult head. Multi-channel, multi-distance broadband NIRS data sets acquired from this pilot functional activation study were used 1) to investigate the spatial variation in the Δ[oxCCO] signal; 2) to investigate the localisation of centres of activation and 3) to facilitate the development of an image reconstruction algorithm to reconstruct images of Δ[oxCCO] for the first time in a human study. These analyses highlight the benefits of having a multi-channel system for data collection in vivo.

4.1 Introduction

As discussed in the previous chapter, commercial NIRS systems do not have the capability to measure Δ[oxCCO] accurately and in-house systems developed specifically to measure Δ[oxCCO] only have one or two channels, limiting their capability to monitor

changes in one or two regions of the brain. Moreover, with only a limited number of channels and no overlapping measurement, the method of DOT to reconstruct images of changes in oxCCO cannot be utilised. This means that the benefits of having tomographic images that can be used for the investigation of the variation in cerebral oxygen metabolism in the healthy brain and in brain pathologies cannot be fully realised.

There is an unmet need for a multi-channel, mutli-distance broadband NIRS system that can monitor Δ[oxCCO] across multiple regions of the adult brain. However developing a full multi-channel broadband NIRS system requires a large investment of both time and money. Therefore, before committing fully to the development of the new system, a smaller step of development was taken to develop a pseudo broadband DOT system. The system is called pseudo DOT because conventional DOT system acquires data from multiple overlapping channels simultaneous. This system does not acquire data from multiple overlapping channels simultaneous but rather require the physical movement of source and detector fibres during a repeated experimental protocol, the detail of which will be discussed in the following session. This step was crucial because it provided the opportunity to 1) validate the feasibility of monitoring Δ[oxCCO] across multiple regions; 2) develop in vivo testing paradigms and results that can be used to benchmark future results from the full system; 3) develop analysis algorithms for and realise the benefits of multi-channel data sets.

In this step of development, a visual functional activation paradigm was used as a testing platform to evaluate the capability of the system. Functional activation paradigms have long been used as a testing platform for NIRS instruments and early NIRS studies have established the typical haemodynamic changes in response to functional activation [1]. Visual functional activation paradigm was chosen because it is a simple task that only requires the subject to look at a computer screen and it can elicit a repeatable response in the visual cortex of the human brain. Additionally, the visual cortex is accessible for NIRS as it is a superficial brain structure in the occipital lobe of the brain.

The aims of the work presented in this chapter are to 1) develop a pseudo broadband DOT system that can assess the feasibility of monitoring Δ[oxCCO] across multiple regions of the healthy adult human brain; 2) to introduce analysis techniques that can be used for multi-channel data sets of $\Delta[HbO_2]$, Δ[HHb] and Δ[oxCCO] 3) to evaluate the feasibility of reconstructing tomographic images of Δ[oxCCO] using the multi-distance, multi-channel broadband NIRS data sets.

4.2 Challenges

4.2.1 Technical challenges for oxCCO measurement

As discussed previously, monitoring Δ[oxCCO] is challenging because of the low in vivo concentration of CCO in comparison to a much higher concentration of haemoglobin and of the overlapping of the absorption spectra of these compounds. This makes it difficult to separate the Δ[oxCCO] signal from the generally much larger haemoglobin signals. However, it has been shown that broadband NIRS technology with the UCLn algorithm can robustly resolve oxCCO signal with minimal cross talk artefacts [88]. Therefore, the pseudo broadband DOT system was based on the the MDBBS broadband NIRS instrument.

4.2.2 Challenges in experimental protocol

In order to evaluate the capability of the pseudo DOT system, a brain activation task with a clear regional variation of the response was necessary. The task also needs to produce a reproducible functional response. Moreover, it is of great preference to have a passive task to minimise the effect of the variation in the level of concentration and attention of volunteers which can introduce more complexity to the haemodynamic response. Visual activation with a flickering checkerboard fulfils all the criteria. Moreover, Heekeren and Uludag have demonstrated that this task can activate the visual cortex with measurable Δ[oxCCO] changes [70], [71].

4.2.3 Challenges in multi-channel measurement

Multi-channel measurement is by itself challenging because of the issues of multi-fibre-scalp coupling, source-detector encoding, array ergonomics and data quality management. Overcoming these issues requires integrative advances in fibre-optic cap design, experimental design, encoding/decoding methods and analysis algorithm.

4.3 Methods

The pseudo broadband DOT system was developed using the optical components of the MDBBS system with a slight modification in the hardware at the subject end.

4.3.1 Basic components of the pseudo broadband DOT system

The pseudo broadband DOT system has one customised halogen bulb light source which is connected to a light source fibre with a fibre diameter of 4 mm. The system has two customised spectrometers, each of which is connected to four detectors fibres. The details of these optical components were given in Chapter 3. As a result, the system can collect data from eight NIRS measurement channels simultaneously. To achieve a higher number of measurement channels using this configuration, the source and detector fibres were physically moved across a probe holder fixed on the occipital cortex while repeating the functional activation paradigm. As a result, the probe holder had to be redesigned to have multiple slots for source fibre and detector fibres. Moreover, a new experimental protocol was developed to facilitate the data collection process.

4.3.2 Probe holder development

A new probe holder was designed using AutoCAD (AutoDesk, USA) to incorporate four source slots (red) and 14 detector slots (blue) as shown in Figure 4.1 and 4.2a to provide the flexibility to move the source and detector fibres to reproduce multi-channel measurements. This design enables measurement channels with source-detector separations of 25 mm and 37.75 mm. The probe holder was 3D printed using Object500 Connex 3D printer (Stratasys, USA) using a mixture of flexible black material (TangoBlack) and hard white material (VeroWhite) (Figure 4.2b). This ensures that the probe holder can hold the fibres in place and is flexible to curve around the curvature of the head for good optical coupling.

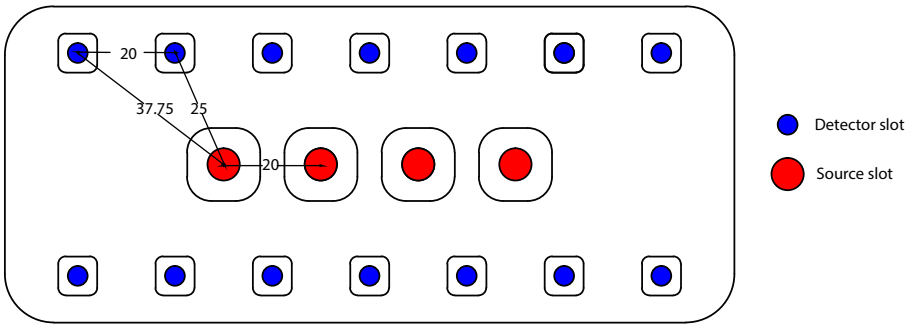

Figure 4.1: Probe holder was redesigned to have multiple slots for source and detector fibres to facilitate multi-distance, multi-channel measurements using one source fibre and eight detector fibres of the pseudo DOT system.

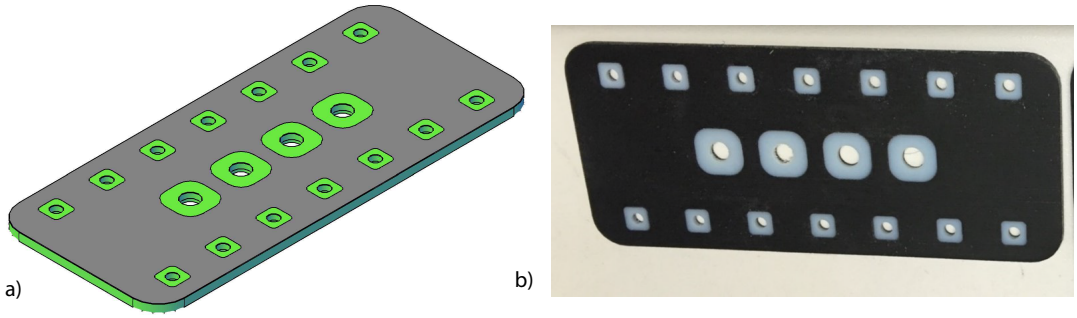

Figure 4.2: a) 3D probe holder design in AutoCaD. b) 3D printed probe holder using a mixture of hard (white) and soft (black) material.

Figure 4.3 shows the channels of measurement that can be acquired when the source fibre is at the first source location and eight detector fibres are arranged symmetrically above and below it. Figure 4.4 shows all 32 measurements channels that can be acquired by repeating the functional activation paradigm four times while moving the source and detector fibres along the fixed probe holder for each repetition.

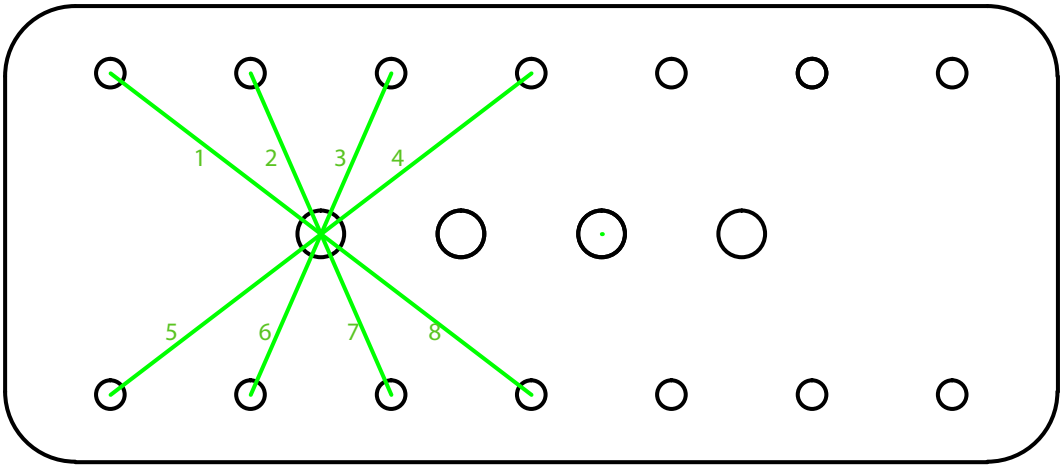

Figure 4.3: Measurement channels acquired in the first repeat of the functional activation paradigm with the source fibre fixed in the first source slot position and eight detector fibres arranged symmetrically above and below it.

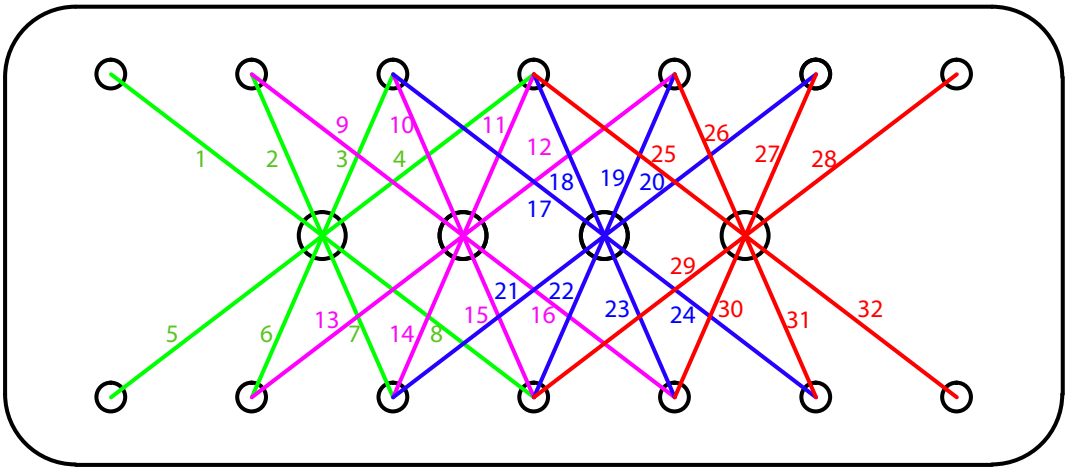

Figure 4.4: All 32 measurement channels acquired after four repeats of the experimental paradigm. Measurement channels acquired during the first repeat are shown in green while those acquired during the second, third and fourth repeats are shown in magenta, blue and red respectively.

4.3.3 Experimental paradigm design

Visual functional activation was achieved with a 4 Hz inverting checkerboard (Figure 4.5a) coded in Matlab (Mathworks, USA) using Psychtoolbox 3. Resting condition was achieved by a black screen with a centred white cross to keep subjects eyes in focus (Figure 4.5b). The experimental paradigm consisted of 10 epochs, each of which had 20 s of stimulation followed by 20 s of rest. The experimental paradigm was repeated four times for each subject. For each repeat, the source fibre and detector fibres were positioned in one of the four sets of locations (as demonstrated in figure 4.4) to collect an aggregate of 32 measurement channels.

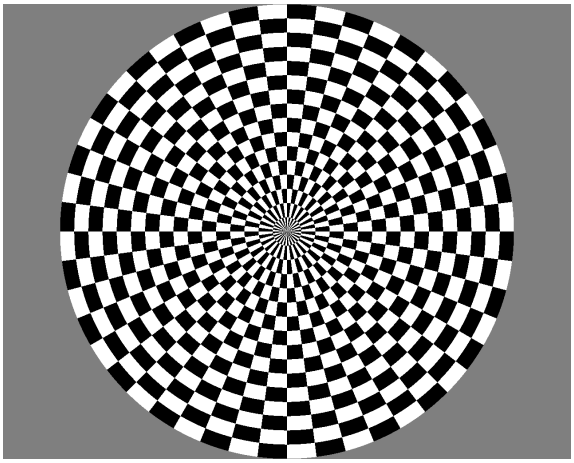

(a) Visual stimulation was achieved by a full field 4 Hz flickering checkerboard. This was coded in Matlab using Psychtoolbox 3.

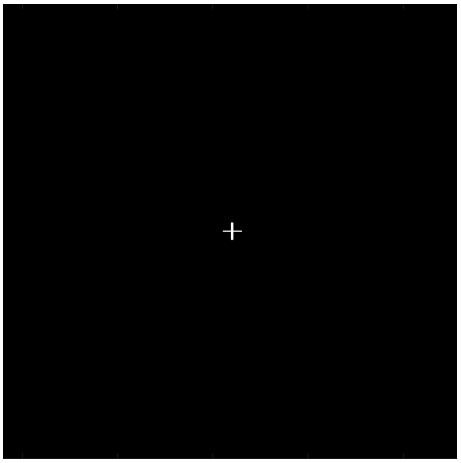

(b) Resting condition with black screen and a centred white cross for keeping eyes at focus.

Figure 4.5: Functional activation paradigm. The paradigm consisted of 10 epochs, each with 20 s of visual stimulation followed by 20 s of resting condition. The paradigm was repeated four times for each of the four source positions of the probe holder. One source fibre and eight detector fibres were used to collect intensity data at each repeat.

4.3.4 Participant set-up and experimental protocol

Following ethics approval and volunteer consent, four healthy adults (two males and two females; age range from 27 to 48 years old) were studied. For each subject, the probe holder was fixed horizontally at the back of the head using velcro straps to cover the left visual cortex with the fourth source slot positioned over Oz (10/20 EEG position) as shown in Figure 4.6. The location of the probe on the subject head was recorded using a Digitiser (Pohemus, USA). With this placement of the probe holder, measurement channels numbered 17 to 32 were expected to probe the primary left visual cortex V1 and therefore could monitor the functional response. Hair was cleared out of all slots before the insertion of optical fibres. One source fibre was placed at the first source slot while eight detector fibres were populated in eight nearest detector slots to collect intensity data continuously during 10 epochs. This was repeated for each of the four source slots by translating the fibres over the fixed probe holder, yielding an aggregate of 32 measurement channels. The whole procedure took two hours for each subject.

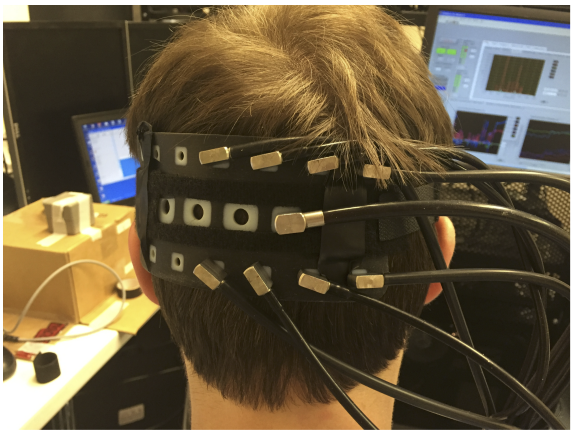

Figure 4.6: Fixation of the probe holder onto subject head using a Velcro strap. The fourth source slot of the probe holder was positioned over Oz (10/20 EEG). The figure shows the source fibre in the fourth source slot position with eight detector fibres arranged above and below the source fibre. The experimental paradigm was repeated four times, one for each source slot position. Detector fibres and source fibre were translated horizontally for each repeat.

4.3.5 Data analysis

An algorithm was developed to analyse the multi-channel data sets collected in this study. All data analysis techniques were coded in Matlab (version R2013a, Mathworks, USA). The intensity data were used to calculate the differential attenuation (ΔA). For each of the 32 channels, concentration changes of oxygenated haemoglobin (ΔHbO_2), deoxygenated haemoglobin(Δ[HHb]), and oxidised cytochrome c oxidase (Δ[oxCCO]) were calculated by fitting the attenuation spectra over the wavelength range from 780 nm to 900 nm using the UCLn algorithm as described previously in chapter 3. Source-detector separation and DPF were used to calculate the optical path length in the UCLn algorithm. The DPF at 807 nm was assumed to be 6.26 for all detectors and the wavelength dependence of the DPF was taken into account as DPF falls with increasing wavelength. This analysis technique is similar to what has been described previously by Kolyva et al. [12]. The concentration changes were band-pass filtered using a fifth-order Butterworth filter with cutoff frequencies of 0.01 and 0.25 Hz. As a result, there were 32 time-series data sets of concentration changes for each of the four subjects, each has 400 data points (10 x 40 s). Concentration changes for each subject were zero-baselined and averaged across epochs producing 32 sets of 40 s traces corresponding to 20 s of stimulation and 20 s of resting. For statistical analysis, the baseline period was defined as the first 10 seconds after the start of the visual stimulation and the activation period was defined as 10 seconds from 25th second to 35th second after the start of the visual stimulation. To calculate the group response to visual stimulation, concentration

changes of ΔHbO_2, Δ[HHb] and Δ[oxCCO] from a channel with maximal oxyhaemoglobin changes from each subject were chosen for averaging. Unpaired student t-test was used to compare the means of the selected baseline and activation points to assess whether there was a group significant change during the activation period in comparison with the baseline period.

Centre of gravity (CoG) analysis was applied to the time-course data sets to investigate the localisation of the centre of activation for each of the three chromophores using the 25 mm channels [116]. The location of the lower left detector slot constituting channel 5 (Figure 4.4) was taken as the origin for calculating x, y coordinates for this analysis and all units were in mm. The NIRS CoG was determined using mean response amplitudes of the changes occurring during time t=15s to 20s of each individual epoch and the coordinates of the channels (equations 4.1 and 4.2). The NIRS CoGs were calculated for HbO_2, HHb and oxCCO separately. Ten epochs produced 10 CoGs for each chromophore. Mean coordinates of the 10 centres were calculated to produce the final CoG for each chromophore with 95% CI.

$$X_{CoG} = \sum a_i X_i / \sum a_i \tag{4.1}$$

$$Y_{CoG} = \sum a_i Y_i / \sum a_i \tag{4.2}$$

where a_i represents the mean amplitude change of $\Delta[HbO_2]$, Δ[HHb] or Δ[oxCCO] at coordinates X_i and Y_i.

4.3.6 Image reconstruction procedure

The multi-distance, multi-channel spectroscopic data sets were used to reconstruct 3D images of concentration changes of $\Delta[HbO_2]$, Δ[HHb] and Δ[oxCCO] by a multispectral approach [110]. This part of the work was done by Dr Brigadoi and I collected and processed the data sets into format that can be used for image reconstruction. Data at seventeen wavelengths were selected from the measured broadband spectrum (every 10 nm from 740 nm to 900 nm) to perform the reconstruction. TOAST++ software was used to run the forward model on the registered adult volumetric mesh and the Tikhonov regularised least-square solution was used to solve the inverse problem. The volumetric images were then projected on the cortical surface mesh.

4.4 Results

4.4.1 Spectroscopic results

Figure 4.7 shows the concentration changes of the three chromophores in channel 1 from subject 1. According to the placement of the source and detector fibres in probe holder on the occipital cortex, this channel was off the visual cortex and as a result, concentration changes measured from this channel did not show the functional response. On the other hand, Figure 4.8 shows the concentration changes measured by channel 20. This channel was likely to probe the visual cortex and as a result, a clear functional response could be seen in the concentration changes of the three chromophores from this channel. A typical haemodynamic response was observed as an increase in $\Delta[HbO_2]$ coupled with a decrease in Δ[HHb] during each stimulation period of the 10 epochs. These signals returned to the pre-activation level during the resting period. Δ[oxCCO] increased during the activation period and returned to pre-activation level during the resting period. Overall, the results suggest that visual stimulation by inverting checkerboard produces a very reproducible response in term of both haemodynamic and metabolic changes that can be measured by NIRS. Figure 4.9 shows Δ[oxCCO] from channel 20 by itself. Δ[oxCCO] signal demonstrated a clear increase in response to each visual stimulation period with a highly reproducible response.

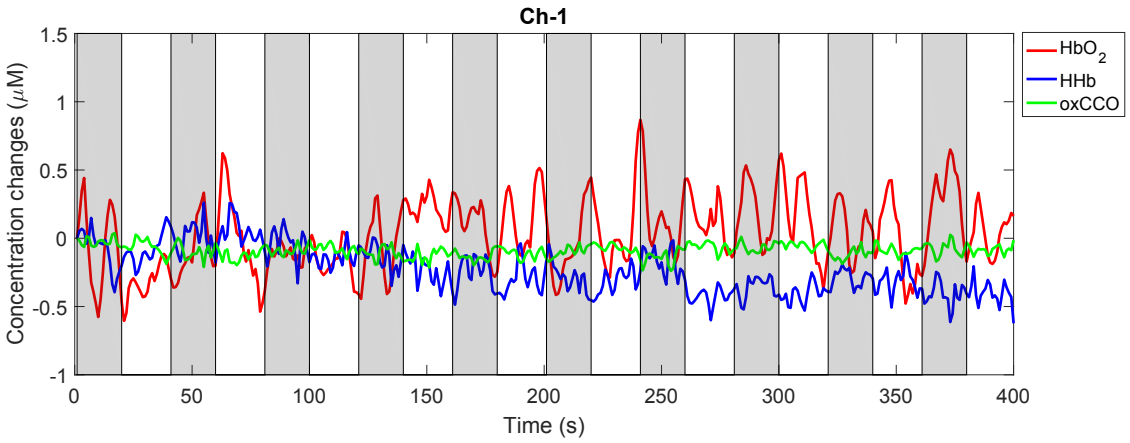

Figure 4.7: Time series concentration changes of HbO_2 (red), HHb (blue) and oxCCO (green) in channel 1 showing no functional response. The 20 s visual stimulation period is shaded in grey.

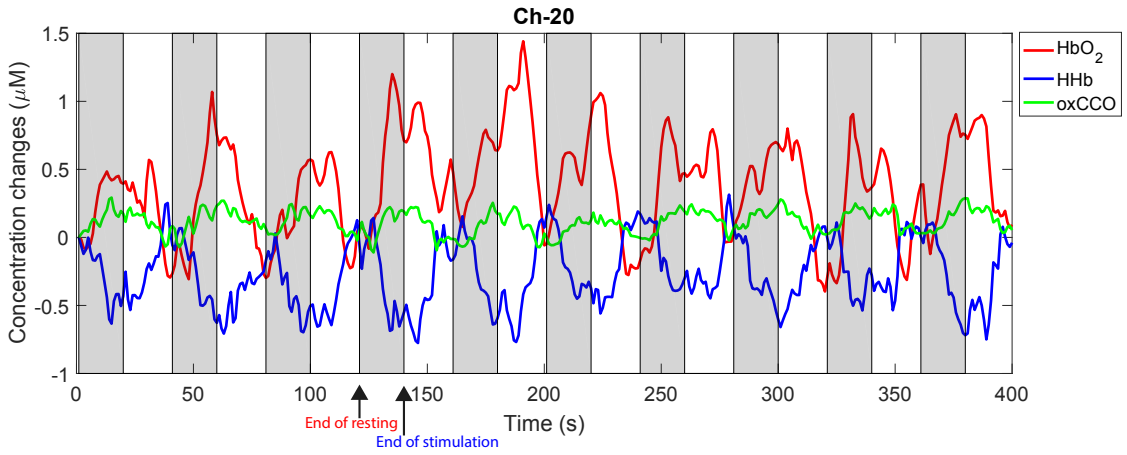

Figure 4.8: Time series concentration changes of HbO_2 (red), HHb (blue) and oxCCO (green) in channel 20 showing a functional response. The 20 s visual stimulation period is shaded in grey. Reproducible changes are evident for each single epoch of the stimulation and rest. Two time points are marked as end of resting and end of stimulation for the comparison of the raw optical signals in later figure.

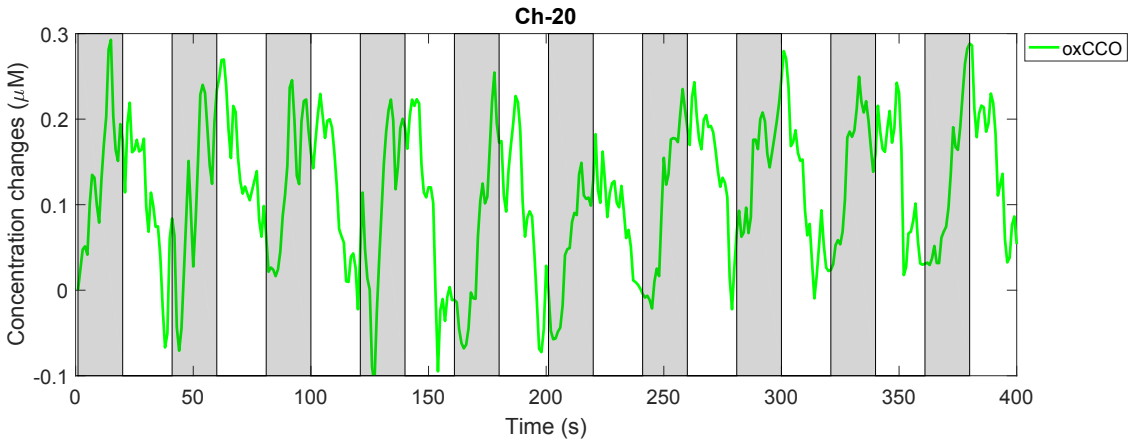

Figure 4.9: Time series concentration changes of oxCCO (green) in channel 20 from subject 1 showing functional activation. The 20 s visual stimulation period is shaded in grey.

Figure 4.10a shows the raw intensity measured during two time points marked as end of resting and end of stimulation in Figure 4.8. At the end of the post-stimulus rest period, an increase in the measured intensity spectrum was evident which may be suggestive of a decrease in CBF. This is evident in the figure as there is a higher intensity spectrum of the red trace in comparison to the blue trace. Figure 4.10b shows the ΔA calculated from the intensity spectrum of the two time points. Attenuation of NIR light at the end of resting was lower than that at the end of stimulation. This may also be explained by the decrease in CBF during the resting period. Figure 4.10c shows the measured ΔA and the back-projected ΔA for two fitting models. The red line represents ΔA back-projected from the concentration changes calculated using the three

component fitting model (including oxCCO). The blue line represents ΔA back-projected from concentration changes calculated using the two component fitting model (excluding oxCCO). Figure 4.10d shows the residual (measured ΔA - back-projected ΔA) of the two-component fitting model, the residual of the three-component fitting model and the residual difference between the two. The shape of the residual difference is similar to the ox-redCCO spectra.

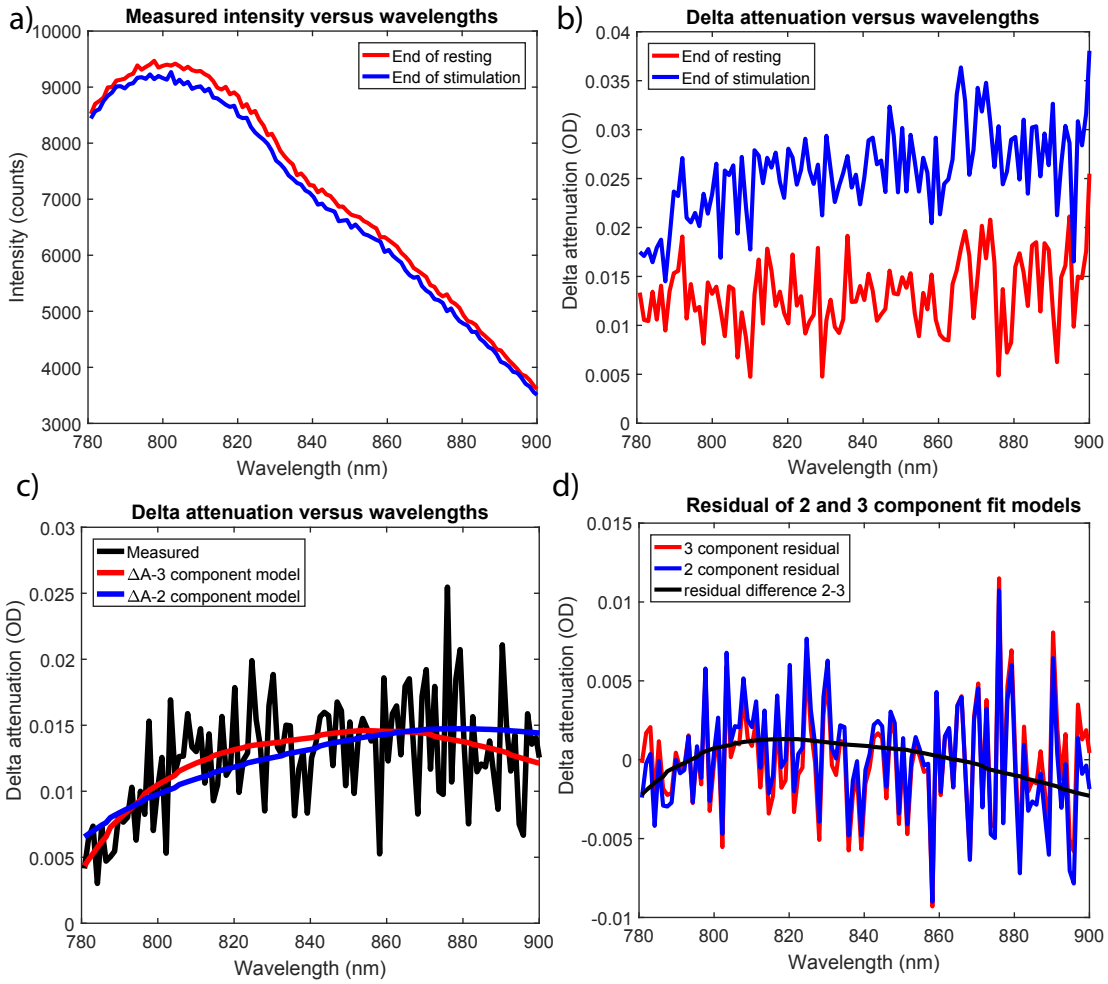

Figure 4.10: a) The measured intensity spectra at the end of resting and end of stimulation in channel 20. b) Calculated delta attenuation at these two time points. c) The measured attenuation and the back-projected attenuation from concentration changes using the 2-component model fit and the 3-component model fit. d) The residual (the difference between the measured attenuation and the back-projected attenuation) of the 2-component fitting model, the residual of the 3-component fitting model and the residual difference.

Figure 4.11 shows the block-averaged concentration changes of HbO_2, HHb and oxCCO with standard deviation calculated from the time-series changes shown in Figure 4.8. Typical haemodynamic response to functional activation was evident as an increase in $\Delta[HbO_2]$ and a decrease in Δ[HHb]. Δ[oxCCO] increased during the stimulation period

and returned the pre-activation level during the resting period.

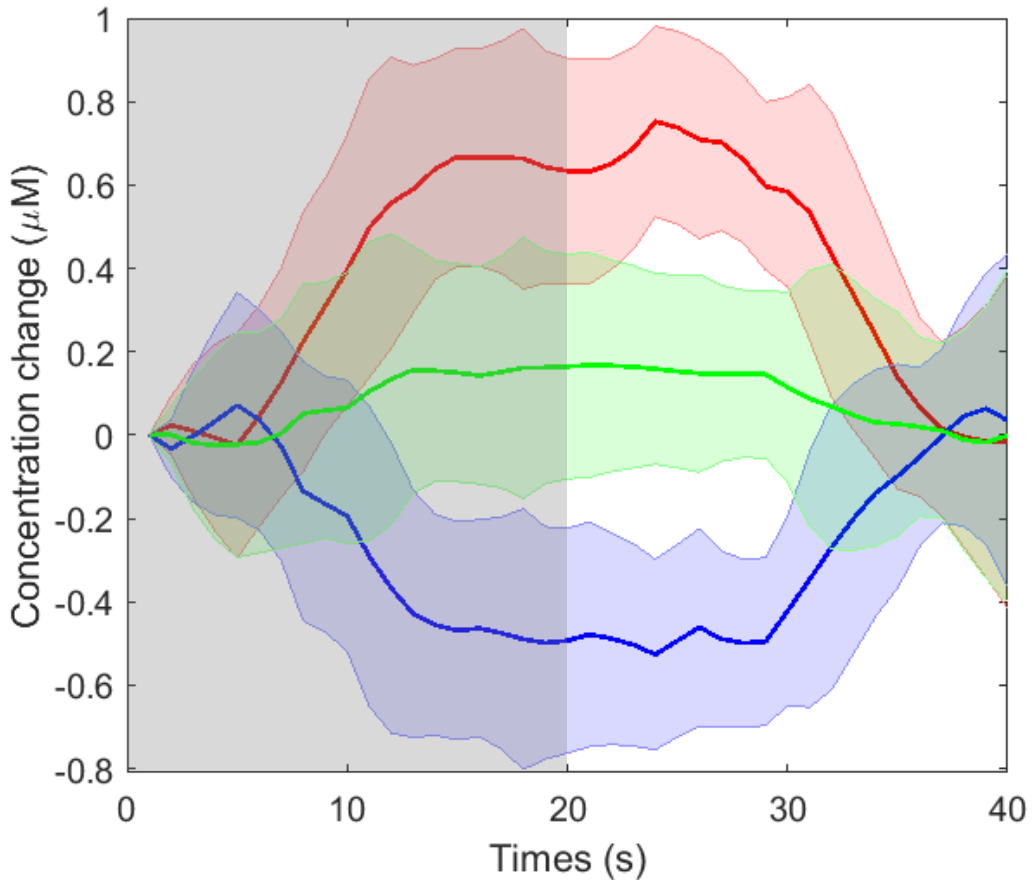

Figure 4.11: Block averaged concentration changes of HbO_2 (red), HHb (blue) and oxCCO (green) in channel 20 of subject 1. The visual stimulation period is shown as the shaded grey area. Typical haemodynamic response to functional activation is evident as an increase in $\Delta[HbO_2]$, a decrease in Δ[HHb]. Δ[oxCCO] increased during the stimulation period and returned the pre-activation level during the resting period

Figure 4.12 shows the block-averaged concentration changes of HbO_2, HHb and oxCCO for all 32 measurement channels from subject 1. The first row of plots (channel 1 to 8) in the figure shows the concentration changes measured by channels when the source fibre was at source position 1 of the probe holder. The second (channel 9 to 16), third (channel 17 to 24) and fourth rows (channel 25 to 32) show the concentration changes measured by channels when the source fibre was at source positions 2, 3 and 4 respectively. Channels are displayed such that 16 channels on the left half of the plot have the same separations of 37.75 mm and 16 channels on the right half have the same separation of 25 mm. Overall, functional activation response is evident in 21 out of 32 channels, probing a localised brain area underneath source position 3 and 4. Figure

4.13 shows the blocked averaged concentration changes of oxCCO by itself. An increase in the concentration of oxCCO was evident in almost all channels originating from source position 3 and 4. This maybe because at those two source locations, the source fibre was directly on top of the left primary visual cortex and as a result, functional activation could be seen in all the channels.

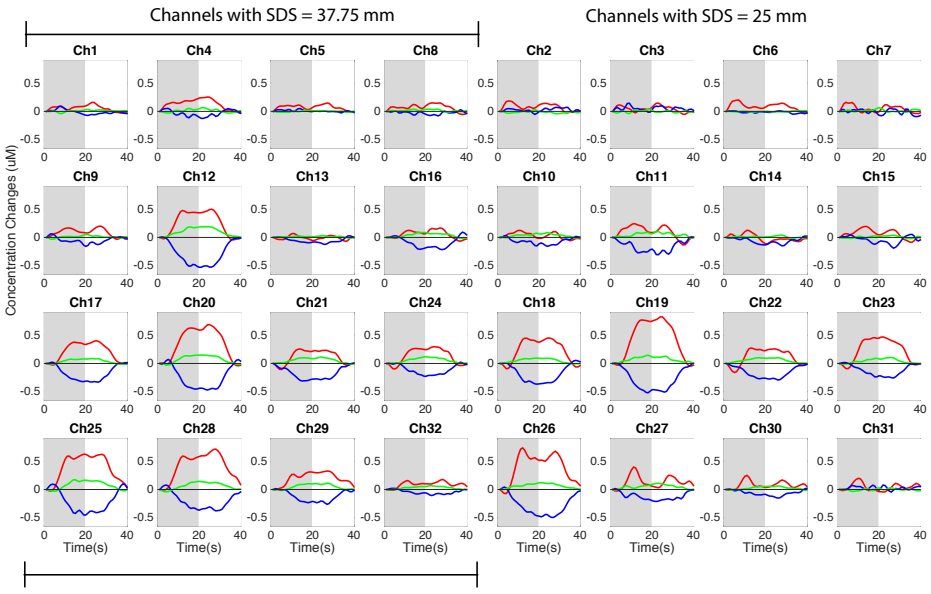

Figure 4.12: Block averaged concentration changes of HbO_2 (red), HHb (blue) and oxCCO (green) in all 32 channels of subject 1. Changes in concentration of HbO_2, HHb and oxCCO corresponding to functional activation are highlighted by red border.

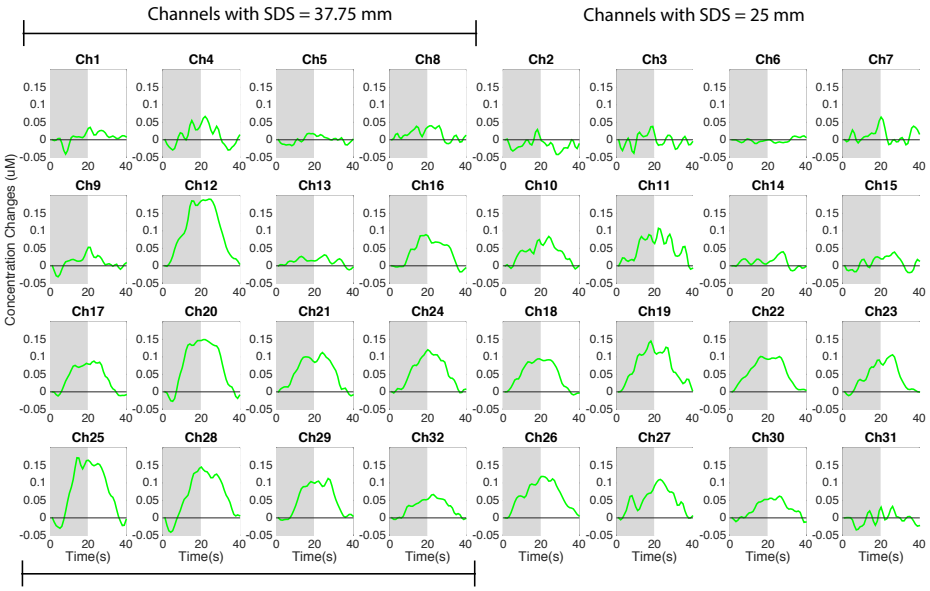

Figure 4.13: Block averaged concentration changes oxCCO in all 32 channels of subject 1.

Table 4.1 shows the mean, standard deviation and the maximum value of the $\Delta[HbO_2]$, Δ[HHb] and Δ[oxCCO] for all 32 channels of subject 1 in μM.

Table 4.1: Mean, standard deviation and the max value of $\Delta[HbO_2]$, Δ[HHb] and Δ[oxCCO] from the block-averaged changes for all 32 channels for subject 1.

	$\Delta[HbO_2]$ (μM)			Δ[HHb] (μM)			Δ[oxCCO] (μM)		
Ch.	mean	std	max Δ	mean	std	max Δ	mean	std	max Δ
1	0.057	0.051	0.160	-0.012	0.040	-0.072	0.008	0.016	0.036
2	0.078	0.063	0.185	0.026	0.030	-0.053	-0.014	0.016	0.029
3	0.044	0.053	0.146	0.049	0.037	-0.014	-0.002	0.018	0.038
4	0.133	0.088	0.255	-0.033	0.055	-0.124	0.012	0.028	0.067
5	0.073	0.044	0.149	0.008	0.017	-0.026	0.000	0.011	0.018
6	0.088	0.060	0.202	-0.014	0.017	-0.048	-0.002	0.006	0.011
7	0.047	0.061	0.160	-0.007	0.045	-0.092	0.012	0.020	0.065
8	0.070	0.058	0.151	-0.026	0.027	-0.080	0.016	0.016	0.040
9	0.087	0.069	0.200	-0.048	0.056	-0.158	0.010	0.019	0.053
10	0.031	0.054	0.125	-0.066	0.056	-0.158	0.035	0.027	0.084
11	0.095	0.110	0.245	-0.157	0.101	-0.306	0.049	0.033	0.107
12	0.260	0.210	0.500	-0.291	0.207	-0.528	0.101	0.070	0.191
13	-0.008	0.035	0.069	-0.053	0.044	-0.124	0.012	0.011	0.031
14	-0.009	0.062	0.128	-0.062	0.051	-0.149	0.010	0.014	0.040
15	0.064	0.077	0.195	-0.042	0.065	-0.190	0.008	0.018	0.039
16	0.057	0.072	0.168	-0.090	0.098	-0.215	0.038	0.035	0.089
17	0.210	0.162	0.402	-0.171	0.136	-0.332	0.040	0.037	0.088
18	0.232	0.204	0.451	-0.179	0.156	-0.367	0.048	0.038	0.095
19	0.432	0.337	0.827	-0.279	0.196	-0.521	0.072	0.045	0.145
20	0.361	0.275	0.690	-0.238	0.207	-0.471	0.073	0.066	0.149
21	0.115	0.124	0.257	-0.175	0.111	-0.310	0.055	0.041	0.112
22	0.119	0.142	0.274	-0.158	0.102	-0.293	0.055	0.037	0.101
23	0.234	0.208	0.470	-0.120	0.098	-0.257	0.043	0.038	0.106
24	0.134	0.139	0.296	-0.105	0.089	-0.229	0.055	0.042	0.120
25	0.387	0.236	0.626	-0.206	0.200	-0.453	0.077	0.073	0.172
26	0.393	0.254	0.738	-0.283	0.180	-0.495	0.064	0.038	0.118
27	0.134	0.109	0.398	-0.120	0.070	-0.212	0.050	0.034	0.110
28	0.414	0.236	0.715	-0.206	0.149	-0.378	0.064	0.060	0.145
29	0.202	0.107	0.327	-0.124	0.096	-0.263	0.051	0.044	0.113
30	0.083	0.066	0.250	-0.063	0.047	-0.152	0.026	0.024	0.062
31	0.044	0.066	0.198	0.027	0.030	-0.044	-0.003	0.017	0.033
32	0.092	0.050	0.178	-0.045	0.037	-0.106	0.031	0.023	0.067

Similarly, Figure 4.14 shows the block-averaged concentration changes of HbO_2, HHb and oxCCO and Figure 4.15 shows the concentration changes of oxCCO for the second subject. Table 4.2 provides a summary of mean changes, standard deviation and maximum changes of the three chromophores from the block-averaged changes from subject 2. In this subject, changes in HbO_2, HHb and oxCCO corresponding to functional activation were evident in 27 out of 32 channels.

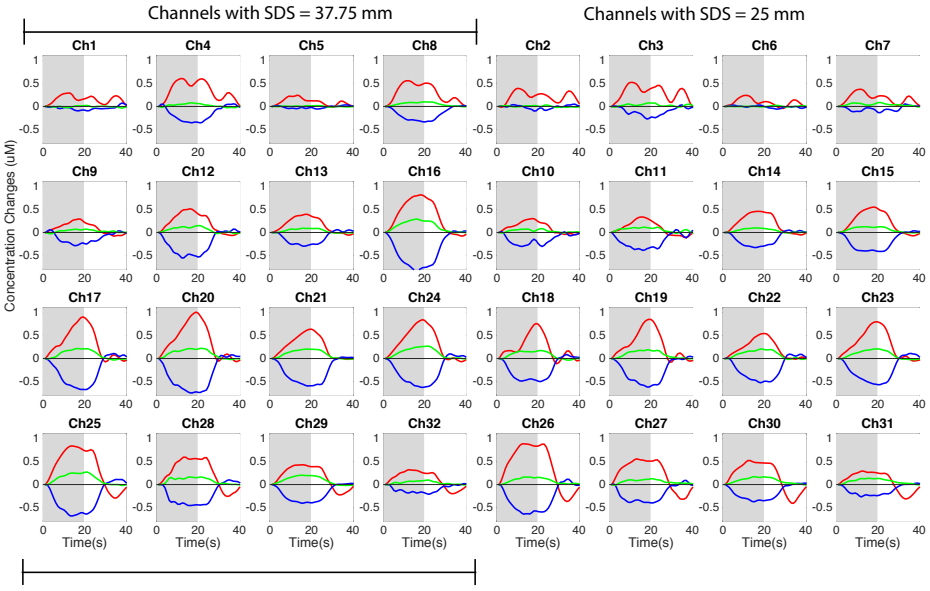

Figure 4.14: Block averaged concentration changes of HbO_2 (red), HHb (blue) and oxCCO (green) in all 32 channels of subject 2.

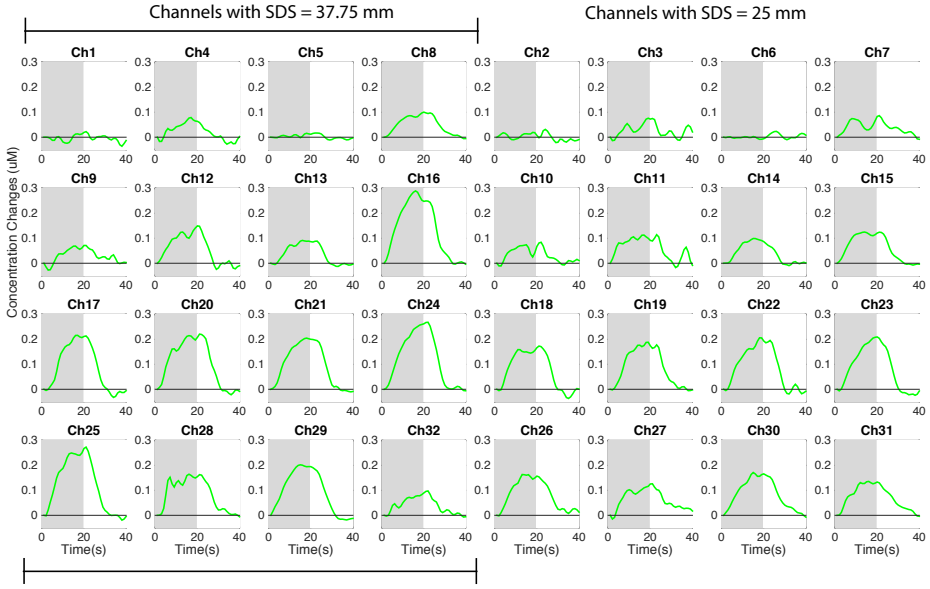

Figure 4.15: Block averaged concentration changes oxCCO in all 32 channels of subject 2.

Table 4.2: Mean, standard deviation and the maximum value of $\Delta[HbO_2]$, Δ[HHb] and Δ[oxCCO] from the block-averaged changes for all 32 channels for subject 2.

	$\Delta[HbO_2]$ (μM)			Δ[HHb] (μM)			Δ[oxCCO] (μM)		
Ch.	mean	std	max Δ	mean	std	max Δ	mean	std	max Δ
1	0.156	0.082	0.292	-0.034	0.041	-0.095	-0.004	0.014	0.022
2	0.212	0.112	0.392	-0.013	0.041	-0.099	0.001	0.014	0.031
3	0.300	0.154	0.523	-0.106	0.091	-0.273	0.027	0.026	0.076
4	0.345	0.200	0.608	-0.155	0.156	-0.357	0.022	0.032	0.079
5	0.102	0.077	0.243	-0.015	0.027	-0.056	0.003	0.008	0.017
6	0.086	0.080	0.241	-0.009	0.024	-0.058	0.002	0.009	0.023
7	0.176	0.109	0.372	-0.049	0.053	-0.136	0.039	0.025	0.086
8	0.299	0.195	0.560	-0.166	0.133	-0.337	0.049	0.037	0.100
9	0.096	0.120	0.294	-0.120	0.111	-0.286	0.030	0.028	0.071
10	0.110	0.121	0.302	-0.152	0.109	-0.304	0.032	0.029	0.084
11	0.097	0.148	0.336	-0.192	0.150	-0.388	0.060	0.042	0.114
12	0.210	0.208	0.514	-0.248	0.234	-0.553	0.057	0.058	0.150
13	0.164	0.164	0.395	-0.119	0.133	-0.298	0.037	0.040	0.091
14	0.200	0.199	0.459	-0.138	0.144	-0.327	0.041	0.040	0.099
15	0.226	0.230	0.552	-0.208	0.181	-0.412	0.062	0.052	0.125
16	0.369	0.341	0.819	-0.399	0.331	-0.826	0.135	0.110	0.290
17	0.336	0.335	0.904	-0.281	0.303	-0.674	0.088	0.093	0.216
18	0.241	0.262	0.760	-0.240	0.228	-0.502	0.076	0.076	0.173
19	0.301	0.310	0.852	-0.279	0.251	-0.620	0.087	0.074	0.188
20	0.387	0.371	1.008	-0.357	0.328	-0.748	0.104	0.091	0.221
21	0.264	0.241	0.637	-0.292	0.251	-0.596	0.097	0.084	0.205
22	0.216	0.198	0.543	-0.226	0.236	-0.527	0.088	0.082	0.206
23	0.312	0.303	0.799	-0.246	0.255	-0.569	0.085	0.087	0.209
24	0.337	0.326	0.844	-0.282	0.277	-0.628	0.120	0.104	0.268
25	0.358	0.414	0.839	-0.307	0.308	-0.682	0.120	0.107	0.273
26	0.392	0.465	0.885	-0.314	0.281	-0.644	0.082	0.060	0.163
27	0.226	0.315	0.557	-0.198	0.178	-0.399	0.064	0.040	0.126
28	0.248	0.309	0.597	-0.223	0.220	-0.456	0.084	0.064	0.164
29	0.173	0.239	0.429	-0.205	0.170	-0.404	0.095	0.085	0.202
30	0.180	0.318	0.521	-0.181	0.152	-0.374	0.085	0.061	0.171
31	0.074	0.208	0.292	-0.126	0.105	-0.267	0.072	0.048	0.136
32	0.115	0.180	0.320	-0.101	0.076	-0.211	0.040	0.033	0.097

Figure 4.16 shows the block-averaged concentration changes of HbO_2, HHb and oxCCO and Figure 4.17 shows the concentration changes of oxCCO for the third subject. Table 4.3 provides a summary of mean changes, standard deviation and maximum changes of the three chromophores from the block-averaged changes from subject 3. In this subject, changes in HbO_2, HHb and oxCCO corresponding to functional activation are observed in 15 out of 32 channels.

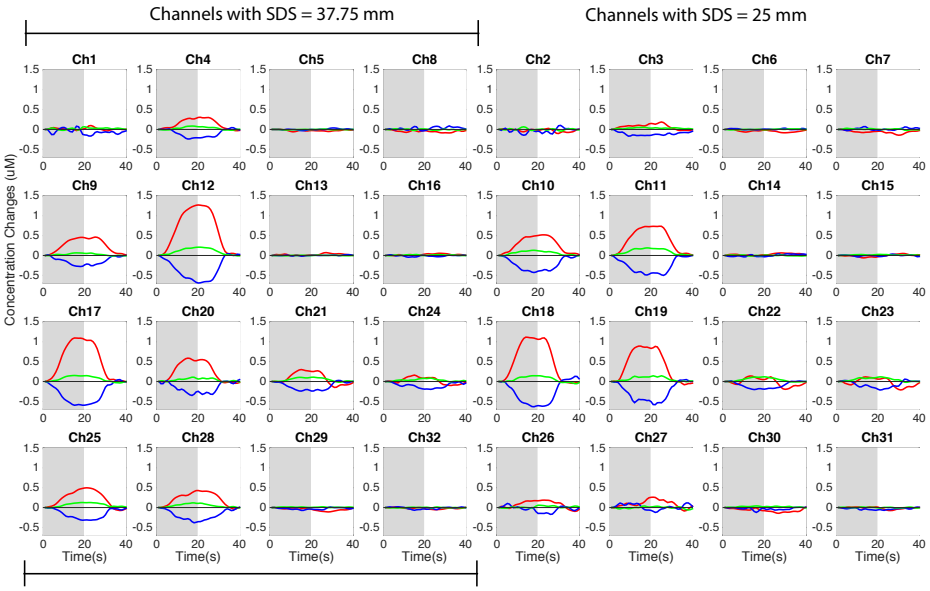

Figure 4.16: Block averaged concentration changes of HbO_2 (red), HHb (blue) and oxCCO (green) in all 32 channels of subject 3.

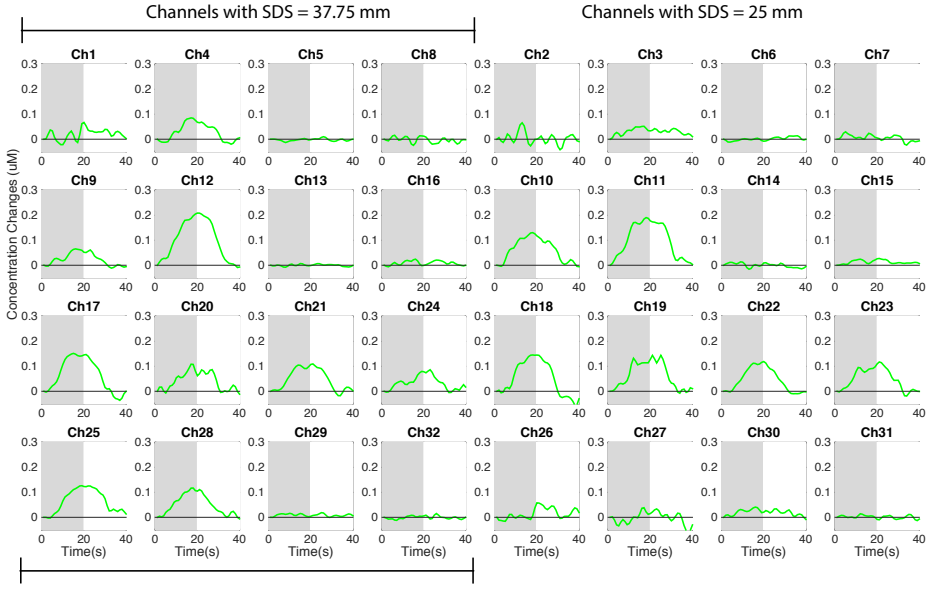

Figure 4.17: Block averaged concentration changes oxCCO in all 32 channels of subject 3.

Table 4.3: Mean, standard deviation and the maximum value of $\Delta[HbO_2]$, Δ[HHb] and Δ[oxCCO] from the block-averaged changes for all 32 channels for subject 3.

	$\Delta[HbO_2]$ (μM)			Δ[HHb] (μM)			Δ[oxCCO] (μM)		
Ch.	mean	std	max Δ	mean	std	max Δ	mean	std	max Δ
1	0.015	0.030	0.098	-0.057	0.063	-0.166	0.020	0.021	0.067
2	-0.025	0.034	0.026	-0.028	0.058	-0.145	0.003	0.022	0.066
3	0.069	0.064	0.188	-0.109	0.043	-0.168	0.031	0.013	0.052
4	0.141	0.124	0.307	-0.099	0.099	-0.241	0.028	0.035	0.085
5	-0.026	0.017	0.002	0.002	0.016	-0.031	-0.002	0.005	0.010
6	-0.040	0.028	0.018	0.006	0.012	-0.011	0.001	0.007	0.014
7	-0.063	0.036	0.007	0.011	0.028	-0.030	0.005	0.012	0.030
8	-0.048	0.024	0.003	0.027	0.034	-0.038	-0.003	0.011	0.016
9	0.255	0.174	0.463	-0.135	0.100	-0.278	0.024	0.025	0.065
10	0.275	0.195	0.519	-0.221	0.161	-0.428	0.061	0.047	0.130
11	0.390	0.293	0.736	-0.261	0.190	-0.501	0.099	0.070	0.191
12	0.647	0.509	1.271	-0.336	0.275	-0.693	0.101	0.080	0.209
13	0.022	0.021	0.072	0.002	0.009	-0.017	0.000	0.004	0.007
14	0.026	0.024	0.064	0.002	0.027	-0.036	0.000	0.008	0.014
15	-0.005	0.030	0.051	-0.002	0.017	-0.035	0.013	0.008	0.027
16	0.021	0.019	0.056	-0.010	0.017	-0.044	0.008	0.008	0.024
17	0.527	0.449	1.095	-0.304	0.244	-0.597	0.065	0.067	0.152
18	0.515	0.481	1.116	-0.278	0.286	-0.635	0.052	0.069	0.145
19	0.405	0.393	0.891	-0.263	0.229	-0.583	0.063	0.053	0.144
20	0.252	0.250	0.588	-0.152	0.133	-0.350	0.041	0.036	0.108
21	0.081	0.154	0.301	-0.117	0.099	-0.241	0.048	0.044	0.109
22	-0.014	0.100	0.139	-0.093	0.082	-0.202	0.046	0.047	0.119
23	-0.023	0.102	0.116	-0.072	0.083	-0.214	0.048	0.043	0.117
24	0.021	0.083	0.161	-0.099	0.065	-0.197	0.033	0.027	0.086
25	0.226	0.203	0.497	-0.162	0.122	-0.319	0.066	0.047	0.127
26	0.077	0.092	0.187	-0.038	0.073	-0.171	0.015	0.022	0.058
27	0.092	0.094	0.261	0.019	0.069	-0.122	-0.003	0.024	0.038
28	0.217	0.166	0.428	-0.186	0.127	-0.383	0.051	0.041	0.117
29	-0.049	0.031	0.001	-0.027	0.023	-0.072	0.009	0.005	0.019
30	-0.069	0.042	0.012	-0.030	0.031	-0.122	0.019	0.012	0.041
31	-0.014	0.027	0.017	-0.032	0.022	-0.070	0.001	0.007	0.014
32	-0.020	0.020	0.015	-0.015	0.025	-0.068	-0.001	0.006	0.015

Figure 4.18 shows the block-averaged concentration changes of HbO_2, HHb and oxCCO and Figure 4.19 shows the concentration changes of oxCCO for the fourth subject. Table 4.4 provides a summary of mean changes, standard deviation and maximum changes of the three chromophores from the block-averaged changes from subject 4. In this subject, changes in HbO_2, HHb and oxCCO corresponding to functional activation were evident in 11 out of 32 channels. Especially in this subject, there was a decrease in $\Delta[HbO_2]$ in some measurement channels such as channel 11. This may be caused by contamination due to extracerebral changes. In the same channel, concentration changes of oxCCO showed a clear increase in response to the functional activation task.

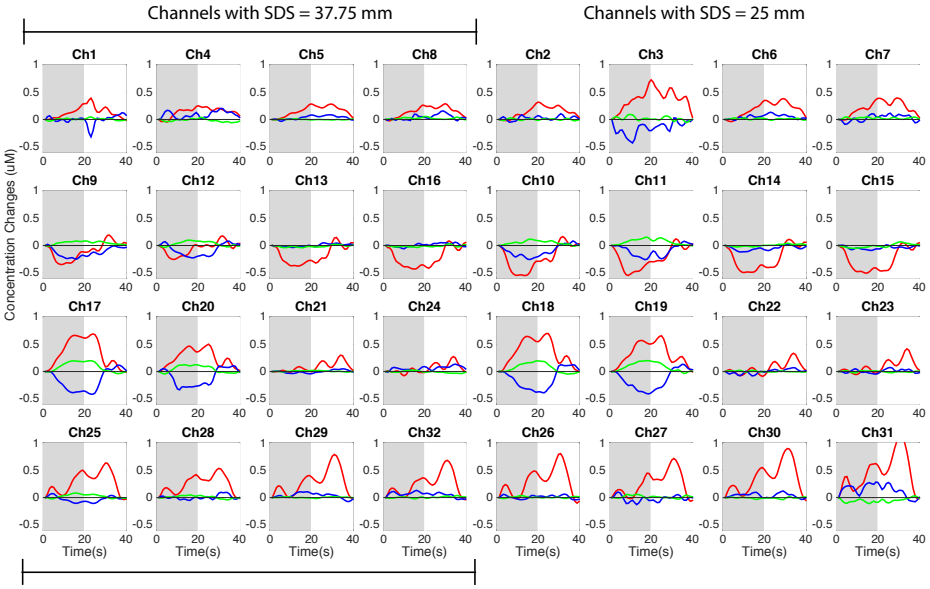

Figure 4.18: Block averaged concentration changes of HbO_2 (red), HHb (blue) and oxCCO (green) in all 32 channels of subject 4.

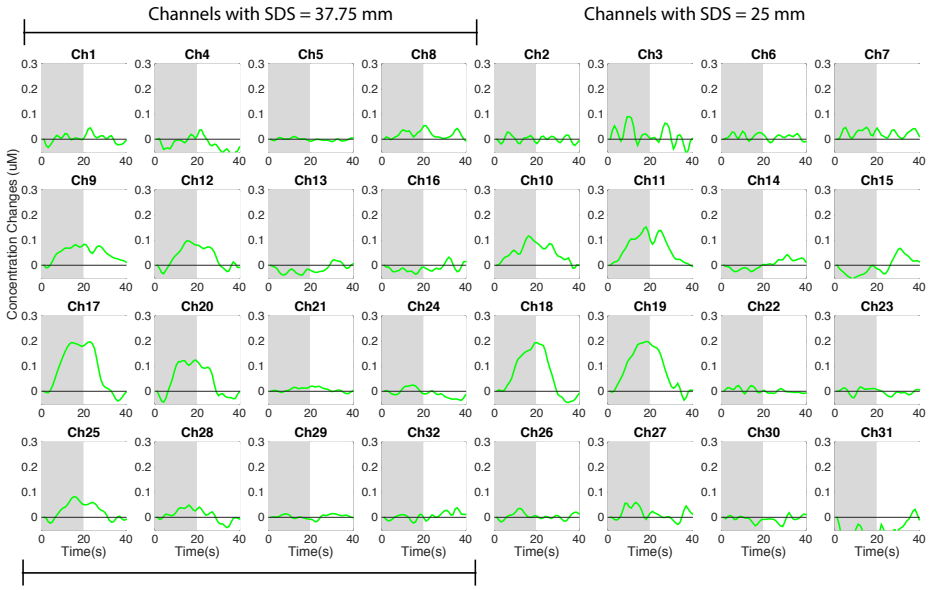

Figure 4.19: Block averaged concentration changes oxCCO in all 32 channels of subject 4.

Table 4.4: Mean, standard deviation and the maximum value of $\Delta[HbO_2]$, Δ[HHb] and Δ[oxCCO] from the block-averaged changes for all 32 channels for subject 4.

	$\Delta[HbO_2]$ (μM)			Δ[HHb] (μM)			Δ[oxCCO] (μM)		
Ch.	mean	std	max Δ	mean	std	max Δ	mean	std	max Δ
1	0.132	0.107	0.390	-0.003	0.086	-0.317	0.003	0.017	0.046
2	0.142	0.102	0.317	0.026	0.036	-0.050	0.000	0.013	0.028
3	0.374	0.184	0.725	-0.153	0.115	-0.429	0.015	0.035	0.091
4	0.139	0.084	0.251	0.089	0.059	-0.006	-0.017	0.026	0.037
5	0.157	0.092	0.284	0.035	0.035	-0.034	-0.001	0.005	0.011
6	0.190	0.129	0.381	0.049	0.037	-0.016	0.010	0.012	0.032
7	0.209	0.129	0.392	0.027	0.059	-0.089	0.024	0.015	0.047
8	0.148	0.092	0.289	0.042	0.049	-0.023	0.019	0.016	0.054
9	-0.099	0.159	0.188	-0.125	0.085	-0.250	0.048	0.028	0.084
10	-0.226	0.233	0.164	-0.099	0.103	-0.256	0.050	0.035	0.117
11	-0.228	0.203	0.122	-0.094	0.106	-0.258	0.069	0.050	0.153
12	-0.049	0.117	0.173	-0.080	0.109	-0.226	0.033	0.043	0.098
13	-0.173	0.168	0.147	0.003	0.026	-0.036	-0.014	0.018	0.022
14	-0.234	0.220	0.113	-0.051	0.041	-0.117	0.003	0.019	0.042
15	-0.262	0.211	0.053	-0.039	0.029	-0.090	-0.005	0.035	0.068
16	-0.218	0.179	0.084	0.009	0.032	-0.059	-0.012	0.016	0.032
17	0.346	0.260	0.688	-0.167	0.193	-0.415	0.086	0.089	0.198
18	0.357	0.237	0.695	-0.135	0.190	-0.388	0.067	0.085	0.195
19	0.326	0.208	0.655	-0.152	0.183	-0.408	0.087	0.080	0.199
20	0.252	0.159	0.500	-0.105	0.158	-0.334	0.044	0.062	0.125
21	0.082	0.087	0.300	-0.001	0.027	-0.042	0.006	0.008	0.020
22	0.065	0.112	0.335	-0.002	0.040	-0.079	0.003	0.010	0.023
23	0.097	0.124	0.416	0.006	0.033	-0.047	-0.001	0.012	0.018
24	0.055	0.086	0.274	0.060	0.036	-0.012	-0.007	0.017	0.025
25	0.280	0.203	0.632	-0.031	0.052	-0.107	0.026	0.033	0.082
26	0.293	0.252	0.804	0.011	0.031	-0.039	0.005	0.013	0.036
27	0.260	0.227	0.715	-0.021	0.055	-0.129	0.014	0.024	0.060
28	0.251	0.163	0.534	0.006	0.040	-0.051	0.009	0.024	0.049
29	0.286	0.233	0.789	0.036	0.048	-0.073	0.003	0.008	0.015
30	0.359	0.274	0.897	0.040	0.040	-0.034	-0.007	0.013	0.018
31	0.461	0.323	1.104	0.137	0.110	-0.077	-0.051	0.037	0.032
32	0.249	0.205	0.682	0.057	0.044	-0.036	0.005	0.014	0.038

Figure 4.20 shows the group average concentration changes of HbO_2, HHb and oxCCO for the visual stimulation experiment. There were significant changes ($p < 0.05$) in the concentration of these chromophores during the functional activation period.

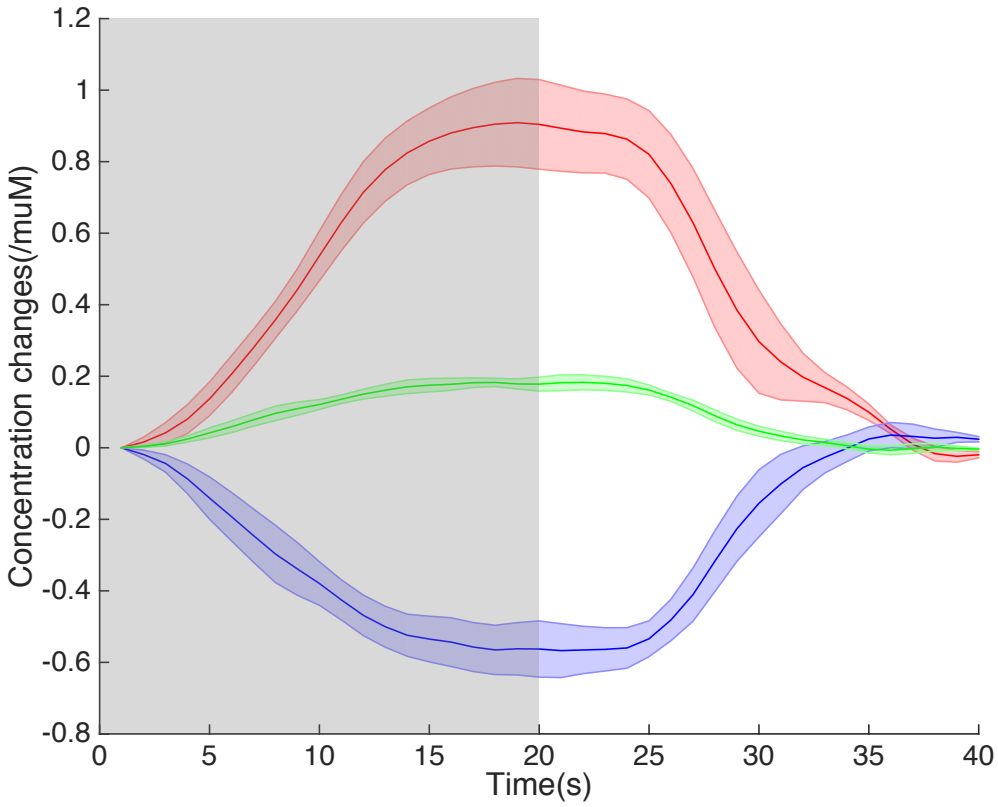

Figure 4.20: Group averaged concentration changes of HbO_2 (red), HHb (blue) and oxCCO (green) and standard error of means calculated using changes from a channel with maximal concentration changes in each subject. The visual stimulation period is shown as the shaded grey window. There were significant changes ($p < 0.05$) in the concentration of the three chromophores during the functional activation period.

4.4.2 Centre of gravity analysis

Figure 4.21 shows the locations of the CoGs for each chromophore relative to the location of the probe holder. Fourteen solid blue circles indicate fourteen locations of detector slots. Four solid red circles indicate the locations of four source slots. Solid black circles indicate the locations of the measurement channels. Individual red, blue and green ring circles denote the x-y location of the calculated CoGs for each of the 10 epochs for HbO_2, HHb and oxCCO respectively. The final CoG for each chromophore is indicated by the crosses. As can be seen from the figure, centres of activation for all three chromophores lie between source slots 2 and 3.

Figure 4.22 shows a close-up view of Figure 4.21 to assess the overlapping between CoGs of different chromophores. As can be seen from the figure, the final CoGs of HbO_2 and oxCCO show some degree of overlapping while the CoG of HHb lies separated from

the other two.

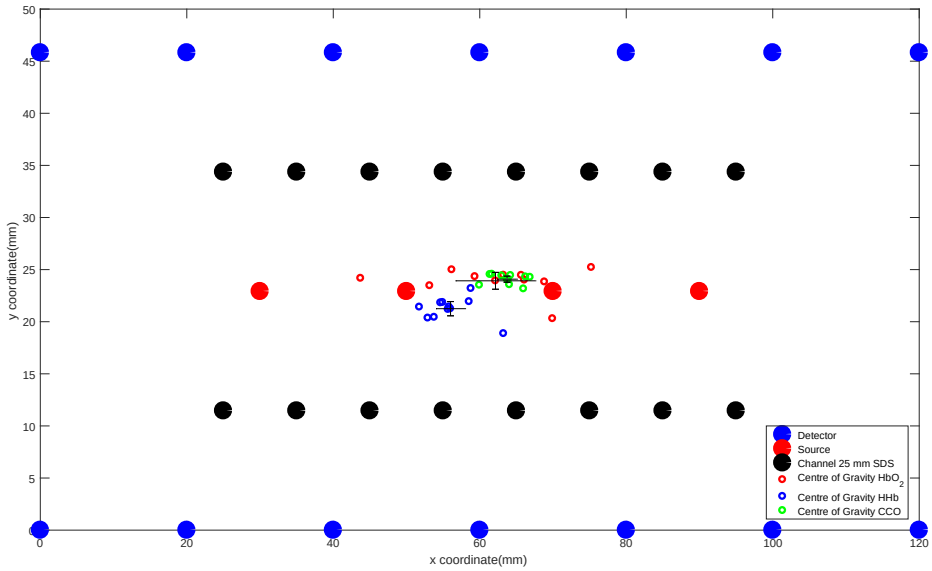

Figure 4.21: The CoGs for each chromophore for subject 1. Fourteen solid blue circles indicate fourteen locations of detector slots. Four solid red circles indicate the locations of four source slots. Solid black circles indicate the locations of the measurement channels. Individual red, blue and green ring circles denote the x-y location of the calculated CoGs for each of the 10 epochs for HbO_2, HHb and oxCCO respectively. The final CoG for each chromophore is indicated by the crosses.

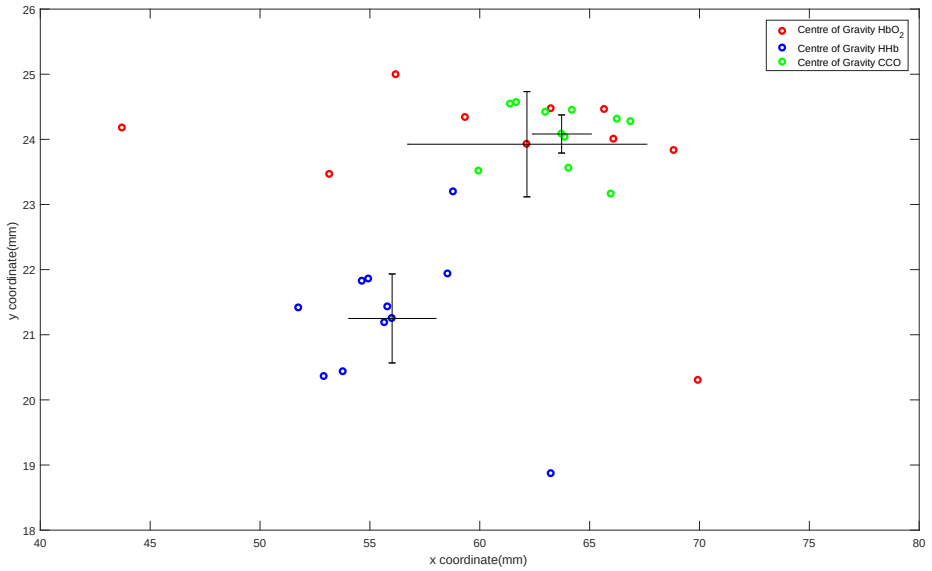

Figure 4.22: A close-up view of the CoGs of three chromophores for subject 1 revealing the overlapping between the centres of HbO_2 and oxCCO.

Similar results were obtained for three other subjects. See Figures 4.23, 4.24 for subject 2, Figures 4.25, 4.26 for subject 3 and Figures 4.27, 4.28 for subject 4. Overall, in all four subjects, the locations of CoGs are between source slots 2 and 3. The final CoGs of HbO_2 and oxCCO are located in close proximity in all subjects. In two subjects, those overlap each other. The CoG of HHb remains separate from others in all subjects, suggesting a distinct spatial localisation.

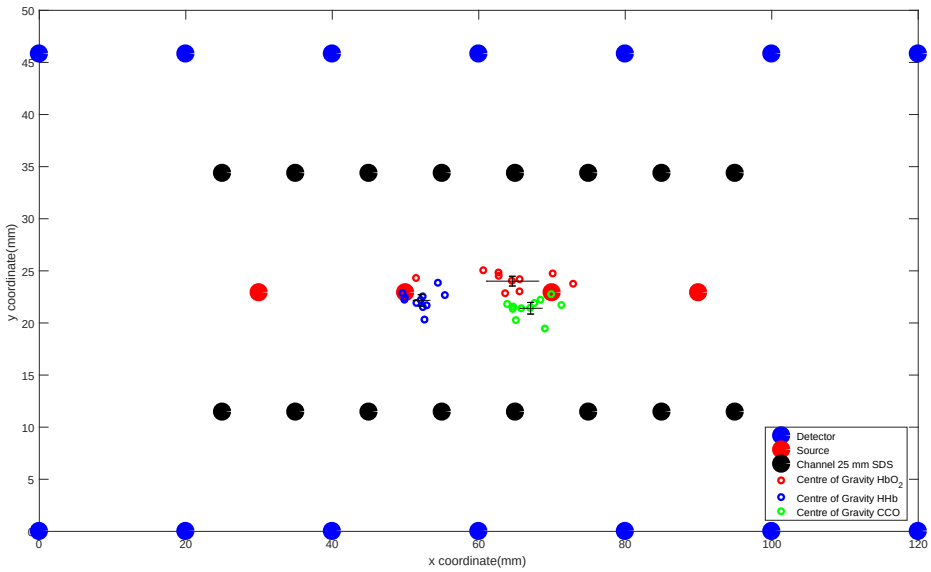

Figure 4.23: CoGs for each chromophore and the final CoGs for subject 2.

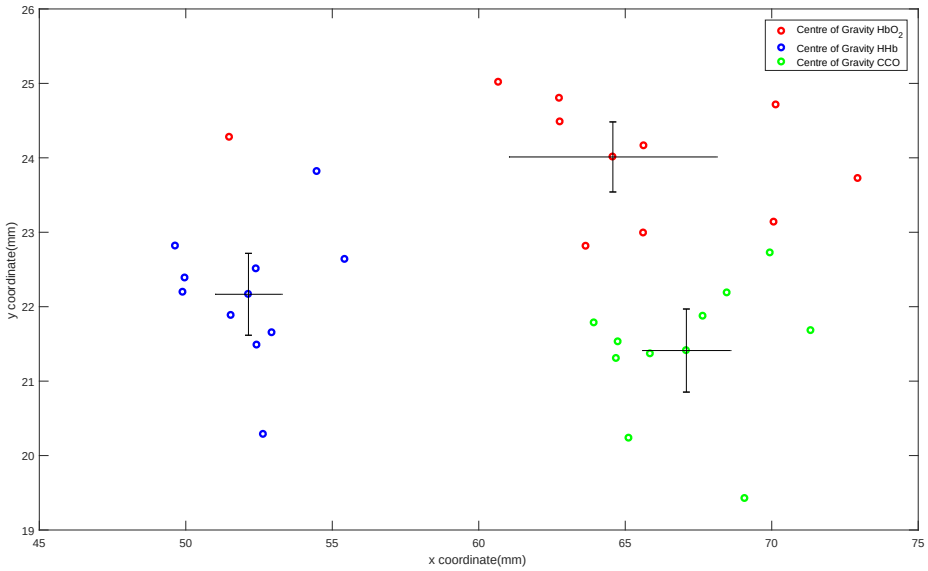

Figure 4.24: A close-up view of the CoGs of three chromophores for subject 2.

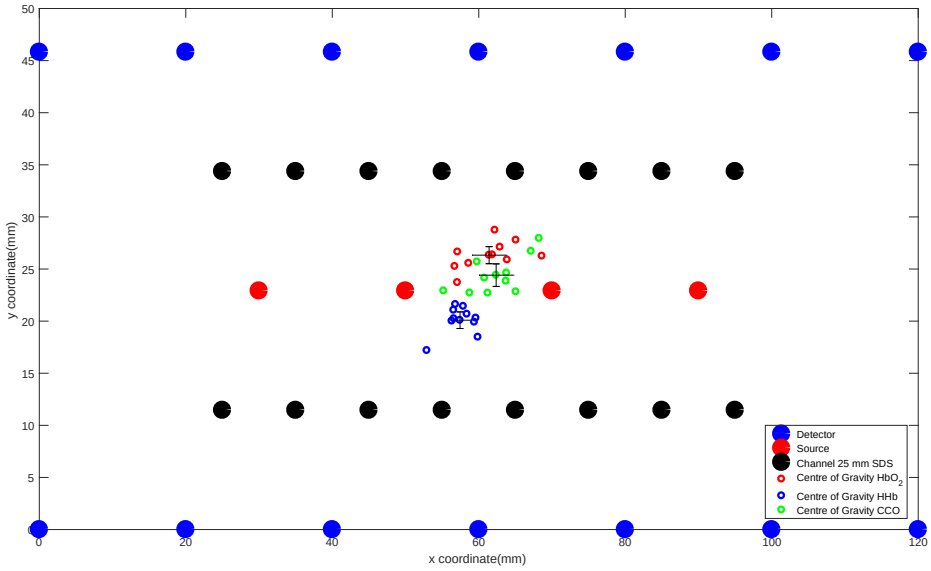

Figure 4.25: CoGs for each chromophore and the final CoGs for subject 3.

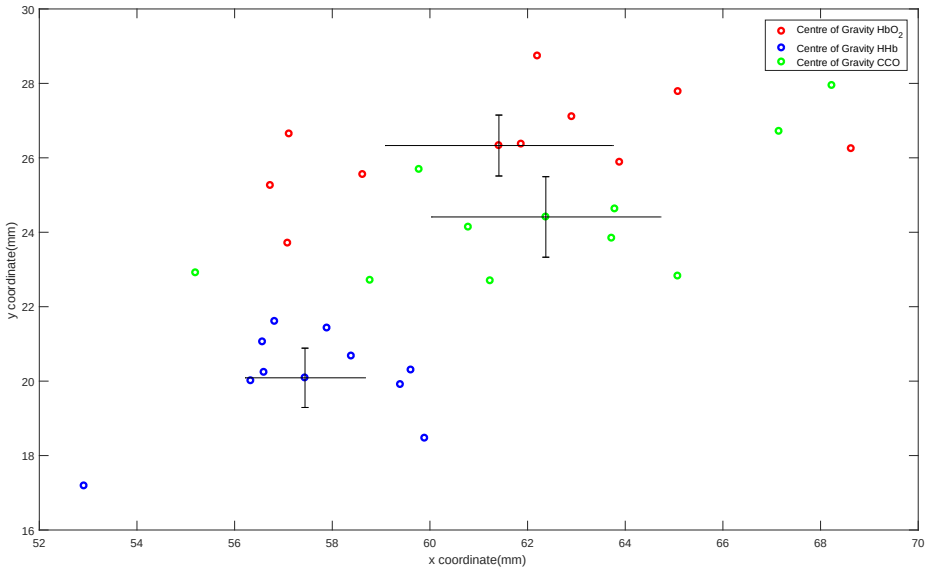

Figure 4.26: A close-up view of the CoGs of three chromophores for subject 3.

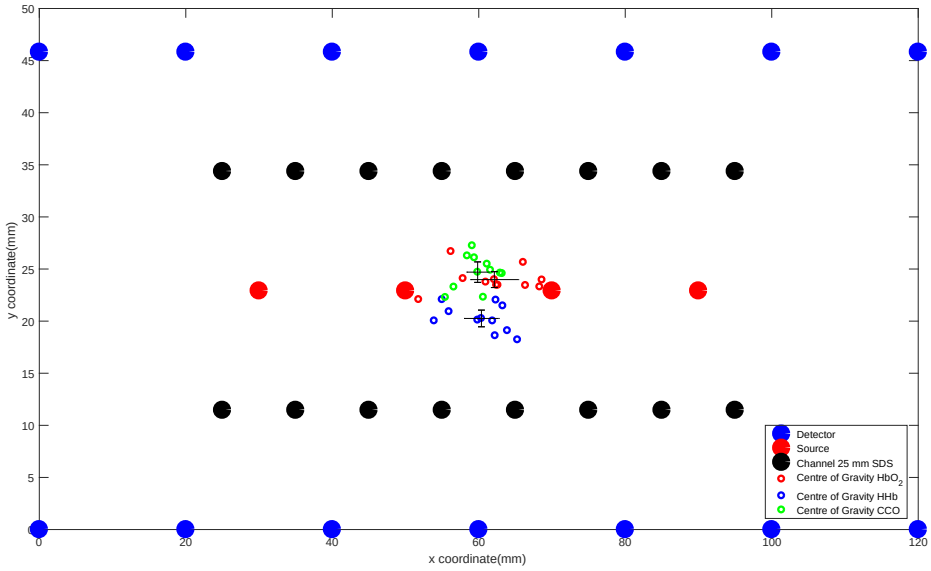

Figure 4.27: CoGs for each chromophore and the final CoGs for subject 4.

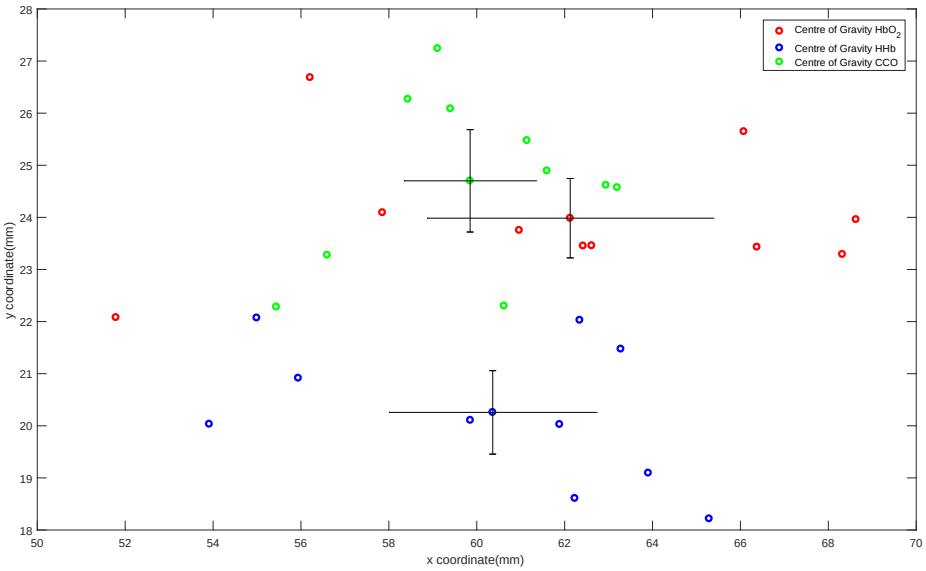

Figure 4.28: A close-up view of the CoGs of three chromophores for subject 4.

4.4.3 Reconstructed images of concentration changes

Figure 4.29 shows the reconstructed images of the block-averaged change of $\Delta[HbO_2]$, Δ[HHb] and Δ[oxCCO] from the left occipital cortex of subject 1 at four time points t = 10s, 20s, 30s and 40s after the onset of the visual stimulation. The visual stimulation finished at t= 20s. There were clear, localised changes corresponding to functional activation as evident in an increase in $\Delta[HbO_2]$, a decrease in Δ[HHb] and an increase in Δ[oxCCO] during the functional stimulation period (from t= 0 s to t = 20 s). These changes returned back to baseline level during the resting period.

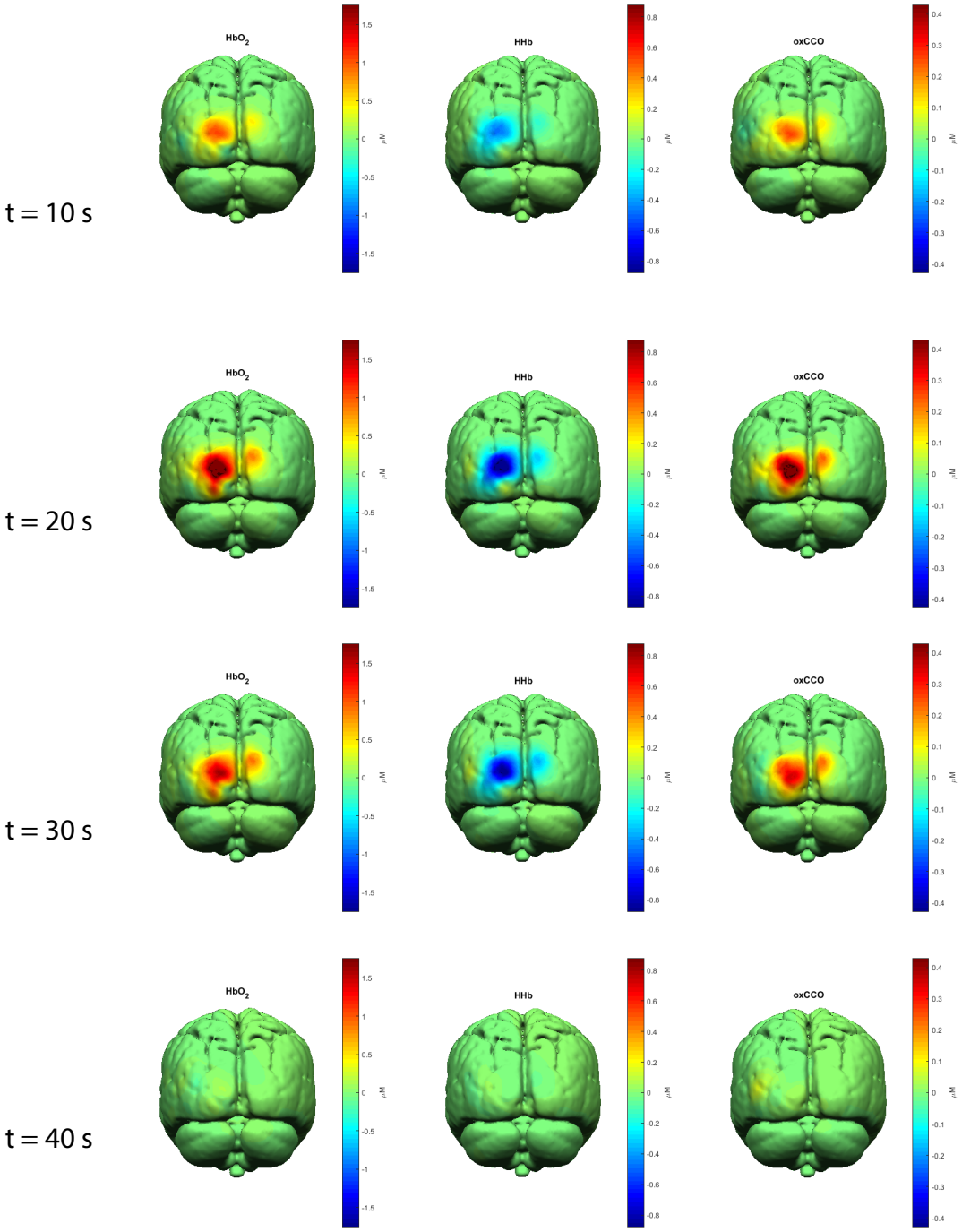

Figure 4.29: Reconstructed images of concentration changes of HbO_2, HHb and oxCCO in subject 1. Four selected time points (10 s , 20 s, 30s and 40s) are shown.

Similar results can be evident in reconstructed images of subject 2 (Figure 4.30), subject 3 (Figure 4.31) and subject 4 (Figure 4.32).

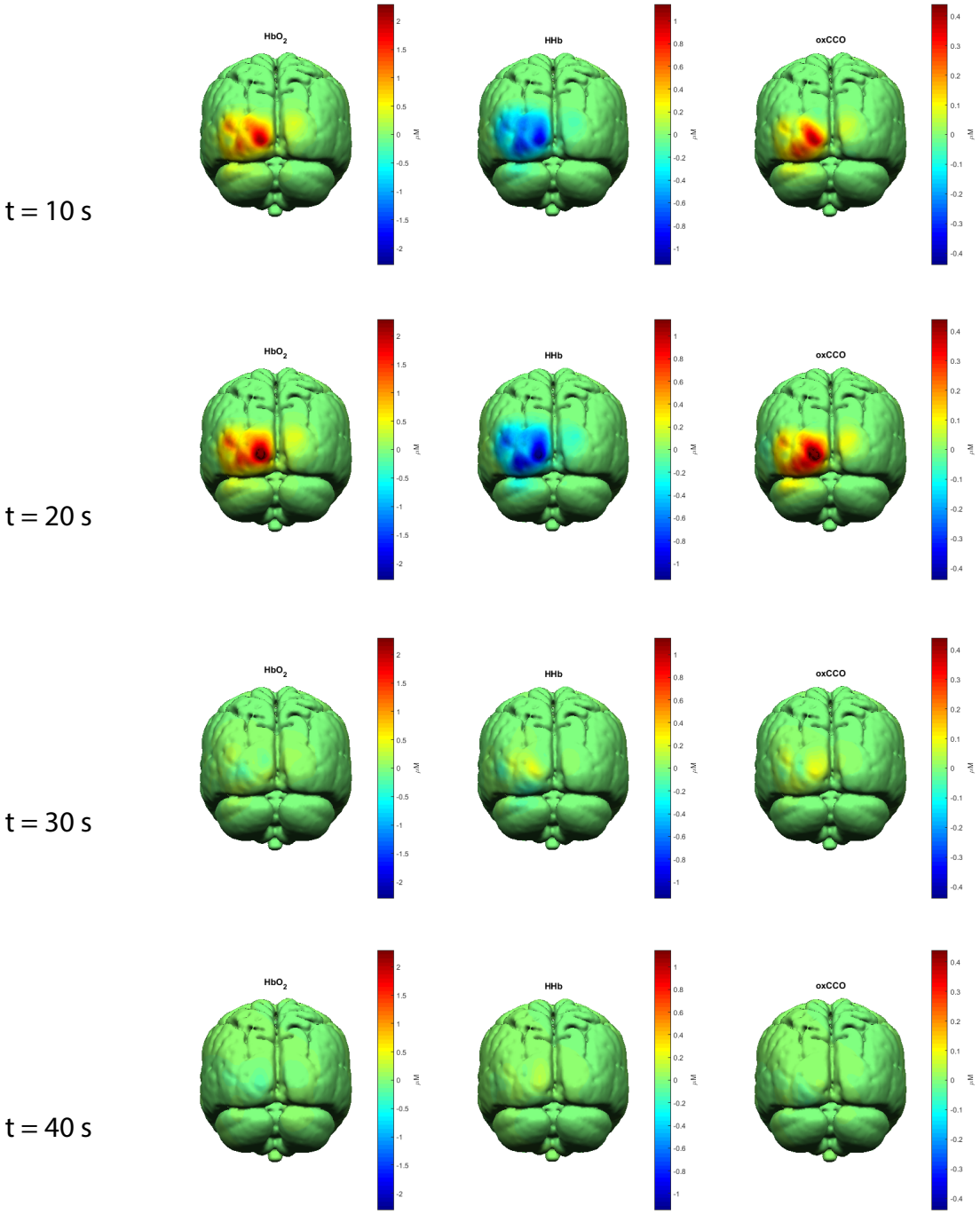

Figure 4.30: Reconstructed images of concentration changes of HbO_2, HHb and oxCCO in subject 2. Four time points are shown to demonstrate the changes over time corresponding to functional activation.

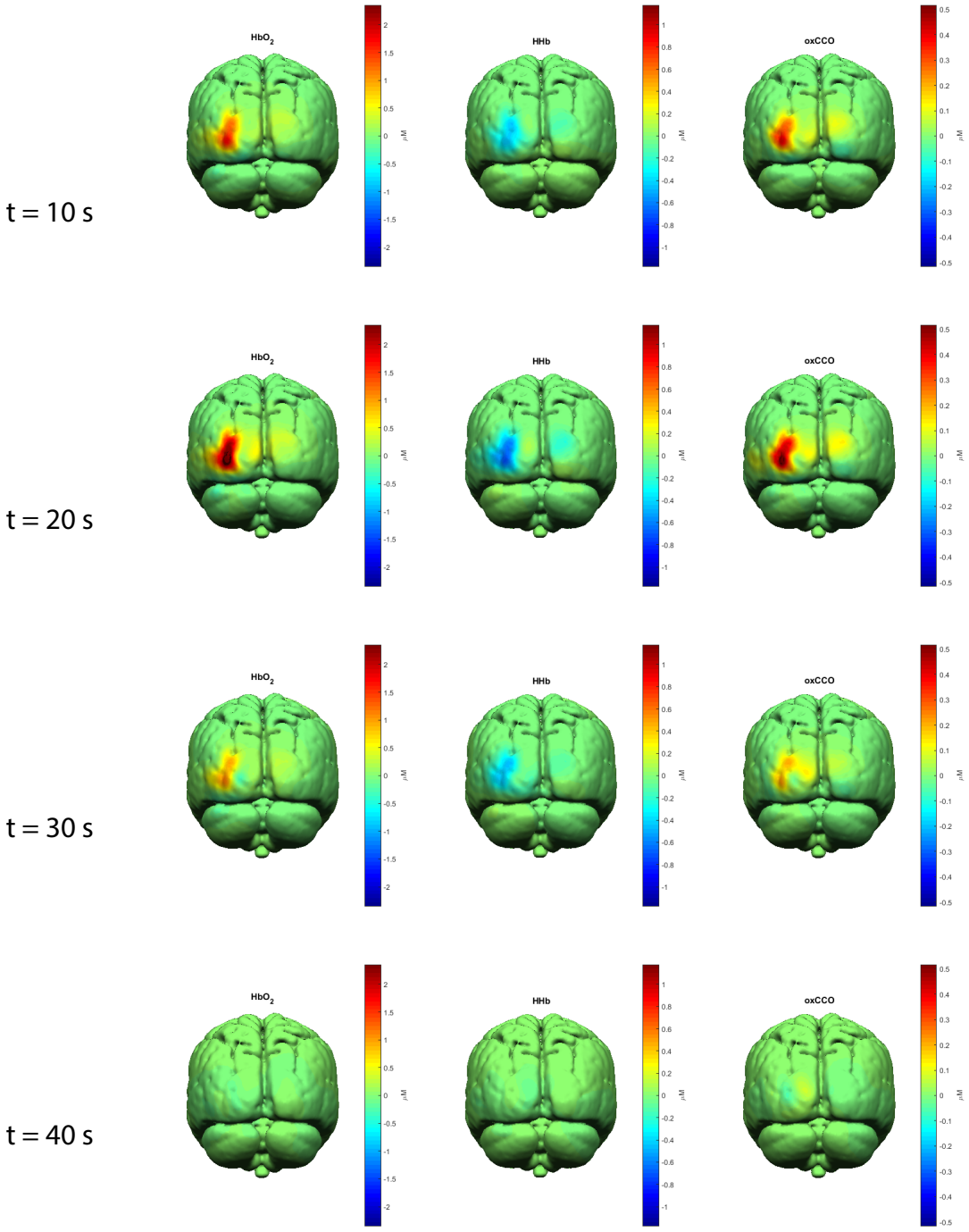

Figure 4.31: Reconstructed images of concentration changes of HbO_2, HHb and oxCCO in subject 3. Four time points are shown to demonstrate the changes over time corresponding to functional activation.

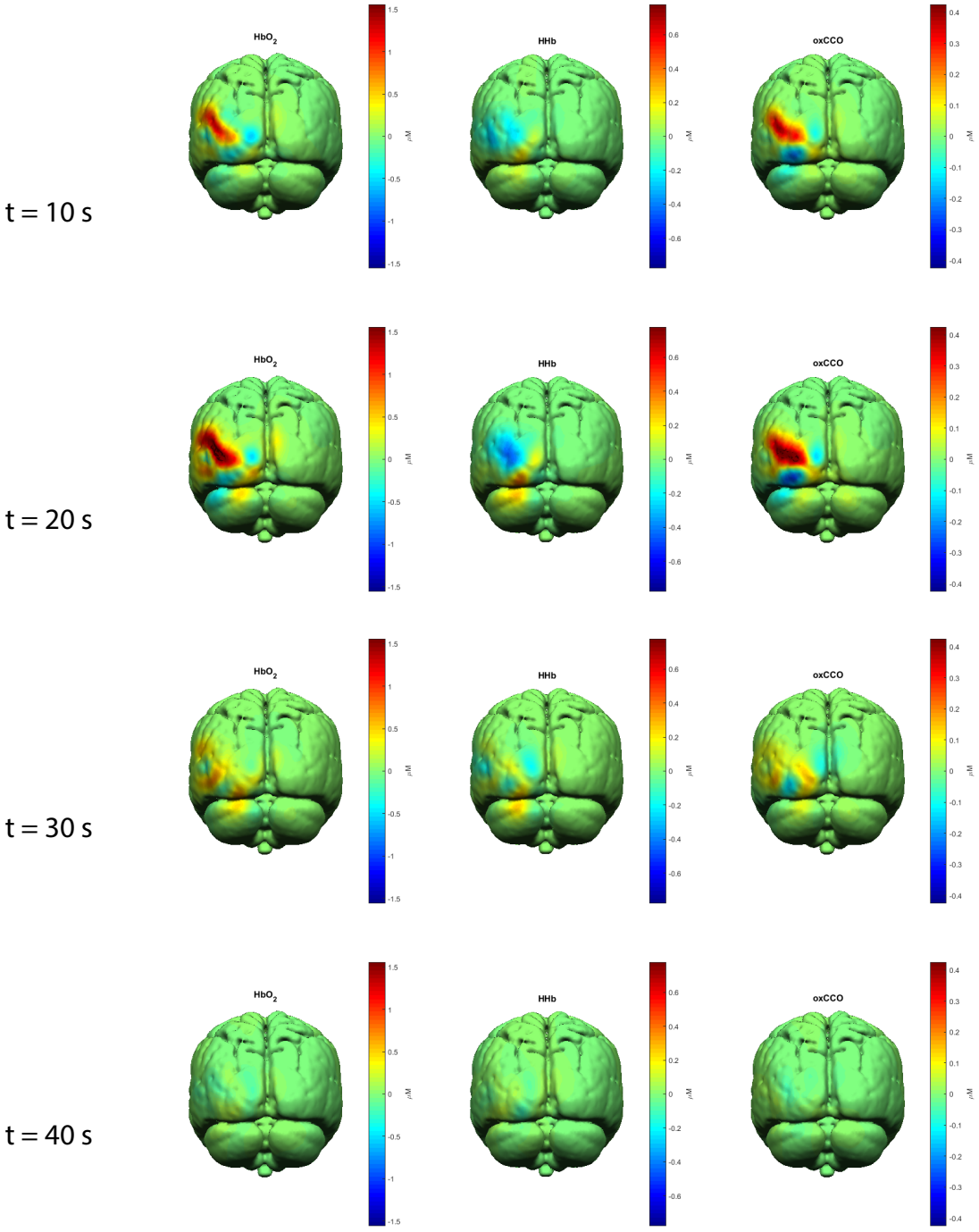

Figure 4.32: Reconstructed images of concentration changes of HbO_2, HHb and oxCCO in subject 4. Four time points are shown to demonstrate the changes over time corresponding to functional activation.

Figure 4.33 shows the images of block-averaged Δ[oxCCO] at the time point t = 20 s for all four subjects. Clear and focused functional activation response is seen in all four reconstructed images.

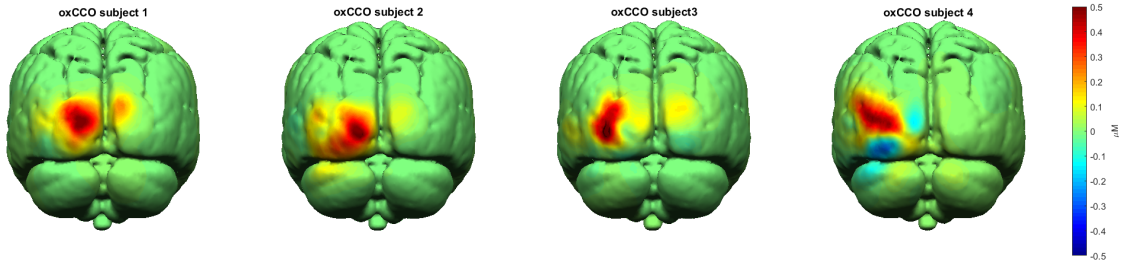

Figure 4.33: Reconstructed images of concentration changes of oxCCO in all four subjects at the peak of the response to visual stimulation.

4.5 Conclusion and discussion

In this chapter, by combining a new probe holder, a new analysis algorithm and a new experimental protocol with optical components of an existing broadband system, we have developed a pseudo broadband DOT system that has the capability of collecting broadband NIRS data from 32 measurement channels. We used the system to explore 1) the feasibility of monitoring Δ[oxCCO] across multiple regions of the brain during visual functional activation; 2) the use of centre of gravity analysis to examine the centre of activation of three NIRS chromophores during functional activation and 3) the feasibility of reconstructing images of Δ[oxCCO] using the multi-distance, multi-channel broadband data.

From the result of the visual functional activation, we believe that the pseudo broadband DOT system could monitor changes in Δ[oxCCO] across multiple regions of the brain. More importantly, it demonstrated that it is feasible to monitor these changes using a broadband approach and there is a spatial variation in the signal. The spatial variation was confirmed by channel-wise block-averaged spectroscopic results from all four subjects showing a clear localised increase in Δ[oxCCO] together with an increase in Δ[HbO_2] and a decrease in Δ[HHb] from a selected number of channels. The changes corresponding to functional response were mostly evident in channels 17 to 24 originating from source slot 3, most likely probing the primary visual cortex based on the location of the probe on the head. Channels that were positioned more laterally (channel 1 to 8, unlikely to probe the visual cortex) did not show the haemodynamic and metabolic responses corresponding to functional activation. Our results of Δ[HbO_2], Δ[HHb] and Δ[oxCCO] are consistent with those of other publications investigating changes in the visual cortex during visual stimulation [70], [71]. However, the intra-subject spatial variation in the measured signal needs further investigation before relating it to actual variation in cerebral physiology. This is because of the partial volume effect in NIRS

which means that different measurement channels may probe different volume of the activated brain region, creating a variation in the amplitude of the measured signal. In other words, different measurement channels may have different sensitivity to the activated brain volume. This issue can be explored further using modelling of light transport in the adult head model. However, it is beyond the scope of this thesis.

Centre of gravity analysis for all four subjects revealed the spatial difference in the CoGs among the three chromophores. While the CoGs of HbO_2 and oxCCO showed some degree of overlapping (in three out of four subjects), the CoG of HHb remained separate from the other two chromophores in all subjects. This may suggest that these chromophores have distinctly separate centres of activation. Moreover, all the CoGs were located in between source slot 2 and source slot 3 in all four subjects. This shows a degree of agreement with the spectroscopic results as changes in chromophore concentration corresponding to functional activation were seen mostly in measurement channels acquired when the source fibre was placed at slot positions 2 and 3 (row 2 and 3 in spectroscopic result figures).

The reconstructed images confirmed the feasibility of using the multi-distance, multi-channel data sets to reconstruct images of Δ[oxCCO]. This is extremely encouraging as for the first time, we have the ability to represent and evaluate the changes in cellular oxygen metabolism using 3D tomographic images. Reconstructed images during functional activation showed a clear and localised activation for all three chromophores in the left occipital cortex during the period of maximum changes in response to functional activation (t= 20 s) in all four subjects. Images at different time points demonstrated an increase in $\Delta[HbO_2]$, a decrease in Δ[HHb] and an increase in Δ[oxCCO] during the stimulation period (t = 0 s to t = 20 s). These changes returned to baseline level during the resting period (t= 20 s to t = 40 s). These results are in line with the channel-wise spectroscopic results. Moreover, in term of localisation, the results from image reconstruction and from spectroscopy showed a high degree of agreement, both demonstrating functional changes localising around source slot locations 2 and 3. However, in one of the subjects (subject 4), the focalised centre of activation in the reconstructed images was localised more laterally in comparison to the expected visual cortex. This may be due to errors in the digitising of the coordinates of the probes on the subject head. This can be prevented in future studies by digitising the locations of the probe on the subject head before and after the studies.

Previous studies have demonstrated the transient oxidation of CCO during visual stimulation characterised by the increase in Δ[oxCCO] signal [70], [71]. The results of

this pilot functional study reported in this chapter show similar findings. However, in this study, we have extended the measurement of Δ[oxCCO] into 32 channels to map a much larger area of the left visual cortex using a pseudo broadband DOT system. With multi-channel, multi-distance data sets, we have demonstrated the spatial variation and spatial localisation Δ[oxCCO] using the centre of gravity analysis and image reconstruction algorithm. The importance of this study does not only lie in the actual results but also in the confidence that the spatial variation in Δ[oxCCO] could be monitored and it could be used to reconstruct tomographic images of the changes in metabolism. This study represents a big step towards monitoring Δ[oxCCO] across multiple regions of the adult human brain.

4.6 Limitations and future improvements

The pseudo broadband DOT system presented in this chapter has certain limitations. The biggest limitation is that the system cannot acquire multi-channel measurements simultaneously. The whole experimental paradigm had to be repeated four times for each subject to acquire a full data set of 32 measurement channels. During each repeat, the source and detector fibres had to be physically moved to different slot positions. This could introduce technical differences among repeats with issues such as slight changes in the hair clearance, slight movement of the probe holder on the head of the subject. Moreover, although visual stimulation is known to elicit reproducible functional changes, subject level of concentration and attention can be different among repeats and this can introduce differences among channels. In addition, it took a long time (around two hours) to collect one full data set which made data collection in a large number of subjects impractical. The only way to tackle all of these limitations at once is to develop a multi-distance, multi-channel optimised broadband NIRS system that has the capability of monitoring Δ[oxCCO] across multiple regions of the brain simultaneously. In the next chapter, further developments will be presented to transform the pseudo broadband DOT system into a truly multi-channel, multi-distance broadband NIRS system.

Chapter 5

Development of a multi-channel multi-distance broadband NIRS system with the capability of monitoring changes in oxCCO signal across multiple brain regions

This chapter describes the development of a multi-channel, multi-distance broadband NIRS system based on the pseudo broadband DOT system described earlier in chapter 4. Developments in hardware, software and the analysis algorithm will be described as well as the preliminary testing and in vivo experiments.

5.1 Overview

To develop the pseudo DOT system into a truly multi-channel, multi-distance system with the capability of monitoring multiple areas of the brain, the number of measurement channels had to be increased. This required developments in the hardware, the software and the resolving algorithm. In terms of the hardware, the same light sources and spectrographs from the pseudo DOT system that was described earlier in chapter 4 were

used. The number of source and detector fibres was increased in order to probe multiple regions of the head simultaneously. The probe holder was redesigned to accommodate the changes in source and detector fibres. The shutter controllers system was changed to sequentially illuminate source fibres. In terms of software development, a new control code was developed and integrated into the existing LabVIEW software to control the order of illumination of sources. A new resolving algorithm based on the UCLn algorithm was developed to accommodate multi-distance, multi-channel arrangement.

An overview of the instrument is provided in Figure 5.1.

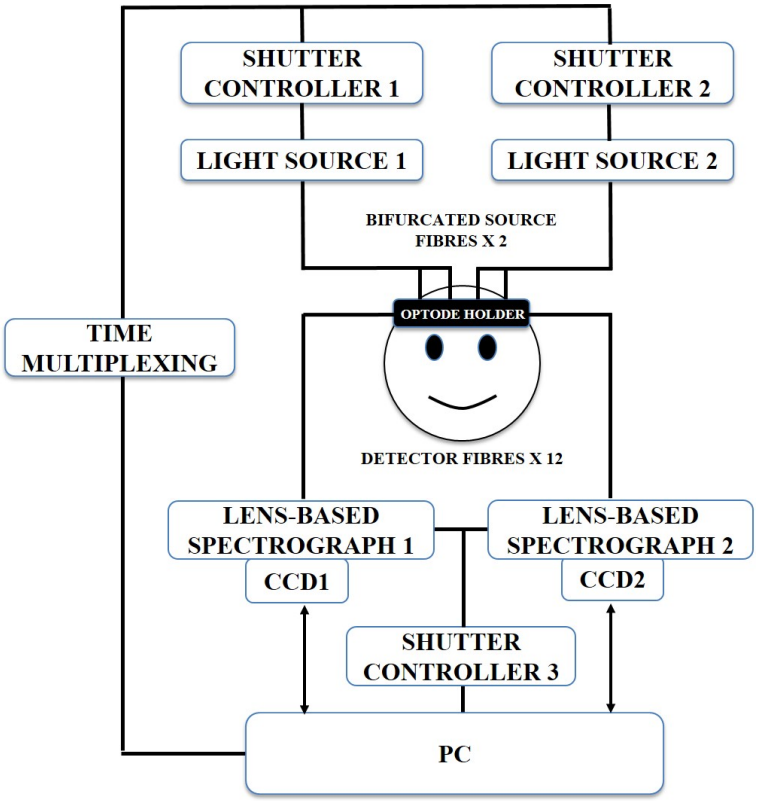

Figure 5.1: Schematic diagram showing the components of the multi-distance, multi-channel broadband NIRS system. The system has two light sources, each has a solenoid shutter that is controlled by an electronic shutter controller with a time multiplexing mechanism. Light from the sources (filtered to 504 nm - 1068 nm) is directed to the subject by means of bifurcated optical fibre bundles, creating four source fibre bundles at the subject end. The diffused light from the subject head is collected using 12 detector fibre bundles branched from two fibre bundles, each of the two is connected to a spectrograph and a CCD camera. Both spectrographs are controlled by another electronic shutter controller. The system is run by LabVIEW software from a computer.

5.2 Hardware

5.2.1 Light sources and spectrograph

The new system employs two halogen bulb light sources, each with a gold plated mirror and a 50 W halogen bulb (Phillips) with an axial filament to emit a broadband NIR enhanced spectrum. The output spectrum is filtered to remove wavelengths below 504 nm and above 1068 nm to reduce UV exposure and heating effects. Each of the two light sources has a solenoid shutter (Melles Griot, USA) that is controlled by an electronic shutter controller (Melles Griot, USA). Light from each light source is directed to the subject via a custom-built bifurcated optical fibre (Loptek, Germany). This effectively creates two pairs of source fibre bundles at the subject end. A time multiplexing mechanism is used to control the opening and closing of the shutters of the light sources hence allowing one light source to be on every 1.4 s, delivering light to the pair of source fibre bundles connected to it. This will be discussed in detail in section 5.2.3.

To collect, separate and measure the intensity of light from the tissue at each wavelength, the instrument has two custom-built spectrographs, each of which is connected to a front illuminated CCD camera (PIXIS: 512f, Princeton Instruments). The spectrograph is lens-based rather than mirror-based to provide higher light throughput. The spectrograph contains Minolta MC Rokkor lenses with the focal length of f = 58 mm and an f-number of f/# = 1:1.2. The grating of the spectrograph (GR50-0310, Thorlabs) has dimensions of 50 x 50 x 9.5 mm with 300 grooves per mm blazed at 1000 nm to optimise reflection in the NIR region. The light spectrum is detected by two CCD cameras (PIXIS: 512f, Princeton Instruments). each with chip dimension of 12.3 x 12.3 mm corresponding to 512 x 512 pixels with a pixel size of 24 x 24 μm. The CCD cameras are cooled to -70^{o}C to reduce thermal noise and increase sensitivity. Each spectrograph is connected to a 3 m long detector fibre bundle which branches into six individual fibre bundles at the subject end. Overall, at the subject end, the system has four source fibre bundles and 12 detector fibre bundles resulting in a total maximum of 24 measurement channels.

5.2.2 Optical fibres

The new source and detector fibre bundles were custom-built by Loptek (Glasfasertechnik GmbH, Germany) using glass fibres with an individual fibre diameter of 70 μm and numerical aperture values of 0.54 and 0.57 for detector and source fibres respectively. The system has two sets of detector fibre bundles, each of which is connected to one spectrograph (Figure 5.2a). Each detector fibre bundle has six individual fibre bundles

for the subject-end, five of which have a bundle diameter of 1.5 mm and one with a diameter of 0.6 mm. The ferule of the bundle at the system-end has six openings (Figure 5.2b) aligned along a straight line to fit into the slit of the spectrograph to transmit the light collected from the subject into the spectrograph for spectral analysis.

The system has two sets of source fibre bundles, each splits into two source fibres at the subject-end (Figure 5.3a). The bundle diameter at the system-end is 4.5 mm and the bundle diameter of individual source fibre at the subject-end is 3.2 mm. This effectively creates two pairs of source fibres, where each pair is turned on and off at the same time at the system-end.

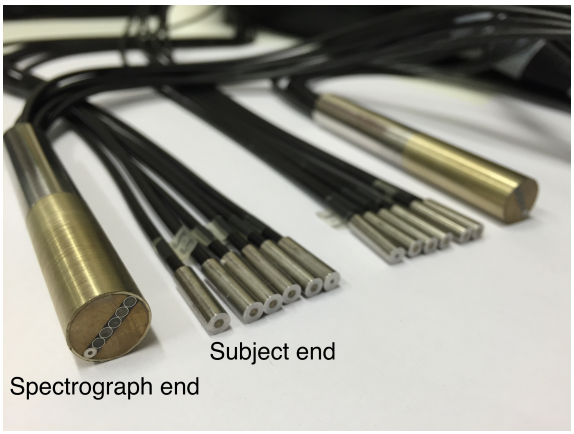

(a) Two set of detector fibre bundles, each has a spectrograph-end and a subject-end.

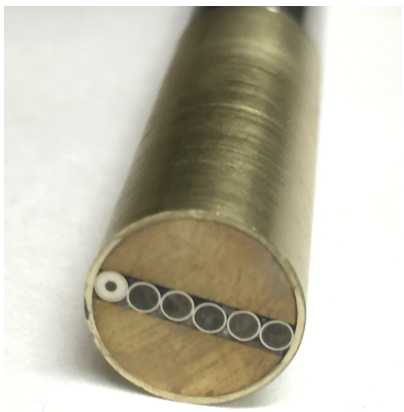

(b) Spectrograph end of a detector fibre bundle has six openings.

Figure 5.2: Specifications of detector fibre bundles.

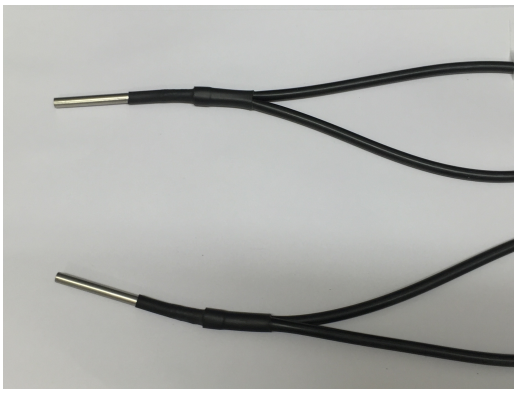

(a) The bifurcation of source fibre bundles to increase the number of sources from two halogen bulbs.

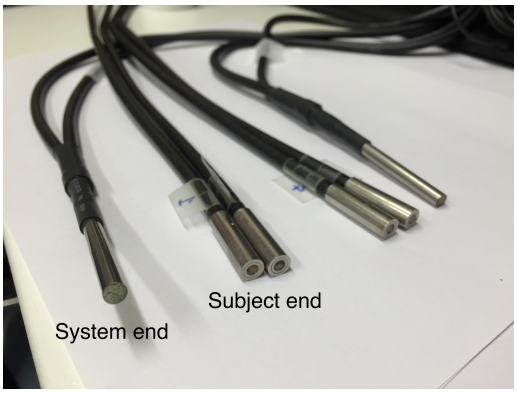

(b) The system end and the subject end of source fibre bundles.

Figure 5.3: Specifications of source fibre bundles.

5.2.3 Mechanical shutter controller boxes and its operation

One shutter controller box was used to control the solenoid shutter of each of the two light sources. A time multiplexing mechanism was developed to control the shutter controllers to alternately open and close the shutters of the two light sources, allowing one light source to be on every 1.4 s, delivering light to the pair of source fibre bundles connected to it (Figure 5.4). It is important to ensure that the CCD cameras finish capturing the data before the multiplexing of the light source occurs (Figure 5.5). This was achieved by introducing a multiplexing control code into the existing LabVIEW software. The LabVIEW software was modified such that after both CCD cameras finish capturing data, they return a local Boolean variable, GotFrame, indicating the process of capturing data has finished. That variable was used to control the time multiplexing of the sources. A counter variable, Pcounter, was created to increase its value after the both CCDs finish one cycle of capturing data. When Pcounter is even, simulated squared wave signals are sent to a DAQ assistance module to send an analogue output to shutter box controllers to open the shutter for light source 1 (fibres 1 & 3) and close the shutter for light source 2 (fibres 2 & 4). When Pcounter is odd, a similar process occurs to close the shutter for light source 1 and open the shutter for light source 2. This process produces a time multiplexing mechanism for sources, sequentially delivering light to the paired source fibres connected to them (Figure 5.4).

(a) Light is delivered from light source 1 to source fibre 1 and 3.

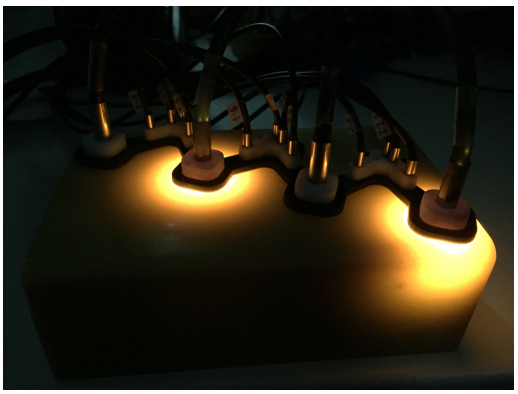

(b) Light is delivered from light source 2 to source fibre 2 and 4

Figure 5.4: The time multiplexing of the light sources to sequentially deliver light to the paired source fibres connected to them.

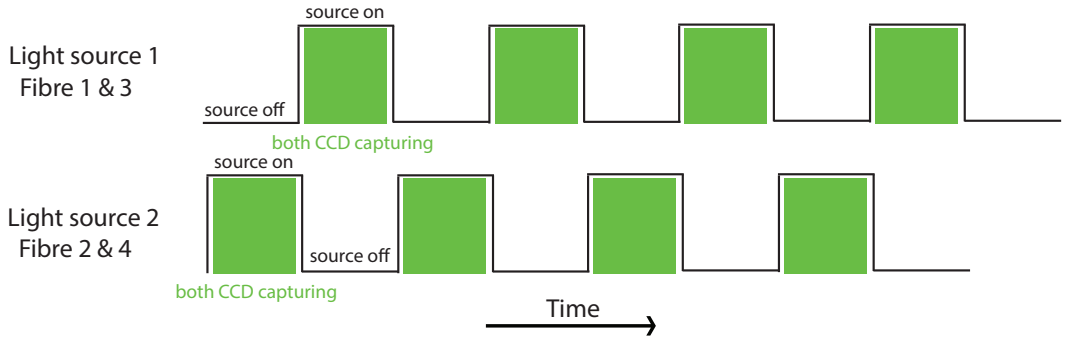

Figure 5.5: Diagram to demonstrate the integration of the time-multiplexing mechanism of the light sources to the capturing of CCD cameras.

5.2.4 Probe holder

The optical interface between optical fibre bundles and the subject is provided by a probe holder. Two types of probe holder were developed for application at the frontal and visual cortices. For the former, optical coupling can be achieved with ease as the forehead is hairless and double sided medical tape can be used to keep the probe holder with optical fibres in place. For the latter, it is more challenging as hair needs to be cleared out of the interface between optical fibres and the scalp for good optical coupling. Special headgear design with an integrated probe holder is needed for this application. In the next section, probe holder designs for both applications will be presented.

5.2.4.1 Holder for visual experiment

The probe holder for visual experiments was designed with an objective of having a good area of coverage to detect visual functional activation. The schematic shown in Figure 5.6 demonstrates the desired locations for sources and detectors. The design incorporated four sources and ten detectors with all source detector separations of 30 mm (Figure 5.6). This source detector separation has been used previously for NIRS measurement of the visual cortex [70], [71]. The distance between neighbour sources is 45 mm, which ensures that individual detector will not receive light from any two sources at the same time using a dual illumination switching mechanism.

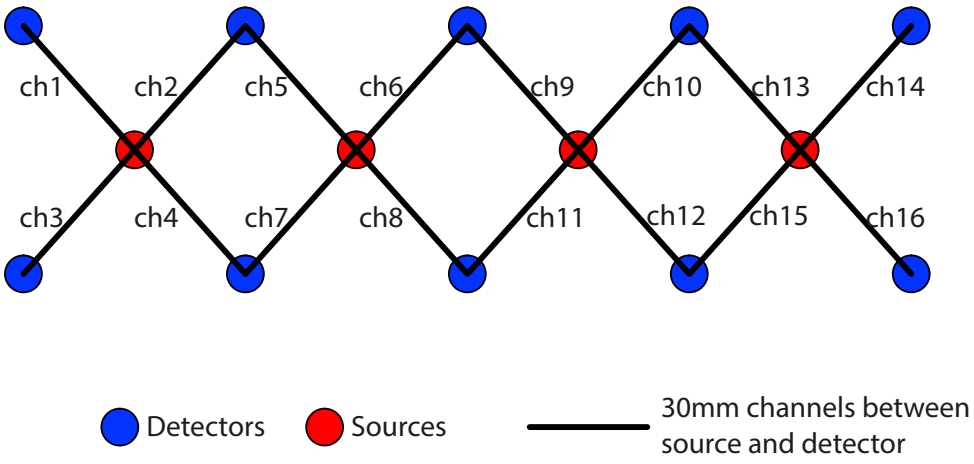

Figure 5.6: Simple diagram to demonstrate the probe holder

There were specific requirements for the probe design to facilitate NIRS measurements in the visual cortex:

- It must be integrated into a headgear so that it can be fixated on the subject head.
- It must enable clearance of hair for good optical coupling between the scalp and optical fibres.
- It must have a fixation mechanism so that it can hold optical fibres in place.
- It must maintain a constant separation between sources and detectors.

To fulfil those requirements, a modular design of probe holder integrated into a headgear was developed. The design for the probe holder has three basic modules: source block, detector block and base block (Figure 5.7). The base block was designed to have a clearance hole with a diameter of 10 mm that is large enough for convenient hair clearance. Fourteen base blocks were 3D printed using TangoBlack hard material and were attached to a neoprene head cap as shown in Figure 5.8a. To prevent the location of the base blocks from shifting while the head cap is stretched, plastic pieces with fixed distance were used to provide constraints in multiple stretching directions as shown in Figure 5.8b. Four source blocks and ten detector blocks were 3D printed and incorporated onto the subject ends of optical fibres (Figure 5.9a and 5.9b) so that they can be locked into the base blocks in the headgear. The final probe holder incorporated in the headgear and its accompanying fibres are shown in Figure 5.10. This design of probe holder and headgear enables 16 NIRS measurement channels to be collected simultaneously.

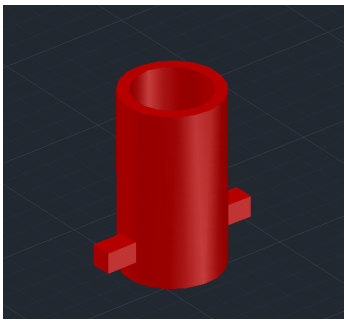

(a) Source block to be attached to source fibre.

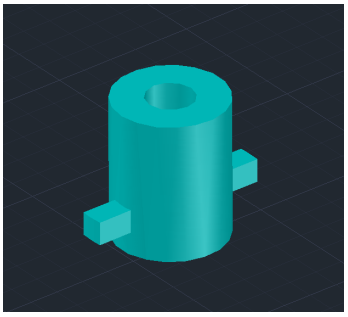

(b) Detector block to be attached to detector fibre.

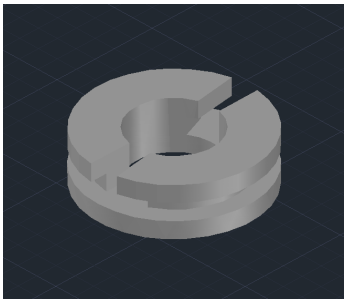

(c) Base block to be attached to the head cap.

Figure 5.7: Three modules to hold optical fibres for visual cortex monitoring.

(a) Fourteen base blocks attached to the headgear.

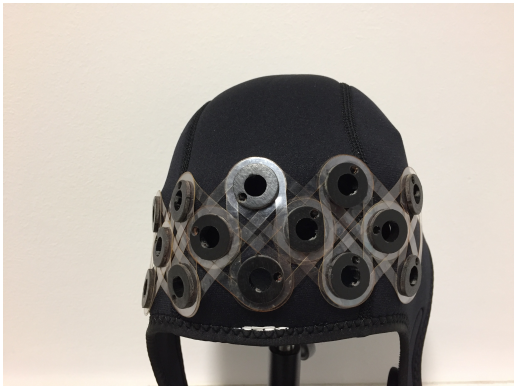

(b) The constraint mechanism inside the headgear to prevent stretching of the fabric.

Figure 5.8: Overview of the headgear design for monitoring of the visual cortex.

(a) Detector blocks attached to the subject ends of the detector fibres.

(b) Source blocks attached to the subject ends of the source fibres.

Figure 5.9: The subject ends of optical fibres for monitoring of the visual cortex.

Figure 5.10: Demonstration of the monitoring of the visual cortex using the new probe holder and headgear.

5.2.4.2 Holder for frontal experiment

As mentioned earlier, it is less challenging to design the probe holder for the frontal lobe application. However, with the objective of collecting multi-distance, multi-channel measurements that are compatible for image reconstruction, a novel design for probe holder was conceptualised. This probe holder was designed in AutoCad (AutoDesk) to have four source locations (numbered 1 to 4) with inter-source distance of 45 mm and multiple detector locations to enable 24 multi-distance NIRS channels and six TOI measurements using four source fibres and 12 detector fibres (numbered 1 to 12) (Figure 5.13). The holder was 3D printed with a combination of hard (Vero White) and flexible (Tango Black) materials (Figure 5.12) using Connex 500 3D printer (Stratasys, USA) to accommodate the curvature of the adult human forehead. The source detector separations set out by the probe holder range from 20 to 35 mm. During operation, source fibres bundles were fixed in the holder such that the two source fibre bundles that are operating simultaneously have a separation of 90 mm. This was to ensure that detector fibre bundles only receive light from one light source bundle at a time.

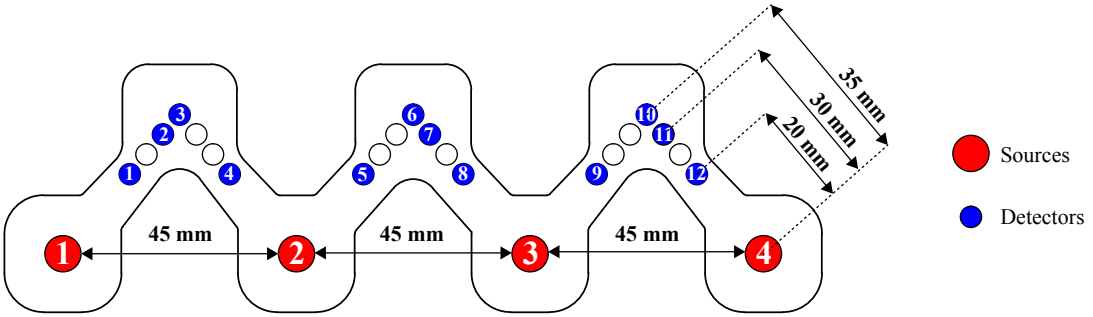

Figure 5.11: Design for probe holders to fix optical fibres in place for frontal experiments

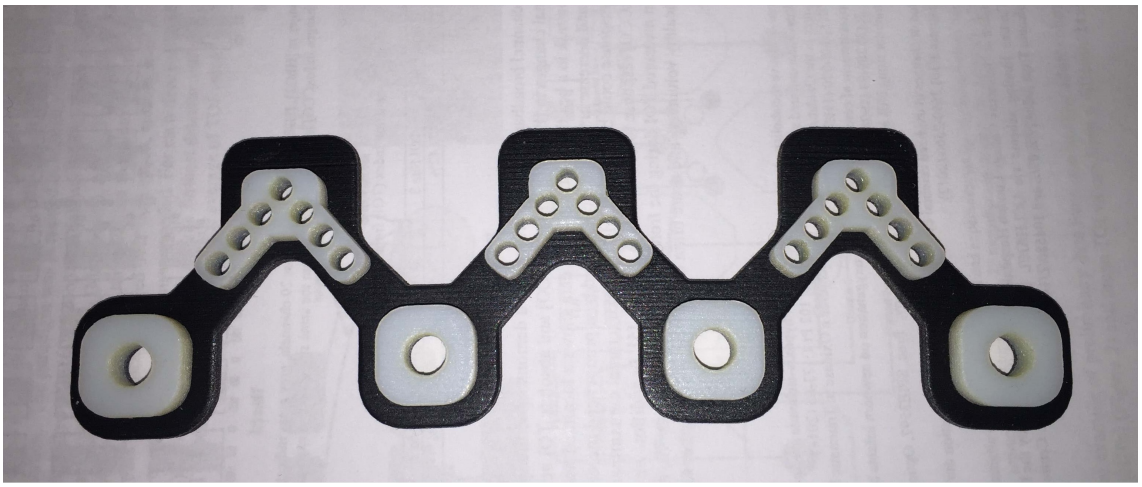

Figure 5.12: 3D printed probe holder with a combination of hard and flexible material

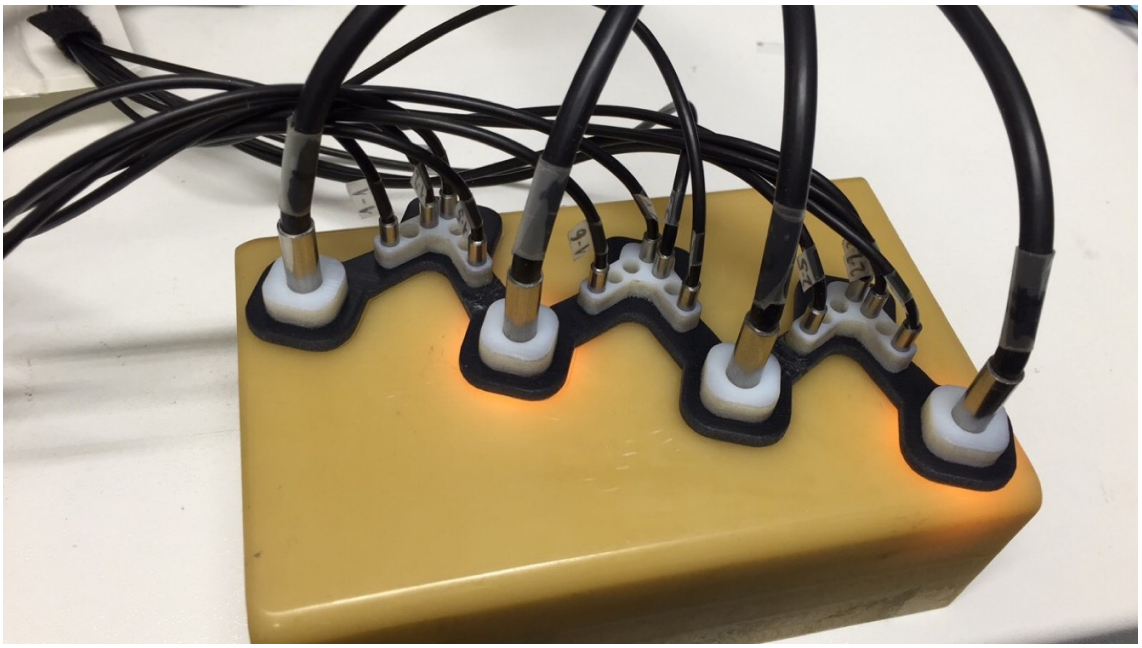

Figure 5.13: Frontal probe holder with optical fibres

5.3 Software Developments

The LabVIEW software of the pseudo DOT system was upgraded to control the multi-channel, multi-distance broadband NIRS system. The main modifications to the original software involved enabling the software to handle a larger number of detectors and to time-multiplex the light sources. The main operation of the LabVIEW software is summarised in Figure 5.14. The system starts when the start button indicated by the arrow in the LabVIEW software is pressed. Both CCD cameras start to cool down to the set temperature (usually -70°C) which can take up to ten minutes. The time multiplexing process of the light source that was integrated into the LabVIEW software starts to multiplex the light source. A cycle of acquisition starts when one source is turned on and stops when both CCD cameras finish capturing the data. Then another cycle starts when the other source is turned on while the previous source is turned off and both CCD cameras start capturing intensity data again. The process repeats until the stop button of the software is activated. After each time the CCD cameras finish capturing the intensity data, the data are displayed and used together with other inputs to calculate the concentration changes. This process will be discussed in detail in a later section.

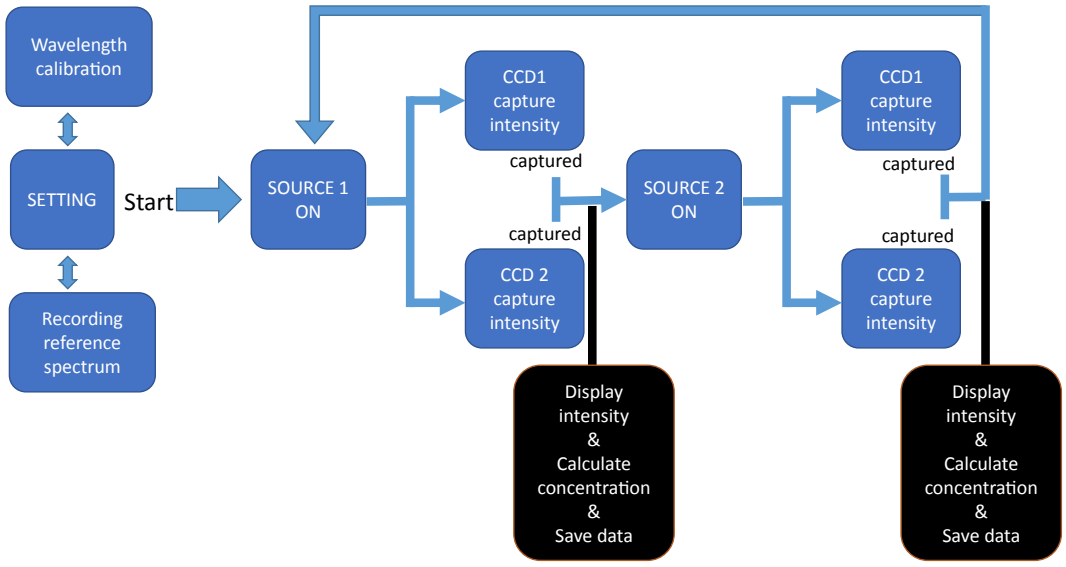

Figure 5.14: Block diagram of the main functions of the LabVIEW software.

5.3.1 Setting

The setting tab is the first panel to appear when starting the LabVIEW software (Figure 5.15). In this panel, all the variables needed for the operation of the system are set.

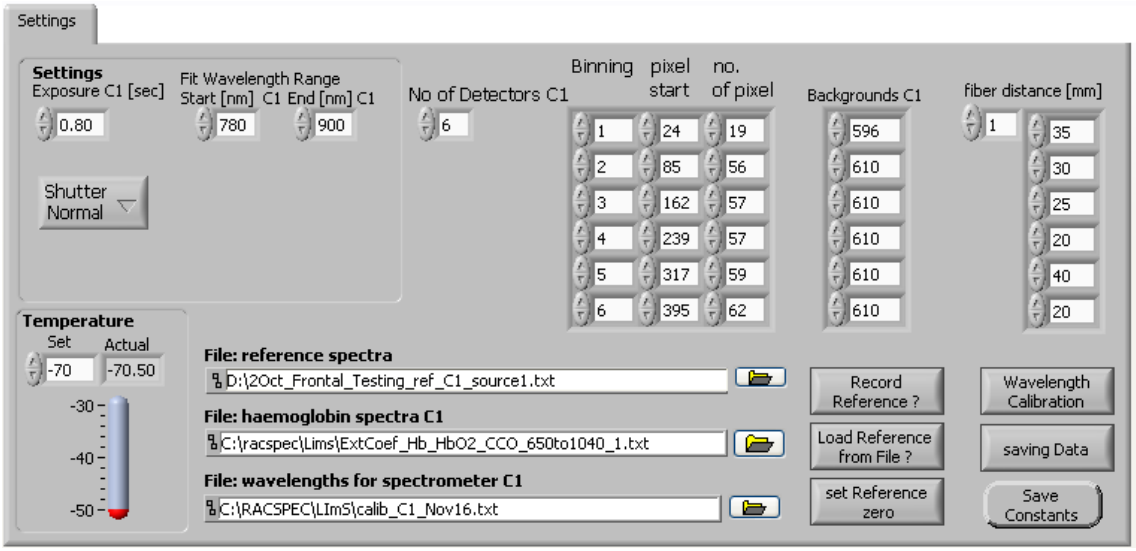

Figure 5.15: The setting tab of the LabVIEW software.

5.3.1.1 Temperature

The setting has a panel to set the temperature to cool the CCD cameras. This is normally set to -70 °C. The actual temperature of the camera is displayed next to that setting panel.

5.3.1.2 Timing parameters

Cycle time and exposure time are two parameters to control the timing of the system. Exposure time determines the duration of acquisition of the CCD camera. The longer the exposure time, the higher the intensity count detected. The cycle time determines the duration of one whole run through the software.

5.3.1.3 Wavelength range

The wavelength range is set to be from 780 nm to 900 nm. These parameters are used for the calculation of the concentration changes. Despite settings of the wavelength range, the system collects the whole intensity spectrum from 500 to 1000 nm.

5.3.1.4 Background subtraction

With the shutter of the spectrographs closed, the CCD cameras collect background counts dependent on the exposure time, the camera temperature and the number of binned pixels. These background counts are subtracted from the measured intensity to minimise the error in the measurement.

5.3.1.5 Source-detector distances

The value of the source-detector separations for each detector can be input for the calculation of concentration change.

5.3.1.6 Binning

Data binning describes the process of adding the data of adjacent pixels in the CCD camera to form a single value. In this software, the data is binned in the y-direction to yield an array with 512 values in the x-direction for each individual detector. Each pixel in the x-direction corresponds to a wavelength value(see Figure 5.16).

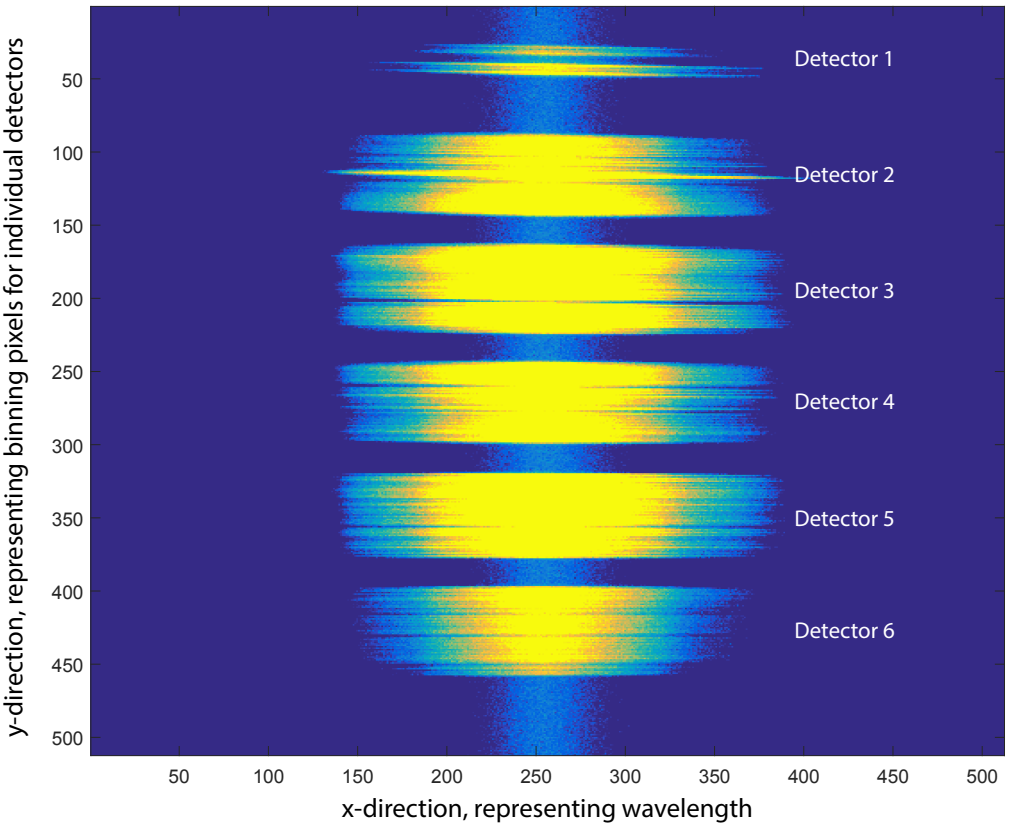

Figure 5.16: A snapshot of one of the two CCD cameras that shows the areas illuminated by the six detectors. Individual detectors are separated in the y-direction of the CCD chip. Binning is the process to add pixels in the y-direction in each detector to produce an intensity spectrum.

5.3.2 Intensity data collection

One of the main modifications to the system is the increased number of measurement channels resulting from an increase in the number of detectors, sources and a time multiplexing mechanism for the light sources. As a result, each of the twelve detectors

collects intensity spectra from two individual measurement channels and these needs to be separated before resolving the concentration changes. This process will be discussed in detail in the algorithm section.

5.3.3 Concentration calculation

The concentration change is calculated from the measured intensity spectra for each measurement channel using the UCLn algorithm as described earlier in chapter 3. Intensity data are used to calculate the change in attenuation (ΔA). ΔA spectra, DPF spectra (corrected for the wavelength dependency), source-detector distances and the specific extinction spectra of three chromophores are used to calculate the concentration changes.

5.4 Analysis algorithm development

A new resolving algorithm was developed using MATLAB (MathWorks, USA) to calculate the concentration changes from the raw intensity data collected by the modified system. As both CCD cameras capture intensity data while the light sources are turned on and off alternately, the intensity data captured by each individual detector contains intensity spectrum for two measurement channels. As a result, the intensity spectra from each detector need to be separated, sorted and allocated into individual measurement channels. This process is demonstrated in Figure 5.17 for one example detector. As shown in the figure, detector 1 receives light originating from source 1 at one cycle and source 2 at the next cycle (Figure 5.17a). As a result, there are two intensity spectra collected by detector 1 and these were separated and allocated to the corresponding channels. Moreover, these intensity spectra are at different levels due to the difference in source-detector separation. This difference can be used to identify the location of the working sources. This information is then used to allocate the intensity spectra of all the detectors to the correct channels as the example demonstrated in Figure 5.17b.

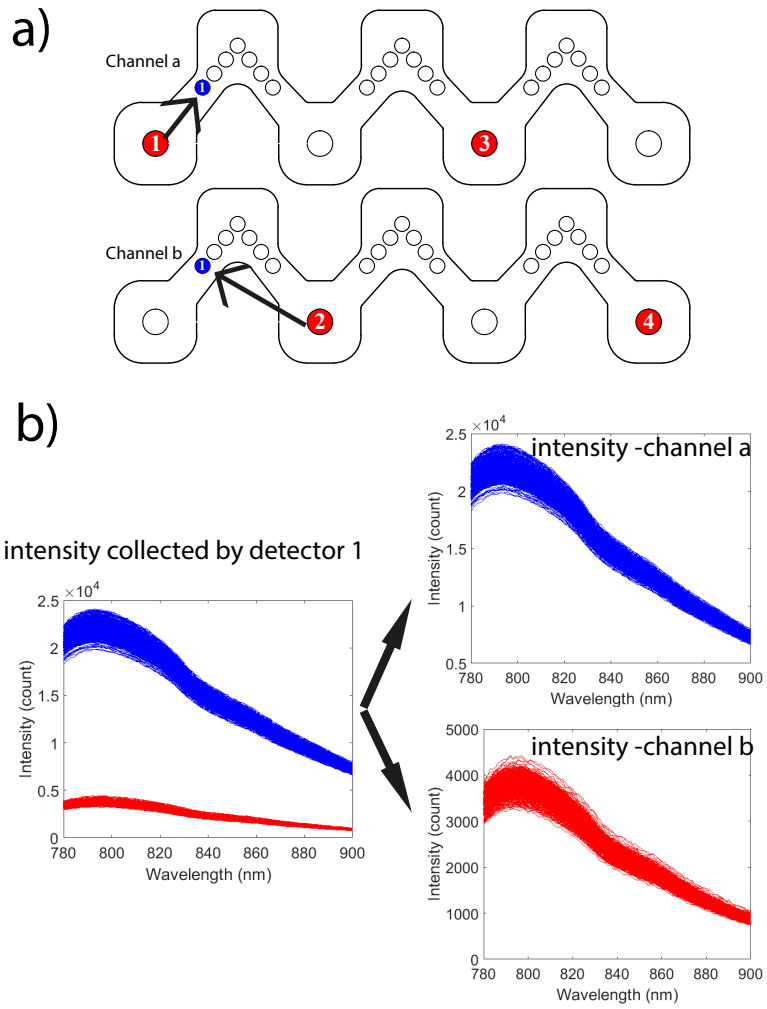

Figure 5.17: Diagram to demonstrate the process of allocating intensity spectra .a) Detector 1 receives the diffusely reflected light through tissue which originally comes from source 1 for measurement channel a and from source 2 for measurement channel b. b) The collected intensity spectra from detector 1 has two individual spectra, each of which is allocated to the corresponding measurement channel.

The sorted intensity spectra for each individual channel is then used to calculate the delta attenuation ΔA and then the concentration changes of chromophores Δc applying the MBLL via the UCLn algorithm (Figure 5.18).

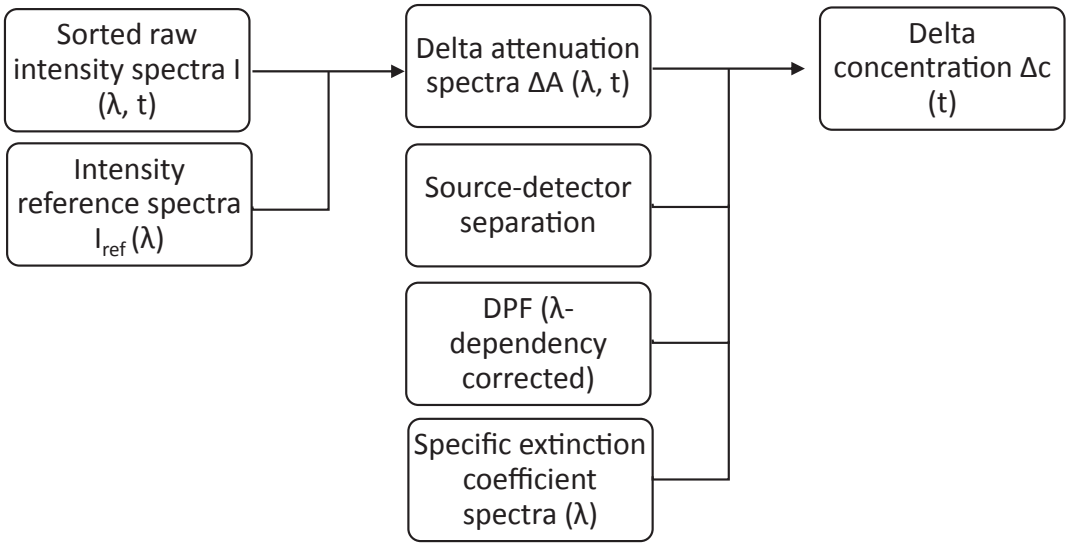

Figure 5.18: Block diagram of the implemented differential spectroscopy technique using the MBLL.

5.5 Preliminary testing

5.5.1 Power output

The power output at the end of the source fibre was measured using a slim photodiode power sensor (Thorlab. S130C) to ensure that it is within the safety standards. The average power output of the four source fibres is 5.0 mW. With a fibre diameter of 3.2 mm, the power density is 0.625 mW per square millimetre, which is within the UK tissue safety limits for an incoherent source of 2 mW per square millimetre. Figure 5.19 shows the power distributed across wavelengths for one typical light source fibre.

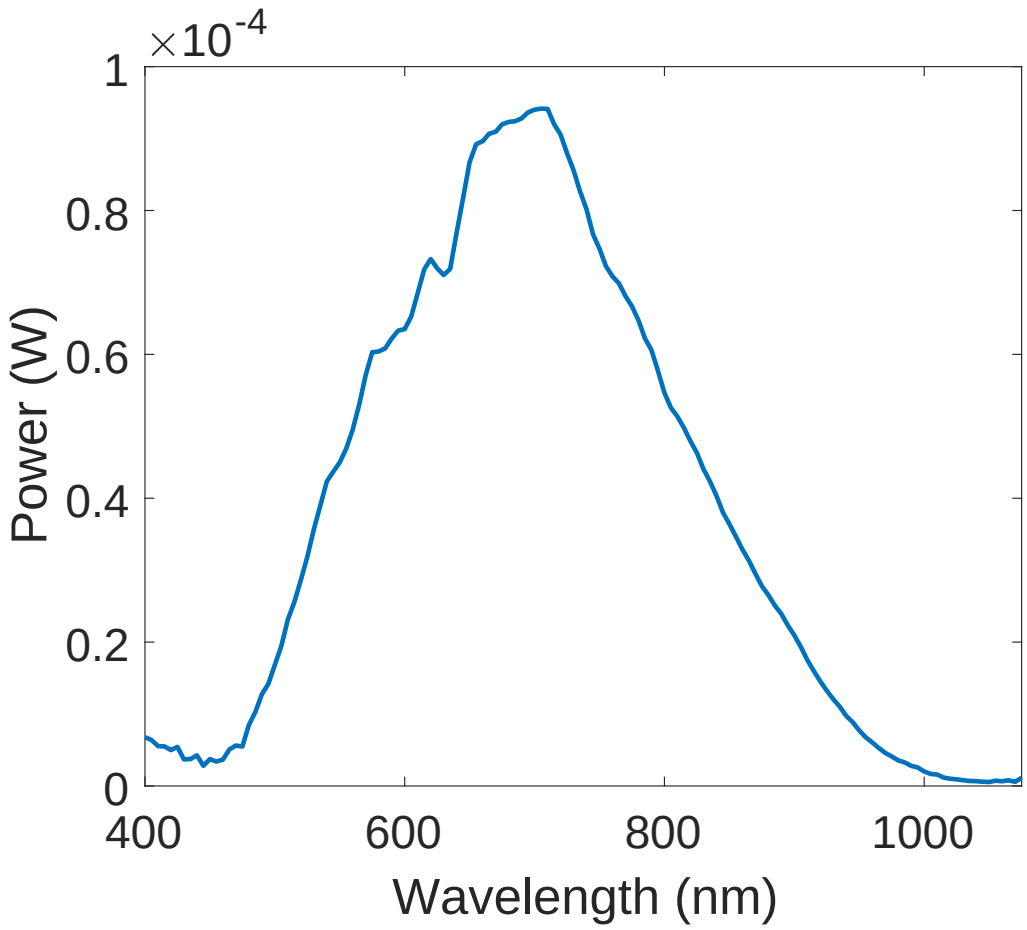

Figure 5.19: Power spectrum of one of the light source fibre.

5.5.2 Phantom Testing

Studies on phantoms were done to assess the stability of the system over time. The frontal probe holder with optical fibres was attached to a solid phantom with tissue-like optical properties as shown in Figure 5.13. The intensity measurements of 24 channels were collected for a one hour period to assess the stability of the system. Figure 5.20 shows the intensity spectra plotted together of one example channel over the one hour measurement period. There was a small variation of intensity over time with maximum variation falling into the region of 0.5 to 1 % of the intensity count.

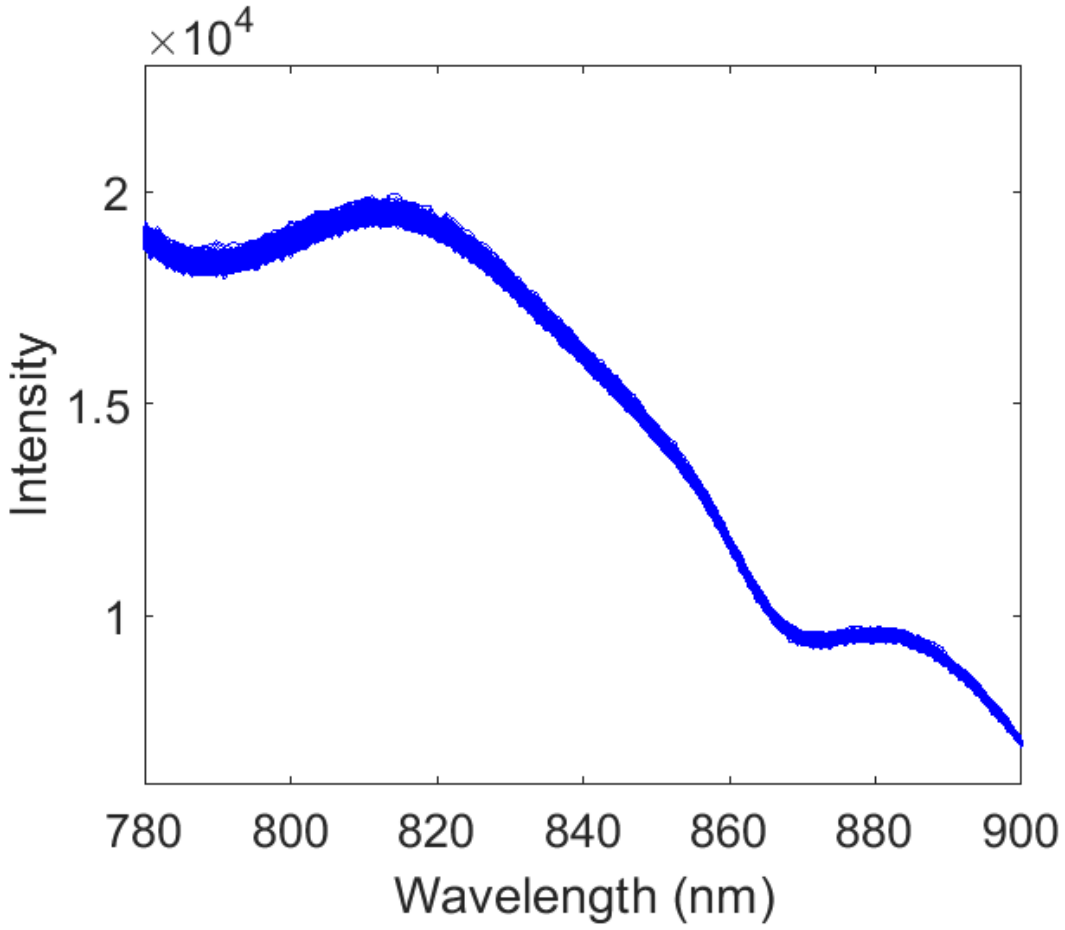

Figure 5.20: Intensity measurement of one channel for one hour stability test. Data were collected once every 2.8 s, and the plot shows each intensity spectrum over the one hour period.

5.5.3 Muscular Cuff Occlusion

Muscular cuff occlusion experiments were done on three healthy volunteers to assess the ability of the multi-channel system to monitor concentration changes of chromophores in vivo. The volunteer was seated comfortably with their forearm resting on a table. Optodes were fixated over the forearm muscle using the frontal probe holder as demonstrated in Figure 5.21. A baseline period was recorded for two minutes before the cuff was inflated to 200 mmHg for another two minutes to occlude both the artery and the vein. This was followed by deflation of the cuff and baseline measurement for another few minutes.

Figure 5.21: Muscular cuff occlusion experiment using the frontal probe. This experiment is to test the response of the three chromophores using the new modified system.

During arterial cuff occlusion which stops blood flow into and away from the forearm, desaturation is expected, producing an increase in Δ[HHb] and a virtually equal decrease in $\Delta[HbO_2]$. Δ[oxCCO] is expected to show a little or no change due to the large oxygen reserve bound to muscle myoglobin and the low oxygen consumption in resting muscle. Figure 5.22 shows the intensity spectra at two time points during the experiment, one in the baseline period and one at the peak changes. At the time of peak changes, there were two characteristic changes in the shape of the intensity spectrum: a lower intensity measurement within the spectral range from 780 to 800 nm and a higher intensity measurement above 820 nm in comparison to the intensity spectrum at the baseline time point. The former characteristic could be explained by the increase in Δ[HHb] as this chromophore has a high absorption level in this spectral region characterised by a peak around 760 nm. The latter characteristic could be explained by the decrease in $\Delta[HbO_2]$ as this chromophore has high absorption in the spectral region above 800 nm.

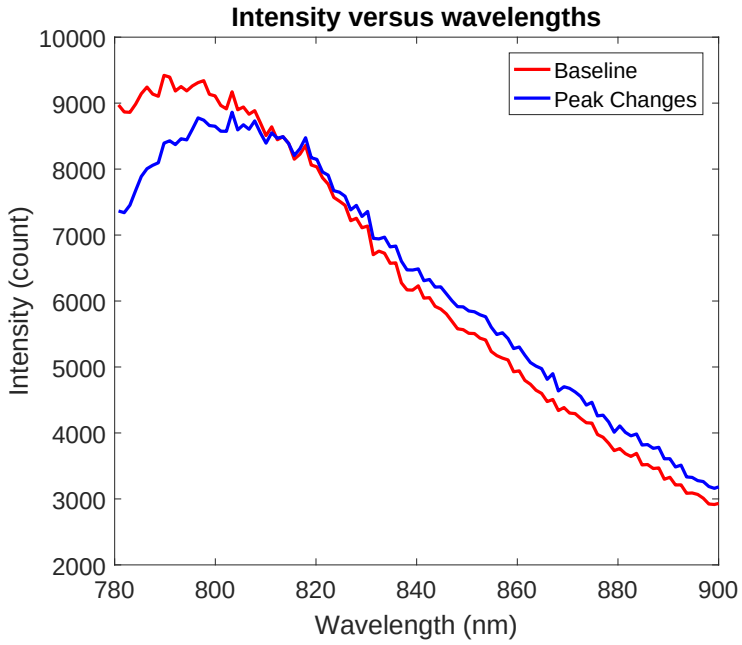

Figure 5.22: Intensity spectra through arm during baseline (red) and arterial cuff occlusion(blue) showing difference in spectral shape in response to changes in concentration of chromophores.

Figure 5.23, shows the resolved concentration changes of three NIRS chromophores from a 35 mm measurement channel using the newly developed resolving algorithm mentioned earlier. During the arterial occlusion period, there was an increase in the Δ[HHb] (blue) and a decrease in $\Delta[HbO_2]$ (red). Δ[oxCCO] (green- multiplied by 10 for visualisation) increased in a small amount during the occlusion period and decreased back to the baseline level after the occlusion period. This result agrees with the general expectations of the physiological processes that occur during arterial cuff occlusion and with the results of our previous system developed in-house [117]. Moreover, the result of this experiment also suggests that the Δ[oxCCO] is independent of the haemoglobin signals as large changes in the haemoglobin concentration did not create a corresponding change in the Δ[oxCCO] signal. Overall, this demonstrated that the upgraded system with the new probe holder, the new software and the new resolving algorithm is able to monitor concentration changes of NIRS chromophores in vivo.

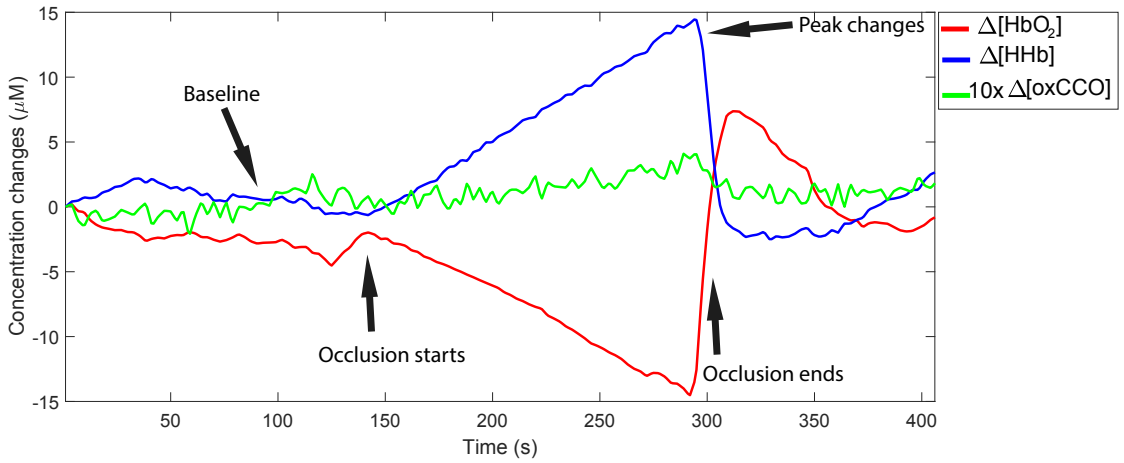

Figure 5.23: Concentration changes of chromophores during arterial cuff occlusion on the forearm. Note that the oxCCO changes are plotted on a x10 scale.

5.6 Visual functional activation

The visual functional activation paradigm presented in chapter 4 was repeated with the upgraded multi-channel, multi-distance broadband NIRS system to test the capability of the new system to monitor simultaneously changes in concentrations of NIRS chromophores across multiple regions of the adult human brain.

5.6.1 Methods

The probe holder and the headgear designed for this visual experiment was presented in section 5.2.4. In brief, the holder allowed easy clearance of hair and fixation of four source fibres and ten detector fibres onto the subject scalp as shown in Figure 5.24. The headgear was positioned such that the midpoint between source slots 2 and 3 was 2 cm above the inion, a small bony protuberance of the occipital bone at the back of the head. This position of the headgear ensured that both the left and right visual cortices located underneath the occipital bone were probed by the system. Notice that the two small detector fibres were not used for the visual functional experiment. Figure 5.25 shows the measurement channels acquired when the paired source fibres were time-multiplexed. This set-up allowed the 16 NIRS measurement channels monitoring different regions of the visual cortex to be collected simultaneously.

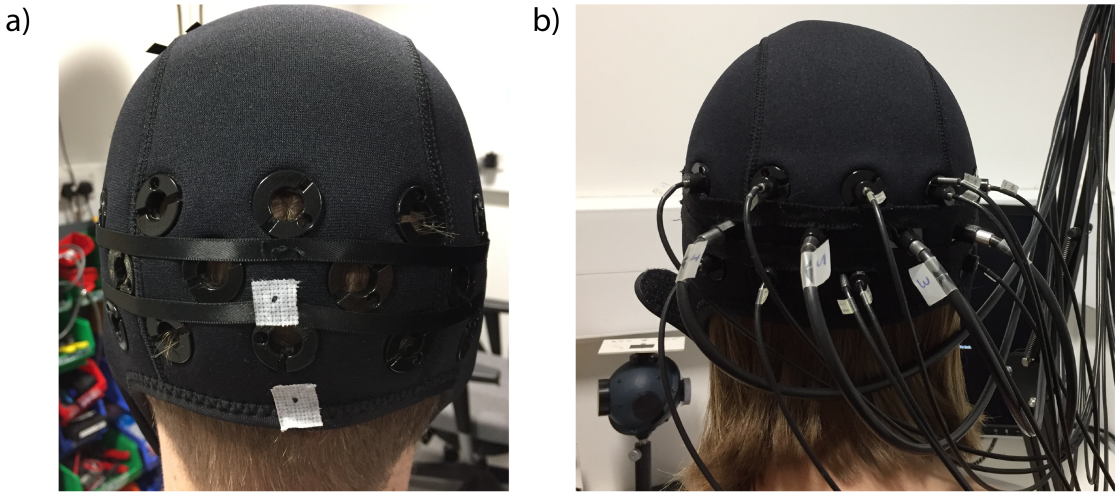

Figure 5.24: The probe holder, headgear and the final subject set-up for the visual functional activation. a) The headgear fixated on the subject head, allowing clearance of hair to provide a good optical interface between the subject scalp and the optical fibres. b) Fixation of optical fibres onto the headgear, allowing the monitoring of changes in the visual cortex.

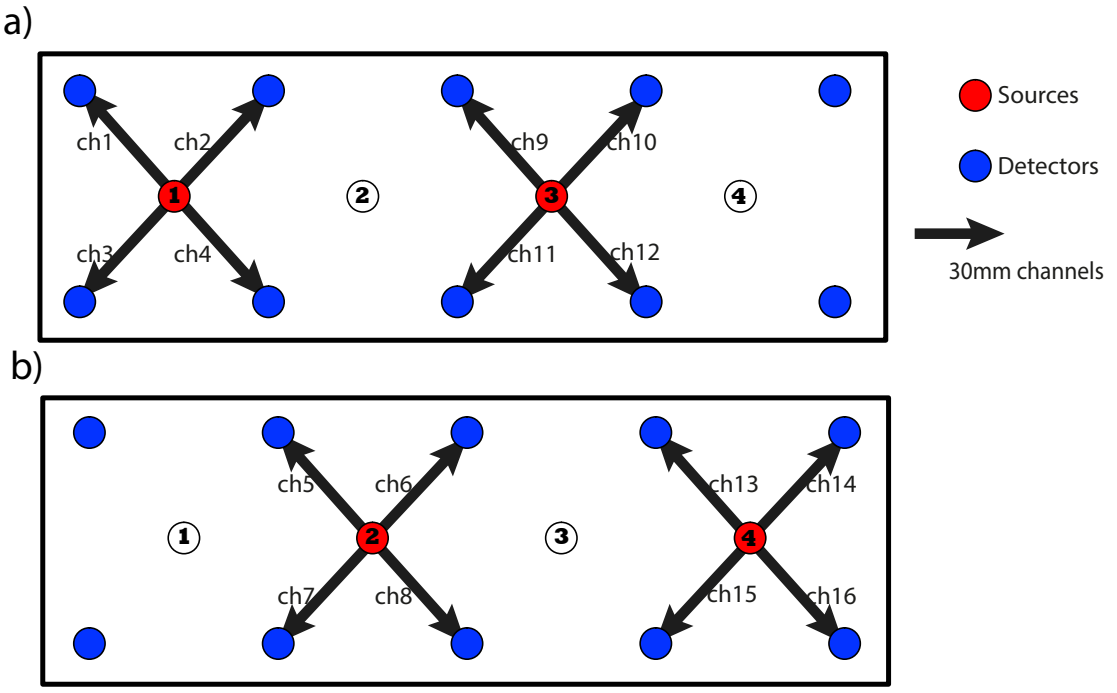

Figure 5.25: NIRS measurement channels collected when the paired source fibres were time-multiplexed. a) Source fibres at location 1 and 3 were illuminated to collect channels 1 to 4 and 9 to 12. b) Source fibres at location 2 and 4 were illuminated to collect channels 5 to 8 and channels 13 to 16.

Visual functional activation was achieved as previously described in chapter 4. The experimental paradigm consisted of 10 epochs, each with 20 s of stimulation achieved by a 4 Hz inverting checkerboard followed by 20 s of resting achieved by a black screen with

a centred white cross. Change in the intensity of diffusely reflected NIR light through the visual cortices was monitored continuously in 16 NIRS measurement channels using 4 source fibres and 10 detector fibres of the multi-channel broadband system. This change in intensity was used to calculate the change in concentration of NIRS chromophores using the algorithm described earlier. The calculated concentration changes were resampled to 1 Hz and were processed with a low-pass second order Butterworth filter with cut-off frequency of 0.08 Hz. There were 16 sets of data for each subject. Each set had the time-series concentration changes of three chromophores $\Delta[HbO_2]$ Δ[HHb] and Δ[oxCCO]. These time-series changes were blocked averaged according to stimulation epoch to produce 16 sets of 40 s block-averaged data for each chromophore. The baseline and the activation periods were defined as in the visual experiment presented previously in chapter 4. Group averaging and statistical tests were performed using the same method as mentioned in chapter 4.

5.6.2 Results

Following ethics approval and volunteer consent, six healthy adult volunteers were studied. Figure 5.26 shows the intensity spectra and the delta attenuation spectra at two time points from one channel probing the visual cortex during the experiment: at the end of a resting period and at the end of a stimulation period. Intensity at the end of the resting period was higher than that at the end of the stimulation period. This may be because during the stimulation period, there was a net increase in CBF, bringing a surplus supply of HbO_2 into the part of the visual cortex probed by the channel. This increase in HbO_2 attenuated the NIR light across the spectral range from 780 to 900 nm. The delta attenuation data also supported this hypothesis as there was higher attenuation at the end of the stimulation period in comparison to that at the end of resting period (Figure 5.26b).

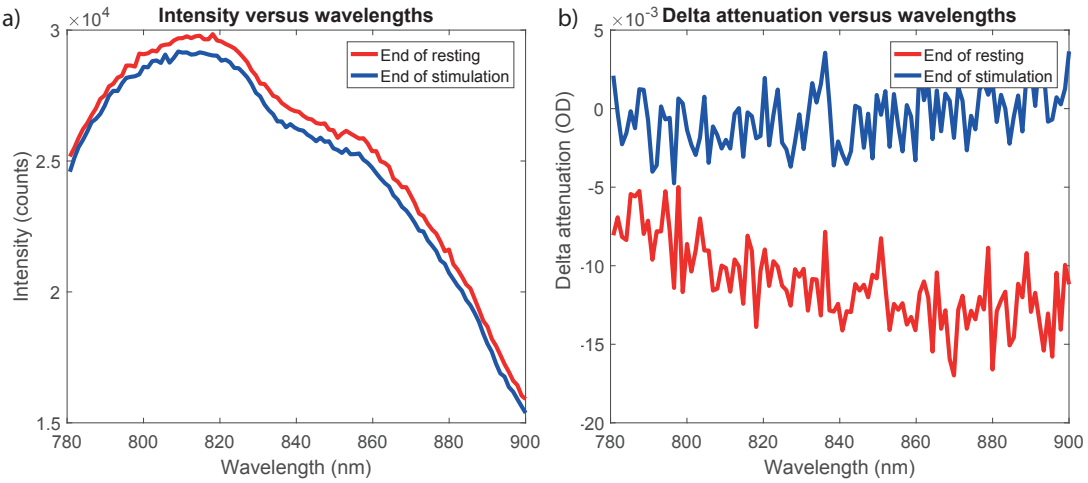

Figure 5.26: a) Intensity of two time points marked as end of resting and end of stimulation b) Delta attenuation at those two time points.

Figure 5.27 shows the raw concentration changes of three chromophores from channel 10 from one subject during functional visual stimulation. The stimulation period is shaded in grey and $\Delta[HbO_2]$, Δ[HHb] and Δ[oxCCO] are plotted in red, blue and green respectively. A typical haemodynamic response was evident with an increase in $\Delta[HbO_2]$, a decrease in Δ[HHb]. Δ[oxCCO] increased during the stimulation period and came back to baseline during the resting period. This result is similar to the previous results presented in chapter 4 using the pseudo DOT system and it agrees with results published by other authors investigating the changes of CCO during visual stimulation [70], [71].

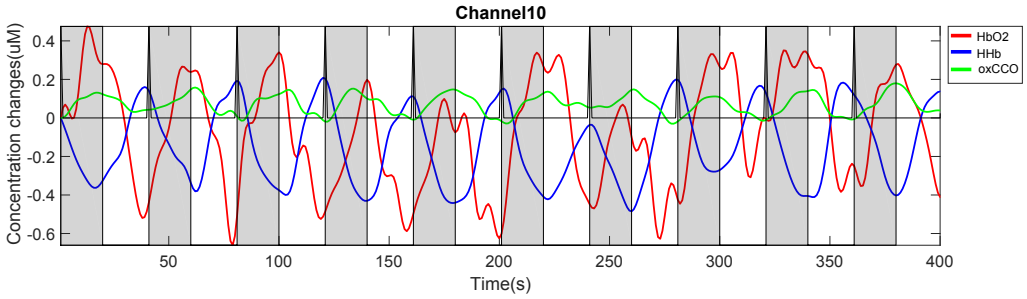

Figure 5.27: Raw concentration changes of three NIRS chromophores in channel 10 measured in an example subject during full field visual stimulation.

Figure 5.28 shows the block-averaged concentration changes of all 16 measurement channels in the same subject. The X in the middle of the plot indicates the centre point of the probe holder which was positioned at 2 cm above the inion. Concentration changes of HbO_2, HHb and oxCCO corresponding to functional activation were seen in a subset of channels. According to the location of these channels, they were likely to probe the visual cortex in this subject. A spatial variation in the concentration changes of the haemoglobin signal and of oxCCO signal could be observed. Large changes in response

to functional activation were seen mostly in the upper channels. This may be due to the position of the probe holder that could be too low in relation to the activated cortices.

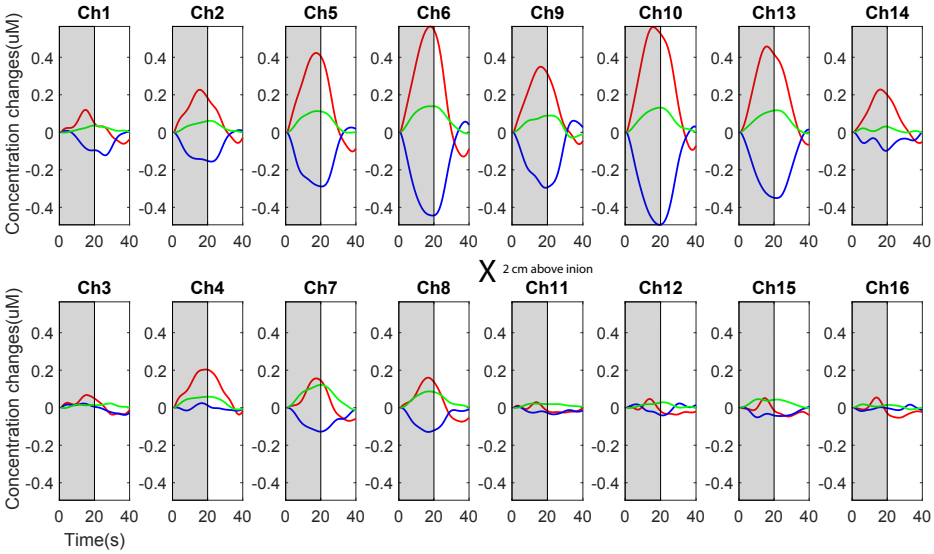

Figure 5.28: Block averaged concentration changes of three NIRS chromophores in 16 channels in the same subject. Typical haemodynamic response and cytochrome c oxidase response with a spatially varying amplitude corresponding to functional activation were evident in a subset of channels localising in proximity to the left and right visual cortices.

The results for five other subjects are similar and is as followed:

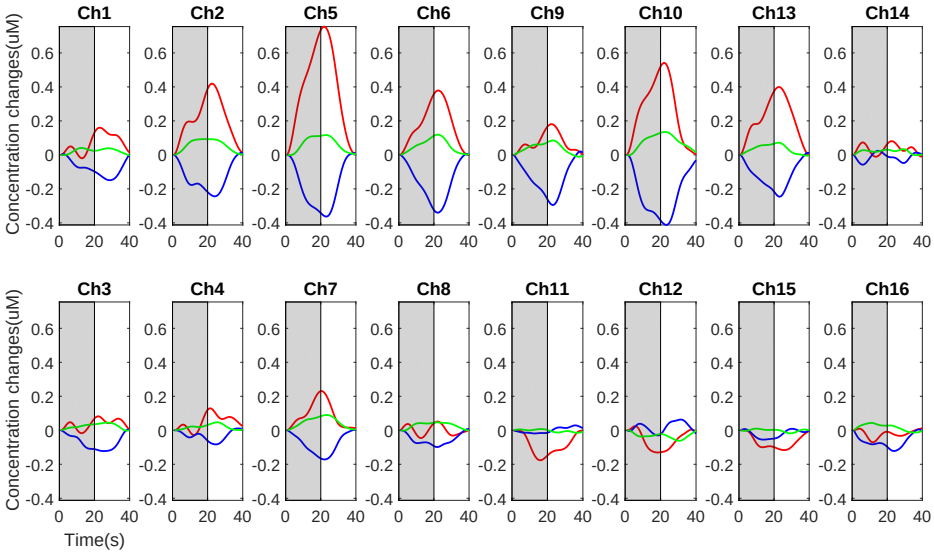

Figure 5.29: Block averaged concentration changes of $\Delta[HbO_2]$, $\Delta[HHb]$ and $\Delta[oxCCO]$ during visual functional activation in subject 2.

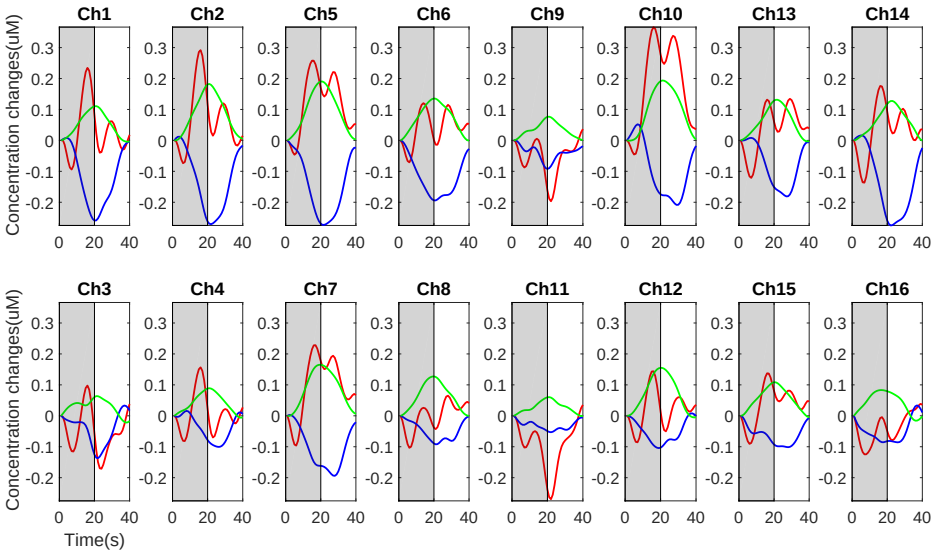

Figure 5.30: Block averaged concentration changes of $\Delta[HbO_2]$, $\Delta[HHb]$ and $\Delta[oxCCO]$ during visual functional activation in subject 3.

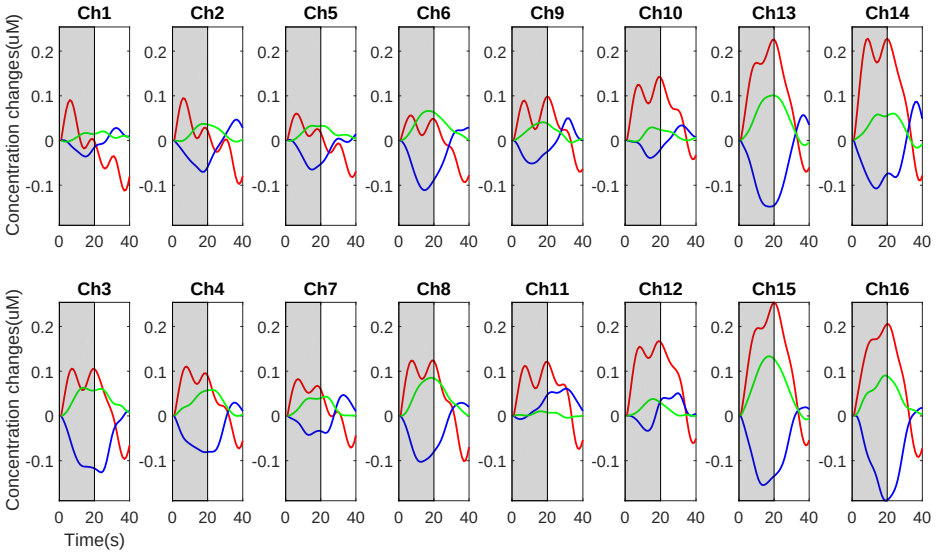

Figure 5.31: Block averaged concentration changes of $\Delta[HbO_2]$, $\Delta[HHb]$ and $\Delta[oxCCO]$ during visual functional activation in subject 4.

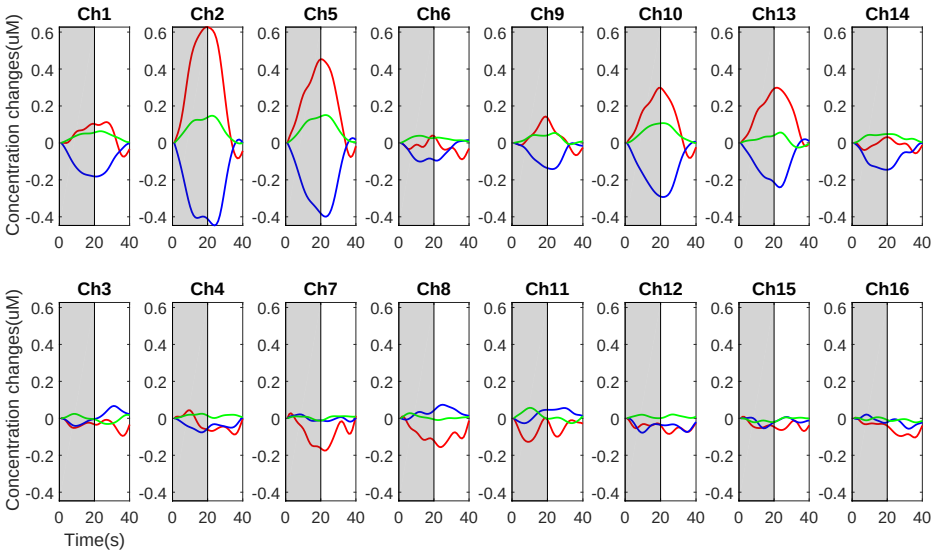

Figure 5.32: Block averaged concentration changes of $\Delta[HbO_2]$, $\Delta[HHb]$ and $\Delta[oxCCO]$ during visual functional activation in subject 5.

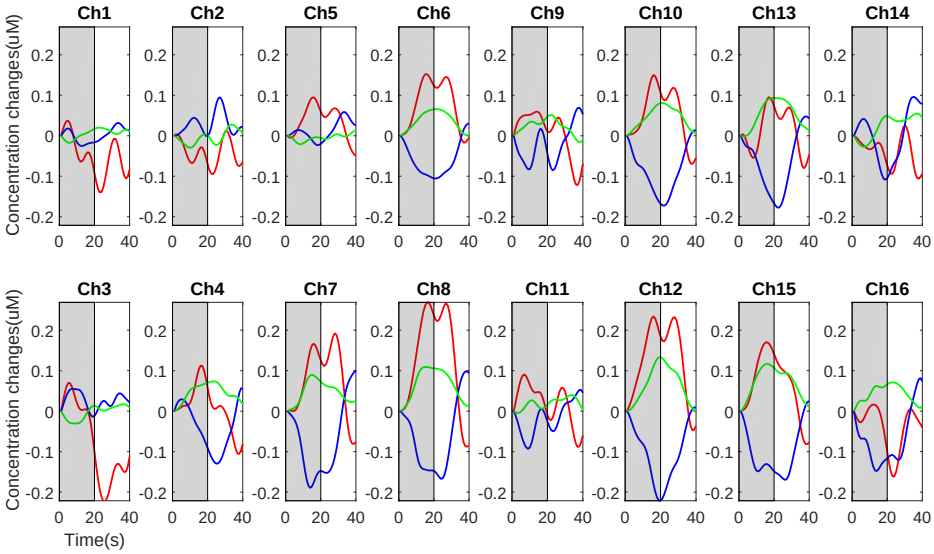

Figure 5.33: Block averaged concentration changes of $\Delta[HbO_2]$, $\Delta[HHb]$ and $\Delta[oxCCO]$ during visual functional activation in subject 6.

Figure 5.34 shows the group-averaged concentration changes across six subjects. There was a significant increase in the $\Delta[HbO_2]$, decrease in $\Delta[HHb]$ and increase in $\Delta[oxCCO]$ during the activation period in comparison to the baseline period.

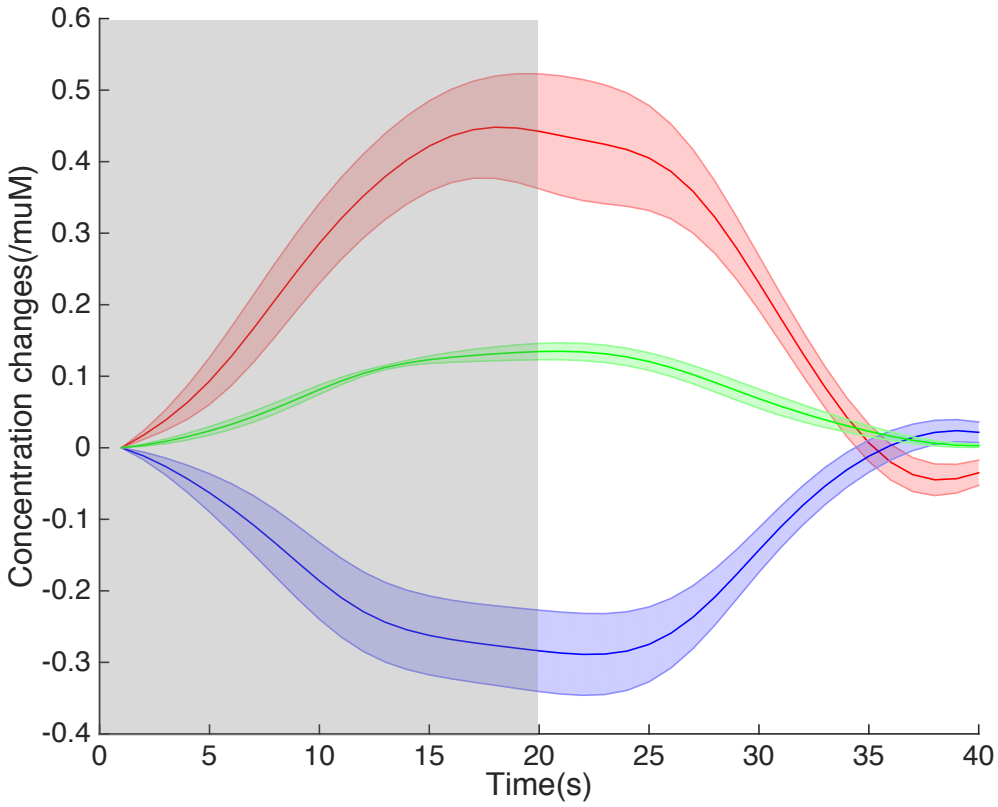

Figure 5.34: Group averaged concentration changes of HbO_2 (red), HHb (blue) and oxCCO (green) and standard error of means across six subjects following visual functional activation. The visual stimulation period is shown as the shaded grey window.

5.6.3 Conclusion and discussion

In this study, we have demonstrated the capability of the multi-channel, multi-distance broadband NIRS system to monitor the concentration change of oxCCO simultaneously across multiple regions in the healthy adult human brain during a functional visual activation task. This study provides evidence that the system developed during the course of this PhD has the capability to resolve changes in Δ[oxCCO] alongside traditional NIRS parameters of haemodynamics (Δ[HbO_2] and Δ[HHb]).

In the previous visual functional experiment presented in chapter 4, the multi-channel NIRS measurements were not acquired simultaneously. They required the physical movement of source and detector fibres to cover a large enough area of the visual cortex. These issues made the measurements not truly simultaneous and presented technical and practical difficulties in collecting data from a larger pool of subjects. With the developments presented in this chapter, multi-channel measurements of Δ[oxCCO] can be

collected simultaneously across multiple regions of the adult human brain without the need for physically moving source and detector fibres, thus reducing the data acquisition time from two hours to twenty minutes and opening up opportunities for the investigation of the spatial variation in the changes of metabolism in the adult human brain in a variety of scenarios.

5.7 Prefrontal Activation

To test the capability of the system to measure more than one region of the brain, the system was used to monitor functional activation over the prefrontal cortex. This was important for future clinical studies investigating changes in the brain of patients with brain injury because the frontal region is the one of the few regions in the head of brain injured patients that NIRS can be used to monitor changes.

5.7.1 Methods

The interface between the optical fibres of the system and the subject was provided by the frontal probe holder, the design of which has been described previously in this chapter. Figure 5.35 demonstrates the interface between the system and the subject (a,b), the working of the time-multiplexed source fibres (c) and the fixation of the optical fibres onto the forehead using double-sided medical tape and a Velcro headband.

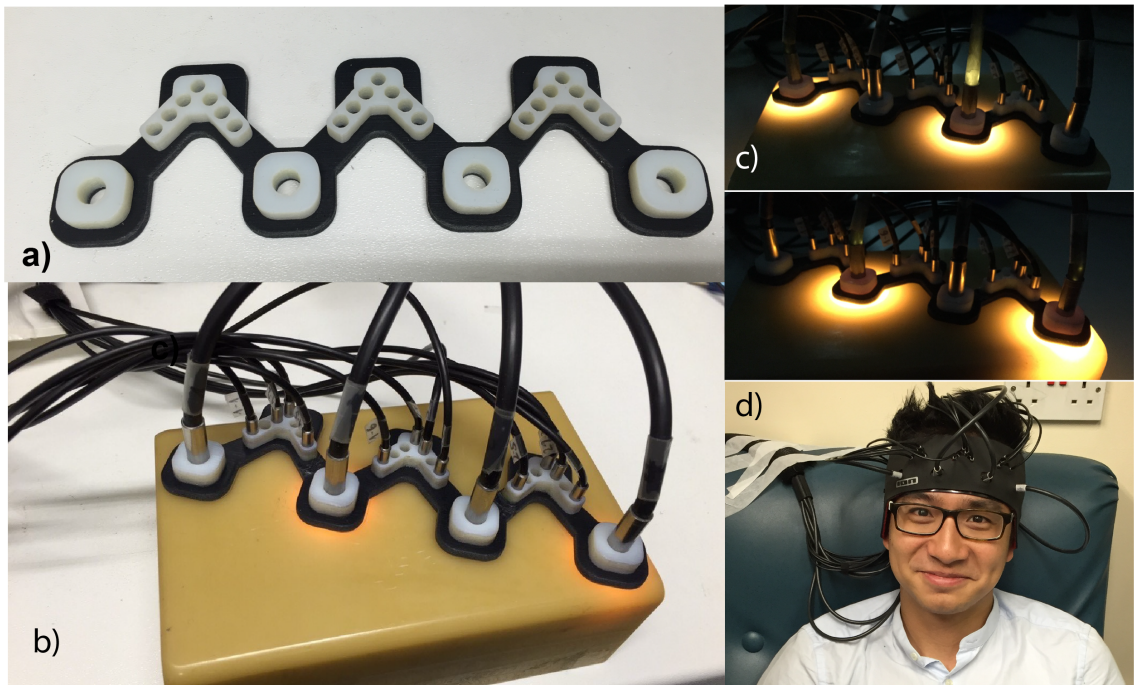

Figure 5.35: The interface between the system and the subject. a) The 3D printed probe holder used for frontal functional activation experiment. b) Four source fibre and 12 detector fibre bundles fixed on the probe holder on a solid phantom. c) Illustration showing one complete acquisition cycle during which each of the two pairs of the source fibre bundles delivers light one after the other. d) the probe holder with fibre bundles is fixed on a subject forehead using a headband.

For prefrontal cortex monitoring, all four source fibres and 12 detector fibres were placed in the probe holder as shown in Figure 5.36a, so that two 0.6 mm diameter detector fibre bundles occupy location 1 and 12 and the other locations were filled with 1.5 mm diameter detector fibre bundles. Detector fibre bundles from location 1 to 6 were from one common bundle connected to the first spectrograph, and detector fibre bundles from location 7 to 12 were from the other common bundle connected to the second spectrograph. The source-detector separations of the 24 measurement channels set out by this arrangement of optical fibres range from 20 mm to 35 mm. During operation, source fibre bundles were fixed in the holder such that the two source fibre bundles that were operating simultaneously had a separation of 90 mm as demonstrated in Figure 5.36c, ensuring that detector fibre bundles only received light from one source fibre bundle at a time. Figure 5.36b shows measurement channels that were acquired when the paired sources are on and Figure 5.36c shows the spatial locations of all 24 possible measurement channels. Figure 5.36d shows the locations of detector fibre bundles that were used for the calculation of TOI. Overall, the system with this fibre arrangement has the capacity to acquire data from 24 NIRS measurement channels using the method of differential spectroscopy to calculate the $\Delta[HbO_2]$, Δ[HHb] and Δ[oxCCO] and from six

TOI channels using the method of spatially resolved spectroscopy from multiple regions of the prefrontal cortex.

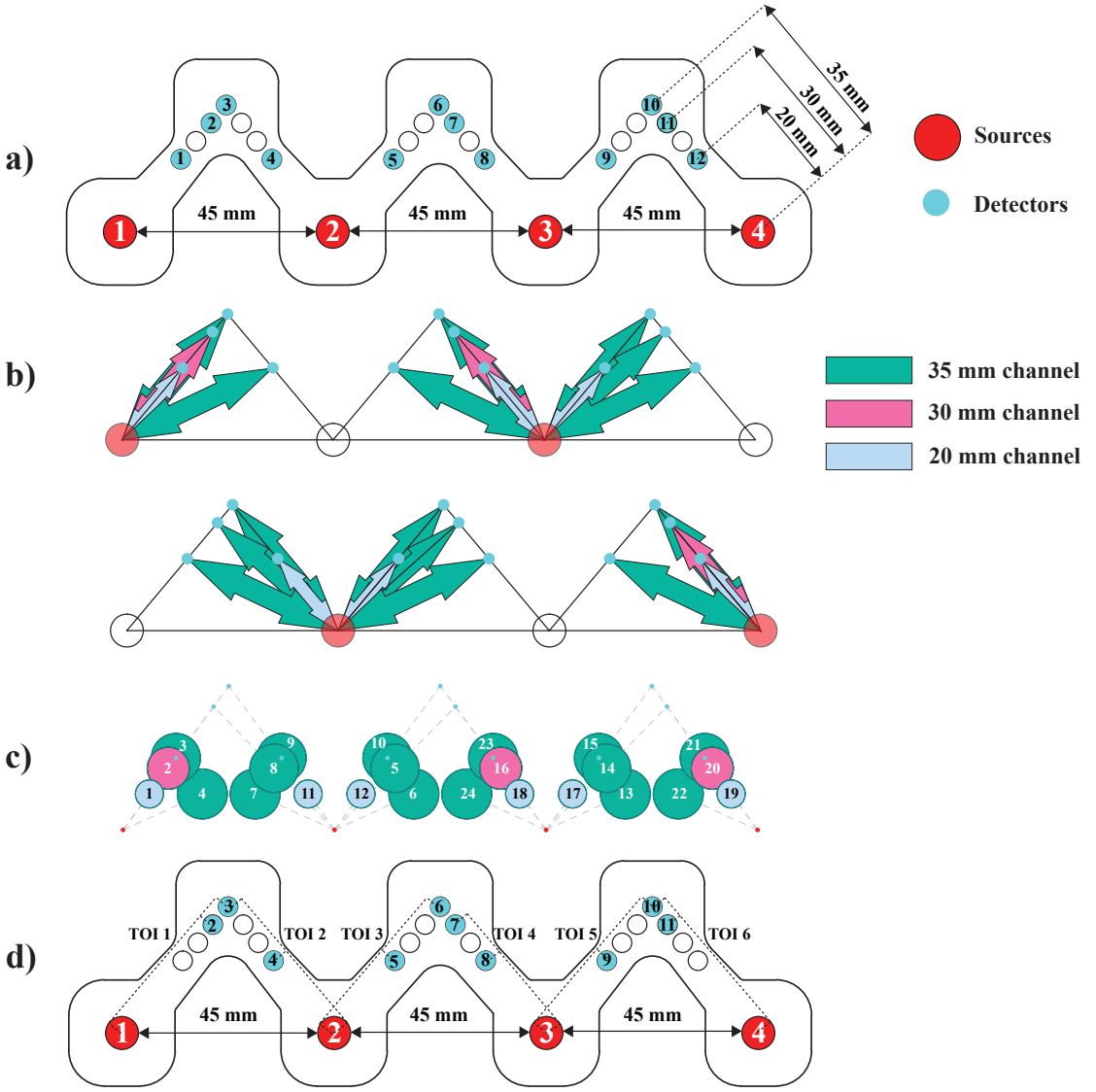

Figure 5.36: a) Probe design showing the locations of four source fibre bundles numbered from 1 to 4 (red circles) and 12 detector fibre bundles numbered from 1 to 12 (cyan circles). The distance between neighbour source bundles is 45 mm and the SDS ranges from 20 mm to 35 mm. b) Measurement channels acquired when alternate paired source bundles are on. Red circles indicate the locations of the working source bundles and cyan circles indicate the locations of the detector fibre bundles. Dark green, magenta and light blue arrows indicate channels with SDS of 35 mm, 30 mm and 20 mm respectively. c) The spatial distribution of all 24 measurement channels. Colour coding for SDS is similar to b. Circle size is proportional to SDS. d) Detector bundles used for each TOI calculation. TOI 1 uses detector bundles 2 and 3, TOI 2 uses detector bundles 3 and 4, TOI 3 uses detector bundles 5 and 6, TOI 4 uses detector bundles 7 and 8. TOI 5 uses detector bundles 9 and 10 and TOI 6 uses detector bundles 10 and 11.

Following ethics approval and volunteer consent, nine healthy adult volunteers were studied with the probe holder positioned across the mid line of the forehead such that source locations 2 and 3 were located at Fp2 and Fp1 according to 10/20 EEG elec-

trode placing system. Prefrontal lobe activation was achieved using a modified version of the Stroop task. The subject was presented with a series of coloured words written in coloured ink and asked to name the colour of the individual word while ignoring its meaning. There were four options for words (RED, GREEN, BLUE AND MAGENTA) and four options for colours (red, green, blue and magenta). A random combination of one of these four words painted in one of the four colours was presented to the subject one after another during the stimulation period. The subject responded by pressing one of the keys R, G, B and M in response to the colour of the presented word. An example of the task is shown in Figure 5.37 and the subject should press G to respond to this example. The block design consisted of 10 epochs, each with a 30 s black screen followed by 60s Stroop task and then a 30 s black screen. Total acquisition time was 1200 s.

Figure 5.37: An example of one of the combinations presented in the Stroop task. In this case, the subject should press G as the answer.

The system collected the intensity spectra from 12 detector fibre bundles while the light source fibres were illuminated alternately. Time-series concentration changes of HbO_2, HHb and oxCCO were calculated using the algorithm described earlier. The concentration changes were filtered using a fifth order Butterworth low-pass filter with cut-off frequency of 0.08 Hz, linearly detrended and resampled to 1 Hz. For each subject, concentration changes were block-averaged according to stimulation epoch to produce three 120 s traces for each of the 24 measurement channels. The mean concentration changes in individual channels were then averaged across nine subjects to produce the grand average activation response across the frontal lobe for the Stroop task. In this study, cortical activation was defined by an increase in $\Delta[HbO_2]$, a decrease in Δ[HHb] and an increase in Δ[oxCCO]. To identify channels with significant changes in response to the functional stimulation, the response of each channel for each subject was defined as the difference between the mean of the first 10 s window of activation and the mean of the first 10 s window during the black screen period. Paired t-tests were used to compare

the responses of each channel across nine subjects to zero (i.e no response). $p < 0.05$ was considered statistically significant.

TOI values were calculated as described earlier for six sites of measurements indicated in Figure 5.35d. Using the slope of the attenuation between the closest detector (20 mm SDS) and the furthest detector (35 mm SDS) for sites 2, 3, 5, between the 30 mm and the 35 mm detectors for sites 1 and 6 and between the 20 mm and the 30 mm detectors for site 4, scaled absorption coefficients (kμa) were calculated and then used to estimate the scaled absolute concentration of HbO_2 and HHb (k[HbO_2 and k[HHb]) for each site. These values were then used to calculate TOI for different sites. To investigate the spatial variation in TOI in different regions, mean TOI was calculated by taking the average of TOI values across the whole experiment period for each of the six sites.

5.7.2 Results

5.7.2.1 Differential spectroscopic results

Figure 5.38 shows the concentration changes of three NIRS chromophores from an example channel in a subject during the Stroop paradigm. The Stroop task periods are indicated by the grey areas. Repeatable changes in concentration of three chromophores (an increase in Δ[HbO_2], a decrease in Δ[HHb] and an increase in Δ[oxCCO]) were observed. However, the increase in the haemodynamic signals seems to precede the actual stimulation. This may be caused by the expectation of the subject to the task.

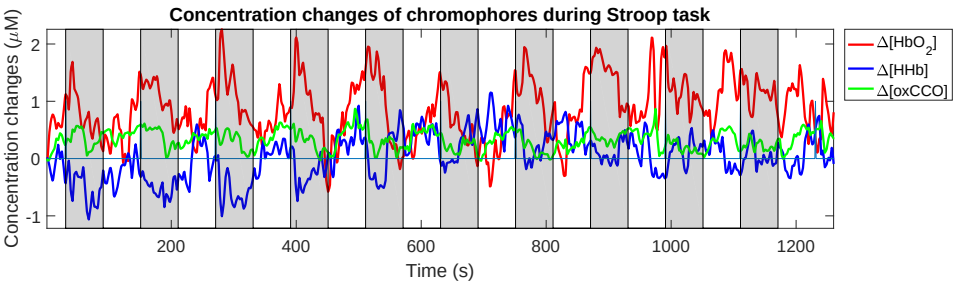

Figure 5.38: Concentration changes from an example channel during the Stroop task.

Figure 5.39a shows the intensity spectra at the baseline and at the peak changes of concentration and Figure 5.39b shows the measured delta attenuation and the fitted delta attenuation using the three component fitting procedure.

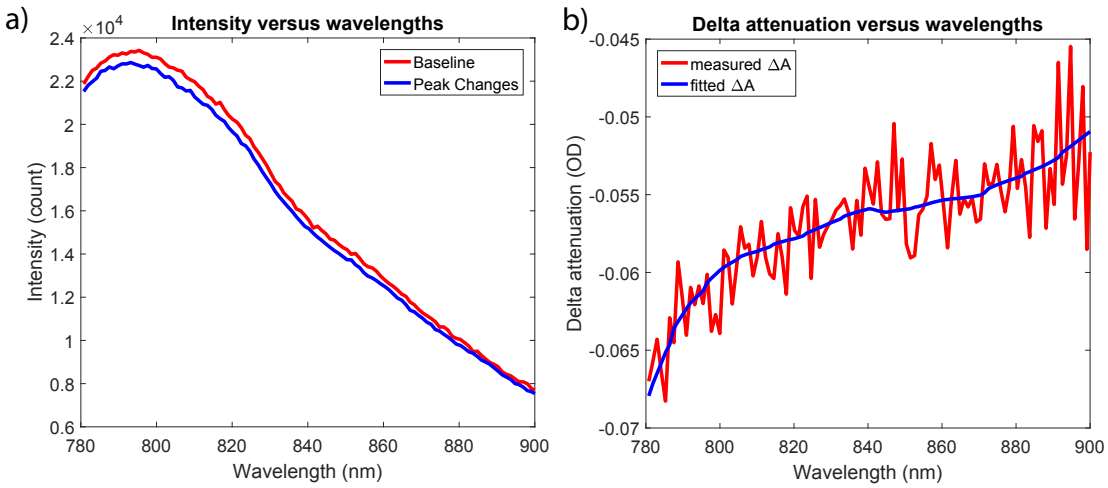

Figure 5.39: a)The measured intensity at baseline and at the peak of concentration changes. b) The measured and the fitted ΔA at peak changes.

Channels 1, 4, 19, 22 and 24 were excluded from further analysis due to low intensity. Figure 5.40a presents the positions of 19 channels on the forehead. Figure 5.40b presents the grand averaged concentration changes and the standard error of mean of the three chromophores during the Stroop task across nine subjects with different SDS indicated by the borders of the plots. The concentration change of oxCCO was multiplied by 10 for ease of visualisation. There was a spatial variation of the oxCCO response to frontal lobe activation among channels with 35 mm SDS induced by the Stroop task with maximum changes in Δ[oxCCO] varying from +0.015 μM (channel 21) to +0.073 μM (channel 23) in the presence of haemodynamic changes correlating to functional activation (increase in Δ[HbO_2], decrease in Δ[HHb]). Figure 5.40c presents locations of the channels with significant response in Δ[HbO_2], Δ[HHb] and Δ[oxCCO]. Out of 12 channels with SDS of 35 mm, 11 channels (92%) showed significant increase in Δ[HbO_2]; nine channels (75%) showed a significant decrease in Δ[HHb] and five channels (42%) showed a significant increase in Δ[oxCCO]. A significant change in Δ[oxCCO] was only present in channels where there were significant changes in both Δ[HbO_2] and Δ[HHb]. A significant change in Δ[oxCCO] was not present in 30 mm or 20 mm SDS channels. However, significant changes in Δ[HbO_2] were present in the 30 mm SDS (two out of three channels) and in 20 mm SDS (three out of four channels). Table 5.1 presents the mean response across nine subjects for Δ[HbO_2], Δ[HHb] and Δ[oxCCO] and the corresponding p value in channels with significant Δ[oxCCO] change as indicated in Figure 5.40c.

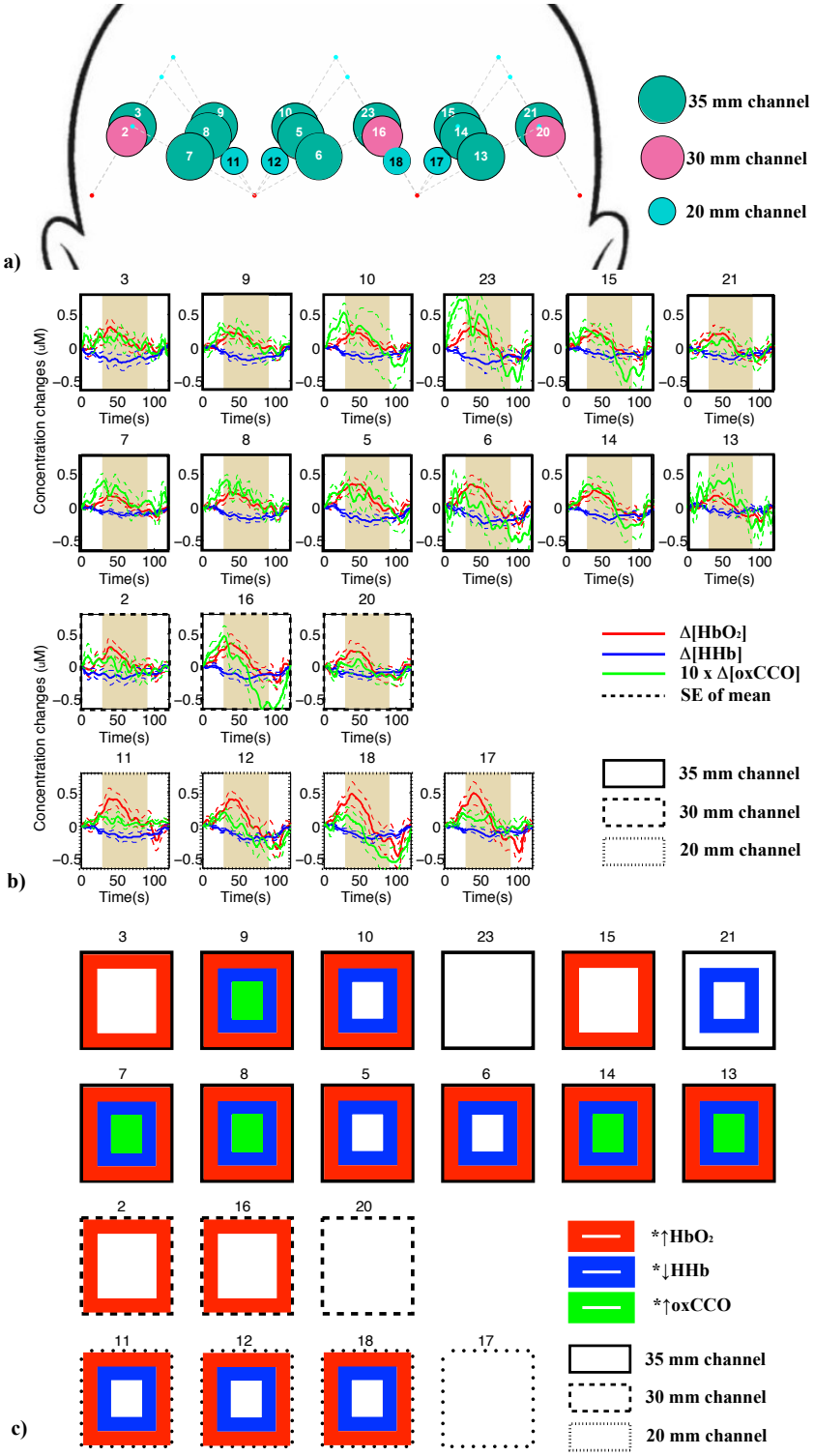

Figure 5.40: Summary result for prefrontal cortex functional activation study. a)Locations of 19 channels on the head. b) Grand averaged concentration changes across nine subjects. c) Locations of channels with significant response in$\Delta[HbO_2]$, Δ[HHb] and Δ[oxCCO].

Table 5.1: The mean response in μM (Resp.) across nine subjects for each chromophore and the corresponding p value in channels with significant oxCCO changes.

	Ch.7		Ch.8		Ch.9		Ch.13		Ch.14	
	Resp.	p	Resp.	p	Resp.	p	Resp.	p	Resp.	p
HbO_2	0.135	0.026	0.176	0.018	0.185	0.022	0.163	0.033	0.193	0.026
HHb	-0.059	0.007	-0.116	0.005	-0.110	0.014	-0.060	0.032	-0.093	0.020
oxCCO	0.024	0.005	0.033	0.009	0.024	0.036	0.028	0.027	0.029	0.035

5.7.2.2 The variation of TOI

There was no observable TOI response during functional activation. Table 5.2 presents the mean TOI values during the experiment across six sites of measurement on the frontal lobe of each individual subject and the mean, standard deviation (SD), maximum and minimum values of TOI across nine subjects.

Table 5.2: TOI (%) across 6 measurement sites of nine subjects

Sub.	**Site 1**	**Site 2**	**Site 3**	**Site 4**	**Site 5**	**Site 6**	**Mean**	**SD**
1	79	73	74	77	80	73	76	3
2	81	73	70	72	76	N/A	74	4
3	65	69	67	69	70	66	68	2
4	89	74	73	78	80	87	80	6
5	66	70	70	73	73	69	70	2
6	78	74	75	73	77	76	76	2
7	81	73	76	82	76	83	78	4
8	61	69	69	71	72	75	69	4
9	79	76	78	77	79	73	77	2
Mean	76	72	72	75	76	75		
SD	9	2	4	4	4	6		
Min	61	69	67	69	70	66		
Max	89	76	78	82	80	87		

5.7.3 Conclusion and discussion

We have demonstrated the use of the multi-channel broadband NIRS system in monitoring the changes of HbO_2, HHb, oxCCO and TOI across multiple locations of the frontal region of healthy adult volunteers during a prefrontal cortex functional activation task. The group average results confirmed that changes of $\Delta[HbO_2]$ and Δ[HHb] were consistent with typical functional activation with an increase in $\Delta[HbO_2]$ and a decrease in Δ[HHb] during the stimulation period. However, the changes started slightly before the stimulation, peaked and declined rapidly during the stimulation period. These results agreed with the results of our previous Stroop task study using another fNIRS system (Oxymon Mk III, Artinis Medical System, the Netherlands). The early changes may be explained by the changes in CBF caused by the expectation of the subject due to the nature of the block design study on the frontal lobe.

The maximum and minimum TOI values for six sites were within the range from 61% to 89 %. This ranges of TOI values are within reasonable physiological range. Given that the measurement of TOI is a challenging one to collect and there is no gold standard to compare it to, it is encouraging that the system was able to collect TOI values across multiple sites. In our study, there were a small variation in TOI values across different sites within the same subject and a small variation of TOI values within the same site across different subjects. TOI does not have sufficient signal to noise ratio to detect changes in oxygenation during functional activation; however, it may be used to assess the variation in oxygenation in clinical scenarios where there is large changes in oxygenation.

Significant changes in haemoglobin signals were seen in both channels with short SDS (20 mm) and with long SDS (35 mm) while significant changes in Δ[oxCCO] were seen in only five channels with long SDS (35 mm) where there were concurrent significant change in both $\Delta[HbO_2]$ and Δ[HHb]. This may be due to the fact that changes in the haemoglobin signals are easily contaminated by the changes in extracerebral circulation caused by systemic changes and anxiety level [118], [119]. This is one of the rationales to investigate the possibility of using the oxCCO signal for functional brain imaging to identify the specific location of the functional activation as the oxCCO signal is less susceptible to changes in systemic variables and more brain specific [12].

The Stroop task is known to activate bilateral dorsolateral prefrontal cortex (DLPFC) [120], [121]. As we have explicitly stated, we identified functional activation as a significant increase in $\Delta[HbO_2]$, a significant decrease in Δ[HHb] and a significant increase in Δ[oxCCO]. With our array positioned on the prefrontal cortex where source locations 2 and 3 were positioned at Fp2 and Fp1 of the 10/20 EEG electrode placement system, our results identified bilateral activation of the DLPFC. Using the oxCCO signal in addition to the traditional haemoglobin signals, we could identify a more localised activation area in response to the Stroop task. The increase in oxygen consumption is previously suggested to be more localised than the increase in blood flow [122] and our data might suggest that. Larger studies are required to differentiate regional variation in the magnitude of the oxCCO and confirm the findings.

To our knowledge, this is the first study demonstrating the difference in the oxCCO response to functional activation across multiple areas of the frontal cortex that are distinct from the haemoglobin responses. Using the multi-channel broadband NIRS system described in this chapter, multi-channel measurements of changes in haemodynamics and metabolism as well as tissue oxygen saturation can be acquired simultaneously.

5.8 Conclusion and discussion

In this chapter, we have described the development of the pseudo DOT system into a multi-channel, multi-distance broadband NIRS system with changes introduced to the hardware, the software and the resolving algorithm. The new system has the capability to monitor changes in the visual and prefrontal cortices with two different types of probe holder and headgear. The system can collect data from 16 NIRS measurement channels monitoring the visual cortex or 24 NIRS measurement channels monitoring the prefrontal cortex. Moreover, the system also has the capability to monitor TOI changes for six regions of the prefrontal cortex. This system is among the first of its kind to have the capability of monitoring changes in Δ[oxCCO] across multiple regions of the adult head.

Most commercial CW-NIRS devices rely on the dual wavelength approach, limiting their capability to the measurement of concentration changes of HbO_2 and HHb [3]. Under the assumption of intact neurovascular coupling, these measurements are an indirect measure of brain activity. However, issues have been raised about the possibility of inadvertently measuring fNIRS haemodynamic responses that are not the result of neurovascular coupling and these can be misinterpreted as brain activity (false positives) or masked brain activity (false negatives). These issues are caused by changes in systemic variables such as heart rate, blood pressure, CO_2 concentration in the blood etc. which can lead to non-neuronal driven changes in haemodynamics and oxygenation in the cerebral and extracerebral compartments. The measurement of Δ[oxCCO], a biomarker of cellular oxygen metabolism, with its brain specificity characteristic [12] may overcome these issues. Moreover, in cases of brain pathology, the assumption of intact neurovascular coupling in the measurement of the haemoglobin signals is usually violated. In these scenarios, an additional colocalised measure of cerebral oxygen metabolism can help elucidate the changes caused by the pathology. In the specific case of acute brain injury, where cerebral energy failure usually occurs, a method for monitoring cerebral energy metabolism may provide useful insight into the injury pathway. However, most NIRS instruments that have the capability to measure Δ[oxCCO] only have a limited number of channels, limiting the measurement to a small area of the cortex, which poses the difficulty of finding the 'right' location to place the probes. Therefore, there is a clinical need for a NIRS system that can monitor changes in Δ[oxCCO] together with $\Delta[HbO_2]$ and Δ[HHb] from several regions of the brain simultaneously. The multi-channel, multi-distance broadband NIRS system developed as part of this PhD provides that much-needed capability.

The development of the multi-channel broadband NIRS system has resulted in several

advancements in the field of NIRS. First and foremost, for the first time, a system with the capability of monitoring Δ[oxCCO] across multiple regions of the brain is developed. As a result of that development, spatially dependent changes in Δ[oxCCO] induced by functional activation tasks could be investigated and characterised in the adult human brain. Having characterised the response of the signal in the healthy adult brain during functional activation task, the next step was to demonstrate the use of the system in the clinical setting of a neurointensive care unit to monitor brain injured patients. This transitional step of bringing the technology developed in a lab environment to a clinical environment is challenging but it is an important step to prove the clinical usefulness of the new instrument. The next chapter will describe several case studies where the instrument was used to investigate the changes of Δ[oxCCO] together with Δ[HbO_2] and Δ[HHb] in the injured brain.

Chapter 6

Monitoring patients with acute brain injury with the multi-channel, multi-distance broadband NIRS system

The capability of the multi-channel, multi-distance broadband NIRS system to monitor changes in cerebral haemodynamics and metabolism in multiple brain regions has been demonstrated in the previous two chapters through the use of functional activation paradigms in the healthy brain. Moving away from the healthy brain, this chapter will describe the use of the system to monitor regional variations in the injured brain. The overall aim of this chapter is to demonstrate the increased capability of the system to contribute to our understanding of the pathophysiology of brain injury. This chapter begins with a brief overview of brain injury and the rationale of monitoring regional variations in cerebral haemodynamics and metabolism before outlining the clinical study to demonstrate the capability of the multi-channel broadband system in monitoring patients with brain injury.

6.1 Introduction

As discussed in chapter 2, the normal brain has several mechanisms to ensure that oxygen and substrates supply meet metabolic demand. Two of the most important mechanisms are cerebral pressure autoregulation and flow metabolism coupling. These mech-

anisms ensure that in the normal healthy brain, there is a balance between oxygen supply and demand. This balance is usually disturbed in brain injury, resulting in cerebral hypoxia/ischemia, a common injury pathway of different types of brain injury that is associated to poor outcome [18]. It is not within the scope of this thesis to discuss the detailed pathophysiology of brain injury; however, it is important to highlight some key aspects of it so as to put the role of cerebral monitoring into perspective.

Brain injury can be traditionally classified into two processes: primary and secondary injuries. Primary injury occurs at the moment of impact for traumatic injury or at the moment of ischaemic/haemorrhagic events for acute injury. Cerebral disturbances from the primary injury can prolong hours after the injury. Primary injury is believed to be irreversible and changes introduced to the anatomy and physiology of the brain as a result of the primary injury lead to secondary damage. The processes involved in secondary damage is still under active investigation. However, several processes have been identified to play key roles and these are characterised by disturbances in the neuronal ionic exchange processes and by metabolic and inflammatory changes. These processes result in cerebral ischemia/hypoxia and the failure of the neuronal cell to maintain its cross membrane ionic gradient and eventually cell death. Cell death in a limited region of the brain may create a more widespread state of metabolic dysfunction in other remote areas characterised by depressed aerobic metabolism and metabolic crisis even in the absence of ischemia. However, it is widely believed that processes that lead to secondary injury may be prevented or minimised given the correct physiological environment that optimises cerebral perfusion to maintain the balance between oxygen supply and demand.

Although the pathophysiology of brain injury is complex and different for different types of injury, two components have been identified as of significant importance: failure of substrate delivery below critical thresholds and failure of mitochondrial substrate utilization leading to cerebral cellular energy failure. The latter has been characterised by a histochemistry study demonstrating a diffuse decrease in the level of CCO activity in rats with lateral fluid percussion injury - a commonly used experimental model of traumatic brain injury [123]. More importantly, this failure of energy metabolism may occur without cerebral ischemia and has regional variation. It was reported in a combined microdialysis and PET study that metabolic crisis without ischaemia was a common finding [19], [124]. It was evident in cats with fluid percussion injury that derangement in brain energy metabolism in the absence of substrate limitations could occur and it had regional heterogeneity [125]. These studies highlight the fact that monitoring cerebral

energy metabolism across multiple regions of the injured brain is crucially important to provide insights into the pathophysiology of brain injury and its analysis may hold the keys to predicting the status of the injury and provide information to assist the modification of systemic physiology to optimise cerebral perfusion to improve clinical outcome.

CCO, as mentioned in chapter 3, is the terminal complex of the ETC and is responsible for more than 95% of cellular oxygen metabolism. Its oxidation status reflects the balance between mitochondrial oxygen supply and demand. The NIRS-derived concentration change of oxidised CCO has been validated in a preclinical study as a measure of change in cerebral energy metabolism [126] and it can offer insight into understanding cerebral energy metabolism in brain injury. The oxCCO signal has been shown to have a significant correlation with cerebral oxygen delivery in the healthy brain [5], [12] and it has also been demonstrated to have a higher specificity to brain tissue than NIRS-derived haemoglobin measures [12]. Moreover, it has been used successfully used to investigate mechanisms of depressed aerobic metabolism in brain injury [6], [127]. These studies highlight the clinical relevance of this biomarker. However, in these studies, due to the limitation of the NIRS instrumentation, only one or two regions of the brain were monitored, neglecting the fact that there is regional heterogeneity in cerebral energy metabolism following brain injury. With the development of the multi-channel broadband NIRS system, we now have the capability to investigate the regional heterogeneity of cerebral energy metabolism following brain injury.

This chapter of the thesis will describe the first attempt to use the multi-channel, multi-distance broadband NIRS system developed as part of this PhD to monitor patients with brain injury to assess regional variation in cerebral energy metabolism and relate it to variation in haemodynamics and non-NIRS neuromonitoring variables.

6.2 Challenges and objectives

This is the first time that a multi-channel, multi-distance broadband NIRS system has been used in the clinical environment to monitor changes in cerebral haemodynamics and metabolism in the frontal region of patients with acute brain injury. There were several challenges to be overcome to enable multi-modal data sets to be acquired from brain injured patients:

- The first challenge was to use the system in the clinical environment without disrupting normal clinical care. The study required monitoring the brain of ABI patients during periods of stability and free from clinical interventions without inter-

ruption for at least 60 minutes in a busy intensive care unit. Moreover, contamination from the changing ambient lighting condition had to be minimised. As a result, studies were done at night after nursing handover to minimise possible disruption and ambient light contamination.

- The other challenge was that the system and its accompanied optical fibres, probe holder have to be designed with the patient in mind. The process of designing took place long before the actual study with testing on phantoms and on healthy volunteers to ensure the safety of the patient and reliability of the data collected. During the actual study, the probe holder and the optical fibres had to be used in conjunction with various probes from other monitoring systems being used to guide clinical care of the patients.

With these challenges in mind, the objectives of this pilot clinical study were:

- To demonstrate the possibility of using the multi-channel, multi-distance broadband NIRS system in a clinical environment along side existing multi-modal monitoring systems.
- To use the oxCCO signal, biomarker for cellular energy metabolism, in combination with other NIRS, non-NIRS and systemic parameters to understand more about regional heterogeneity in cerebral autoregulation in the injured brain.
- To reconstruct tomographic images of Δ[oxCCO] in patients with ABI using the multi-channel broadband data and demonstrate the potential use of these images.

6.3 Methods and Analysis Techniques

Four patients with acute brain injury were studied as part of an ongoing study to investigate metabolic disturbances following brain injury. This study was approved by the Research Ethics Committee of the National Hospital for Neurology and Neurosurgery and the Institute of Neurology. Written consent was obtained from a family representative as all patients were unconscious at the time of the study. All patients were managed using standardised protocol-based therapy specific to their brain injury type.

6.3.1 Systemic and cerebral monitoring

Muti-modal monitoring was recorded during an undisturbed 60-minute of clinical stability while the patients were ventilated, sedated and positioned with 30-degree head

tilt. Cerebral variables included intraparenchymal intracranial pressure (ICP) (Codman microsensor, Johnson & Johnson, USA), transcranial Doppler (TCD) flow velocity flow velocity (FV) of the left and right middle cerebral arteries (Vmca1 and Vmca2) (DWL Doppler Box, Compumedics, Singen Germany) and NIRS parameters. Systemic variables included mean arterial blood pressure (ABP) and arterial partial pressure of carbon dioxide ($PaCO_2$). All physiological data were captured at 125Hz using TrendFace software (ixellence Gmbh, Germany).

NIRS parameters were acquired with the multi-distance, multi-channel broadband NIRS system described earlier in chapter 5 using the frontal probe. This system with the frontal probe allowed 24 NIRS measurement channels using the technique of differential spectroscopy and six TOI measurement channels using the technique of SRS as described earlier in chapter 2. The source detector separations (SDS) for 24 NIRS channels range from 20 to 35 mm. The location of all measurement channels is shown in Figure 6.1. The frontal probe was positioned symmetrically on the forehead using double-sided medical tape to minimise movement artefacts. All optical data were captured using the LabView software that runs the broadband system.

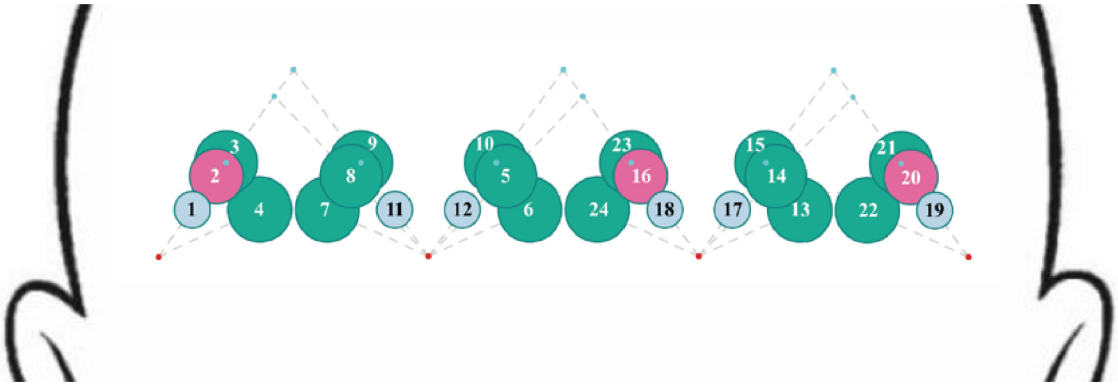

Figure 6.1: Locations of 24 channels on the forehead. Light blue circles indicate the location of channels with SDS of 20 mm, pink circles indicate the location of channels with SDS of 30 mm and green circles indicate the location of channels with SDS of 35 mm.

6.3.2 Data preprocessing and analysis

Concentration changes of HbO_2, HHb and oxCCO were calculated using the UCLn algorithm over the wavelength range of 780 - 900 nm as described in details in chapter 5. The wavelength dependency of DPF was applied to take into account the fact that DPF falls with increasing wavelengths. Six TOI values were derived from six spatially resolved pairs of channels using the SRS principle as described earlier. Systemic and cerebral variables were synchronised using computer time stamps and resampled to 1 Hz through cubic

spline interpolation. The processed multi-distance, multi-channel broadband NIRS data were sent to Dr Brigadoi for image reconstruction.

For each of the patients, the multimodal data set included systemic variables, non-NIRS cerebral parameters, 24 channels of NIRS measurements, six channels of TOI and 3D tomographic images. To analyse and extract useful insights about the pathophysiology of brain injury, multiple analysis techniques were utilised. In this thesis, data analysis began with visualising all the data together to summarise the details for each patient. The analysis was done using NIRS parameters, non-NIRS parameters, systemic variables as well as the reconstructed images to extract potentially useful information to inform about the heterogeneity of the brain injury.

6.3.2.1 Standard autoregulation index analyses

For each patient case, standard autoregulation indices were calculated. Pressure reactivity index (PRx) was derived using the moving Pearson correlation coefficient between ABP and ICP [128] on 10-second time-averaged data points over a 300 s window. Impaired cerebral pressure autoregulation is indicated by a positive PRx value, showing that there is a passive transmission of the slow waves of ABP to ICP. With intact cerebral pressure autoregulation, ICP is inversely correlated with ABP, resulting in a negative PRx value. Clinical studies showed evidence of the association between an abnormally high mean PRx value ($>$0.35) and high mortality rate ($>$50%). PRx values could be used to differentiate patients with a good outcome, moderate disability, severe disability and death [128]. More importantly, PRx could be used to define optimal CPP range for an individual patient [129]. Similar to PRx, the mean velocity index (Mx) was derived using the moving Pearson correlation coefficient between ABP and TCD-FV. However, the difference between PRx and Mx is that Mx assesses the global autoregulatory state while PRx indicates the autoregulatory state of a specific region monitored by the ICP probe.

6.3.2.2 Slow wave analyses

Slow wave oscillations (0.05-0.003 Hz) of cerebral haemodynamics are believed to be the result of myogenic, neurogenic and metabolic regulatory mechanisms on the cerebrovasculature [130]. These oscillations reflect the physiological adaptation of the brain to changes in systemic physiology and metabolic demand. Therefore, the analysis of these oscillations may hold the key to the assessment of the state of cerebral autoregulation in ABI patients. For each patient case, slow wave analysis was conducted using wavelet-based techniques to compare the similarity and the phase difference between

cerebral slow wave oscillations measured by NIRS and non-NIRS neuromonitoring and systemic variables. The wavelet-based analysis technique is an advanced signal processing technique that can offer high time-frequency resolution and is frequently applied to measure the similarity and phase relationship between highly dynamic signals, varying in both the time and frequency domains. This technique is superior to standard signal processing methods in that it does not only provide excellent time and frequency resolution but also does not assume the frequency content of a data set is constant with time and therefore allows changes in frequency to be analysed. In short, continuous wavelet transform with the Morlet-wavelet was applied to each of the two signals of interest using the wavelet scale factor of 150, investigating the frequency between 0.05 and 0.003 Hz. Wavelet coherence [131] and wavelet semblance [132] were calculated to compare the similarity and the phase difference between the two signals of interest. The technique has been previously applied to assess the relationship between ABP and NIRS-derived parameters in brain injury patients [133].

6.3.2.3 NIRS-based autoregulation indices

Systemic variables and non-NIRS parameters can be used to calculate indices to assess cerebral autoregulation. However, the calculation of these indices requires invasive monitoring (for the case of ICP) or technically challenging method and not suitable for long-term monitoring (for the case of TCD). NIRS with its non-invasive nature and its ease of use may provide another tool to monitor the injured brain. Moreover, for the first time, using the multi-channel broadband NIRS, measures of haemodynamics and metabolism can be derived regionally over multiple regions. These regional NIRS parameters can be correlated with systemic variables to derive NIRS-based autoregulation indices that can be used to assess the autoregulation status of multiple regions of the injured brain simultaneously.

6.3.2.4 Image reconstruction and calculation of indices in the image space

A 1000 s period of non-contaminated data was chosen for image reconstruction. The multi-channel attenuation data was extracted and sent to Dr Brigadoi to run through the image reconstruction algorithm developed specifically for oxCCO [110]. This algorithm uses the multi-channel, multi-distance broadband NIRS data sets to reconstruct images of $\Delta[HbO_2]$, Δ[HHb] and Δ[oxCCO] every 10 s using the multi-spectral approach as discussed early in chapter 3. All the images were used to make an animated video showing the changes for each patient. The video was sped up 10 times for visualisation.

Individual points in the images of [HbO_2], [HHb] and [oxCCO] were correlated with ABP using a moving Pearson correlation coefficient with a window length of 30 data points to derive NIRS-based cerebrovascular and cerebrometabolic reactivity indices in the image space.

6.4 Results

This section presents the results of the pilot clinical study. Due to time limitation, only four patients with different types of brain injury were studied. This makes it inappropriate to formulate group observation and analysis. Therefore, the analysis was done on the individual level and the results are presented as patient case studies. The summary of all the findings for all four patients is presented in Table 6.1. This table provides the complete overview of the results for each patient including details of the brain injury, the details of non-NIRS monitoring and NIRS monitoring, the results of standard autoregulation index calculation, the results of the wavelet-based analysis and the details of the reconstructed tomographic images. Figures 6.2, 6.3, 6.4, 6.5 provides the summary of the multi-modal data set collected for each of the four patients which provides the basis for all the data analysis.

6.4.1 Summary results for all four patient cases

Table 6.1: The complete overview of the results for all four patients

		patient 1 (age 70, GCS:11, GOS:2)	patient 2 (age 40, GCS:14, GOS:4)	patient 3 (age 58, GCS:10, GOS:2)	patient 4 (age 44, GCS:4, GOS:0)
	Injury type	post-operative right frontal intraparenchymal haemorrhage	subarachnoid haemorrhage	intraventricular haemorrhage	left basal ganglia bleed intraparenchymal haemorrhage
Monitoring	Non-NIRS	ABP, ICP, VmCa	ABP, ICP, VmCa	ABP, VmCa	ABP, ICP, VmCa
	NIRS	multi-channel broadband	multi-channel broadband	multi-channel broadband	multi-channel broadband
Results	PRx	0.37	0.18	N/A	0.15
	Mx1	0.51	0.09	0.09	0.32
	Mx2	0.34	0.28	-0.07	0.38
	ABP & ICP semblance	presence of in-phase relationship	intermittent periods of in-phase and anti-phase relationship	N/A	intermittent periods of in-phase and anti-phase relationship
	Presence or absence of slow wave oscillations	slow waves present in NIRS and non-NIRS variables in frequency range 0.01 - 0.02Hz	slow waves present in NIRS and non-NIRS variables in frequency range 0.01 - 0.02 Hz	absence of slow waves in frequency range 0.01 - 0.02 Hz	absence of slow waves in frequency range 0.01 - 0.02 Hz
	NIRS & non-NIRS variables correlation	spatially varied coherence and semblance between ABP and NIRS parameters	spatially varied coherence and semblance between ABP and NIRS parameters	spatially varied coherence and semblance between ABP and NIRS parameters	spatially varied coherence and semblance between ABP and NIRS parameters
	TOI & VmCa comparison	slow waves present in TOI that correlate with that in Vmca	slow waves present in TOI that correlate with that in Vmca	No slow wave present in TOI	No slow wave present in TOI
	Tomographic Images	localised increase in Δ[oxCCO] in the left hemisphere; localised decrease in Δ[HHb] in the left hemisphere; distributed localised response in $\Delta[HbO_2]$	localised decrease in Δ[oxCCO] in left hemisphere; localised decrease in Δ[HHb] in the right hemisphere; distributed localised response in $\Delta[HbO_2]$	localised decrease in Δ[oxCCO] in both hemispheres; localised decrease in Δ[HHb] in the left hemisphere; distributed response in $\Delta[HbO_2]$	localised increase in Δ[oxCCO] in the left hemisphere; distributed localised response of Δ[HHb] and $\Delta[HbO_2]$

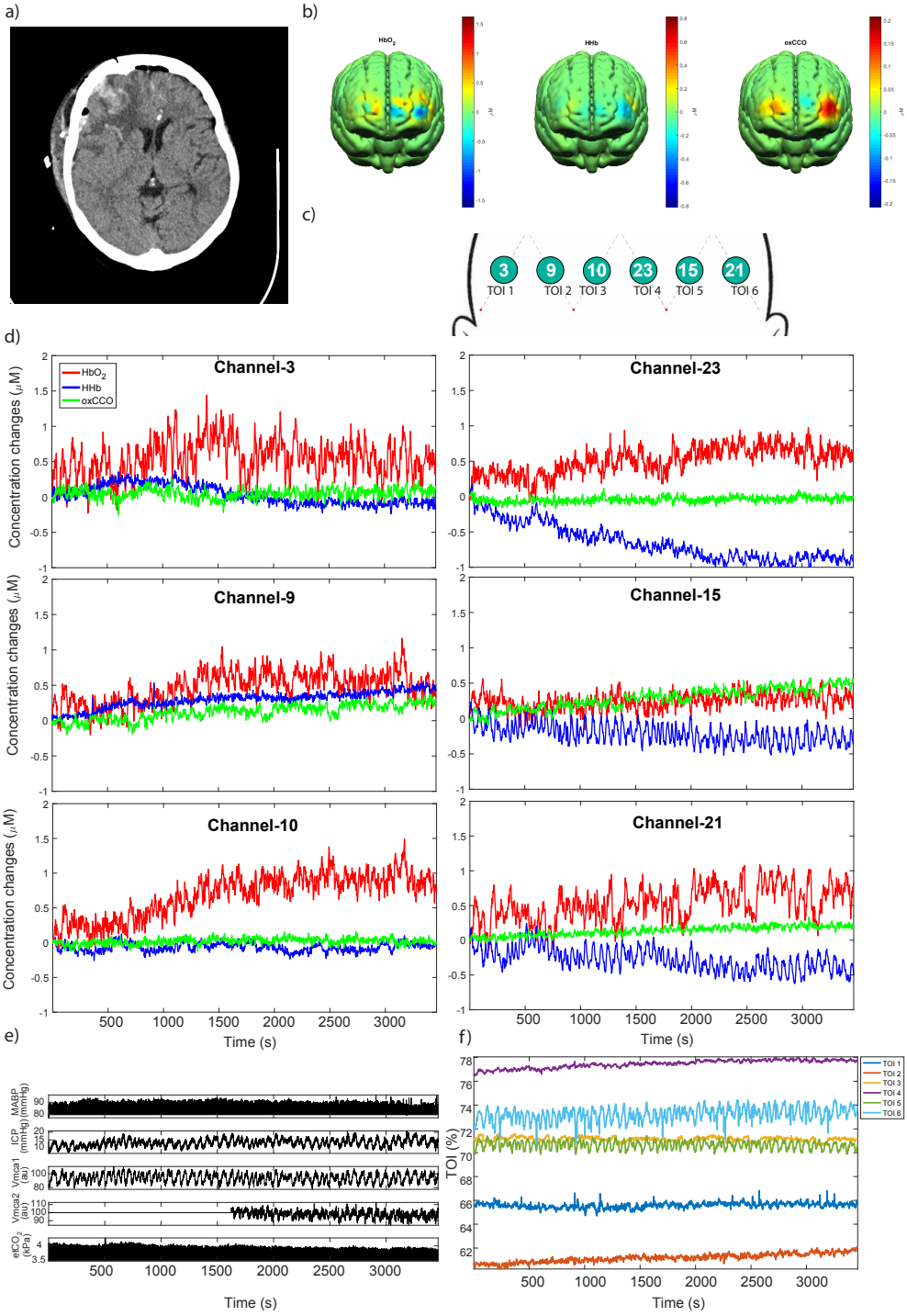

Figure 6.2: Summary of data from patient 1 having a post-operative right frontal intraparenchymal haemorrhage. a) CT scan showing the location of the injury. b) Averaged reconstructed images of $\Delta[HbO_2]$, Δ[HHb] and Δ[oxCCO] over a period of 1000 s of clinical stability showing regional variation in cerebral haemodynamics and metabolism. c) The locations of six 35 mm NIRS measurement channels (in green circles) and six TOI channels across the forehead of the patient. d)$\Delta[HbO_2]$, Δ[HHb] and Δ[oxCCO] in six NIRS channels. Clear spontaneous slow wave oscillations are evident in NIRS parameters in channels 15 and 21 monitoring the left brain regions e) Time-series plots of systemic variables including ABP and $PaCO_2$ and of non-NIRS cerebral parameters including ICP, Vmca1, Vmca2. f) Six TOI measurements across the forehead. Slow-wave oscillations are evident in two TOI channels 5 and 6 monitoring the left brain regions.

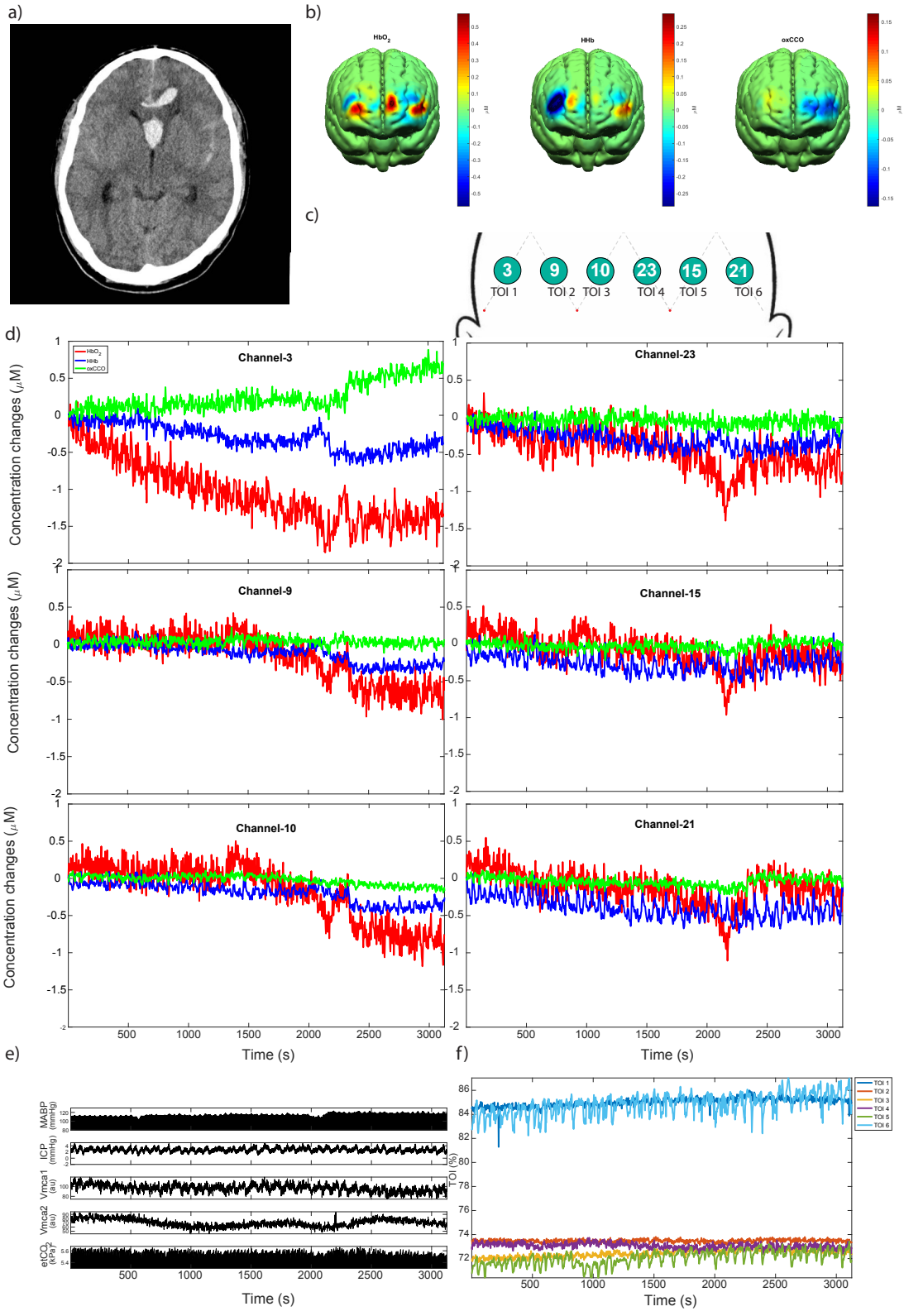

Figure 6.3: Summary of data from patient 2 having subarachnoid haemorrhage due to rupture of an aneurysm on the left anterior communicating artery. The panels are presented in the same order as in the previous patient. Spontaneous slow wave oscillations are evident in NIRS parameters in channels 23, 15, 21 monitoring the left brain regions in this patient. Slow wave oscillations are also evident in two TOI channels 5 and 6 monitoring the left brain regions.

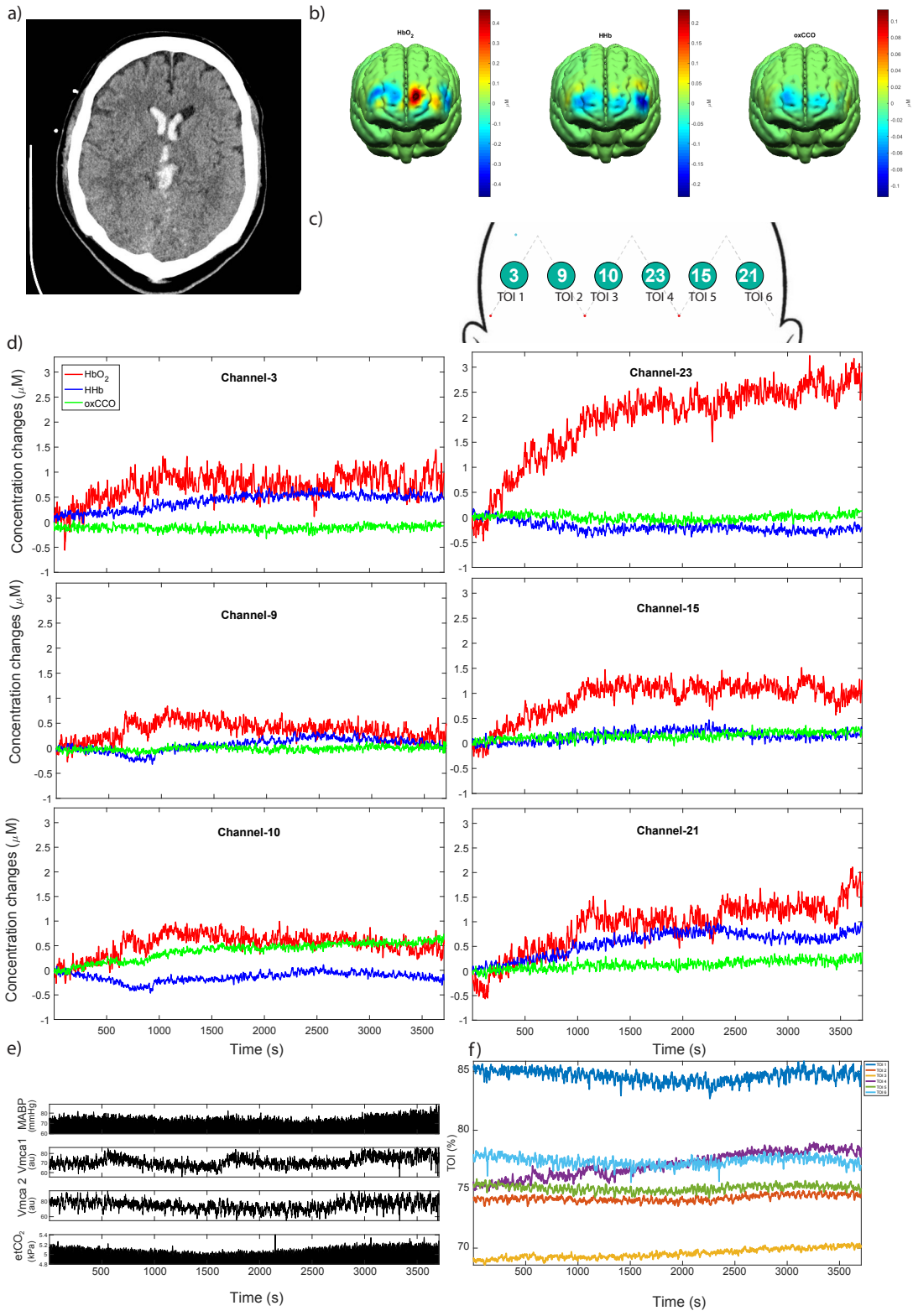

Figure 6.4: Summary of data from patient 3 having an intraventricular haemorrhage. The panels are presented in the same order as in previous patients. In this patient, ICP was not monitored as part of routine care. No obvious slow wave oscillations are evident in both NIRS parameters and TOI channels.

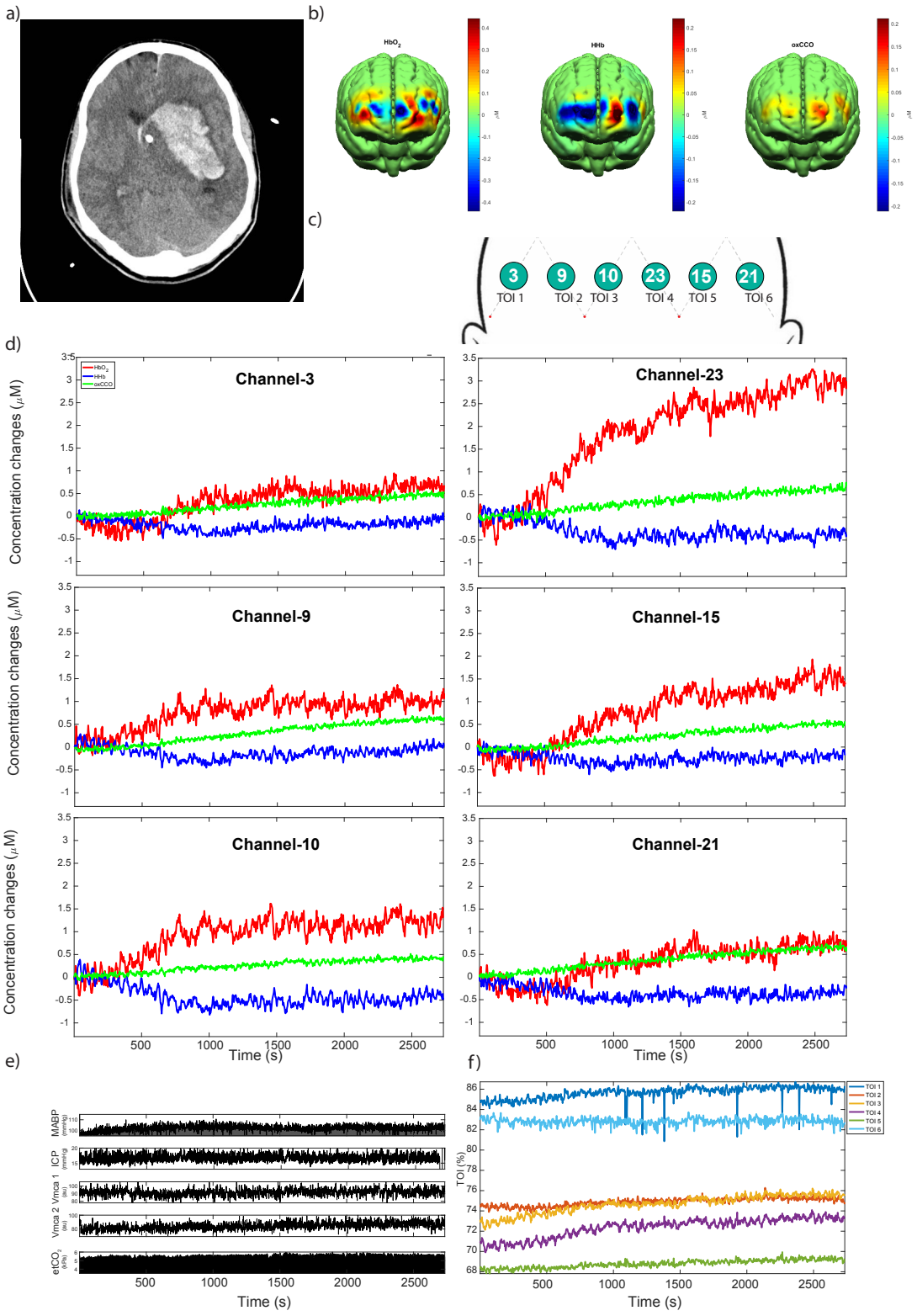

Figure 6.5: Summary of data from patient 4 having intraparenchymal haemorrhage as a result of a left basal ganglia bleed. The panels are presented in the same order as in previous patients. No obvious slow wave oscillations are evident in both NIRS parameters and TOI channels.

6.4.2 Full results

Patient 1 is a 70-year-old female with a post-operative right frontal intraparenchymal haemorrhage. Her Glasgow Coma Scale (GCS) at admission was 11/15 and her Glasgow Outcome Scale (GOS) was 2/5. Multimodal monitoring variables were collected within 24 hours after admission. Figure 6.2 gives the summary of the multimodal data set from this patient. This includes a) a CT scan showing the location of the injury. b) averaged reconstructed images of $\Delta[HbO_2]$, Δ[HHb] and Δ[oxCCO] over a period of 1000 s of clinical stability showing regional variation in cerebral haemodynamics and metabolism. c) the locations of six 35 mm NIRS measurement channels (in green circles) and six TOI channels across the forehead of the patient. d) $\Delta[HbO_2]$, Δ[HHb] and Δ[oxCCO] in six NIRS channels, two of which (channels 15 and 21 monitoring the left brain regions) show clear spontaneous slow wave oscillations e) time-series plots of systemic variables including ABP and $PaCO_2$ and of non-NIRS cerebral parameters including ICP, Vmca1, Vmca2. f) six TOI measurements across the forehead, two of which (channels 5 and 6 monitoring the left brain regions) show slow-wave oscillations. Slow wave oscillations are evident in NIRS parameters and TOI measurements monitoring the left brain region. They are also evident in non-NIRS cerebral parameters (ICP and Vmca1).

Patient 2 is a 40-year-old male with subarachnoid haemorrhage due to rupture of an aneurysm on the left anterior communicating artery. His GCS was 14/15 and his GOS was 4/5. The same multimodal monitoring method was used to monitor this patient three days after brain injury. Figure 6.3 gives the summary of the multimodal data set from this patient. Slow wave oscillations are evident in NIRS parameters and TOI measurements monitoring the left brain regions in this patient. They are also evident in non-NIRS cerebral parameters (ICP and Vmca1).

Patient 3 is a 58-year-old male with posterior fossa intracranial haemorrhage. His GCS was 10/15 and his GOS was 2/5. The same multimodal monitoring method was used to monitor this patient three days after brain injury. ICP was not monitored in this patient as part of routine clinical care. Figure 6.4 gives the summary of the multimodal data set from this patient.

Patient 4 is a 44-year-old male with left basal ganglia intracranial haemorrhage. His GCS was 4/15 and his GOS was 0/5. The same multimodal monitoring method was used to monitor this patient two days after brain injury. Figure 6.5 gives the summary of the multimodal data set from this patient.

6.4.2.1 Analysis using standard autoregulation indices

Patient 1 PRx was calculated for this patient in the standard manner as described earlier. Mean PRx value for the whole period was 0.37 ($>$ 0.3), indicating impaired cerebral pressure autoregulation. Continuous PRx calculation shows evidence of a long period of highly positive PRx value (Figure 6.6). Similar results are evident in the Mx calculation (Figure 6.7) with mean Mx1 for the whole period was 0.51.

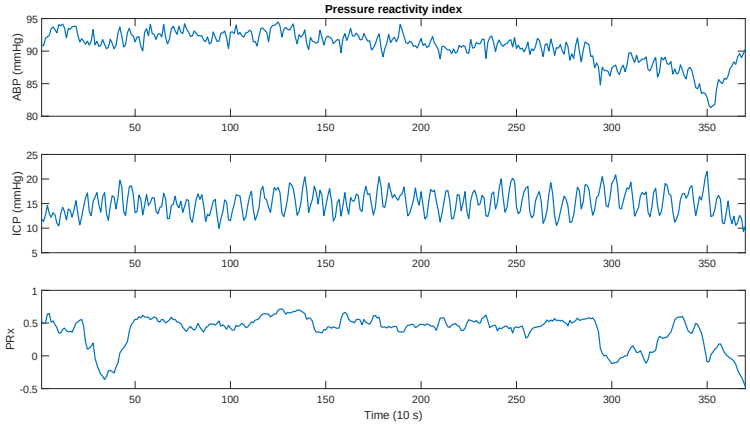

Figure 6.6: ABP, ICP and PRx of patient 1. Mean PRx for the whole duration is 0.37 $>$ 0.3 indicating impaired autoregulation. Continuous PRx trace shows a sustained period of positive PRx indicating impaired cerebral pressure autoregulation.

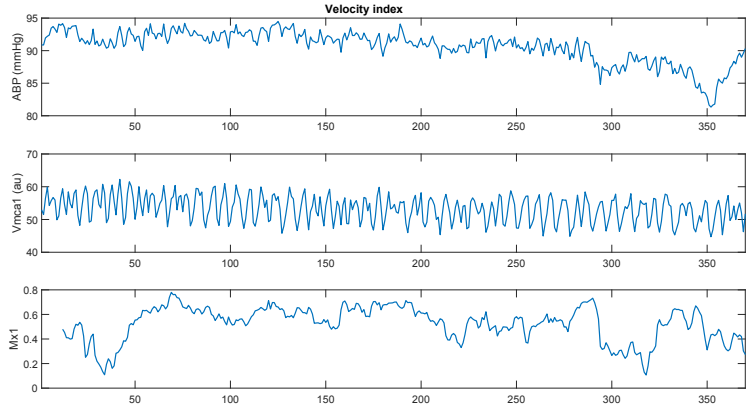

Figure 6.7: ABP, Vmca1 and Mx1 of patient 1. Mean Mx1 for the whole duration is 0.51 $>$ 0.3 indicating impaired autoregulation. Continuous Mx trace shows a long sustain positive period of impaired cerebral pressure autoregulation.

Pressure passive slow wave oscillations transferred between ABP and ICP are evident in the semblance plot within the frequency range from 0.05 to 0.003 Hz (Figure 6.8) with most areas having wavelet semblance values close to 1 (red), indicating an in-phase relationship between ABP and ICP correlating to pressure passive response of impaired

cerebral autoregulation.

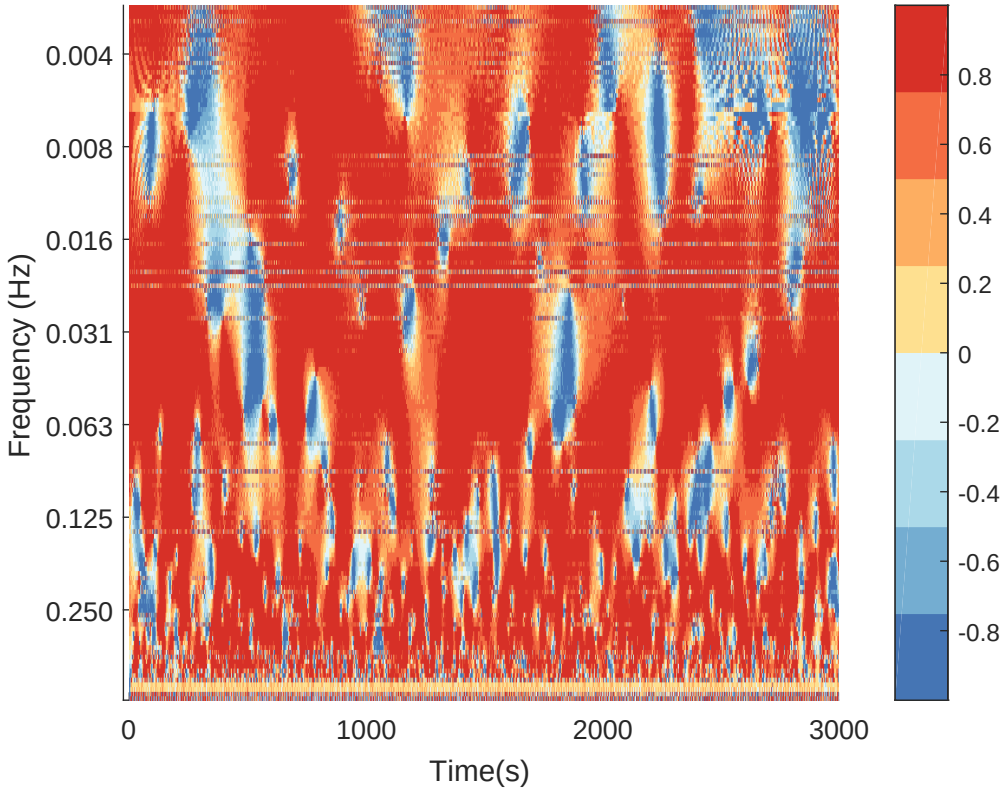

Figure 6.8: Wavelet semblance between ABP and ICP for patient 1. Wavelet plot shows large red areas where semblance is close to 1 in the time frequency domain, indicating zones of in-phase relationship between ABP and ICP, suggesting pressure passive responses.

Patient 2 Mean PRx is 0.18 and mean Mx1 is 0.09. Continuous PRx shows large variation (Figure 6.9), starting at high level and decreasing to below 0 at the end of the measurement period. Vmca1 measured by TCD in this patient suffered a large drop indicated by the spike in the middle plot of Figure 6.10. Wavelet semblance plot for the relationship between ABP and ICP shows large blue areas across time and frequency domain, indicating anti-phase relationship between the two variables correlating to pressure active response of intact cerebral autoregulation (Figure 6.11).

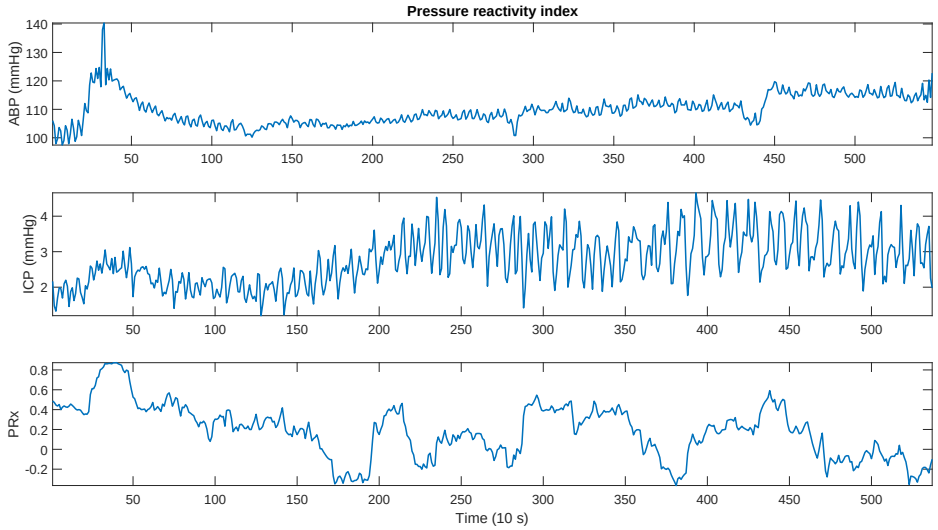

Figure 6.9: ABP, ICP and PRx of patient 2. Mean PRx for the whole duration is 0.18, indicating impaired autoregulation. Continuous PRx shows large variation starting at high level and decreasing to below 0 at the end of the measurement period.

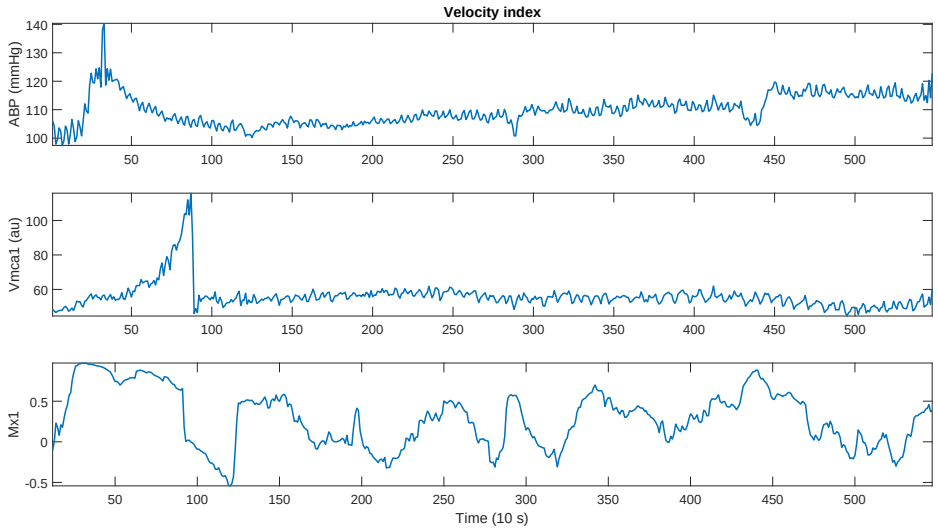

Figure 6.10: ABP, Vmca1 and Mx1 of patient 2. Mean Mx1 for the whole duration is 0.09. Vmca1 (middle plot) suffered from a large drop during the initial period of monitoring.

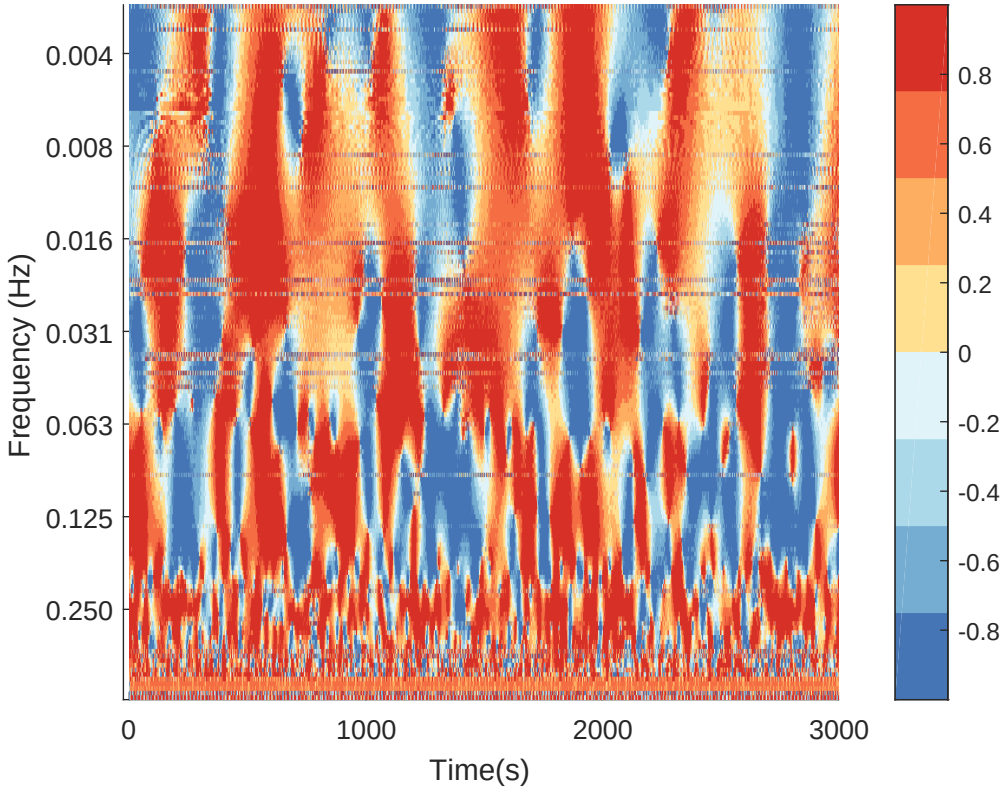

Figure 6.11: Semblance between ABP and ICP for patient 2. Wavelet plot shows more large blue areas where semblance is close to -1 across the time frequency domain, indicating zones of anti-phase relationship between neuromonitoring variable correlating to pressure-active response.

Patient 3 As ICP was not monitored in patient 3, PRx could not be calculated. Standard autoregulation index based on TCD-measured flow velocity was calculated. Mean Mx values derived from the correlation between ABP and TCD-flow velocity from the left (Vmca1) and right (Vmca2) middle cerebral arteries were 0.09 and -0.07 respectively. This does not indicate impaired autoregulation. However, as can be seen from the continuous measures of these indices (Figure 6.12 and 6.13) there were periods where continuous Mx values were highly positive, indicating periods of impaired autoregulation. Figure 6.14 shows the semblance plot between ABP and Vmca1. Several blue areas in the frequency range between 0.05-0.003 Hz show anti-phase relationship between Vmca and ABP, indicating intact cerebral pressure autoregulation. This result is in agreement with the standard autoregulation indices calculation.

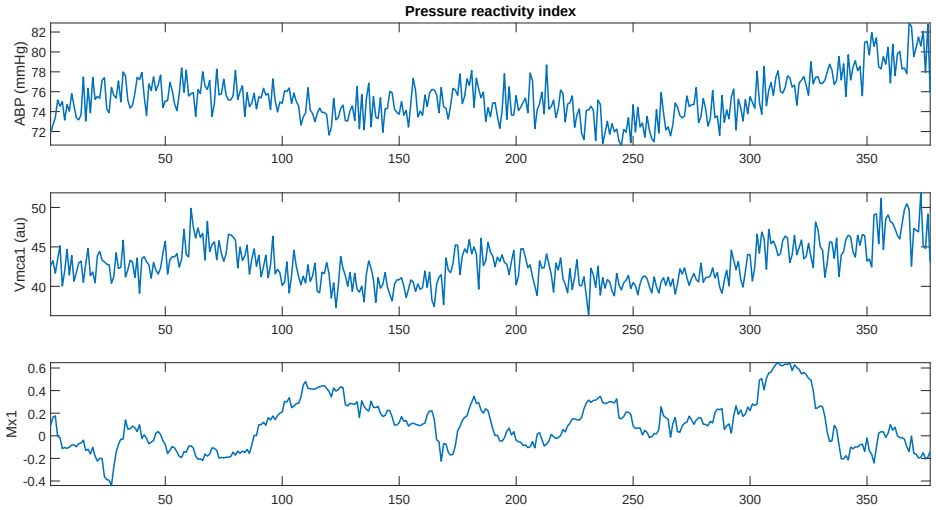

Figure 6.12: ABP, Vmca1 and flow velocity reactivity index Mx1 of patient 3. Mean Mx1 for the whole during of monitoring is 0.09. Continuous Mx1 trace shows periods of positive Mx indicating impaired vascular reactivity.

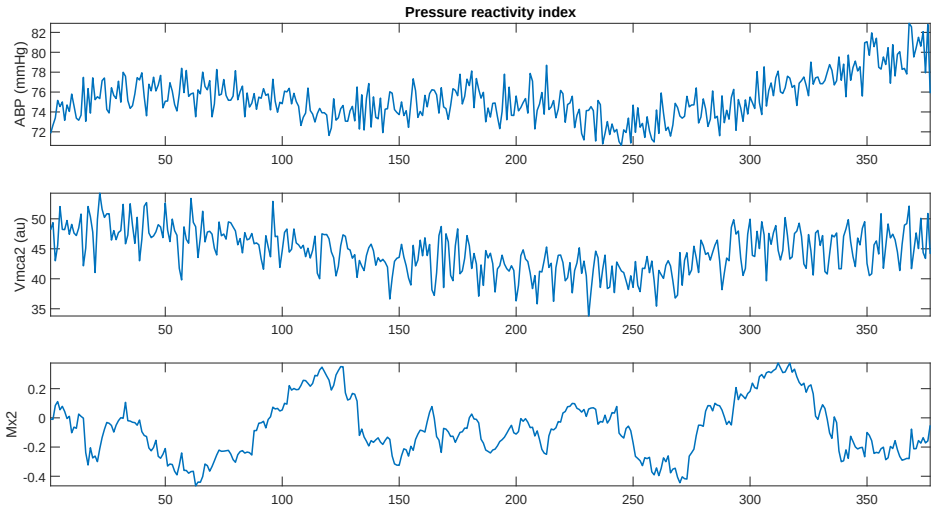

Figure 6.13: ABP, Vmca2 and flow velocity reactivity index Mx2 of patient 3. Mean Mx2 for the whole during of monitoring is -0.07. Continuous Mx2 trace shows shorter periods of positive value in comparison to Mx1 trace.

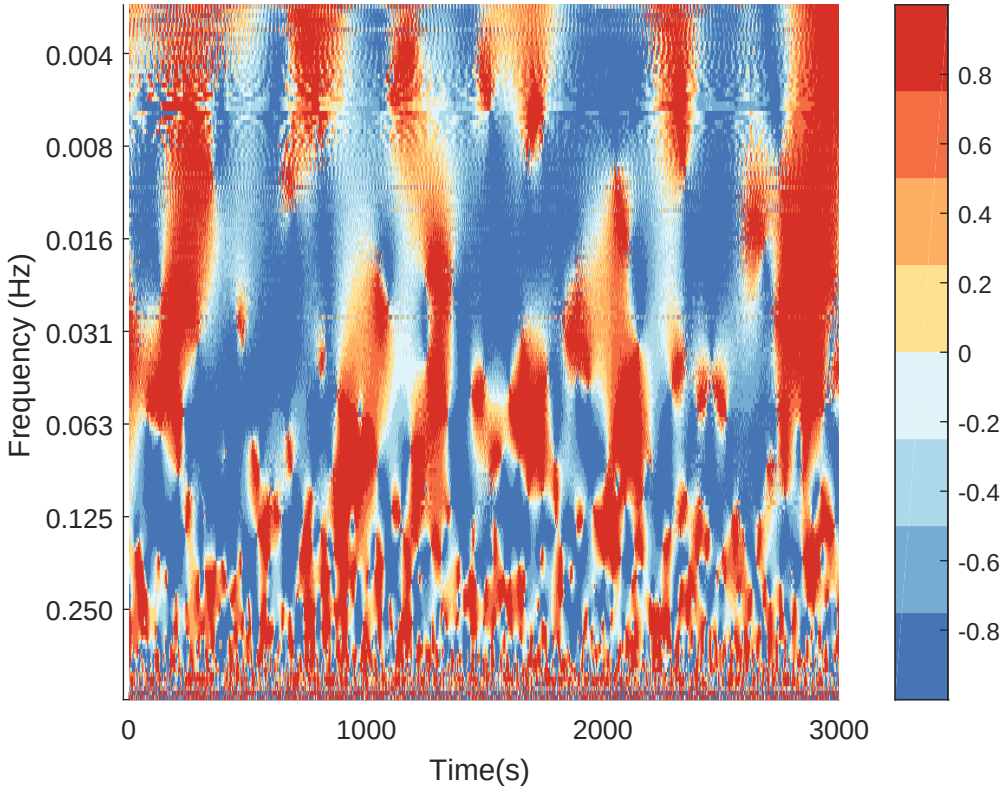

Figure 6.14: Semblance analysis between ABP and Vmca1 for patient 3. Blue areas in the frequency range (0.05-0.003 Hz) indicate anti-phase relationship between the two signals, suggesting intact vascular reactivity.

Patient 4 Mean PRx, Mx1 and Mx2 are 0.15, 0.32 and 0.38 respectively. These values indicates impaired cerebral pressure autoregulation. Large changes in ABP as well as instability in Vmca measurements were evident in this patient case (Figure 6.15, 6.16 and 6.17).

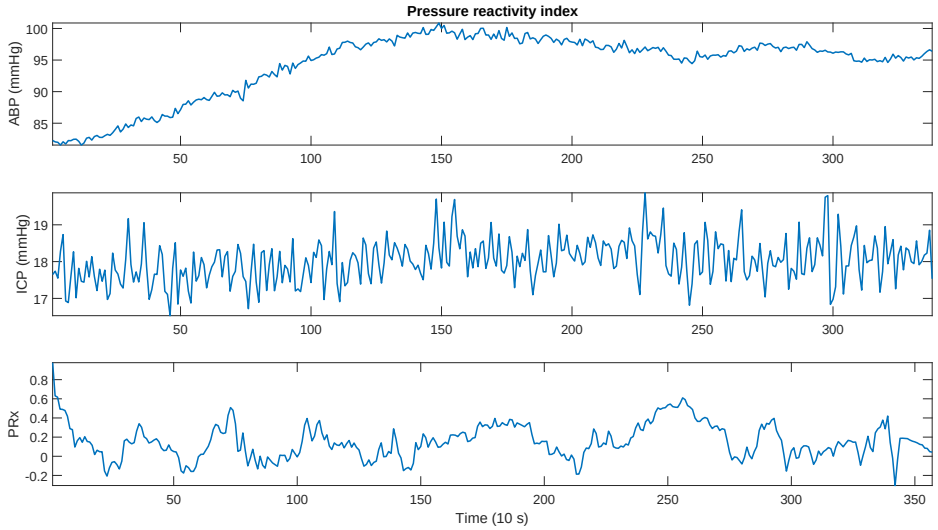

Figure 6.15: ABP, ICP and continuous PRx for patient 4. Mean PRx for the whole during of monitoring is 0.15. Continuous PRx trace shows periods of fluctuation around 0, indicating periods of impaired vascular reactivity.

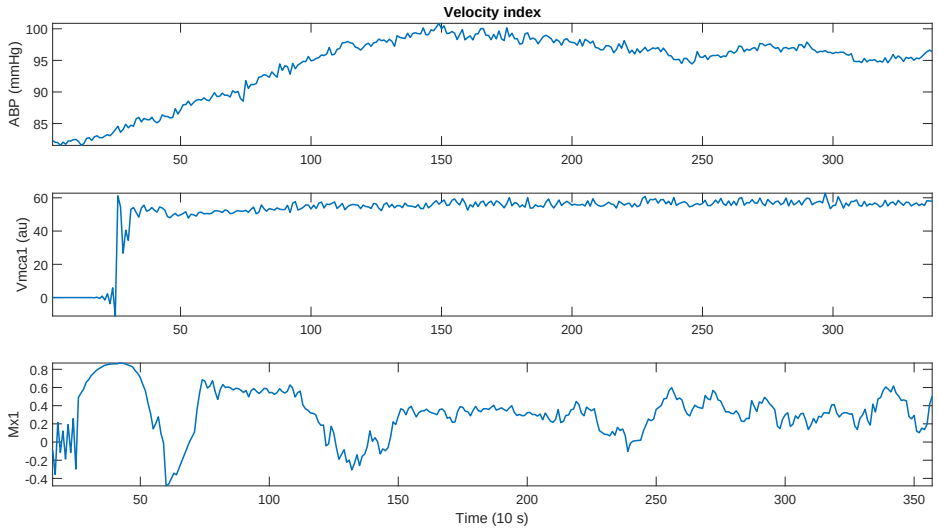

Figure 6.16: ABP, Vmca1 and continuous Mx1 for patient 4. Mean Mx1 for the whole during of monitoring is 0.32, indicating impaired vascular reactivity.

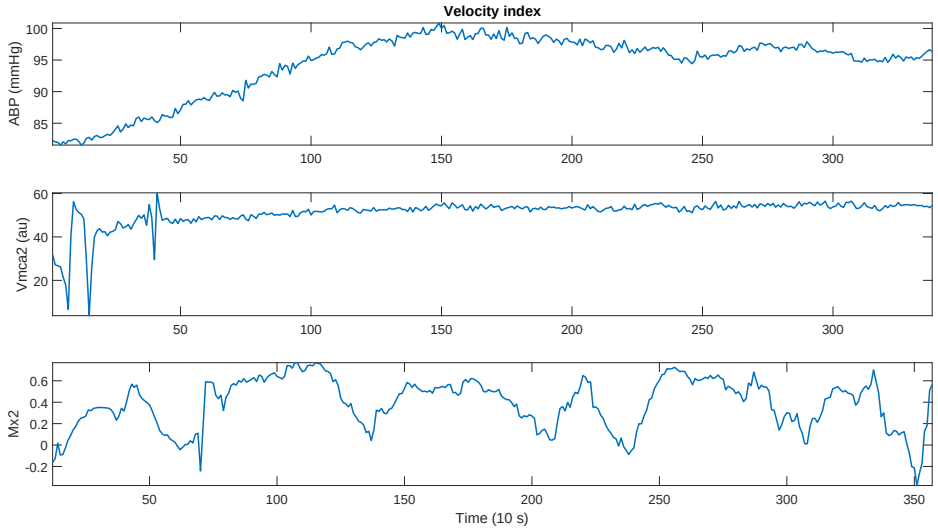

Figure 6.17: ABP, Vmca2 and Mx2 for patient 4. Mean Mx2 for the whole during of monitoring is 0.38, indicating impaired vascular reactivity.

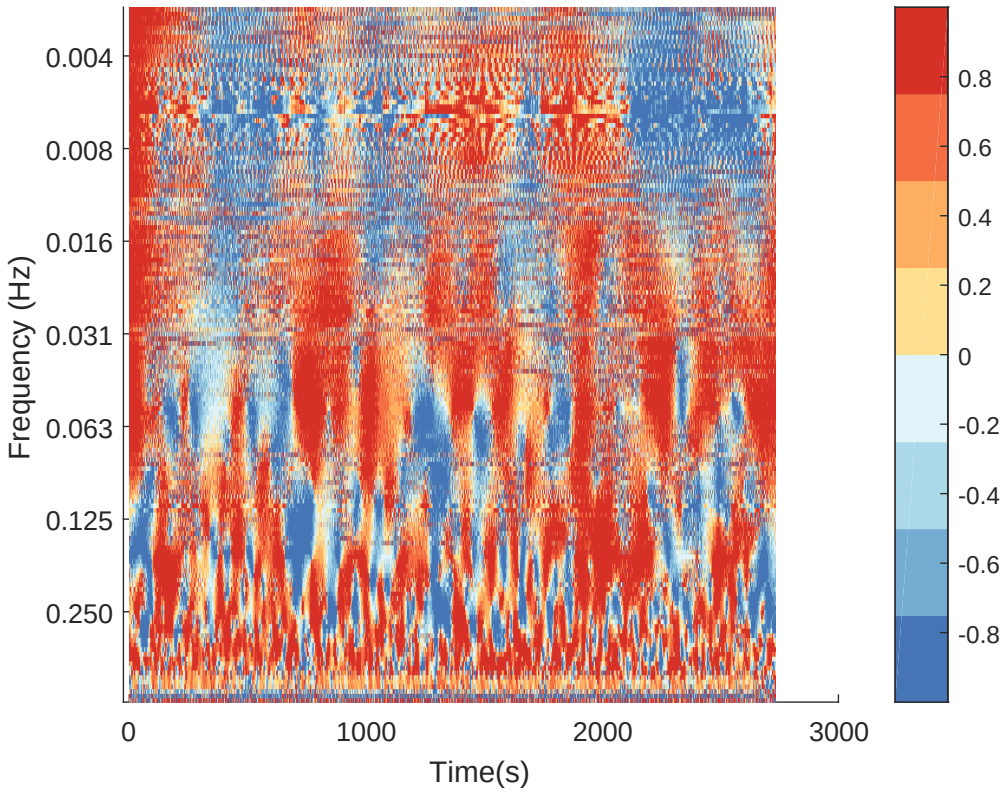

Figure 6.18: Semblance analysis between ABP and ICP for patient 4. Red areas in the frequency range (0.05-0.003 Hz) indicate in-phase relationship between the two signals, suggesting impaired vascular reactivity.

6.4.2.2 Comparing NIRS and non-NIRS neuromonitoring parameters

Patient 1 Figure 6.19 shows the variation in blood pressure, non-NIRS parameters and NIRS parameters of channel 15 monitoring the left hemisphere of patient 1. Slow wave oscillations are evident in both non-NIRS cerebral parameters and NIRS parameters in this patient. Power spectral density analysis shows that those oscillations in non-NIRS and NIRS parameters have the same frequencies (Figure 6.20). These slow wave oscillations in NIRS parameter may contain information regarding the state of cerebral autoregulation and this will be investigated in more detail using wavelet analysis techniques in a later section.

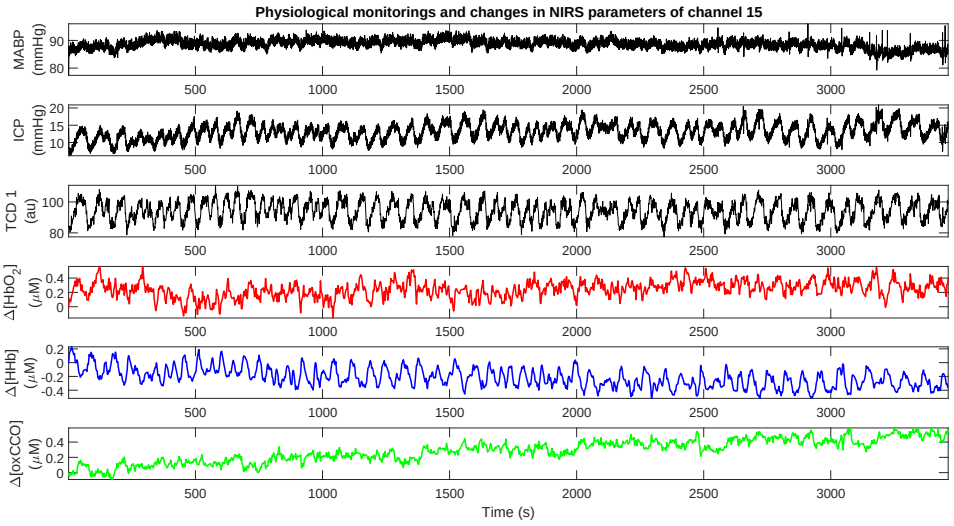

Figure 6.19: Slow wave oscillations in non-NIRS and in NIRS parameters from channel 15 monitoring the left hemisphere (non-injured region) of patient 1.

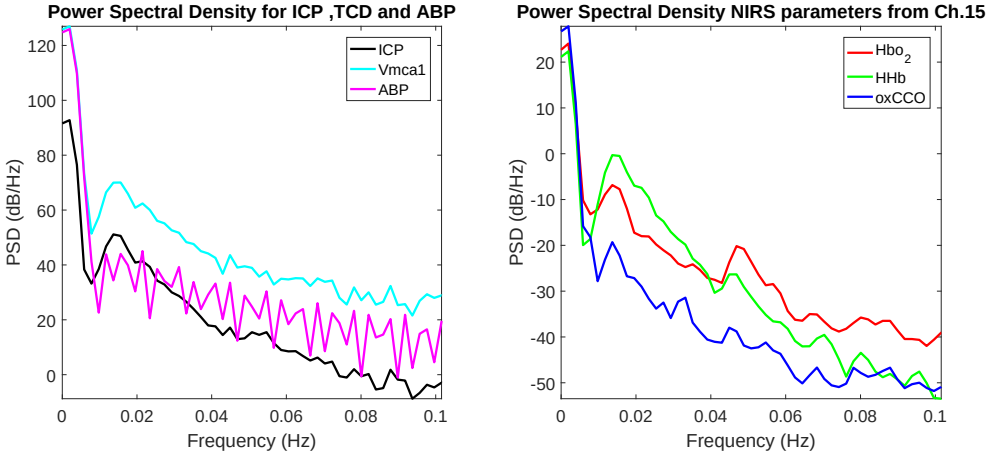

Figure 6.20: Power spectral density analysis to compare the distribution of power across the low-frequency range in non-NIRS cerebral variables and NIRS parameters in patient 1. Similar spectral features are evident among these variables.

Figure 6.21 shows the time-series changes of TCD-measured flow velocity from the left middle cerebral artery (Vmca1) and TOI-5 from patient 1. High coherence was evident between TOI parameter measured by NIRS and Vmca1 parameter measured by TCD.

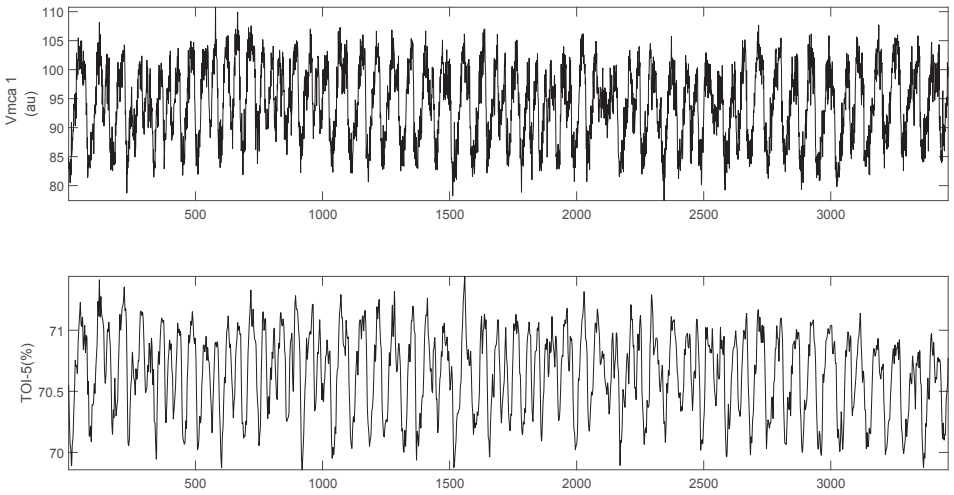

Figure 6.21: TCD-measured Vmca1 and TOI from channel 5 demonstrating strong coherence.

Coherence analysis confirmed the high coherence between NIRS parameters and non-NIRS variables in the slow frequency range. Figure 6.22 and 6.23 show the coherence between NIRS and non-NIRS cerebral parameters in channel 3 monitoring the injured region and in channel 15 monitoring the non-injured region in patient 1. Yellow areas indicate periods of high coherence in the time frequency domain. Much higher coherence was evident between signals derived from the non-injured region of the brain in

comparison to those derived from the injured region of the brain.

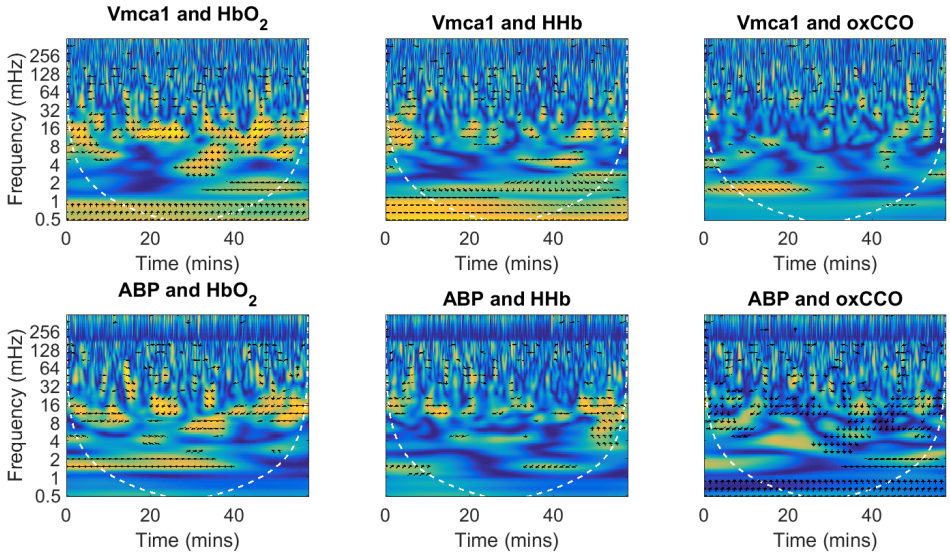

Figure 6.22: Squared cross-wavelet coherence between non-NIRS and NIRS parameters in channel 3 monitoring the *injured* brain region of patient 1 in the time-frequency domain. The x-axis represents time; the y-axis represents frequency and the colour scale represents the squared magnitude of the cross-wavelet coherence with yellow areas indicating high coherence and blue areas indicating low coherence. The white dashed line indicates the cone of influence.

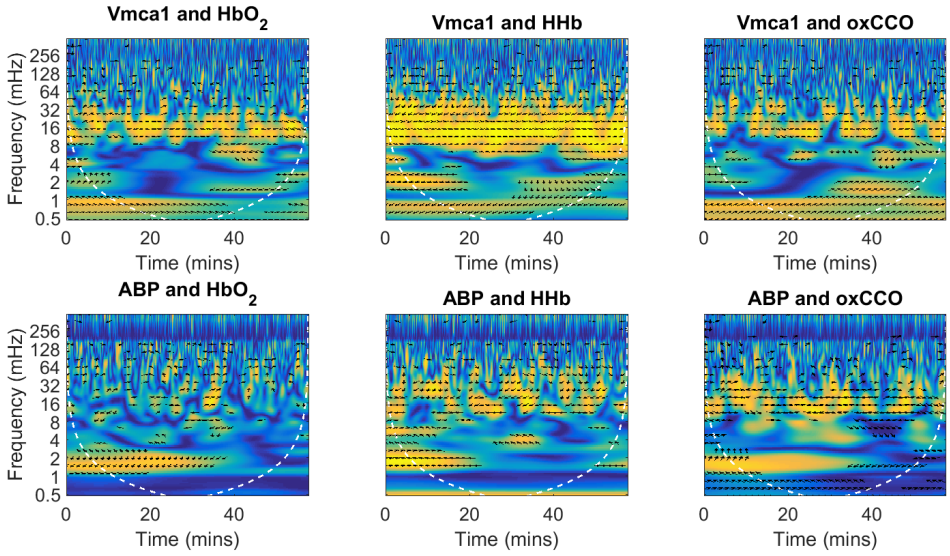

Figure 6.23: Squared cross-wavelet coherence between non-NIRS and NIRS parameters in channel 15 monitoring the *non-injured* brain region of patient 1 in the time-frequency domain.

Patient 2 Similar to the results presented for patient 1, Figure 6.24 shows systemic variables, non-NIRS cerebral parameters and changes in NIRS parameters of channel 10

monitoring right hemisphere of patient 2. Slow wave oscillations were evidenced in both non-NIRS neuromonitoring and NIRS parameters in this patient. Power spectral density analysis shows that the oscillations in those parameters have the same frequencies (Figure 6.25)

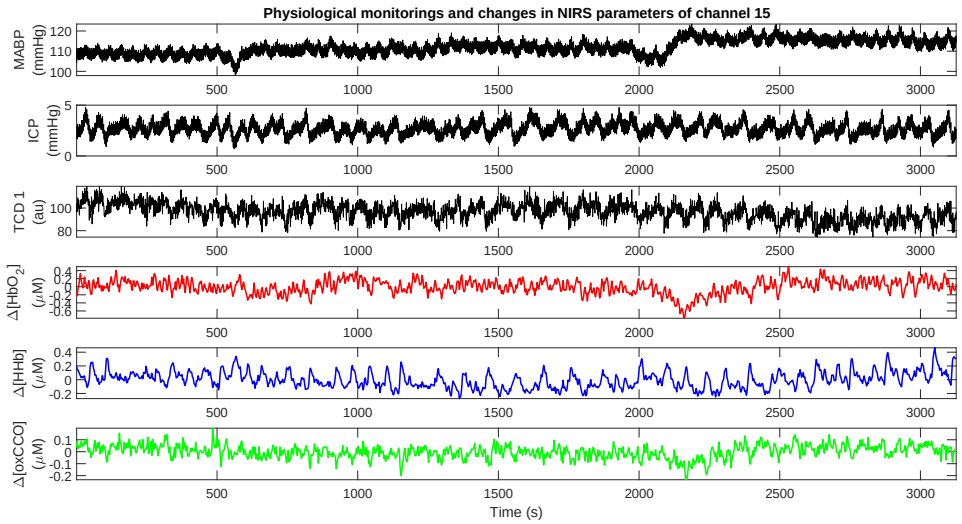

Figure 6.24: Slow wave oscillations in non-NIRS cerebral variables and in NIRS parameters from channel 10 monitoring the right hemisphere (non-injured region) of patient 2. Significant correlations were evident between NIRS parameters and Vmca1 and ICP.

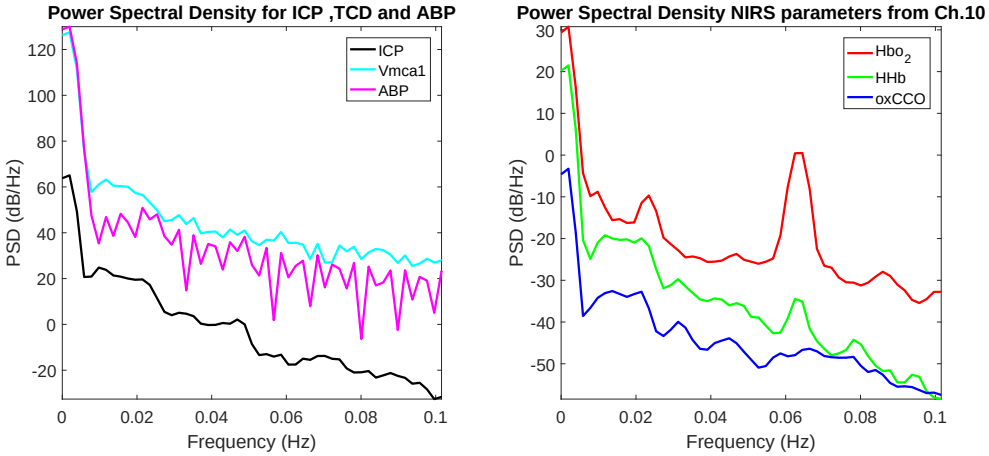

Figure 6.25: Power spectral density analysis to compare the distribution of power across the low frequency range in non-NIRS and NIRS parameters in patient 2. Similar spectral features were evident between these parameters.

For patient 2, similar agreement between Vmca measured by TCD and TOI are evident (Figure 6.26)

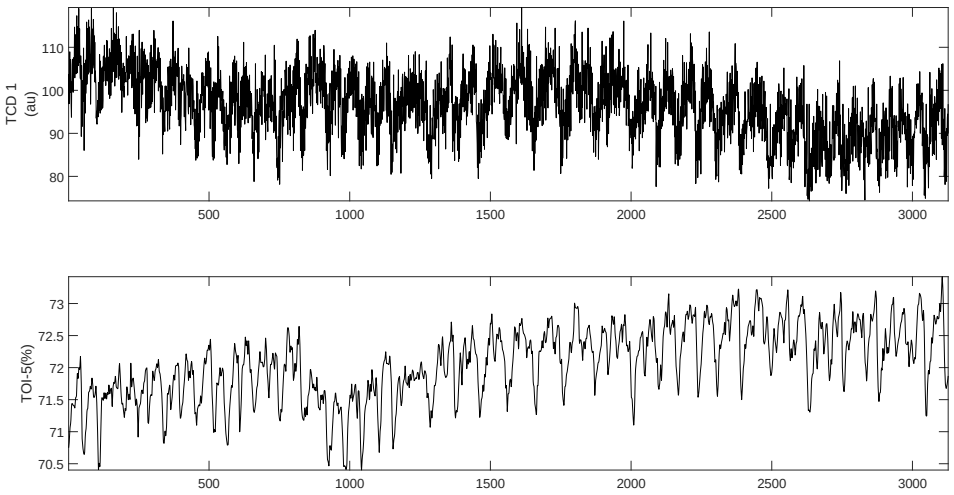

Figure 6.26: TCD-measured Vmca1 and TOI from channel 5 monitoring the oxygenation of a region on the left hemisphere in patient 2.

In patient 2 with subarachnoid haemorrhage, the difference in coherence among signals between the left and the right frontal regions was less apparent in the haemoglobin signals. However, using the oxCCO signals, difference in coherence was evident (Figure 6.27 and 6.28).

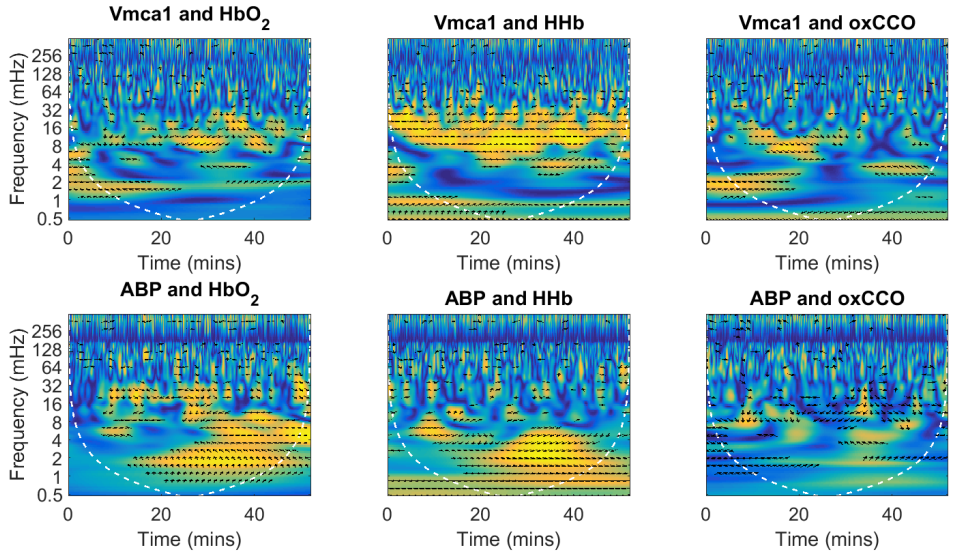

Figure 6.27: Squared cross-wavelet coherence between systemic and NIRS parameters in channel 23 monitoring right frontal region of patient 2.

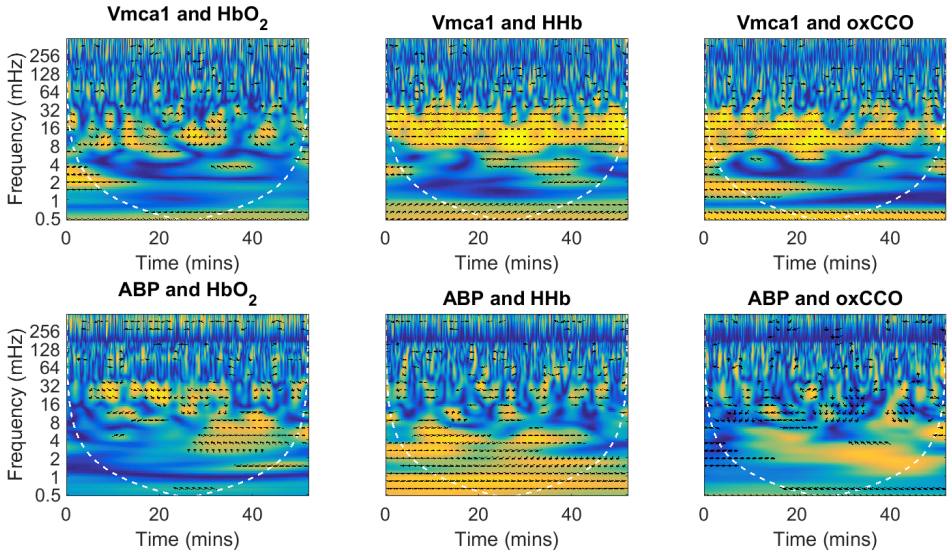

Figure 6.28: Squared cross-wavelet coherence between systemic and NIRS parameters in channel 10 monitoring the left frontal region of patient 2.

Patient 3 Figure 6.29 shows systemic, non-NIRS cerebral variables and changes in NIRS parameters of channel 3 monitoring the right hemisphere of the patient. Slow wave oscillations were not apparent in non-NIRS and NIRS parameters.

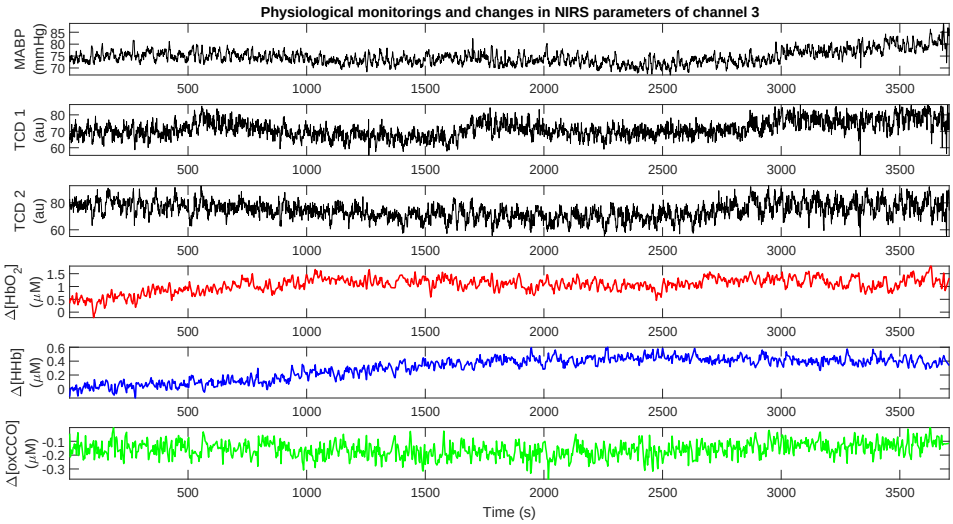

Figure 6.29: Non-NIRS and NIRS parameters in channel 3 from patient 3. There is no apparent relationship between these monitoring variables.

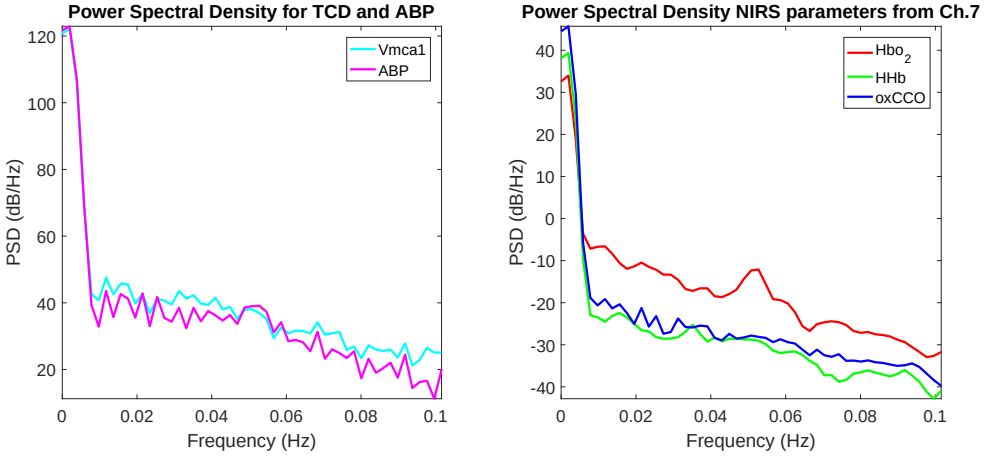

Figure 6.30: Power spectral density analysis to compare the distribution of power across the low frequency range in systemic variables and NIRS parameters in patient 3. Similar spectral features were evident between these parameters.

Slow wave oscillations in TCD-measured Vmca and TOI values were not as obvious as in the first two patients for patient 3 (Figure 6.31).

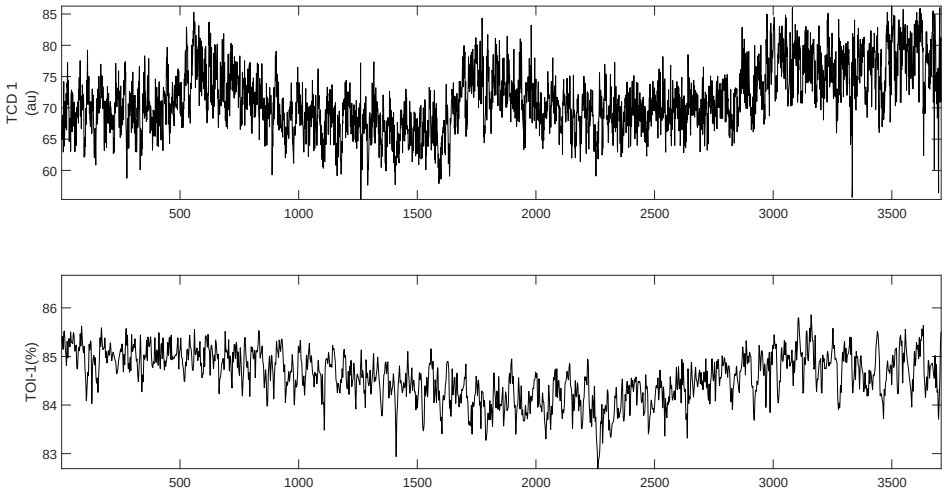

Figure 6.31: TCD-measured Vmca1 and TOI from channel 1 monitoring the oxygenation of a region on the right hemisphere in patient 3.

In patient 3 with intraventricular haemorrhage, the coherence between non-NIRS cerebral parameters and NIRS parameters was higher on the right brain region than on the left brain region. (Figure 6.32 and 6.33)

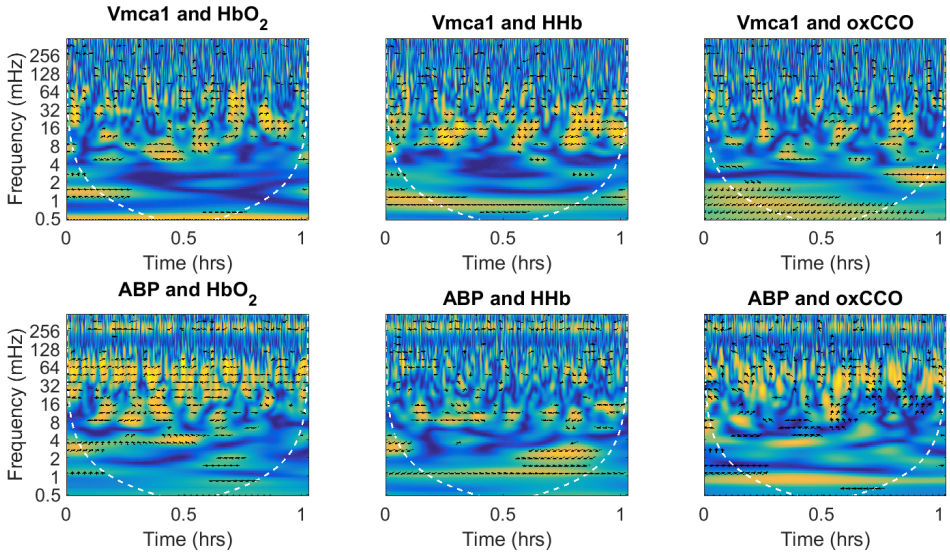

Figure 6.32: Squared cross-wavelet coherence between non-NIRS and NIRS parameters in channel 9 monitoring the right frontal region of patient 3.

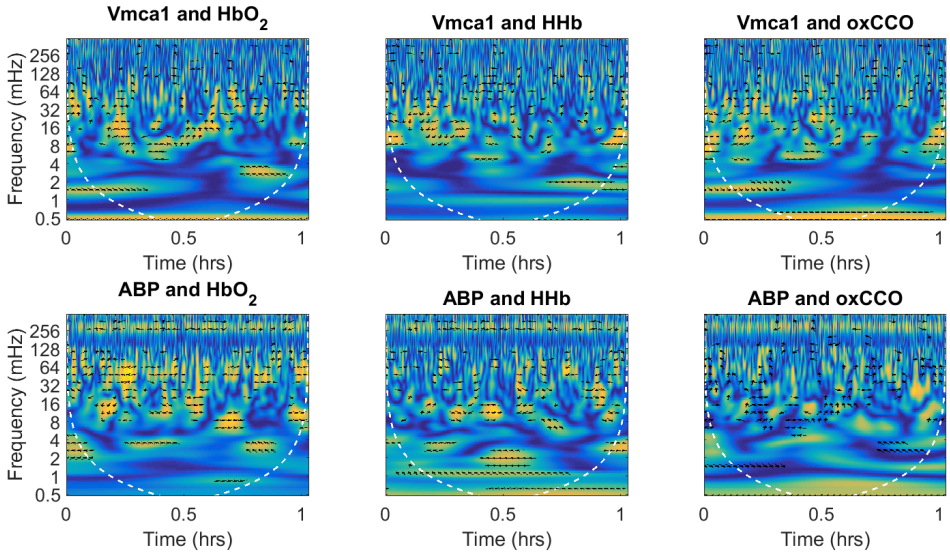

Figure 6.33: Squared cross-wavelet coherence between non-NIRS and NIRS parameters in channel 15 monitoring the left frontal region of patient 3.

Patient 4 Similarly in patient 4, slow wave oscillations are not apparent in all parameters. An example channel was shown in Figure 6.34. Slow wave oscillations in TCD-measured Vmca and TOI values were not as obvious as in the first two patients for patient 4 (Figure 6.36).

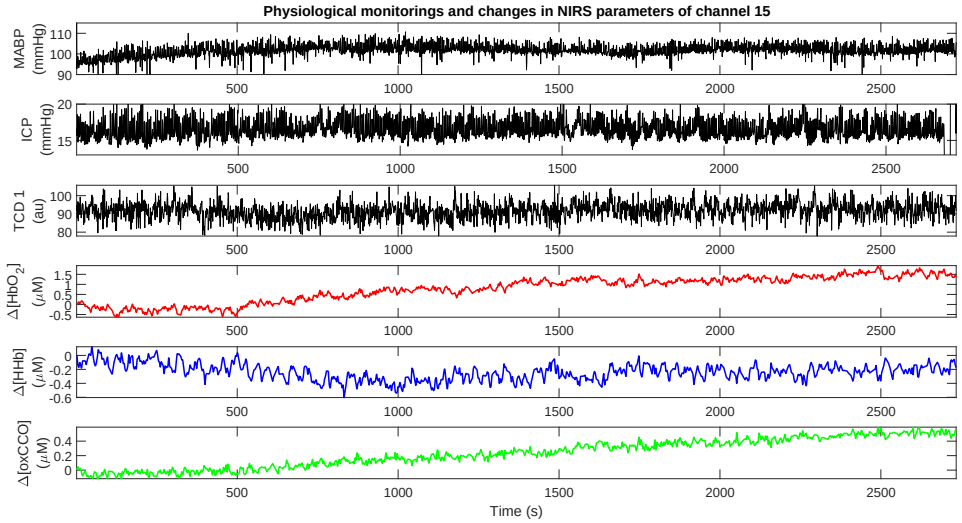

Figure 6.34: Non-NIRS neuromonitoring and NIRS parameters in channel 15 from patient 4. There is no apparent relationship between these monitorings

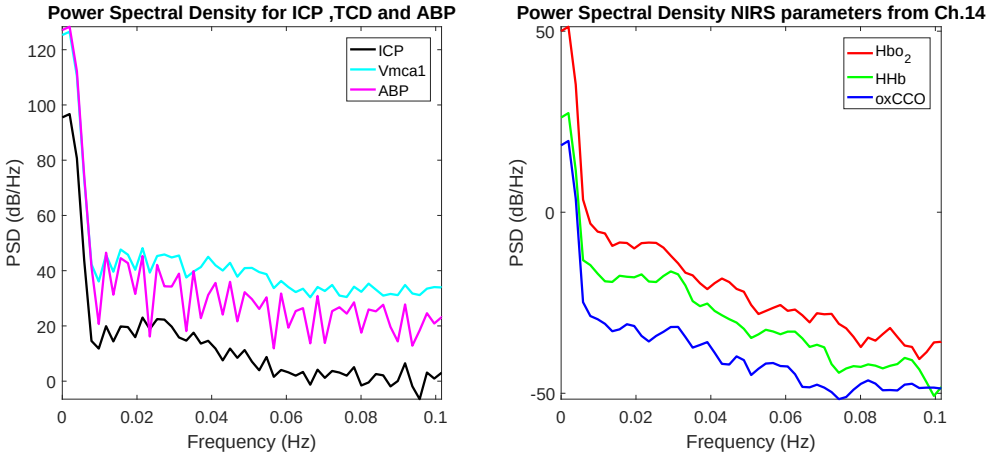

Figure 6.35: Power spectral density analysis to compare the distribution of power across the low frequency range in non-NIRS and NIRS parameters in patient 4. Similar spectral features were evident between these parameters.

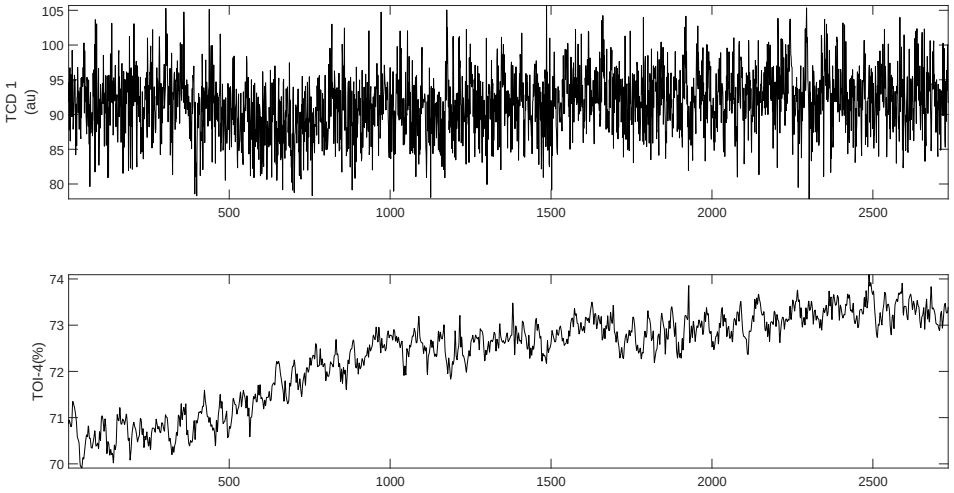

Figure 6.36: TCD-measured Vmca1 and TOI from channel 4 monitoring the oxygenation of a region on the left hemisphere in patient 4.

In patient 4 with left basal ganglia intraparenchymal haemorrhage, the coherence between non-NIRS cerebral parameters and NIRS parameters was higher on the right brain region than on the left brain region. (Figure 6.37 and 6.38)

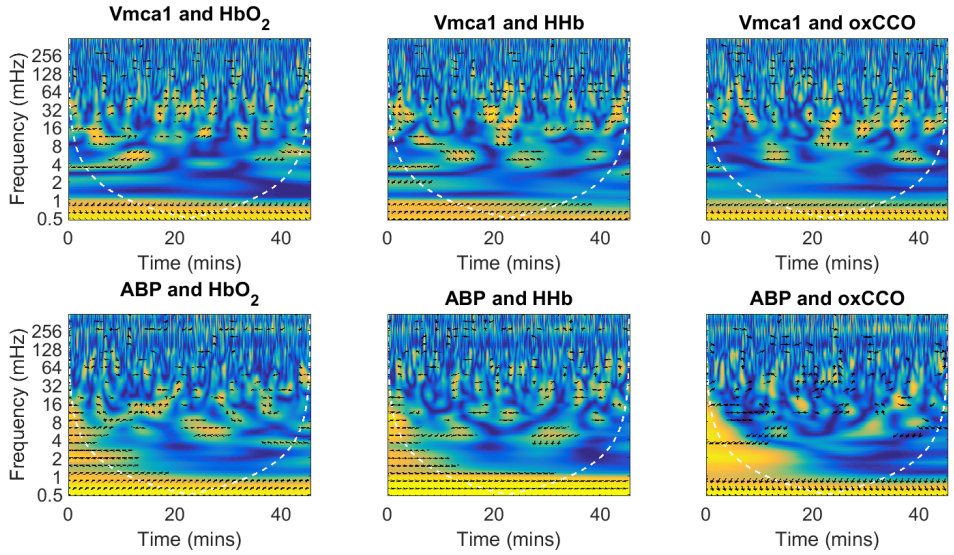

Figure 6.37: Squared cross-wavelet coherence between non-NIRS and NIRS parameters in channel 3 monitoring the right frontal region of patient 4.

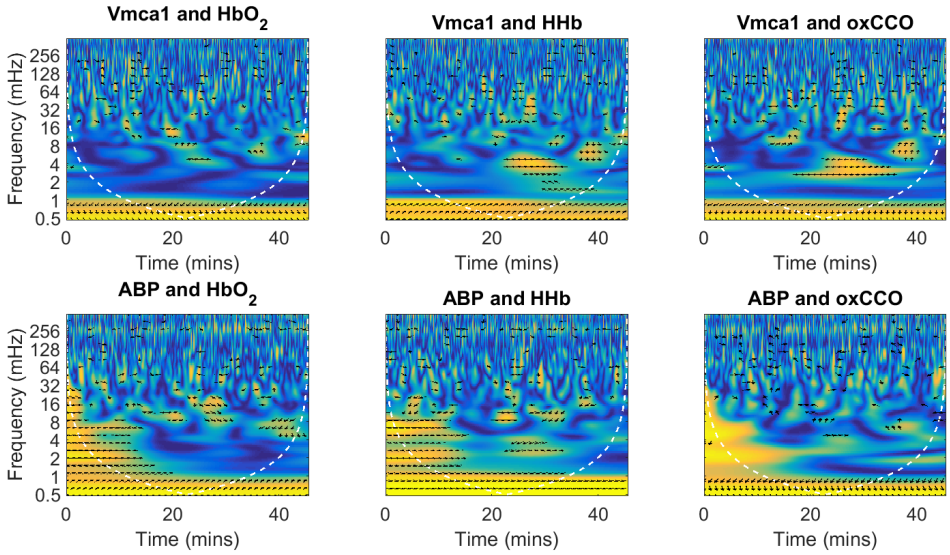

Figure 6.38: Squared cross-wavelet coherence between non-NIRS and NIRS parameters in channel 15 monitoring the left frontal region of patient 4.

6.4.2.3 Semblance analysis between NIRS and non-NIRS parameters

Patient 1 As can be appreciated from the previous comparison, slow wave oscillations in NIRS parameters are highly correlated with those in non-NIRS neuromonitoring variables. As a result, NIRS parameters may be used as surrogates for neuromonitoring and autoregulation indices can be derived using NIRS parameters by correlating them with ABP. With the advance of the multi-channel broadband NIRS system, regional variation in cerebral autoregulation can be evaluated using regional NIRS measurements of $\Delta[HbO_2]$,Δ[HHb] and Δ[oxCCO]. Semblance analysis was applied to calculate the phase relationship between NIRS parameters and ABP to derive the NIRS-based reactivity indices in the time-frequency domain. These could be used to assess cerebral autoregulation status of the brain, similar to the idea of using semblance analysis between ABP and ICP to derive the state of cerebral autoregulation [133].

Figure 6.39 shows the semblance between ABP and HbO_2 and Figure 6.40 shows the semblance between ABP and oxCCO using data from 12 NIRS channels with SDS of 35 mm across the forehead in patient 1. In-phase and anti-phase relationship are indicated in red and blue areas respectively. There was a strong agreement between semblance plots for HbO_2 reactivity (Figure 6.39) and for CCO reactivity (Figure 6.40) which may be explained by the coupling between oxygenation and metabolism. However, there were distinct differences in the low frequency range (0.003 -0.008 Hz) between the HbO_2 reactivity map and the CCO reactivity map in channels populating the right hemisphere

(channels 3, 9, 10, 4, 7, 8) which was the brain injured area in this patient. These differences may be due to the nature of the two signals, one reflects the haemodynamic changes while the other reflects the changes in cerebral oxygen metabolism.

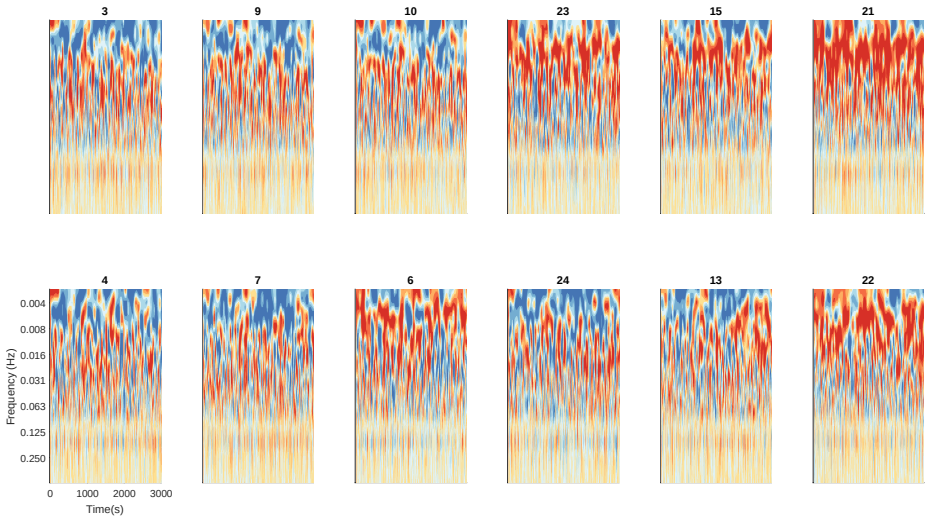

Figure 6.39: Semblance between ABP and $\Delta[HbO_2]$ in 12 channels across the forehead of patient 1. In-phase oscillations are indicated in red and antiphase oscillations are indicated by blue areas.

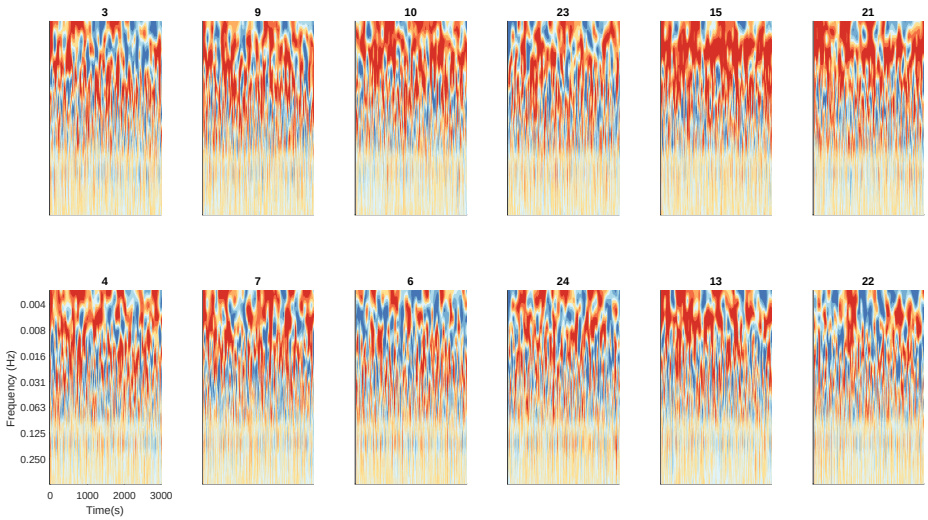

Figure 6.40: Semblance between ABP and Δ[oxCCO] in 12 channels across the forehead of patient 1.

Semblance analysis was applied between HbO_2 and oxCCO signals. The rationale behind this analysis is that in the healthy brain, intact flow-metabolism coupling creates in-phase changes in the concentration changes of HbO_2 and oxCCO. This is usually evident in functional activation study where concentration change of HbO_2 and oxCCO increase together. This relationship may be altered in pathology with variation in flow-

metabolism coupling in different regions of the brain, creating areas of anti-phase relationship between the two signals. However, this relationship may be more complex in brain injury as the oxCCO signal is influenced by many other factors [69]. Figure 6.41 shows the semblance plots for the phase relationship between HbO_2 and oxCCO from 12 channels across the forehead from patient 1. Blue areas are prevalent in most channels except channels 16 and 21 monitoring the left hemisphere. These blue areas may indicate impaired flow-metabolism coupling in the brain regions monitored by these channels.

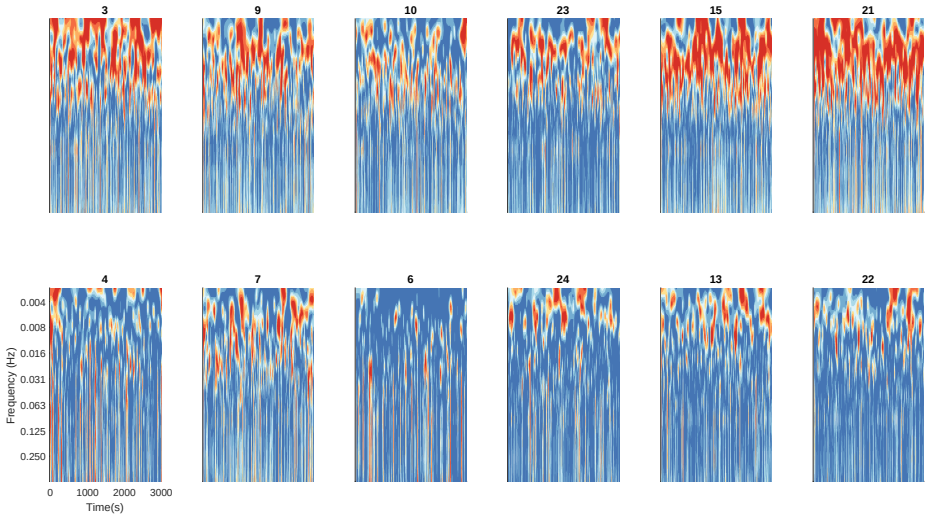

Figure 6.41: Semblance between HbO_2 and Δ[oxCCO] in 12 channels across the forehead in patient 1.

The correlation between Vmca and TOI has been used as a dynamic index of cerebral autoregulation [134]. Using the multi-channel NIRS system, TOI can be measured at six different regions and regional variation in the relationship between TOI and TCD may be used to assess the state of cerebral autoregulation. Semblance analysis between Vmca1 and six TOI measurements is shown in Figure 6.42. A strong in-phase relationship was evident between Vmca1 and TOI from channels monitoring the non-injured left hemisphere (TOI 4 to 6) whereas large variation in phase relationship in the time-frequency domain is observed in the semblance plots from the injured hemisphere.

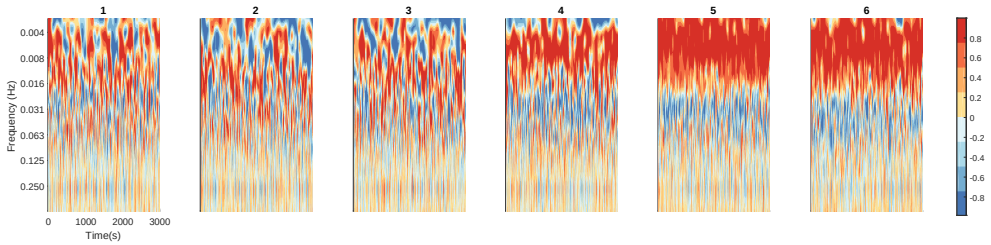

Figure 6.42: Wavelet semblance plots between TCD measured flow velocity in the left cerebral artery and TOI values across the forehead. This demonstrates that TOI measurements from channels 4, 5 and 6 monitoring the left hemisphere (non-injured brain region) are closely correlated with TCD flow measure.

Patient 2 Figure 6.43, 6.44 show the semblance between ABP and HbO_2 and oxCCO signals at 12 NIRS measurement channels with SDS of 35 mm across the forehead in patient 2. No distinct difference could be seen in semblance plots for oxyhaemoglobin and CCO reactivity indices of this patient. Figure 6.45 shows the semblance plots for the phase relationship between HbO_2 and oxCCO from 12 channels across the forehead of patient 2. Channels at higher location (9, 10, 23, 15, 21) have predominantly red areas indicating normal flow-metabolism coupling whereas other channels have predominantly blue areas indicating impaired flow metabolism coupling.

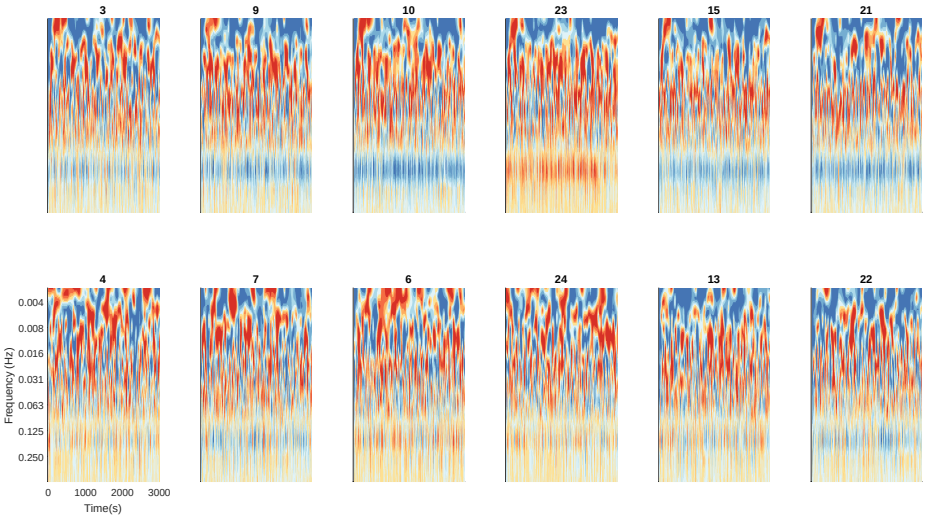

Figure 6.43: Semblance between ABP and $\Delta[HbO_2]$ in 12 channels across the forehead of patient 2.

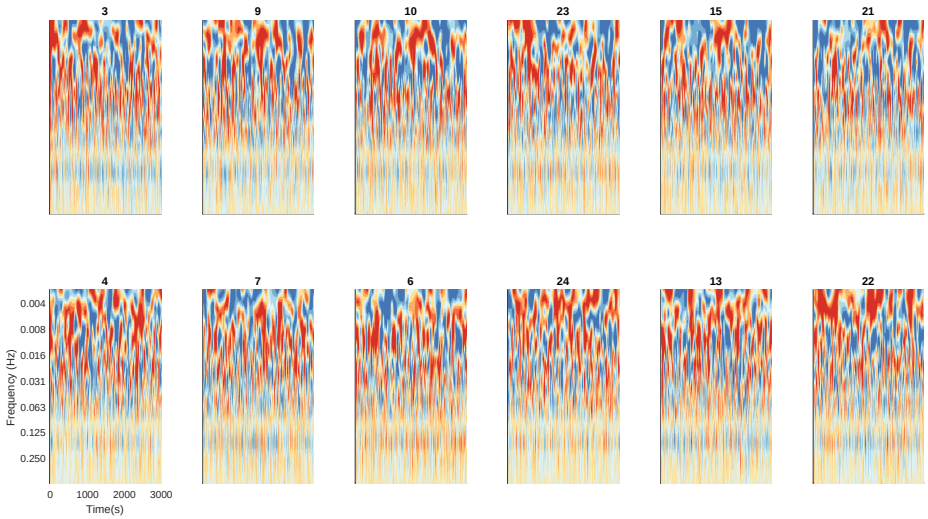

Figure 6.44: Semblance between ABP and Δ[oxCCO] in 12 channels across the forehead of patient 2.

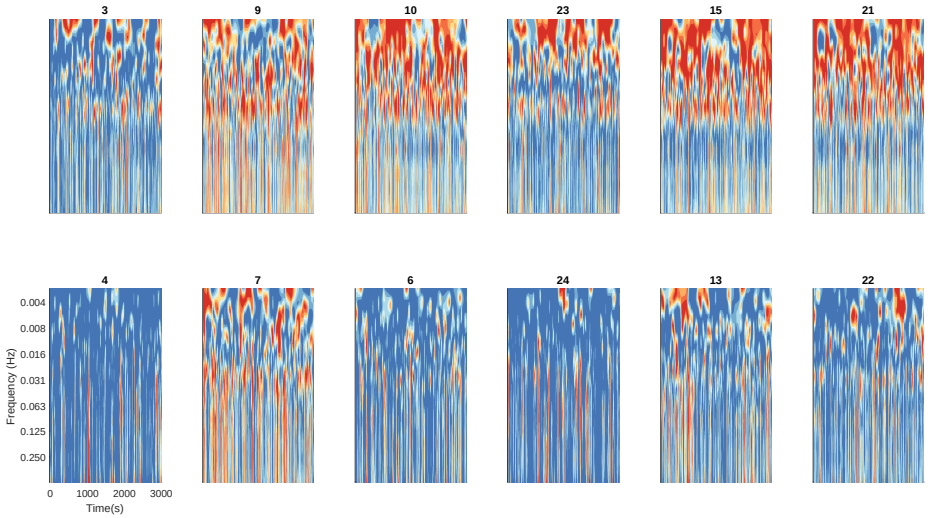

Figure 6.45: Semblance between Δ[HbO_2] and Δ[oxCCO] in 12 channels across the forehead in patient 2.

Semblance analysis between Vmca1 and six TOI measurements demonstrated a strong agreement between the two measures (Figure 6.46). In this case , Vmca was largely in agreement with TOI parameters in all six regions monitored.

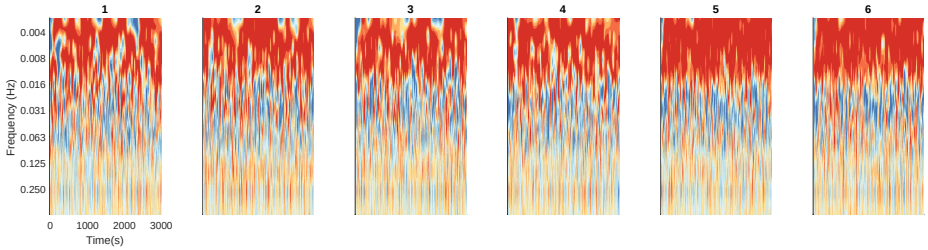

Figure 6.46: Semblance plots between Vmca1 and six TOI measuring monitoring different regions of the frontal lobe. Strong in-phase relationship is seen in all six plots, demonstrating strong agreement between Vmca1 and TOI values.

Patient 3 Figure 6.47, 6.48 show the semblance between ABP and HbO_2 and oxCCO signals at 12 NIRS measurement channels with SDS of 35 mm across the forehead in patient 3. No distinct difference could be seen in semblance plots for oxyhaemoglobin and CCO reactivity indices of this patient.

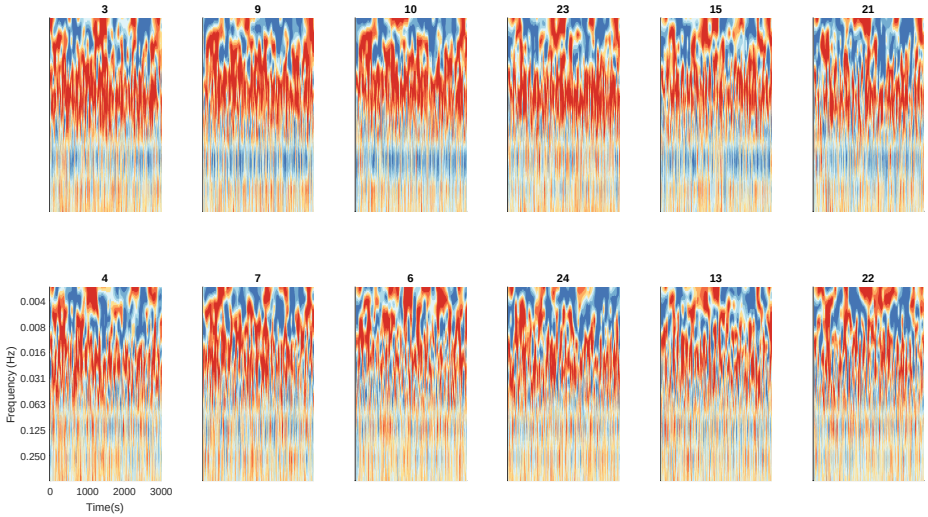

Figure 6.47: Semblance between ABP and HbO_2 in 12 channels across the forehead of patient 3. Pressure passive oscillations of ABP and HbO_2 are evident and are reflected by large red areas, reflecting in-phase oscillations between the two variables.

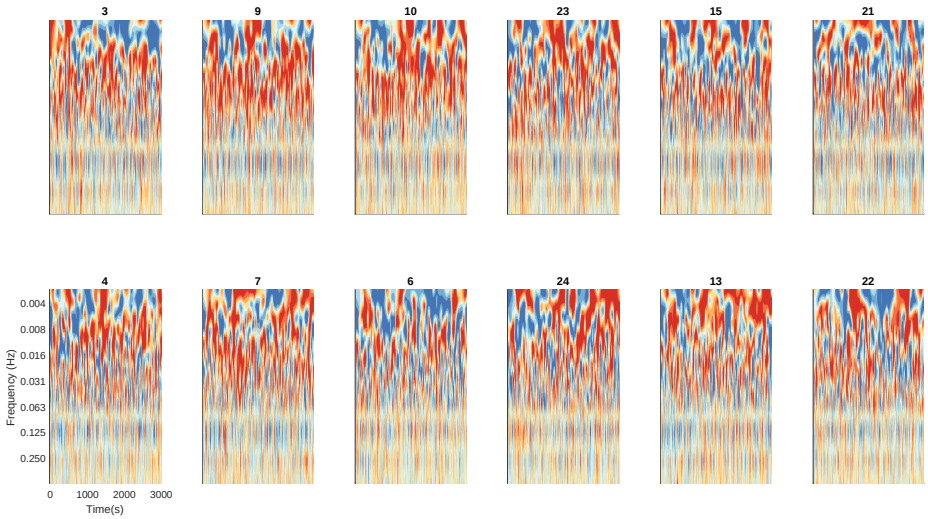

Figure 6.48: Semblance between ABP and oxCCO in 12 channels across the forehead of patient 3. There is evidence of passive oscillations between ABP and oxCCO.

The semblance analysis between HbO_2 and oxCCO signal in patient 3 (Figure 6.49) shows a similar pattern to that of patient 1. However, in this patient, anti-phase relationship between HbO_2 and oxCCO only existed in channels monitoring the lower area of the frontal region, suggesting impaired flow-metabolism coupling in these brain regions monitored by these channels.

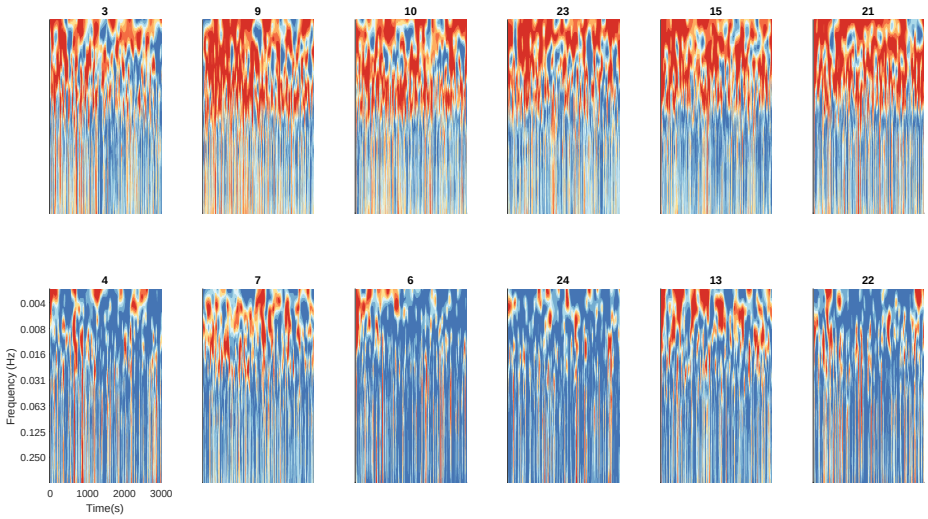

Figure 6.49: Semblance between HbO_2 and oxCCO in patient 3.

Patient 4 Figure 6.50, 6.51 show the semblance between ABP and HbO_2 and oxCCO signals at 12 NIRS measurement channels with SDS of 35 mm across the forehead in patient 4. No distinct feature could be seen in semblance plots for oxyhaemoglobin and CCO reactivity indices of this patient.

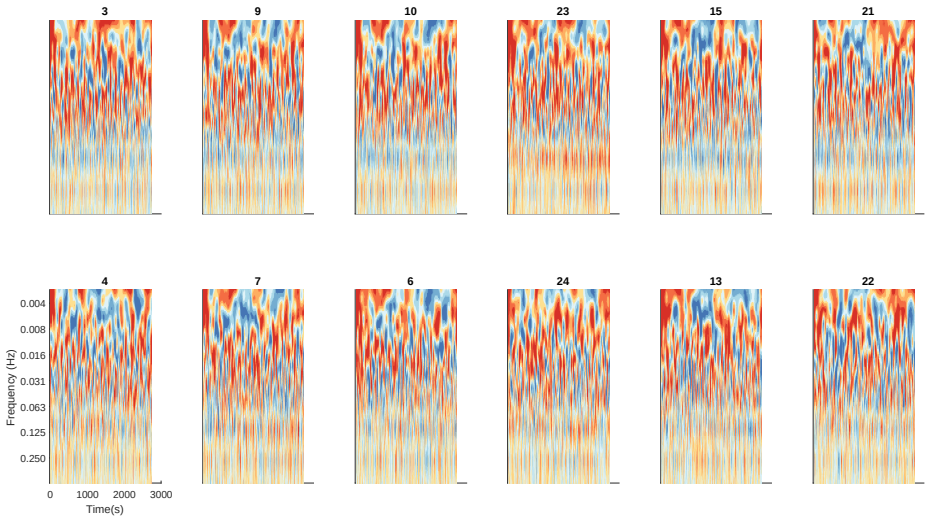

Figure 6.50: Semblance between ABP and HbO_2 in 12 channels across the forehead of patient 4. Pressure passive oscillations of ABP and HbO_2 are evident and are reflected by large red areas, reflecting in-phase oscillations between the two variables.

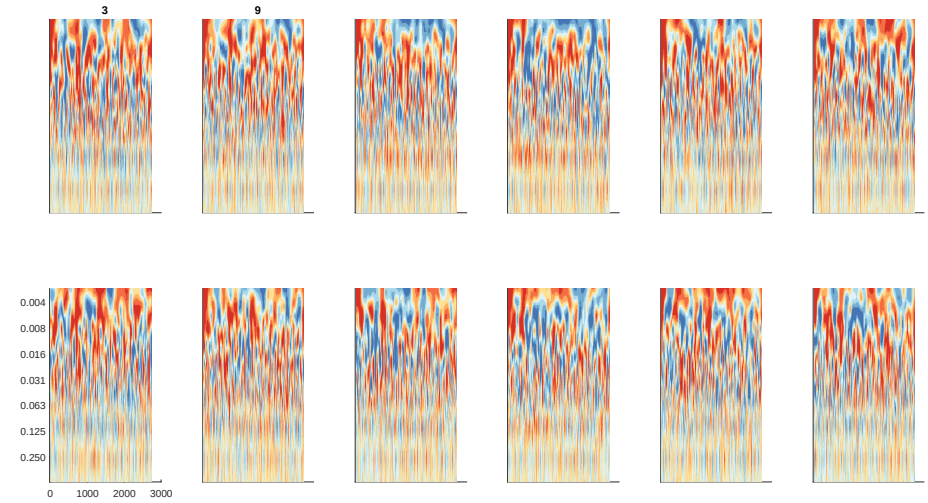

Figure 6.51: Semblance between ABP and oxCCO in 12 channels across the forehead of patient 4.

The semblance analysis between HbO_2 and oxCCO signal in patient 4 (Figure 6.52) shows a similar pattern to that of patient 1. However, in this patient, anti-phase relationship between HbO_2 and oxCCO was only evident in channels monitoring the lower area of the frontal region, suggesting impaired flow-metabolism coupling in these brain regions monitored by these channels.

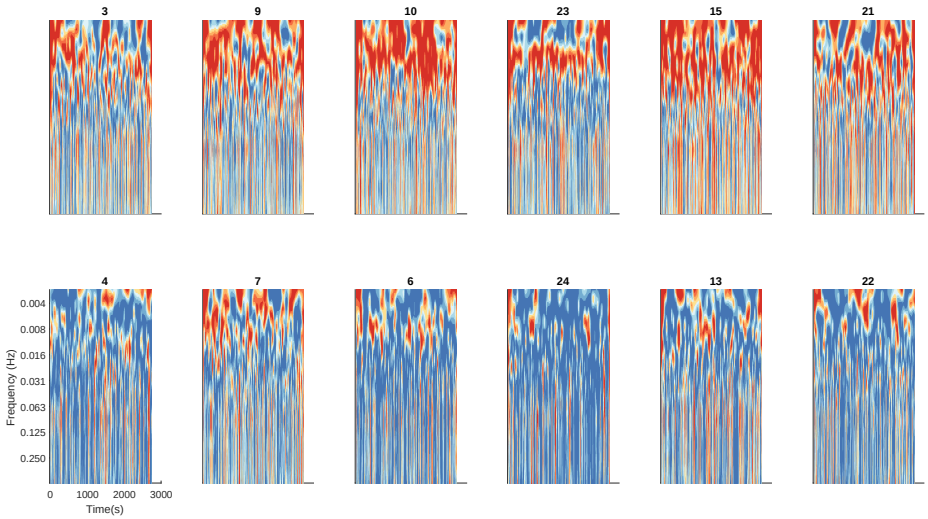

Figure 6.52: Semblance between HbO_2 and oxCCO in patient 4.

Semblance analysis between Vmca1 and six TOI measurements demonstrate a large variation in the time frequency domain (Figure 6.53). This may indicate impaired cerebral autoregulation.

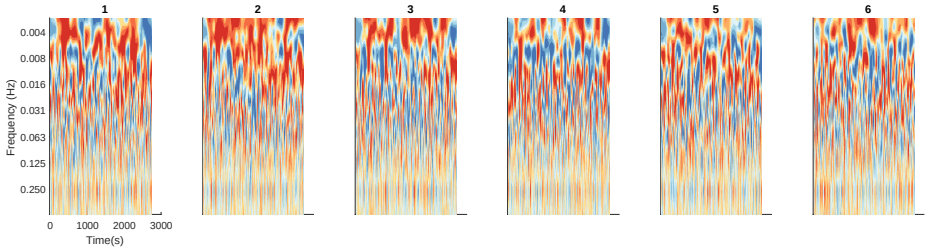

Figure 6.53: Semblance plots between Vmca1 and six TOI measuring monitoring different regions of the frontal lobe in patient 4.

6.4.2.4 Reconstructed images of changes in haemodynamics and metabolism in patient 1

One of the most important advances presented in this thesis is the ability to reconstruct images of changes in cerebral oxygen metabolism. This was enabled by the development of the multi-channel, multi-distance broadband NIRS system and the collection of in vivo data from human subjects. Figure 6.54 shows the reconstructed images of $\Delta[HbO_2]$,Δ[HHb] and Δ[oxCCO] at five time points demonstrating the temporal and regional variation in haemodynamics and metabolism in the frontal region of patient 1. The full reconstructed video can be found in the URL `https://goo.gl/o8vD64`.

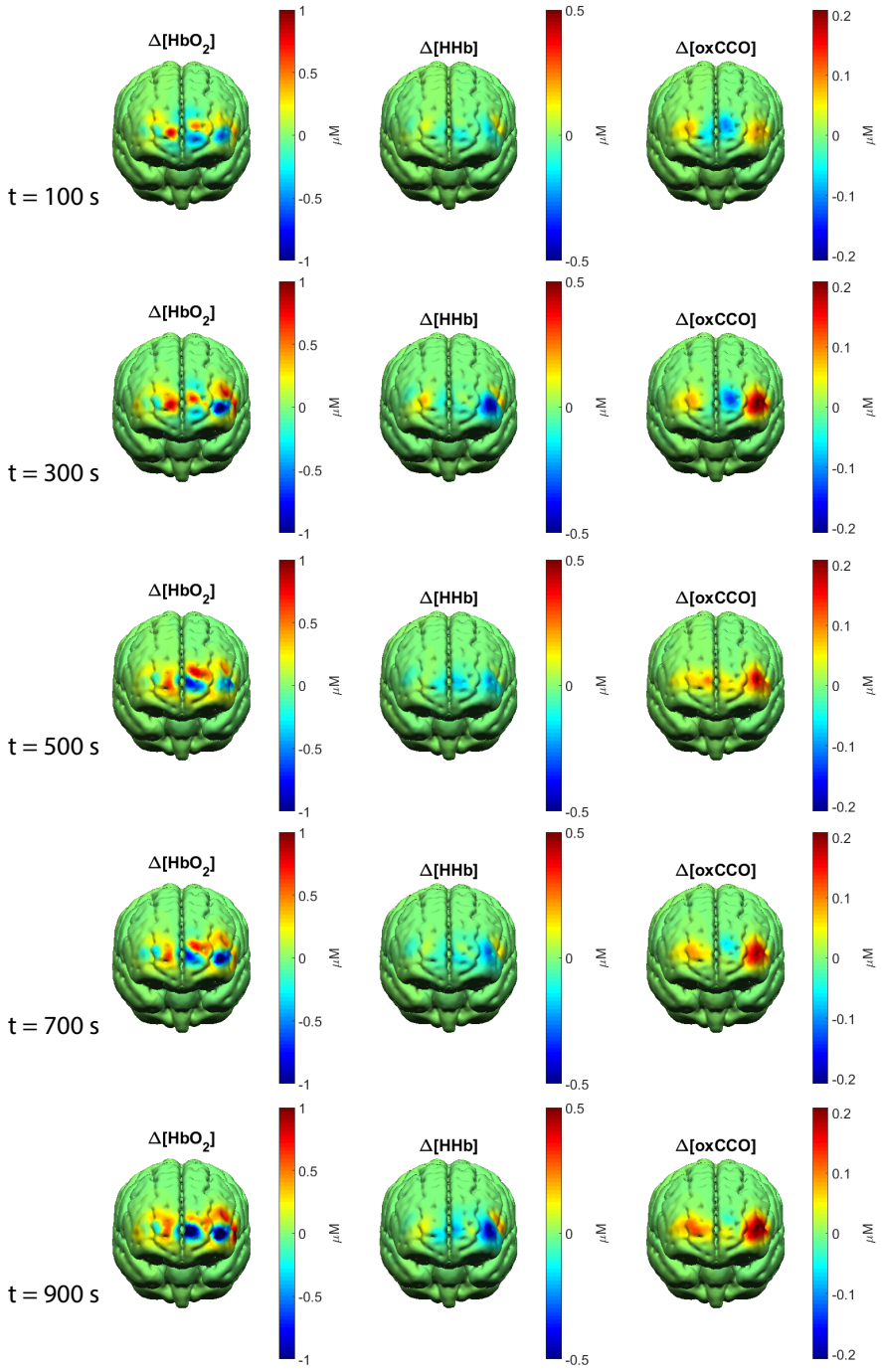

Figure 6.54: Reconstructed images of $\Delta[HbO_2]$,Δ[HHb] and Δ[oxCCO] for five time points in patient 1. Large temporal and spatial variations in haemodynamics and metabolism can be evident from the images.

As can be appreciated by the figure and the video, there was a distinct difference in the spatial variation in the oxCCO image in comparison to the haemoglobin images. Increase in metabolic activity appeared to be localised in specific localised areas in the left and right hemisphere, with much higher amplitude in the left hemisphere, the non-injured brain region. Figure 6.55 shows images of Δ[oxCCO] at two time points to demonstrate the regional and temporal variation in metabolism in the patient 1. The distinct differ-

ence in the distribution of the Δ[oxCCO] signal at different time points was evident.

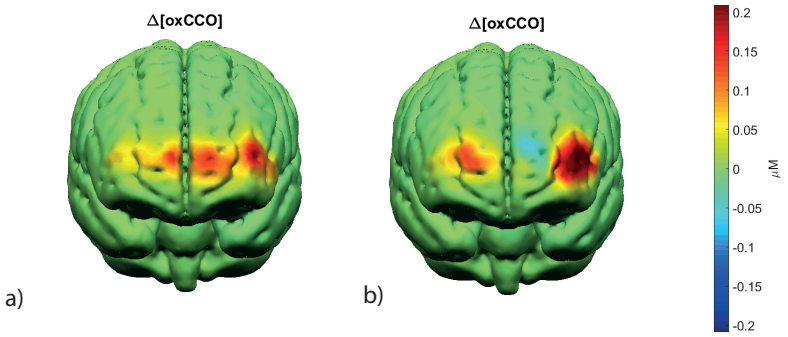

Figure 6.55: Image of Δ[oxCCO] at a) t = 550 s and b) t= 860 s in patient 1.

Figure 6.56 shows the mean NIRS-based cerebrovascular (HbOx, HHbx) and the cerebrometabolic (oxCCOx) reactivity indices in the image domain calculated by correlating the changes in ABP and the individual voxel-based concentration changes of Δ[HbO_2], Δ[HHb] and Δ[oxCCO]. Red regions indicate a high correlation between ABP and concentration changes of NIRS parameters. oxCCOx reactivity image suggested a large region of impaired cerebral autoregulation on the left hemisphere.

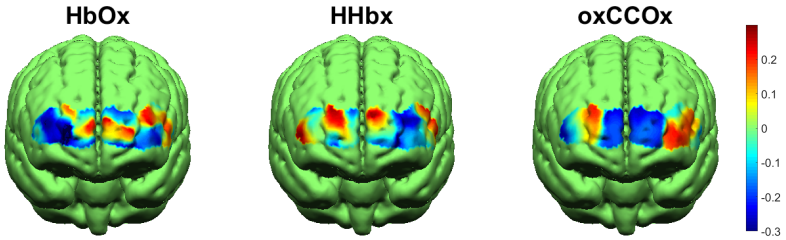

Figure 6.56: NIRS-based cerebrovascular (HbOx and HHbx) and cerebrometabolic (oxCCOx) reactivity indices calculated by correlating the voxel-based concentration changes and ABP in patient 1.

6.4.3 Reconstructed images of changes in haemodynamics and metabolism in patients 2, 3 and 4

6.4.3.1 Patient 2

Figure 6.57 shows the reconstructed images of Δ[HbO_2], Δ[HHb] and Δ[oxCCO] at five time points for patient 2 having subarachnoid haemorrhage. The full reconstructed video can be found in the URL `https://goo.gl/o8vD64`. Changes in Δ[oxCCO] signal were again localised to certain areas of the brain. In this case, a localised decrease in the left hemisphere and a slight increase in the right hemisphere were evident. Δ[HHb] images also show some localised features whereas Δ[HbO_2] images appeared to have more scattered changes.

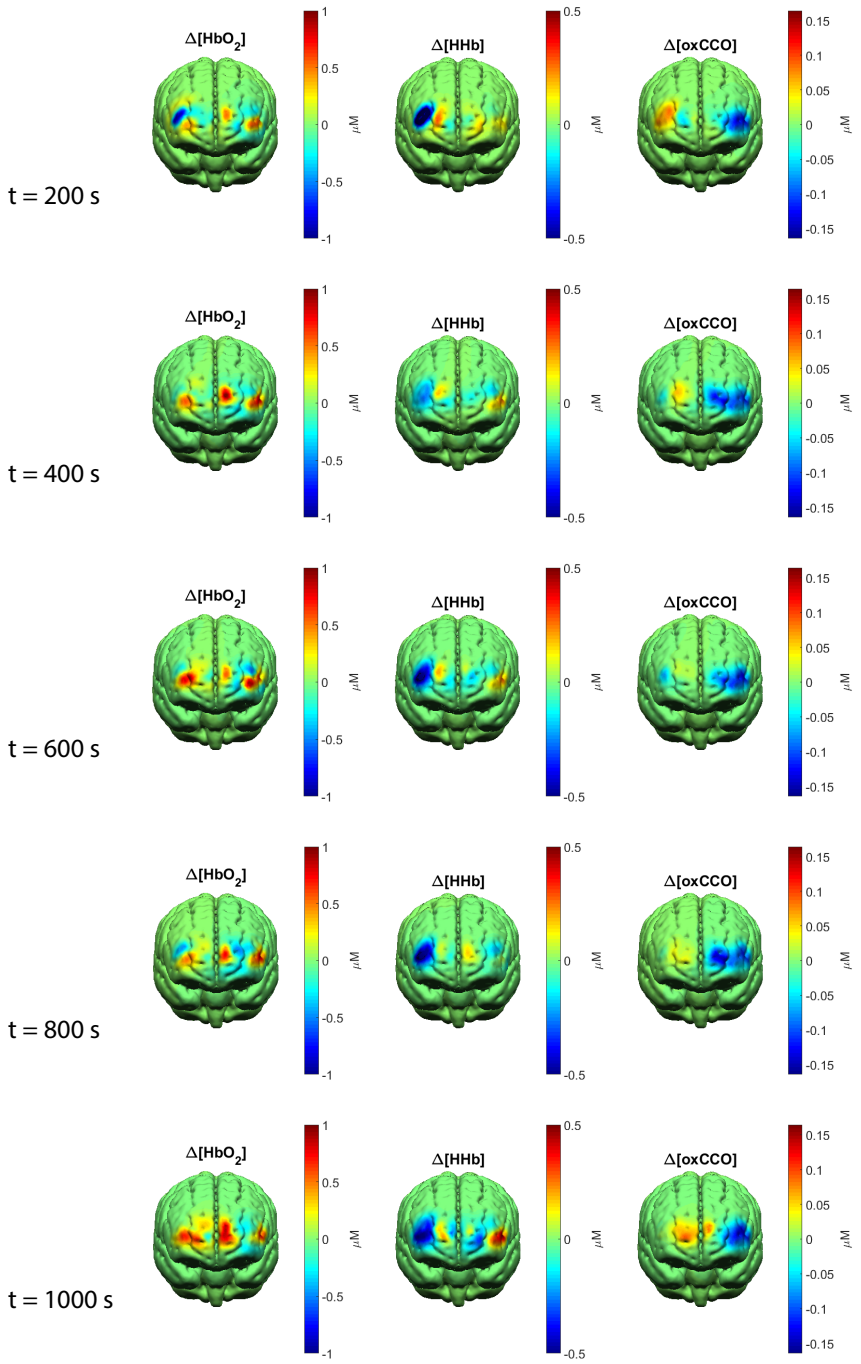

Figure 6.57: Reconstructed images of $\Delta[HbO_2]$, Δ[HHb] and Δ[oxCCO] for five time points in patient 2 having subarachnoid haemorrhage.

Figure 6.58 shows the mean NIRS-based reactivity indices in the image domain for patient 2. oxCCOx reactivity image suggests a focal region of impaired cerebral autoregulation on the right hemisphere.

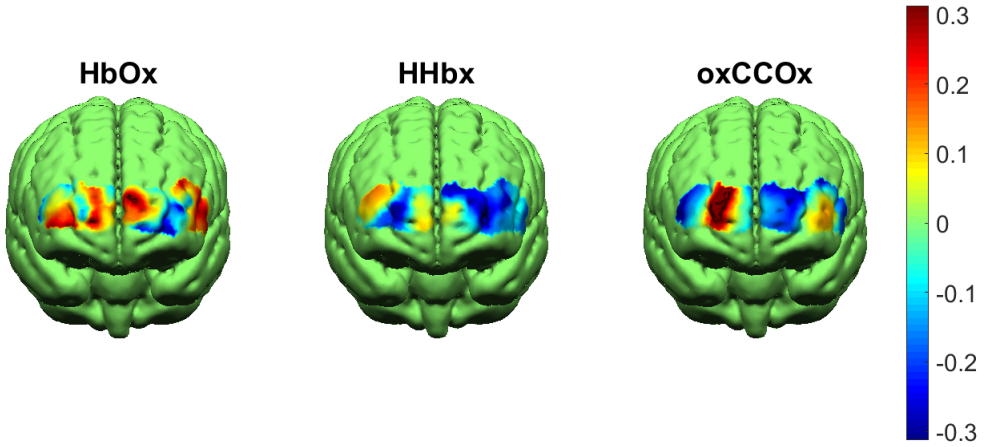

Figure 6.58: NIRS-based cerebrovascular reactivity indices calculated by correlating the voxel-based concentration changes and ABP in patient 2.

6.4.3.2 Patient 3

Figure 6.59 shows the reconstructed images of $\Delta[HbO_2]$, Δ[HHb] and Δ[oxCCO] for five time points for patient 3 having intraventricular haemorrhage. The full reconstructed video can be found in the URL `https://goo.gl/o8vD64`. There was a distinct difference in the spatial variation present in the oxCCO image in comparison to that present in the haemoglobin images. A decrease in metabolic activity appeared to be localised in specific areas in the left and right hemispheres.

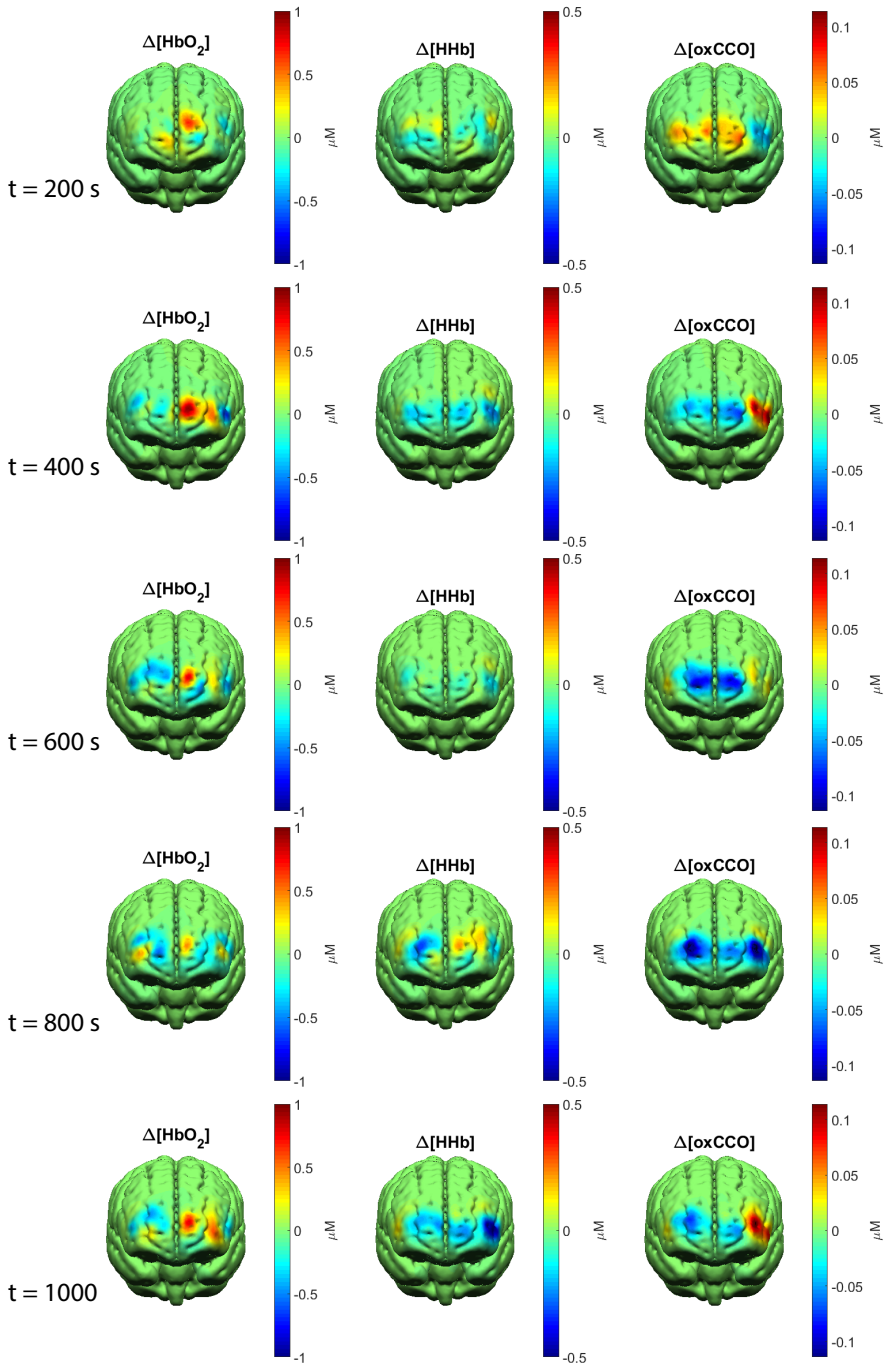

Figure 6.59: Reconstructed images of $\Delta[HbO_2]$,Δ[HHb] and Δ[oxCCO] for five time points in patient 3.

Figure 6.60 shows the mean NIRS-based reactivity indices in the image domain for patient 3. oxCCOx reactivity image suggested a small region of impaired cerebral autoregulation on the left hemisphere.

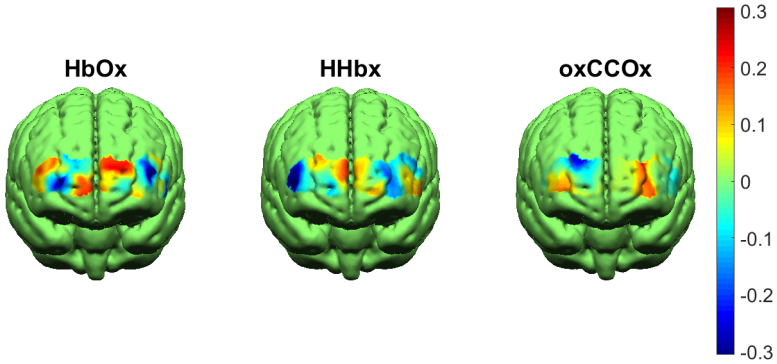

Figure 6.60: Autoregulation reactivity indices calculated by correlating ABP and $\Delta[HbO_2]$,Δ[HHb] and Δ[oxCCO] from patient 3

6.4.3.3 Patient 4

Figure 6.61 shows the reconstructed images of $\Delta[HbO_2]$,Δ[HHb] and Δ[oxCCO] for five time points for patient 4 having left intraparenchymal haemorrhage. The full reconstructed video can be found in the URL `https://goo.gl/o8vD64`. There was a distinct difference in the spatial variation present in the oxCCO image in comparison to that present in the haemoglobin images. Increase in metabolic activity appeared to be localised in specific areas in the left hemisphere.

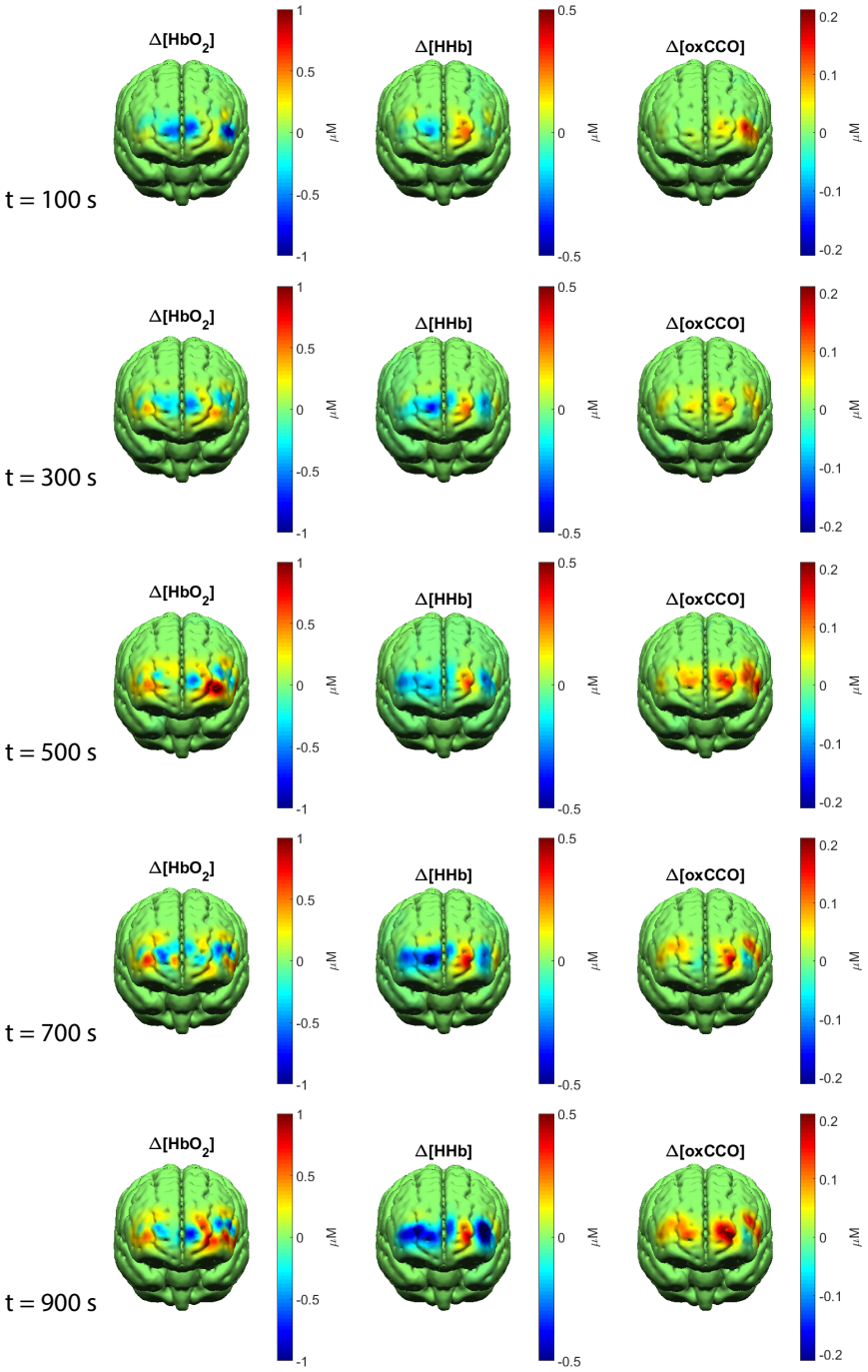

Figure 6.61: Reconstructed images of $\Delta[HbO_2]$,Δ[HHb] and Δ[oxCCO] for five time points in patient 4.

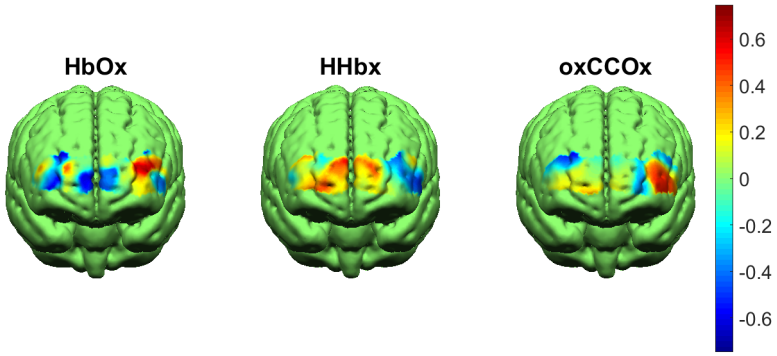

Figure 6.62: Autoregulation reactivity indices calculated by correlating ABP and $\Delta[HbO_2]$,Δ[HHb] and Δ[oxCCO] from patient 4

6.5 Conclusion and discussion

We have investigated the use of the multi-distance, multi-channel broadband NIRS system developed as part of this PhD in the neurocritical care unit, together with other neuromonitoring systems used as part of routine care for patients with acute brain injury. The use of this system in the clinical environment was feasible and allowed multi-site monitoring of the frontal region of patients with ABI. Overcoming the challenges of acquiring data in this clinical environment is an achievement in itself. This has enabled the collection of four multi-modal data sets including systemic physiological variables, non-NIRS cerebral variables and multi-distance, multi-channel broadband NIRS measurements across multiple regions of the frontal region of brain injury patients. These data sets have been analysed using multiple techniques to provide a better understanding of the regional heterogeneity of cerebral haemodynamics and more importantly, metabolism during brain injury.

Regarding the reliability of the system, we have demonstrated the ability of the system to collect complete 24-channel NIRS data on all patients without any interruption. This is not a trivial matter because (standard) neuromonitoring modalities may fail to collect data due to technical difficulties (e.g. TCD), or may be invasive and not indicated (e.g. ICP). Multi-channel NIRS monitoring with its non-invasive nature and ease of application may provide another element to improve the understanding of the state of the brain in specific clinical scenarios where there is an increased risk of cerebral ischaemia. Moreover, this has demonstrated the reliability of multi-channel broadband NIRS for long-term monitoring of brain injury patients. Unlike TCD which may have problems in long-term monitoring due to probe dislocation or drying of gel, multi-channel NIRS does

not have practical limitations in long-term monitoring.

In terms of analysis, we have demonstrated the use of existing analysis techniques on physiological variables in these four data sets and then expanded the use of these techniques to NIRS parameters to calculate regional NIRS-based reactivity indices. Using a moving Pearson correlation coefficient with 300 s time window, autoregulation indices were derived from non-NIRS variables for each of the four data sets to assess the degree of impaired cerebral autoregulation. The wavelet-based analysis was then applied to further investigate the variation in the phase relationship of these variables in the time-frequency domain. This analysis was then applied to investigate the similarity and the phase relationship between NIRS and non-NIRS variables to assess the regional heterogeneity in brain injury. With the reliability of NIRS measurements, NIRS autoregulation indices can be derived with confidence for the whole period of recording. With the advance of multi-channel broadband NIRS, autoregulation indices can be derived for specific regions from the regional measures of haemodynamics and metabolism.

Interestingly, as part of this pilot study, we have observed synchronised oscillations of slow frequency in cerebral blood flow, oxygenation (0.05-0.003 Hz) measured by non-NIRS neuromonitoring and NIRS parameters in a number of channels in two out of four patient cases with acute brain injury. These oscillations are suggested to be the result of the combined influences of myogenic, metabolic and neuronal mechanisms on the cerebral vascular tone [130]. Analysis of those slow wave oscillations using coherence and semblance analyses reveals a stronger correlation between non-NIRS cerebral variables and NIRS parameters in the non-injured regions of the brain than in the injured regions. However, more data are needed to elucidate these findings.

TOI measurement in the adult brain has always been challenging due to technical complexity in the optical interface design and the SRS resolving algorithm. The multi-channel, multi-distance broadband NIRS system with the novel system design has enabled monitoring of TOI across multiple sites in the frontal region of the adult head. In this pilot study, we have demonstrated the measurement of TOI across multiple locations in the frontal region of patients with ABI. Within all four patients, TOI values were within the physiological range and they were highly correlated with Vmca measure of blood flow in the middle cerebral artery in two out of four patients. Using TOI as a surrogate measure of TCD-FV for the assessment of cerebral autoregulation is a promising direction because of its reliability and ease of application. However, more data in both the healthy and injured brains having both TCD-FV and TOI measurements are needed to elucidate this finding.

We have demonstrated the feasibility of using semblance analysis between HbO_2 and oxCCO to assess flow-metabolism coupling across multiple regions of the frontal region of patients with ABI. There is evidence that areas with impaired flow-metabolism coupling may demonstrate an anti-phase relationship between the two parameters. This finding is in agreement with a previous study investigating the phase relationship between NIRS parameters in patients with subarachnoid haemorrhage [135].

Multi-distance, multi-channel broadband NIRS data sets collected in this study have allowed image reconstruction algorithm to be developed to assess changes in haemodynamics and metabolism in the image space following ABI. With the use of multi-channel broadband NIRS, images of Δ[oxCCO] together with $\Delta[HbO_2]$ and Δ[HHb] were reconstructed in ABI patients for the first time, revealing the temporal and spatial variation in haemodynamics and metabolism across different brain regions. These images can be used to assess the regional variation and the localisation of changes in haemodynamics and metabolism. Using these images, we have demonstrated the ability to derive NIRS-based cerebrovascular and cerebrometabolic indices in the image domain which may provide insights into the regional variation in impaired cerebral autoregulation and depressed oxygen metabolism. Although further work is required to optimise the image reconstruction technique, this has opened up new opportunities for the investigation of the spatial haemodynamic response to changes in blood pressure and its effect on mitochondrial metabolic activity.

Previous studies have demonstrated the use of systemic, non-NIRS and NIRS parameters to assess cerebral autoregulation [6], [127], [133]. However, these authors only monitored one or two locations of the injured brain, neglecting the presence of heterogeneity in brain injury. This study has brought the advances of multi-channel broadband NIRS to assess changes in tissue oxygenation, cerebral haemodynamics and metabolism at multiple regions across the frontal region of patients with ABI. These NIRS parameters can be correlated to non-NIRS cerebral and systemic variables to derive autoregulation status of the injured brain. Monitoring multiple brain regions in combination with advanced data analysis techniques can help elucidate relationships between oxygen delivery and metabolism to understand more about regional heterogeneity in impaired cerebral autoregulation and flow-metabolism coupling, two key processes underlying cerebral ischaemia.

This study has given the first insights into the regional variation in oxygen metabolism and flow-metabolism coupling and has allowed different analysis techniques to be assessed for future clinical studies. One of the most important contributions of this study

to NIRS research community is validating the feasibility of reconstructing tomographic images of Δ[oxCCO] in brain injured patients. Together with tomographic images of $\Delta[HbO_2]$ and Δ[HHb], these can be used to investigate regional heterogeneity of impaired cerebral pressure autoregulation and deranged flow-metabolism coupling not only in ABI but in other clinical scenarios where there is a high risk of cerebral ischaemia.

This pilot study is the first step in investigating the spatial variation in cellular oxygen metabolism in the injured brain using a non-invasive optical method. As a result, there are certain limitations. The first limitation is the number of patients monitored. Due to time constraints, it was only possible to study four patients. Moreover, we could only monitor patients without any intervention because of the limitation in ethical approval. Another limitation is the fact that these four patients have different brain injury types, which made it inappropriate to attempt any grouped results. These issues can be mitigated in future clinical studies with specific protocol design in a large cohort of patients with a specific type of brain injury. Physiological challenges such as hyperoxia can be used to investigate spatial variation in depressed oxygen metabolism following ABI as this challenge has been used successfully by Ghosh and Tisdall ([7], [127] to investigate cellular oxygen metabolic processes in brain injury.

Despite these limitations, it is important to realise that achieving the monitoring and the analysis of these four patient data sets with different types of brain injury marks a significant milestone. We now have a monitoring system and analysis techniques that can monitor the variations in cerebral haemodynamics and more importantly cerebral oxygen metabolism that is applicable across the whole spectrum of brain injury. Given that metabolic failure underlies all type of brain injury, we now have a new non-invasive tool to investigate it.

Chapter 7

Conclusion, discussion and future work

This thesis has presented lots of advances in the field of NIRS both in terms of instrumentation development and in vivo results in the healthy and injured adult human brain. This last chapter will summarise the work presented in this thesis, discuss various results as a whole and suggest future areas of research that have arisen from this work.

7.1 Conclusion

7.1.1 Summary

This PhD thesis describes the progressive development and applications of a multi-channel, multi-distance broadband NIRS system with the capability of measuring changes in haemoglobin concentrations, the oxidation state of cytochrome c oxidase and tissue oxygenation in the adult human brain.

7.1.2 Instrumentation

The main components of the multi-channel broadband NIRS system are two customised spectrographs and two light sources. Each spectrograph receives light input from a custom-built fibre bundle comprised of six individual fibres. Each light source is connected to a custom-built bifurcated fibre bundle to create two source fibre bundles. The light sources are time-multiplexed to alternately deliver light to the pair of fibres connected to them. Two probe holders were designed and 3D printed, one for frontal lobe application and the other for visual cortex application. Overall, the system can monitor

the frontal cortex over 24 NIRS measurement channels and the visual cortex over 16 NIRS measurement channels with the frequency of 0.36Hz (one full measurement cycle in 2.8 s).

7.1.3 Functional activation studies

The system was used to measure the response of Δ[oxCCO] over multiple channels probing the visual and the prefrontal cortices during functional activation tasks. Δ[oxCCO] signal showed an increase during the stimulation period followed by a decrease during the resting period while the haemoglobin signals showed the typical haemodynamic response to functional activation. This response of the Δ[oxCCO] signal was seen in multiple channels probing a localised brain area, presumably responding to the functional activation task. Moreover, there is a spatial variation in the response of the Δ[oxCCO] signal with channels probing different areas showing different amplitudes of the signal. More modelling work is needed for further interpretation of these data, taking into account the relative sensitivity of the system to different regions of the cortex.

7.1.4 Acute brain injury patient case studies

The system with the frontal probe holder was used in a pilot study to monitor the frontal region of four patients with acute brain injury over 24 measurement channels. This was to demonstrate that the system could be used in a clinical environment alongside other monitoring systems and there is potential that clinically useful insights can be derived from the combination of multi-channel NIRS data and systemic physiological data. Multiple analysis techniques were applied to showcase the potential benefits of having multi-channel Δ[oxCCO] data from brain injured patients. As discussed in Chapter 6, the pilot study presented had limitations; however, its result can be used to guide future clinical studies with multi-channel CCO measurements. More details of this will be discussed in the future work section.

7.1.5 Reconstructed images of △[oxCCO]

Multi-channel, multi-distance broadband data sets collected during this PhD has enabled the development of an image reconstruction algorithm that was used to reconstruct the very first sets of tomographic images of concentration changes of oxCCO. This has enabled the visualisation and the analysis of the spatial variation in the Δ[oxCCO] signal in the healthy adult brain during functional activation and in the injured brain

during periods of clinical stability without intervention.

Reconstructed images of Δ[oxCCO] during visual functional activation showed clear localised changes in all subjects. These changes were localised to the same functional area as evident in the reconstructed images of Δ[HbO_2] and Δ[HHb]. This technique provides a unique opportunity to investigate the cerebral energy metabolism during functional activation in addition to the traditional haemodynamic response.

Reconstructed images Δ[oxCCO], Δ[HbO_2] and Δ[HHb] in patients with acute brain injury during periods of clinical stability without clinical intervention showed large variation in both the haemodynamics and metabolism in various localised areas of the prefrontal region. The calculated NIRS-based reactivity indices in the image domain show some degree of heterogeneity. Some regions have a highly positive reactivity index, correlating to impaired cerebral autoregulation whereas other regions have a negative reactivity index, correlating to intact cerebral autoregulation. This demonstrates the feasibility of calculating autoregulation indices of haemodynamics and metabolism using the reconstructed images of Δ[HbO_2], Δ[HHb] and Δ[oxCCO] in patients with brain injury. Although further work is required to optimise the technique, there is considerable potential to use this technique to characterise the spatial haemodynamic and metabolic response to changes in blood pressure in patients with acute brain injury.

7.2 Discussion

The work presented in this PhD thesis has introduced lots of advances to the field of NIRS. A broadband NIRS instrumentation has been developed with advances introduced to the hardware, software and resolving algorithm. This instrument was used to investigate the changes in the visual and the prefrontal cortices during functional activation tasks, producing the first spatially resolved changes of the oxCCO signal, a measure of cerebral oxygen metabolism across various areas of the adult human brain. After these functional experiments in the healthy adult brain, the system was then used to monitor the frontal brain region of patients with ABI, producing the first spatially resolved changes of the oxCCO signal from the injured brain. Moreover, using the multi-channel, multi-distance broadband NIRS data, tomographic images of Δ[oxCCO] were reconstructed for the first time in the healthy brain during a functional activation task and in the injured brain during periods of clinical stability. These images reveal an interesting spatial pattern of changes in cerebral oxygen metabolism alongside the traditional pattern of changes in haemodynamics and oxygenation.

7.3 Future work

The development introduced by this work has also opened up opportunities for future areas of research which will be discussed in this section.

7.3.1 Ongoing studies

Following the success of the functional activation studies on the visual cortex, the multi-channel, multi-distance broadband NIRS system is currently being used to monitor the visual cortex of subjects in a more challenging neuroscience experiment to test the role of perceptual load in visual awareness. The hypothesis is that visual distractors (inverting checkerboard) will intrude upon awareness in low load experimental conditions resulting in an increase in oxCCO whereas awareness will be restricted to the content of focused attention when the attended information involves high perceptual load, resulting in little change in oxCCO. The results of this experiment could shine a light onto the neuroscience of visual awareness and provide supporting evidence to answer the question of to what degree do distractor stimuli get process.

7.3.2 NIRS system upgrades

Despite being used successfully in two functional activation studies and in a pilot clinical study, the multi-channel broadband NIRS system can be improved in several aspects.

The number of light sources can be increased to increase the number of measurement channels. This can be done by building and integrating a new multiplexing unit into the system to multiplex the output of the light source. This multiplexing unit could use a 1D axis galvanometer-based scanning mirror, focusing optics and a source plug disk holding multiple optical fibres. The angle of the incident beam can be changed by changing the orientation of the galvanometer mirrors. It is, therefore, possible to sequentially inject the incident beam into one of the output source fibres. If four source fibres are connected to the each source plug disk, from the two halogen bulb light sources, the system can have eight sequentially illuminated source fibres.

Larger CCD cameras can be used to increase the number of detector fibres that can be fitted into the CCD camera imaging area. Currently, the system uses the PIXIS:512f CCD camera that has an imaging area of 12.3 mm x 12.3 mm. Princeton Instruments now has a larger CCD camera, the PIXIS:1300 with imaging area of 26.8 mm x 26 mm. This potentially can fit a double number of detector fibres.

These changes in hardware need corresponding changes in the software to control the

system and collect the intensity spectra from an increased number of channels. However, full head coverage with overlapping multi-channel, multi-distance NIRS measurements can be acquired and this can present a huge advance in the field of fNIRS.

7.3.3 Clinical studies

The main advancement introduced by this thesis is the ability to monitor the Δ[oxCCO] signal across multiple regions of the brain and visualise these changes using a tomographic image reconstruction algorithm. Regional monitoring of cerebral oxygen metabolism from multiple brain areas in patients can provide more information to help identify regions with profound cerebral energy failure and therefore target management therapy to prevent it. These are important for patient groups where there is an increased risk of cerebral ischemic injury and a resulting metabolic crisis. These patient groups include but are not limited to patients undergoing cardiac surgery, carotid endarterectomy, general anaesthesia and patients with brain injury. In the case of brain injury where metabolic failure has been recognised as a key component of the pathophysiology, the benefits of monitoring Δ[oxCCO] signal across multiple regions are considerable. In this thesis, Δ[oxCCO] has been monitored over multiple regions of patients with ABI. However, due to time limitation, we could only monitor four patients, each with a different type of injury. As for future work, a full clinical study where the system is used to monitor the changes of oxCCO in a large group of brain injury patients with a specific type of injury is recommended. This can contribute greatly to the understanding of the pathophysiology of brain injury.

A more complex study can be done using the system to investigate the spatial variation in the injury pathway following brain injury. In brain injury, as mentioned earlier, metabolic dysfunction without ischaemia is a common finding. This may be implicated by diffusion-limited oxygen transport or mitochondrial dysfunction. These pathways can be investigated using hyperoxia challenges. Hyperoxia can induce an increase in cerebral oxygen availability which would lead to an increase in oxCCO in regions where diffusion-limited oxygen transport is the injury pathway whereas no significant change would be observed in regions where mitochondrial dysfunction is the injury pathway.

Bibliography

[1] H. Obrig and A. Villringer, "Beyond the visible - Imaging the human brain with light," *Journal of Cerebral Blood Flow and Metabolism*, vol. 23, no. 1, pp. 1–18, 2003.

[2] M. Wolf, M. Ferrari, and V. Quaresima, "Progress of near-infrared spectroscopy and topography for brain and muscle clinical applications.," *Journal of Biomedical Optics*, vol. 12, no. 6, p. 062 104, 2007.

[3] F. Scholkmann, S. Kleiser, A. J. Metz, R. Zimmermann, J. Mata Pavia, U. Wolf, and M. Wolf, "A review on continuous wave functional near-infrared spectroscopy and imaging instrumentation and methodology," *NeuroImage*, vol. 85, pp. 6–27, 2014.

[4] R. Springett, J. Newman, M. Cope, and D. T. Delpy, "Oxygen dependency and precision of cytochrome oxidase signal from full spectral NIRS of the piglet brain.," *American Journal of Physiology - Heart and Circulatory Physiology*, vol. 279, no. 5, H2202–H2209, 2000.

[5] M. M. Tisdall, I. Tachtsidis, T. S. Leung, C. E. Elwell, and M. Smith, "Near-infrared spectroscopic quantification of changes in the concentration of oxidized cytochrome c oxidase in the healthy human brain during hypoxemia.," *Journal of Biomedical Optics*, vol. 12, no. 2, p. 024 002, 2007.

[6] ——, "Changes in the Attenuation of Near Infrared Spectra by the Healthy Adult Brain During Hypoxaemia Cannot be Accounted for Solely by Changes in the Concentrations of Oxy- and Deoxy-Haemoglobin," *Advances in Experimental Medicine and Biology*, vol. 614, pp. 217–225, 2008.

[7] ——, "Increase in cerebral aerobic metabolism by normobaric hyperoxia after traumatic brain injury.," *Journal of Neurosurgery*, vol. 109, no. 3, pp. 424–32, Sep. 2008.

[8] I. Tachtsidis, M. Tisdall, T. S. Leung, C. E. Cooper, D. T. Delpy, M. Smith, and C. E. Elwell, "Investigation of in vivo measurement of cerebral cytochrome- c -oxidase redox changes using near-infrared spectroscopy in patients with orthostatic hypotension," *Physiological Measurement*, vol. 28, no. 2, pp. 199–211, 2007.

[9] I. Tachtsidis, T. S. Leung, A. Ghosh, M. Smith, C. E. Cooper, and C. E. Elwell, "Multi-Wavelength, Depth Resolved, Scattering and Pathlength Corrected in vivo Near-Infrared Spectroscopy of Brain Tissue," *Biomedical Optics and 3-D Imaging*, vol. 2, BTuB7, 2010.

[10] I. Tachtsidis, L. Gao, T. S. Leung, M. Kohl-Bareis, C. E. Cooper, and C. E. Elwell, "A hybrid multi-distance phase and broadband spatially resolved spectrometer and algorithm for resolving absolute concentrations of chromophores in the near-infrared light spectrum," *Advances in Experimental Medicine and Biology*, vol. 662, no. v, pp. 169–175, 2010.

[11] C. Kolyva, I. Tachtsidis, A. Ghosh, T. Moroz, C. E. Cooper, M. Smith, C. E. Elwell, N. C. Unit, L. Hospitals, and L. Wcn, "Systematic investigation of changes in oxidized cerebral cytochrome c oxidase concentration during frontal lobe activation in healthy adults," *Biomedical Optics Express*, vol. 3, no. 10, p. 2550, 2012.

[12] C. Kolyva, A. Ghosh, I. Tachtsidis, D. Highton, C. E. Cooper, M. Smith, and C. E. Elwell, "Cytochrome c oxidase response to changes in cerebral oxygen delivery in the adult brain shows higher brain-specificity than haemoglobin.," *NeuroImage*, vol. 85 Pt 1, pp. 234–44, Jan. 2014.

[13] G. Bale, S. Mitra, J. Meek, N. Robertson, and I. Tachtsidis, "A new broadband near-infrared spectroscopy system for in-vivo measurements of cerebral cytochrome-c-oxidase changes in neonatal brain injury.," *Biomedical Optics Express*, vol. 5, no. 10, pp. 3450–66, Sep. 2014.

[14] S. Mitra, G. Bale, S. Mathieson, C. Uria-Avellanal, J. Meek, I. Tachtsidis, and N. J. Robertson, "Changes in Cerebral Oxidative Metabolism during Neonatal Seizures Following Hypoxic-Ischemic Brain Injury.," *Frontiers in Pediatrics*, vol. 4, no. August, p. 83, 2016.

[15] P. Phan, D. Highton, S. Brigadoi, I. Tachtsidis, M. Smith, and C. E. Elwell, "Spatial Distribution of Changes in Oxidised Cytochrome C Oxidase During Visual Stimulation Using Broadband Near Infrared Spectroscopy Imaging," in *Oxygen Transport to Tissue XXXVIII*, Q. Luo, L. Z. Li, D. K. Harrison, H. Shi, and D. F. Bruley, Eds. Cham: Springer International Publishing, 2016, pp. 195–201.

[16] P. Phan, D. Highton, J. Lai, M. Smith, C. Elwell, and I. Tachtsidis, "Multi-channel multi-distance broadband near-infrared spectroscopy system to measure the spatial response of cellular oxygen metabolism and tissue oxygenation," *Biomedical Optics Express*, vol. 7, no. 11, p. 4424, 2016.

[17] J. M. Murkin and M. Arango, "Near-infrared spectroscopy as an index of brain and tissue oxygenation.," *British Journal of Anaesthesia*, vol. 103 Suppl, pp. i3–i13, 2009.

[18] M. Smith, "Shedding light on the adult brain: a review of the clinical applications of near-infrared spectroscopy.," *Philosophical Transactions. Series A, Mathematical, Physical, and Engineering Sciences*, vol. 369, no. 1955, pp. 4452–69, 2011.

[19] P. Vespa, M. Bergsneider, N. Hattori, H.-M. Wu, S.-C. Huang, N. A. Martin, T. C. Glenn, D. L. McArthur, and D. A. Hovda, "Metabolic Crisis without Brain Ischemia is Common after Traumatic Brain Injury: A Combined Microdialysis and Positron Emission Tomography Study," *Journal of Cerebral Blood Flow & Metabolism*, vol. 25, no. 6, pp. 763–774, 2005.

[20] A. Zauner, W. P. Daugherty, M. R. Bullock, D. S. Warner, W. R. Selman, and R. J. Dempsey, "Brain oxygenation and energy metabolism: Part I - Biological function and pathophysiology," *Neurosurgery*, vol. 51, no. 2, pp. 289–302, 2002.

[21] M. Pagani, D. Salmaso, G. G. Sidiras, C. Jonsson, H. Jacobsson, S. a. Larsson, and F. Lind, "Impact of acute hypobaric hypoxia on blood flow distribution in brain.," *Acta Physiologica (Oxford, England)*, vol. 202, no. 2, pp. 203–209, 2011.

[22] W. M. Armstead and R. Raghupathi, "Endothelin and the neurovascular unit in pediatric traumatic brain injury.," *Neurological Research*, vol. 33, no. 2, pp. 127–32, 2011.

[23] T. Maki, K. Hayakawa, L.-D. D. Pham, C. Xing, E. H. Lo, and K. Arai, "Biphasic Mechanisms of Neurovascular Unit Injury and Protection in CNS Diseases," *CNS & Neurological Disorders - Drug Targets*, vol. 12, no. 3, pp. 302–315, 2013. arXiv: NIHMS150003.

[24] E. C. Peterson, Z. Wang, and G. Britz, "Regulation of cerebral blood flow," *International Journal of Vascular Medicine*, vol. 2011, 2011.

[25] D. R. Harder, C. Zhang, and D. Gebremedhin, "Astrocytes function in matching blood flow to metabolic activity.," *News in Physiological Sciences*, vol. 17, no. February, pp. 27–31, 2002.

[26] B. T. Hawkins and T. P. Davis, "The Blood-Brain Barrier / Neurovascular Unit in Health and Disease," *Pharmacological Reviews*, vol. 57, no. 2, pp. 173–185, 2005.

[27] E. H. Lo, J. P. Broderick, and M. A. Moskowitz, "tPA and Proteolysis in the Neurovascular Unit," *Stroke*, vol. 35, no. 2, pp. 354–356, 2004.

[28] C. R. Figley and P. W. Stroman, "The role(s) of astrocytes and astrocyte activity in neurometabolism, neurovascular coupling, and the production of functional neuroimaging signals," *European Journal of Neuroscience*, vol. 33, no. 4, pp. 577–588, 2011.

[29] D. A. Pelligrino, F. Vetri, and H. L. Xu, "Purinergic mechanisms in gliovascular coupling," *Seminars in Cell and Developmental Biology*, vol. 22, no. 2, pp. 229–236, 2011.

[30] S. Duchemin, M. Boily, N. Sadekova, and H. Girouard, "The complex contribution of NOS interneurons in the physiology of cerebrovascular regulation," *Frontiers in Neural Circuits*, vol. 6, 2012.

[31] N. J. Abbott, L. Rönnbäck, and E. Hansson, "Astrocyte–endothelial interactions at the blood–brain barrier," *Nature Reviews Neuroscience*, vol. 7, no. 1, pp. 41–53, 2006.

[32] K. Kisler, A. R. Nelson, A. Montagne, and B. V. Zlokovic, "Cerebral blood flow regulation and neurovascular dysfunction in Alzheimer disease," *Nature Reviews Neuroscience*, no. May, 2017.

[33] R. Aaslid, K. F. Lindegaard, W. Sorteberg, and H. Nornes, "Cerebral autoregulation dynamics in humans," *Stroke*, vol. 20, no. 1, pp. 45–52, 1989.

[34] H. a. Kontos, E. P. Wei, R. M. Navari, J. E. Levasseur, W. I. Rosenblum, and J. L. Patterson, "Responses of cerebral arteries and arterioles to acute hypotension and hypertension.," *The American Journal of Physiology*, vol. 234, no. 4, H371–H383, 1978.

[35] O. B. Paulson, S. Strandgaard, and L. Edvinsson, "Cerebral autoregulation," *Cerebrovascular and Brain Metabolism Reviews*, vol. 2, no. 2, pp. 161–92, 1990.

[36] R. V. Immink, B.-J. H. van den Born, G. A. van Montfrans, R. P. Koopmans, J. M. Karemaker, and J. J. van Lieshout, "Impaired cerebral autoregulation in patients with malignant hypertension.," *Circulation*, vol. 110, no. 15, pp. 2241–5, 2004.

[37] W. M. Bayliss, "On the local reactions of the arterial wall to changes of internal pressure.," *The Journal of Physiology*, vol. 28, no. 3, pp. 220–31, 1902.

[38] S. Mellander, "Functional aspects of myogenic vascular control.," *Journal of Hypertension. Supplement : Official Journal of the International Society of Hypertension*, vol. 7, no. 4, S21–30, discussion S31, 1989.

[39] G. Osol, J. F. Brekke, K. McElroy-Yaggy, and N. I. Gokina, "Myogenic tone, reactivity, and forced dilatation: a three-phase model of in vitro arterial myogenic behavior.," *American Journal of Physiology. Heart and Circulatory Physiology*, vol. 283, no. 6, H2260–7, 2002.

[40] L. Kuo, M. J. Davis, and W. M. Chilian, "Myogenic activity in isolated subepicardial and subendocardial coronary arterioles," *American Journal of Physiology*, vol. 255, no. 6, pp. 1558–1562, 1988.

[41] P. A. Jackson and B. R. Duling, "Myogenic response and wall mechanics of arterioles," *American Journal of Physiology - Heart and Circulatory Physiology*, vol. 257, no. 4, H1147–H1155, 1989.

[42] R. Schubert and M. J. Mulvany, "The myogenic response: established facts and attractive hypotheses.," *Clinical Science*, vol. 96, no. 4, pp. 313–326, 1999.

[43] G. M. Rubanyi, A. D. Freay, K. Kauser, A. Johns, and D. R. Harder, "Mechanoreception by the endothelium: Mediators and mechanisms of pressure- and flow-induced vascular responses," *Journal of Vascular Research*, vol. 27, no. 2-5, pp. 246–257, 1990.

[44] G. M. Rubanyi, J. C. Romero, and P. M. Vanhoutte, "Flow-induced release of endothelium-derived relaxing factor.," *The American Journal of Physiology*, vol. 250, no. 6 Pt 2, H1145–9, 1986.

[45] G. M. Rubanyi, "Endothelium-dependent pressure-induced contraction of isolated canine carotid arteries," *American Journal of Physiology - Heart and Circulatory Physiology*, vol. 255, no. 4, pp. 24/4, 1988.

[46] J. E. Deanfield, J. P. Halcox, and T. J. Rabelink, "Endothelial Function and Dysfunction," *Circulation*, vol. 115, pp. 1285–1295, 2007.

[47] P. T. Fox and M. E. Raichle, "Focal physiological uncoupling of cerebral blood flow and oxidative metabolism during somatosensory stimulation in human subjects.," *Proceedings of the National Academy of Sciences of the United States of America*, vol. 83, no. February 1986, pp. 1140–4, 1986.

[48] D. Malonek, U. Dirnagl, U. Lindauer, K. Yamada, I. Kanno, and A. Grinvald, "Vascular imprints of neuronal activity: Relationships between the dynamics of cortical blood flow, oxygenation, and volume changes following sensory stimulation," *Proceedings of the National Academy of Sciences*, vol. 94, no. 26, pp. 14 826–14 831, 1997.

[49] E. M. C. Hillman, A. Devor, M. B. Bouchard, A. K. Dunn, G. W. Krauss, J. Skoch, B. J. Bacskai, A. M. Dale, and D. A. Boas, "Depth-resolved optical imaging and microscopy of vascular compartment dynamics during somatosensory stimulation," *NeuroImage*, vol. 35, no. 1, pp. 89–104, 2007. arXiv: NIHMS150003.

[50] B. Stefanovic, E. Hutchinson, V. Yakovleva, V. Schram, J. T. Russell, L. Belluscio, A. P. Koretsky, and A. C. Silva, "Functional Reactivity of Cerebral Capillaries," *Journal of Cerebral Blood Flow & Metabolism*, vol. 28, no. 5, pp. 961–972, 2008. arXiv: NIHMS150003.

[51] J. P. Culver, A. M. Siegel, M. A. Franceschini, J. B. Mandeville, and D. A. Boas, "Evidence that cerebral blood volume can provide brain activation maps with better spatial resolution than deoxygenated hemoglobin," *NeuroImage*, vol. 27, no. 4, pp. 947–959, 2005.

[52] P. Li, Q. Luo, W. Luo, S. Chen, H. Cheng, and S. Zeng, "Spatiotemporal characteristics of cerebral blood volume changes in rat somatosensory cortex evoked by sciatic nerve stimulation and obtained by optical imaging," *Journal of Biomedical Optics*, vol. 8, no. 4, pp. 629–635, 2003.

[53] A. C. Ngai and H. R. Winn, "Pial arteriole dilation during somatosensory stimulation is not mediated by an increase in CSF metabolites," *American Journal of Physiology - Heart and Circulatory Physiology*, vol. 282, no. 3, H902–H907, 2002.

[54] H. Girouard and C. Iadecola, "Neurovascular coupling in the normal brain and in hypertension, stroke, and Alzheimer disease.," *Journal of Applied Physiology*, vol. 100, no. 1, pp. 328–335, 2006.

[55] A. A. Phillips, F. H. Chan, M. M. Z. Zheng, A. V. Krassioukov, and P. N. Ainslie, "Neurovascular coupling in humans: Physiology, methodological advances and clinical implications.," *Journal of Cerebral Blood Flow and Metabolism*, vol. 36, no. 4, pp. 647–664, 2016.

[56] V. Muoio, P. B. Persson, and M. M. Sendeski, "The neurovascular unit - concept review," *Acta Physiologica*, vol. 210, no. 4, pp. 790–798, 2014.

[57] a. M. Harper and H. I. Glass, "Effect of alterations in the arterial carbon dioxide tension on the blood flow through the cerebral cortex at normal and low arterial blood pressures.," *Journal of Neurology, Neurosurgery, and Psychiatry*, vol. 28, no. 5, pp. 449–452, 1965.

[58] E. M. C. Hillman, "Coupling Mechanism and Significance of the BOLD Signal: A Status Report.," *Annual review of neuroscience*, vol. 37, pp. 161–181, 2014.

[59] K. Nizar, H. Uhlirova, P. Tian, P. A. Saisan, Q. Cheng, L. Reznichenko, K. L. Weldy, T. C. Steed, V. B. Sridhar, C. L. MacDonald, J. Cui, S. L. Gratiy, S. Sakadzic, D. A. Boas, T. I. Beka, G. T. Einevoll, J. Chen, E. Masliah, A. M. Dale, G. A. Silva, and A. Devor, "In vivo Stimulus-Induced Vasodilation Occurs without IP3 Receptor Activation and May Precede Astrocytic Calcium Increase," *Journal of Neuroscience*, vol. 33, no. 19, pp. 8411–8422, 2013. arXiv: NIHMS150003.

[60] W. Sun, E. McConnell, J.-F. Pare, Q. Xu, M. Chen, W. Peng, D. Lovatt, X. Han, Y. Smith, and M. Nedergaard, "Glutamate-dependent neuroglial calcium signaling differs between young and adult brain.," *Science (New York, N.Y.)*, vol. 339, no. 6116, pp. 197–200, 2013.

[61] B. R. Chen, M. B. Bouchard, A. F. H. McCaslin, S. A. Burgess, and E. M. C. Hillman, "High-speed vascular dynamics of the hemodynamic response," *NeuroImage*, vol. 54, no. 2, pp. 1021–1030, 2011. arXiv: NIHMS150003.

[62] N. Takata, T. Nagai, K. Ozawa, Y. Oe, K. Mikoshiba, and H. Hirase, "Cerebral Blood Flow Modulation by Basal Forebrain or Whisker Stimulation Can Occur Independently of Large Cytosolic Ca2+ Signaling in Astrocytes," *PLoS ONE*, vol. 8, no. 6, 2013.

[63] H. Hotta, S. Uchida, F. Kagitani, and N. Maruyama, "Control of cerebral cortical blood flow by stimulation of basal forebrain cholinergic areas in mice," *Journal of Physiological Sciences*, vol. 61, no. 3, pp. 201–209, 2011.

[64] B. Cauli, "Cortical GABA Interneurons in Neurovascular Coupling: Relays for Subcortical Vasoactive Pathways," *Journal of Neuroscience*, vol. 24, no. 41, pp. 8940–8949, 2004.

[65] D. Attwell, A. Buchan, S. Charpak, M. Lauritzen, B. MacVicar, and E. Newman, "Glial and neuronal control of brain blood flow," *Nature*, vol. 468, pp. 232–241, 2010.

[66] E. N. E. Marieb and K. Hoehn, *Human Anatomy & Physiology*. 2010, vol. 7, pp. 664–668.

[67] B. Alberts, A. Johnson, J. Lewis, M. Raff, K. Roberts, and P. Walter, *Molecular Biology of the Cell*. 2002, 1616 pages.

[68] A. Namslauer and P. Brzezinski, "Structural elements involved in electron-coupled proton transfer in cytochrome c oxidase," in *FEBS Letters*, vol. 567, 2004, pp. 103–110.

[69] M. Banaji, "A generic model of electron transport in mitochondria," *Journal of Theoretical Biology*, vol. 243, no. 4, pp. 501–516, 2006.

[70] H. R. Heekeren, M. Kohl, H. Obrig, R. Wenzel, W. von Pannwitz, S. J. Matcher, U. Dirnagl, C. E. Cooper, and A. Villringer, "Noninvasive assessment of changes in cytochrome-c oxidase oxidation in human subjects during visual stimulation.," *Journal of Cerebral Blood Flow & Metabolism*, vol. 19, no. 6, pp. 592–603, Jun. 1999.

[71] K. Uludağ, J. Steinbrink, M. Kohl-Bareis, R. Wenzel, A. Villringer, and H. Obrig, "Cytochrome-c-oxidase redox changes during visual stimulation measured by near-infrared spectroscopy cannot be explained by a mere cross talk artefact.," *NeuroImage*, vol. 22, no. 1, pp. 109–19, May 2004.

[72] N. Schaul, "The fundamental neural mechanisms of electroencephalography," *Electroencephalography and Clinical Neurophysiology*, vol. 106, no. 2, pp. 101–107, 1998.

[73] P. L. Nunez and R. Srinivasan, *Electric Fields of the Brain: The neurophysics of EEG*. 2009, pp. 1–611.

[74] D. Chitnis, D. Airantzis, D. Highton, R. Williams, P. Phan, V. Giagka, S. Powell, R. J. Cooper, I. Tachtsidis, M. Smith, C. E. Elwell, J. C. Hebden, and N. Everdell, "Towards a wearable near infrared spectroscopic probe for monitoring concentrations of multiple chromophores in biological tissue in vivo," *Review of Scientific Instruments*, vol. 87, no. 6, 2016.

[75] F. F. Jöbsis, "Noninvasive, infrared monitoring of cerebral and myocardial oxygen sufficiency and circulatory parameters.," *Science*, vol. 198, no. 4323, pp. 1264–1267, 1977.

[76] D. R. Woodard, H Q and White, "The composition of body tissues," *The British Journal of Radiology*, vol. 59, no. December, pp. 1209–1218, 1986.

[77] *https://www.ucl.ac.uk/medphys/research/borl/intro/spectra (Accessed July 2017).*

[78] O.-M. H. Richter and B. Ludwig, "Cytochrome c oxidase — structure, function, and physiology of a redox-driven molecular machine," in *Reviews of Physiology, Biochemistry and Pharmacology*. Berlin, Heidelberg: Springer Berlin Heidelberg, 2003, pp. 47–74.

[79] C. E. Cooper, S. J. Matcher, J. S. Wyatt, M. Cope, G. C. Brown, E. M. Nemoto, and D. T. Delpy, "Near-infrared spectroscopy of the brain: relevance to cytochrome oxidase bioenergetics.," *Biochemical Society Transactions*, vol. 22, no. 4, pp. 974–980, 1994.

[80] D. T. Delpy, M. Cope, P. van der Zee, S. Arridge, S. Wray, and J. Wyatt, "Estimation of optical pathlength through tissue from direct time of flight measurement.," *Physics in Medicine and Biology*, vol. 33, no. 12, pp. 1433–1442, 1988. arXiv: 0407003 [physics].

[81] S. J. Matcher, M. Cope, and D. T. Delpy, "Use of the water absorption spectrum to quantify tissue chromophore concentration changes in near-infrared spectroscopy.," *Physics in Medicine and Biology*, vol. 39, no. 1, pp. 177–96, 1994.

[82] D. Highton, I. Tachtsidis, A. Tucker, C. Elwell, and M. Smith, "Near Infrared Light Scattering Changes Following Acute Brain Injury," *Advances in Experimental Medicine and Biology*, vol. 876, DOI 1, E. C. Elwell, S. T. Leung, and K. D. Harrison, Eds., pp. 35–40, 2016.

[83] E. Okada, M. Firbank, M. Schweiger, Arridge, M. Cope, and D. Delpy, "Theoretical and experimental investigation of near-infrared light propagation in a model of the adult head," *Applied Optics*, vol. 36, no. 1, pp. 21–31, 1997.

[84] G. C. Brown, M. Crompton, and S. Wray, "Cytochrome oxidase content of rat brain during development.," *Biochimica et Biophysica Acta*, vol. 1057, no. 2, pp. 273–275, 1991.

[85] C. E. Cooper and R. Springett, "Measurement of cytochrome oxidase and mitochondrial energetics by near-infrared spectroscopy.," *Philosophical Transactions of the Royal Society of London. Series B, Biological Sciences*, vol. 352, no. 1354, pp. 669–76, Jun. 1997.

[86] C. E. Cooper, M. Cope, R. Springett, P. N. Amess, J. Penrice, L. Tyszczuk, S. Punwani, R. Ordidge, J. Wyatt, and D. T. Delpy, "Use of mitochondrial inhibitors to demonstrate that cytochrome oxidase near-infrared spectroscopy can measure mitochondrial dysfunction noninvasively in the brain.," *Journal of Cerebral Blood Flow & Metabolism*, vol. 19, no. 1, pp. 27–38, 1999.

[87] K. Uludag, M. Kohl, J. Steinbrink, H. Obrig, and A. Villringer, "Cross talk in the Lambert-Beer calculation for near-infrared wavelengths estimated by Monte Carlo simulations.," *Journal of Biomedical Optics*, vol. 7, no. 1, pp. 51–9, 2002.

[88] S. Matcher, C. Elwell, C. Cooper, M. Cope, and D. Delpy, "Performance Comparison of Several Published Tissue Near-Infrared Spectroscopy Algorithms," *Analytical Biochemistry*, vol. 227, no. 1, pp. 54–68, 1995.

[89] S. Suzuki, S. Takasaki, T. Ozaki, and Y. Kobayashi, "A tissue oxygenation monitor using NIR spatially resolved spectroscopy," *Proceedings of SPIE*, vol. 3597, no. January 1999, pp. 582–592, 1999.

[90] P. G. Al-Rawi, P. Smielewski, and P. J. Kirkpatrick, "Evaluation of a near-infrared spectrometer (NIRO 300) for the detection of intracranial oxygenation changes in the adult head.," *Stroke*, vol. 32, no. 11, pp. 2492–2500, 2001.

[91] M. S. Patterson, B. Chance, and B. C. Wilson, "Time resolved reflectance and transmittance for the non-invasive measurement of tissue optical properties," *Applied Optics*, vol. 28, no. 12, pp. 2331–2336, 1989.

[92] a. P. Gibson, J. C. Hebden, and S. R. Arridge, "Recent advances in diffuse optical imaging.," *Physics in Medicine and Biology*, vol. 50, no. 4, R1–R43, 2005.

[93] A. T. Eggebrecht, S. L. Ferradal, A. Robichaux-Viehoever, M. S. Hassanpour, H. Dehghani, A. Z. Snyder, T. Hershey, and J. P. Culver, "Mapping distributed brain function and networks with diffuse optical tomography," *Nature Photonics*, vol. 8, no. 6, pp. 448–454, 2014. arXiv: NIHMS150003.

[94] S. R. Arridge and M. Schweiger, "Part 2 : Finite-element-method calculations e e e e," *Applied Optics*, 1995.

[95] D. Chitnis, R. Cooper, L. Dempsey, S. Powell, S. Quaggia, D. Highton, C. Elwell, J. Hebden, and N. Everdell, "Functional imaging of the human brain using a modular, fibre-less, high-density diffuse optical tomography system," *Biomedical Optics Express*, vol. 7, no. 10, pp. 4275–4288, 2016.

[96] J. E. Brazy and D. V. Lewis, "Changes in cerebral blood volume and cytochrome aa3 during hypertensive peaks in preterm infants," *The Journal of Pediatrics*, vol. 108, no. 6, pp. 983–987, 1986.

[97] N. B. Hampson, E. M. Camporesi, B. W. Stolp, R. E. Moon, J. E. Shook, J. A. Griebel, and C. A. Piantadosi, "Cerebral oxygen availability by NIR spectroscopy during transient hypoxia in humans.," *Journal of Applied Physiology*, vol. 69, no. 3, pp. 907–913, 1990.

[98] J. S. Wyatt, D. T. Delpy, M. Cope, S. Wray, and E. O. R. Reynolds, "Quantification of cerebral oxygenation and haemodynamics in sick newborn infants by near infrared spectrophotometry," *The Lancet*, vol. 328, no. 8515, pp. 1063–1066, 1986.

[99] K. D. Liem, J. C. W. Hopman, B. Oeseburg, A. F. J. De Haan, and L. A. A. Kollée, "The effect of blood transfusion and haemodilution on cerebral oxygenation and haemodynamics in newborn infants investigated by near infrared spectrophotometry," *European Journal of Pediatrics*, vol. 156, no. 4, pp. 305–310, 1997.

[100] F. van Bel, C. a. Dorrepaal, M. J. Benders, P. E. Zeeuwe, M. van de Bor, and H. M. Berger, "Changes in cerebral hemodynamics and oxygenation in the first 24 hours after birth asphyxia.," *Pediatrics*, vol. 92, no. 3, pp. 365–372, 1993.

[101] D. C. McCormick, a. D. Edwards, G. C. Brown, J. S. Wyatt, A. Potter, M. Cope, D. T. Delpy, and E. O. Reynolds, "Effect of indomethacin on cerebral oxidized cytochrome oxidase in preterm infants.," *Pediatric Research*, vol. 33, no. 6, pp. 603–608, 1993.

[102] G. Grubhofer, W. Tonninger, P. Keznickl, P. Skyllouriotis, M. Ehrlich, M. Hiesmayr, and A. Lassnigg, "A comparison of the monitors INVOS 3100 and NIRO 500 in detecting changes in cerebral oxygenation," *Acta Anaesthesiol Scand*, vol. 43, no. 4, pp. 470–475, 1999.

[103] I. Tachtsidis, M. M. Tisdall, C. Pritchard, T. S. Leung, A. Ghosh, C. E. Elwell, and M. Smith, "Analysis of the Changes in the Oxidation of Brain Tissue Cytochrome-c-Oxidase in Traumatic Brain Injury Patients during Hypercapnoea," in *Oxygen Transport to Tissue XXXII*, J. C. LaManna, M. A. Puchowicz, K. Xu, D. K. Harrison, and D. F. Bruley, Eds. Boston, MA: Springer US, 2011, pp. 9–14.

[104] R. Nosrati, K. Vesely, T. A. Schweizer, and V. Toronov, "Event-related changes of the prefrontal cortex oxygen delivery and metabolism during driving measured by hyperspectral fNIRS," *Biomedical Optics Express*, vol. 7, no. 4, p. 1323, 2016.

[105] I. Tachtsidis, T. S. Leung, B. Tahir, C. E. Elwell, M. Kohl-Bareis, M. Gramer, and C. E. Cooper, "A Hybrid Multi-Distance Phase and Broadband Spatially Resolved Algorithm for Resolving Absolute Concentrations of Chromophores in the Near-Infrared Light Spectrum: Results from Studies in Dynamic Phantoms," *Biomedical Optics*, no. v, BSuE76, 2008.

[106] M. Gramer, "Further Development and Validation of a Multi-Distance NIR Broadband Spectrometer for Monitoring Brain Tissue Haemodynamics on the Adult Head : Application on Dynamic Phantoms . Diploma Thesis," 2007.

[107] D. S. Bacon, M. Sherif Afifi, J. A. Griebel, and E. M. Camporesi, "Cerebrocortical oxygenation and ventilatory response during sustained hypoxia," *Respiration Physiology*, vol. 80, no. 2-3, pp. 245–257, 1990.

[108] I. Tachtsidis, M. M. Tisdall, T. S. Leung, C. Pritchard, C. E. Cooper, M. Smith, and C. E. Elwell, "Relationship between brain tissue haemodynamics, oxygenation and metabolism in the healthy human adult brain during hyperoxia and hypercapnea," *Advances in Experimental Medicine and Biology*, vol. 645, pp. 315–320, 2009.

[109] I. Tachtsidis and F. Scholkmann, "False positives and false negatives in functional near-infrared spectroscopy: issues, challenges, and the way forward," *Neurophotonics*, vol. 3, no. 3, p. 039 801, 2016.

[110] S. Brigadoi, P. Phan, D. Highton, S. Powell, R. J. Cooper, J. Hebden, M. Smith, I. Tachtsidis, C. E. Elwell, and A. P. Gibson, "Image reconstruction of oxidized cerebral cytochrome C oxidase changes from broadband near-infrared spectroscopy data.," *Neurophotonics*, vol. 4, no. 2, p. 021 105, 2017.

[111] A. Custo, D. A. Boas, D. Tsuzuki, I. Dan, R. Mesquita, B. Fischl, W. E. L. Grimson, and W. Wells, "Anatomical atlas-guided diffuse optical tomography of brain activation," *NeuroImage*, vol. 49, no. 1, pp. 561–567, 2010. arXiv: NIHMS150003.

[112] R. J. Cooper, M. Caffini, J. Dubb, Q. Fang, A. Custo, D. Tsuzuki, B. Fischl, W. Wells, I. Dan, and D. A. Boas, "Validating atlas-guided DOT: A comparison of diffuse optical tomography informed by atlas and subject-specific anatomies," *NeuroImage*, vol. 62, no. 3, pp. 1999–2006, 2012. arXiv: NIHMS150003.

[113] S. Brigadoi and R. J. Cooper, "How short is short? Optimum source–detector distance for short-separation channels in functional near-infrared spectroscopy," *Neurophotonics*, vol. 2, no. 2, p. 025 005, 2015.

[114] V. Fonov, A. C. Evans, K. Botteron, C. R. Almli, R. C. McKinstry, and D. L. Collins, "Unbiased average age-appropriate atlases for pediatric studies," *NeuroImage*, vol. 54, no. 1, pp. 313–327, 2011. arXiv: NIHMS150003.

[115] M. Schweiger and S. Arridge, "The Toast++ software suite for forward and inverse modeling in optical tomography.," *Journal of Biomedical Optics*, vol. 19, no. 4, p. 040 801, 2014.

[116] K. L. M. Koenraadt, J. Duysens, M. Smeenk, and N. L. W. Keijsers, "Multi-channel NIRS of the primary motor cortex to discriminate hand from foot activity," *Journal of Neural Engineering*, vol. 9, no. 4, p. 046 010, 2012.

[117] G. Bale, "Development of Optical Instrumentation and Methods to Monitor Brain Oxygen Metabolism : Application to Neonatal Birth Asphyxia," no. April, 2014.

[118] T. J. Germon, P. D. Evans, N. J. Barnett, P. Wall, a. R. Manara, and R. J. Nelson, "Cerebral near infrared spectroscopy: emitter-detector separation must be increased.," *British Journal of Anaesthesia*, vol. 82, no. 6, pp. 831–837, 1999.

[119] E. Kirilina, A. Jelzow, A. Heine, M. Niessing, H. Wabnitz, R. Brühl, B. Ittermann, A. M. Jacobs, and I. Tachtsidis, "The physiological origin of task-evoked systemic artefacts in functional near infrared spectroscopy," *NeuroImage*, vol. 61, no. 1, pp. 70–81, 2012.

[120] M. Banich, M. Milham, R. Atchley, N. Cohen, A. Webb, T. Wszalek, A. Kramer, Z. Liang, A. Wright, J. Shenker, and R. Magin, "fMri studies of Stroop tasks reveal unique roles of anterior and posterior brain systems in attentional selection.," *Journal of Cognitive Neuroscience*, vol. 12, no. 6, pp. 988–1000, 2000.

[121] M. P. Milham, M. T. Banich, E. D. Claus, and N. J. Cohen, "Practice-related effects demonstrate complementary roles of anterior cingulate and prefrontal cortices in attentional control," *NeuroImage*, vol. 18, no. 2, pp. 483–493, 2003.

[122] D. Malonek and A. Grinvald, "Interactions Between Electrical Activity and Cortical Microcirculation Revealed by Imaging Spectroscopy: Implications for Functional Brain Mapping," *Science*, vol. 272, no. 5261, pp. 551–554, 1996.

[123] D. A. Hovda, A. Yoshino, T. Kawamata, Y. Katayama, and D. P. Becker, "Diffuse prolonged depression of cerebral oxidative metabolism following concussive brain injury in the rat: a cytochrome oxidase histochemistry study," *Brain Research*, vol. 567, no. 1, pp. 1–10, 1991.

[124] P. M. Vespa, D. McArthur, K. O'Phelan, T. Glenn, M. Etchepare, D. Kelly, M. Bergsneider, N. A. Martin, and D. A. Hovda, "Persistently Low Extracellular Glucose Correlates With Poor Outcome 6 Months After Human Traumatic Brain Injury Despite a Lack of Increased Lactate: A Microdialysis Study," *Journal of Cerebral Blood Flow & Metabolism*, pp. 865–877, 2003.

[125] M. S. Yang, D. S. DeWitt, D. P. Becker, and R. L. Hayes, "Regional brain metabolite levels following mild experimental head injury in the cat.," *Journal of Neurosurgery*, vol. 63, no. 4, pp. 617–621, 1985.

[126] a. Bainbridge, I. Tachtsidis, S. D. Faulkner, D. Price, T. Zhu, E. Baer, K. D. Broad, D. L. Thomas, E. B. Cady, N. J. Robertson, and X. Golay, "Brain mitochondrial

oxidative metabolism during and after cerebral hypoxia-ischemia studied by simultaneous phosphorus magnetic-resonance and broadband near-infrared spectroscopy," *NeuroImage*, vol. 102, pp. 173–183, 2013.

[127] A. Ghosh, D. Highton, C. Kolyva, I. Tachtsidis, C. E. Elwell, and M. Smith, "Hyperoxia results in increased aerobic metabolism following acute brain injury," *Journal of Cerebral Blood Flow & Metabolism*, p. 0271678X16679171, 2016.

[128] C. Zweifel, A. Lavinio, L. A. Steiner, D. Radolovich, P. Smielewski, I. Timofeev, M. Hiler, M. Balestreri, P. J. Kirkpatrick, J. D. Pickard, P. Hutchinson, and M. Czosnyka, "Continuous monitoring of cerebrovascular pressure reactivity in patients with head injury," *Neurosurgical Focus*, vol. 25, no. 4, E2, 2008.

[129] L. A. Steiner, M. Czosnyka, and S. K. Piechnik, "Continuous monitoring of cerebrovascular pressure reactivity allows determination of optimal cerebral perfusion pressure in patients with traumatic brain injury," *Critical Care*, vol. 30, no. 4, pp. 733–738, 2002. arXiv: `0609029v1 [arXiv:nlin]`.

[130] R. Steinmeier, C. Bauhuf, U. Hübner, R. D. Bauer, R. Fahlbusch, R. Laumer, and I. Bondar, "Slow Rhythmic Oscillations of Blood Pressure, Intracranial Pressure, Microcirculation, and Cerebral Oxygenation Dynamic Interrelation and Time Course in Humans," *Stroke*, vol. 27, no. 12, pp. 2236–2243, 1996.

[131] A. Grinsted, J. C. Moore, and S. Jevrejeva, "Application of the cross wavelet transform and wavelet coherence to geophysical time series," *Nonlinear Processes in Geophysics*, vol. 11, no. 5/6, pp. 561–566, 2004. arXiv: `hal-00302394,version1`.

[132] G. R. J. Cooper and D. R. Cowan, "Comparing time series using wavelet-based semblance analysis," *Computers and Geosciences*, vol. 34, no. 2, pp. 95–102, 2008.

[133] D. Highton, A. Ghosh, I. Tachtsidis, J. Panovska-Griffiths, C. E. Elwell, and M. Smith, "Monitoring cerebral autoregulation after brain injury: Multimodal assessment of cerebral slow-wave oscillations using near-infrared spectroscopy," *Anesthesia and Analgesia*, vol. 121, no. 1, pp. 198–205, 2015.

[134] L. A. Steiner, D. Pfister, S. P. Strebel, D. Radolovich, P. Smielewski, and M. Czosnyka, "Near-infrared spectroscopy can monitor dynamic cerebral autoregulation in adults," *Neurocritical Care*, vol. 10, no. 1, pp. 122–128, 2009.

[135] D. Highton, D. Highton, A. Ghosh, I. Tachtsidis, C. Elwell, and M. Smith, "Analysis of slow wave oscillations in cerebral haemodynamics and metabolism following

subarachnoid haemorrhage," *Advances in Experimental Medicine and Biology*, vol. 812, pp. 195–201, 2014.